OPTICAL AND CHEMICAL CHARACTERISATION OF THE EFFECTS OF HIGH-PRESSURE HYDRODYNAMIC CAVITATION ON DIESEL FUEL

Zeeshan Fatmi

This thesis is submitted in fulfilment of the requirements of the degree of

Doctor of Philosophy

School of Mathematics, Computer Science and Engineering

Department of Mechanical Engineering

February 2018

Table of Contents

Chapter 1 - Introduction **1**

Chapter 2 – Literature Review **7**

2.1 Diesel Fuel 7

2.1.1 Distillation from Crude Oil and Conversion Processes 7

2.1.2 Diesel Fuel Components 10

2.1.3 Diesel Fuel Properties and Performance Parameters 14

2.1.4 Additives 20

2.1.5 Alternative Fuels 21

2.2 Modern Diesel FIE 25

2.2.1 Spill Valves and In-Vehicle Fuel Recirculation 26

2.3 Deposits in Diesel FIE 30

2.3.1 Internal Injector Deposits 31

2.4 Cavitation 34

2.4.1 Cavitation Bubble Dynamics 37

2.4.2 Acoustic Cavitation 46

2.4.3 Hydrodynamic Cavitation 55

2.5 Effects of Cavitation on Diesel 63

2.5.1 Cavitation Induced Pyrolysis 63

2.5.2 Hydrodynamic Cavitation and Pyrolytic Effects 67

Chapter 3 – Experimental Arrangement **73**

3.1 High Pressure Cavitation Test Rig 75

3.1.1 Temperature Control System 77

3.1.2 Nozzle Description 78

3.1.3 Pressurised Receiving Cylinder 80

3.2 In-situ Laser Transmission Setup 82

3.3 Ultraviolet-Visible Spectroscopy 84

3.4 Laser Particle Count 86

Chapter 4 – Experimental Methodology 89

4.1 Fuel Filling, Flushing and Draining Procedures 90

4.2 In-situ Laser Transmission Setup Calibration 91

4.2.1 Spectral Attenuation Data Analysis 93

4.3 UV-Visible Spectra Measurement Sample Dilution Methodology 94

4.3.1 Dilution Repeatability and Statistics 97

4.4 Author's Note 100

4.5 Laser Particle Count Dilution Methodology 102

4.6 Two Dimensional – Gas Chromatography (GC x GC) 103

4.6.1 GC x GC Sample Preparation and Analysis 107

Chapter 5 – High Pressure Cavitation Tests for Five Fuels 109

5.1 High Pressure Cavitation Experiments and the Spectral Attenuation Coefficient Measurements 109

5.2 Fuel Dependence Tests 112

5.3 Particle Count Distributions 150

5.4 Combined Discussion of Fuel Tests 154

Chapter 6 – Injection Pressure Dependence Tests.....161

6.1 Combined Discussion of Pressure Dependence Tests 176

Chapter 7 – Long Duration Tests.....181

Chapter 8 – Pressurised Receiver Tests.....193

8.1 Combined Discussion for Receiver Pressure Tests.....209

Chapter 9 – Two-Dimensional Gas Chromatography Results 213

9.1 Paraffins 215

9.2 Mono-Aromatics 217

9.3 Di- and Tri (+)-Aromatics.....219

9.4 FAME.....221

9.5 Overall Change in Chemical Composition from GC x GC Results.....221

Chapter 10 – Overall Summary and Discussion of Cavitation Test Results.....225

10.1 Fundamental Observations of Hydrodynamic Cavitation 225

10.2 Chemical Behaviour of Diesel Fuels Subjected to Cavitation 227

10.3 Observation of Deposit Formation 230

Chapter 11 – Chemical Kinetic Modelling 233

11.1 Kinetic Model and Setup 236

11.2 Modelling Results.....244

11.2.1 CASE I: Model Surrogate Diesel Fuel without Dissolved Oxygen.....245

11.2.2 CASE II: Model Surrogate Diesel Fuel with Dissolved Oxygen 256

11.3 Overall Discussion of Kinetic Modelling and Comparison with Cavitation Experiments 265

Chapter 12 – Conclusion and Future Work 271

12.1 Observations for the Fundamentals of Cavitation 271

12.2 Observations for the Chemical Behaviour of Diesel Fuels 273

12.3 Recommendations for Future Work 275

Appendix A – Fuel Dependence Tests (40 hours) .....

A.1 Spectra Measurements in the 190 nm – 405 nm range .....

Appendix B – Pressure Dependence Tests.....

B.1 Fuel 1 (BDN) Experiments .....

Appendix C – GC x GC Chromatograms for Repeated Fuel Tests .....

C.1 Pre-cavitation Sample Chromatograms.....

Appendix D – Kinetic Modelling.....

D.1 Model Fuel without dissolved Oxygen gas (Case I) .....

Appendix E – Experimental Procedures.....

E.1 High-pressure Test-rig Draining, Refilling and Flushing Procedures.....

E.2 Sample dilution method for UV-Visible Spectra measurements .....

E.3 Sample dilution method for Laser Particle Count.....

Bibliography.....

List of Figures

Figure 2.1 Paraffins with the chemical formula C_8H_{18}: a) normal octane b) isooctane or 2,4-dimethylhexane 11

Figure 2.2 Naphthenes with a single and double ring formation a) ethylcyclohexane b) decalin (bicyclodecane) 12

Figure 2.3 A hexene molecule with a double bond between third and fourth carbon atoms... 13

Figure 2.4 A benzene molecule with six carbon atoms. The dotted line represents the aromatic bond..... 14

Figure 2.5 Typical distillation curve for diesel fuel. [8] 17

Figure 2.6 Transesterification of vegetable oil to produce FAME and glycerol, using methanol[34] 22

Figure 2.7 Operation of a common rail solenoid injector [19] 28

Figure 2.8 Behaviour of $\boldsymbol{R(t)}$ and $\boldsymbol{R(t)}$ during bubble collapse.[54] 44

Figure 2.9: Formation of liquid microjets at cavitation bubble collapse near a solid boundary[59]. 45

Figure 2.10 A cavity forms and grows in episodes of negative pressure. When it attains critical size it implodes generating intense heat and pressure[17] 47

Figure 2.11 Effect of injection pressure on flowrate and cavitating flow characteristics for two nozzles of different L/W ratios.[83] 58

Figure 2.12 Left: An example of string-type cavitation connecting two nozzle holes. Right: schematic of flow inside the sac volume leading to formation of string cavitation[79] 60

Figure 2.13: Schematic representation of the 3 regions of cavitation where sonochemical reactions occur during bubble collapse. 66

Figure 3.1 Schematic diagram of the high-pressure recirculation cavitation test-rig 76

Figure 3.2 Injector and receiving cylinder assembly. 79

Figure 3.3 Drawing of the 213 µm single-hole old injector nozzle. 80
Figure 3.4 Schematic of the pressurised receiving cylinder setup 81
Figure 3.5 Schematic of the laser measurement setup 82
Figure 3.6 Optical measurement setup (top-view) 83
Figure 3.7 Laser Photo-detector 84
Figure 3.8 The double beam-double detector configuration used on UV-1800 Spectrophotometer[96]. 85
Figure 3.9 Optical schematic of the Laser Particle Counter, highlighting the scanned region inside the sample bottle[97]. 87
Figure 3.10 A sample summary report from the laser particle counter. 88
Figure 4.1 Scheme of spectra measurements in the subrange of 240 nm - 305 nm for all fuels except Fuel 5 (BD+MN) 96
Figure 4.2 Scheme of spectra measurements in the subrange of 190 nm - 405 nm for all fuels except Fuel 5 (BD+MN) 96
Figure 4.3 Mean spectra of the 40 DRF-520 samples in measurement range of 240 nm - 285 nm. Error bars represent 2σ standard deviation 98
Figure 4.4 Mean spectra of the 40 DRF-10,000 samples in measurement range of 195 nm - 250 nm. Error bars represent 2σ standard deviation 98
Figure 4.5 Histogram of 40 DRF-520 diluted sample absorbances at 260 nm wavelength (left). Histogram of 40 DRF-10,000 diluted sample absorbances at 205 nm (right). 99
Figure 4.6 Coefficients of Variation of the 40 DRF 520 samples in measurement range of 240 nm - 285 nm (left). Coefficient of Variation of the 40 DRF 10,000 samples in measurement range of 195 - 250 nm (right). 100
Figure 4.7 Mean spectra of the 30 DRF-520 samples in measurement range of 240 nm - 290 nm. Error bars represent 2σ standard deviation 101

Figure 4.8 Mean spectra of the 30 DRF-10,000 samples in measurement range of 195 nm - 250 nm. Error bars represent 2σ standard deviation.....101
Figure 4.9 Coefficients of Variation for the 30 DRF 520 samples in measurement range of 240 nm - 285 nm by Dr. Kuti (left). Coefficient of Variation for the 30 DRF 10,000 samples in measurement range of 195 - 250 nm by Dr. Kuti (right).....102
Figure 4.10 Schematic of a GC x GC system, showing the injector, modulator, detector, with the 1st and 2nd separation columns in their respective ovens.....105
Figure 4.11 GC x GC transformation of continuous linear signal from the detector into a contour plot and a three-dimensional[100].....107
Figure 5.1 Comparison of 15-second averaged raw transmission data with 15-minute averaged correction.....111
Figure 5.2 Normalised laser transmission at 405 nm against cavitation time for initial (top) and repeated tests on Fuels 1 to 5.....113
Figure 5.3 Time-dependent spectral attenuation coefficient at 405 nm against cavitation time for initial (top) and repeated tests on Fuels 1 to 5.....117
Figure 5.4 Spectral absorbance of Fuel 1 (BDN) samples at 405 nm as a function of cavitation duration for initial (left) and repeated tests.....119
Figure 5.5 Spectral absorbance of Fuel 2 (B10) samples at 405 nm as a function of cavitation duration for initial (left) and repeated tests.....120
Figure 5.6 Spectral absorbance of Fuel 3 (B30) samples at 405 nm as a function of cavitation duration for initial (left) and repeated tests.....121
Figure 5.7 Spectral absorbance of Fuel 4 (BD+H) samples at 405 nm as a function of cavitation duration for initial (left) and repeated tests.....121
Figure 5.8 Spectral absorbance of Fuel 5 (BD+MN) samples at 405 nm as a function of cavitation duration for initial (left) and repeated tests.....122

Figure 5.9 Fuel 1 (BDN) discrete sample spectra for pure samples in the 350 – 405 nm range (initial test) 123
Figure 5.10 Fuel 1 (BDN) discrete sample spectra for pure samples in the 350 – 500 nm range (repeated test) 123
Figure 5.11 Fuel 2 (B10) discrete sample spectra for pure samples in the 350 – 405 nm range (initial test) 126
Figure 5.12 Fuel 2 (B10) discrete sample spectra for pure samples in the 350 – 500 nm range (repeated test) 126
Figure 5.13 Fuel 3 (B30) discrete sample spectra for pure samples in the 350 – 405 nm range (initial test) 128
Figure 5.14 Fuel 3 (B30) discrete sample spectra for pure samples in the 350 – 500 nm range (repeated test) 129
Figure 5.15 Fuel 4 (BD+H) discrete sample spectra for pure samples in the 350 – 405 nm range (initial test) 129
Figure 5.16 Fuel 4 (BD+H) discrete sample spectra for pure samples in the 350 – 500 nm range (repeated test) 130
Figure 5.17 Fuel 5 (BD+MN) discrete sample spectra for pure samples in the 350 – 405 nm range (initial test) 131
Figure 5.18 Fuel 5 (BD+MN) discrete sample spectra for pure samples in the 350 – 500 nm range (repeated test) 131
Figure 5.19 Absorbance spectrum of benzene showing the 'benzenoid band' as a series of absorbance peaks in the wavelength range of 220 nm – 270 nm. (adapted from Friedel and Orchin (1951)[104]) 133
Figure 5.20 Fuel 1 (BDN) discrete sample spectra for DRF 520 diluted samples in the 240 – 305 nm range (initial test) 134

Figure 5.21 Absorbance spectrum showing the ‘benzenoid band’ of dodecahydrochrysene $C_{18}H_{24}$, a naphthenic mono-aromatic hydrocarbon.....135
Figure 5.22 Fuel 1 (BDN) discrete sample spectra for DRF 520 diluted samples in the 240 – 305 nm range (repeated test).....136
Figure 5.23 Fuel 1 (BDN) repeated test sample spectra normalised at the 245 nm trough to show the ‘Benzenoid band’.....136
Figure 5.24 Fuel 2 (B10) discrete sample spectra for DRF 520 diluted samples in the 240 – 305 nm range (initial test).....137
Figure 5.25 Fuel 2 (B10) discrete sample spectra for DRF 520 diluted samples in the 240 – 305 nm range (repeated test).....138
Figure 5.26 Fuel 2 (B10) repeated test sample spectra normalised at the 245 nm trough to show the change in ‘Benzenoid band’ absorption.....138
Figure 5.27 Fuel 3 (B30) discrete sample spectra for DRF 520 diluted samples in the 240 – 305 nm range (initial test).....139
Figure 5.28 Fuel 3 (B30) discrete sample spectra for DRF 520 diluted samples in the 240 – 305 nm range (repeated test).....140
Figure 5.29 Fuel 3 (B30) repeated test sample spectra normalised at the 245 nm trough to show the change in ‘Benzenoid band’ absorption.....140
Figure 5.30 Fuel 4 (BD+H) discrete sample spectra for DRF 520 diluted samples in the 240 – 305 nm range (initial test).....141
Figure 5.31 Fuel 4 (BD+H) discrete sample spectra for DRF 520 diluted samples in the 240 – 305 nm range (repeated test).....142
Figure 5.32 Fuel 4 (BD+H) repeated test sample spectra normalised at the 245 nm trough to show the change in ‘Benzenoid band’ absorption 142

Figure 5.33 Fuel 5 (BD+MN) discrete sample spectra for DRF 3000 diluted samples in the 240 – 305 nm range (initial test) 144
Figure 5.34 Fuel 5 (BD+MN) discrete sample spectra for DRF 3000 diluted samples in the 240 – 305 nm range (repeated tests) 144
Figure 5.35 Fuel 1 (BDN) discrete sample spectra for DRF 10,000 diluted samples in the 190 – 405 nm range (repeated test) 145
Figure 5.36 Fuel 1 (BDN) repeated test samples in the 200 – 230 nm range (diluted to DRF 10,000) 146
Figure 5.37 Fuel 2 (B10) discrete sample spectra for DRF 10,000 diluted samples in the 190 – 405 nm range (repeated test) 148
Figure 5.38 Fuel 3 discrete sample spectra for DRF 10,000 diluted samples in the 190 – 405 nm range (repeated test) 148
Figure 5.39 Fuel 4 (BD+H) discrete sample spectra for DRF 10,000 diluted samples in the 190 – 405 nm range (repeated test) 149
Figure 5.40 Fuel 5 (BD+MN) discrete sample spectra for DRF 17,000 diluted samples in the 190 – 405 nm range (repeated test) 149
Figure 5.41 Fuel 5 (BD+MN) repeated test sample spectra showing the 314 nm absorbance structure which is a characteristic of 1-methylnaphthalene. 150
Figure 5.42 Particle size distribution of cavitated Fuel 1 (BDN) samples in the particle size range of 1 µm to 100 µm. 151
Figure 5.43 Particle size distribution of cavitated Fuel 1 (BDN) samples in the particle size range of 1 µm to 30 µm. 151
Figure 5.44 Particle size distribution of cavitated Fuel 2 (B10) samples in the particle size range of 1 µm to 30 µm. 152

Figure 5.45 Particle size distribution of cavitated Fuel 3 (B30) samples in the particle size range of 1 µm to 30 µm. 152
Figure 5.46 Particle size distribution of cavitated Fuel 4 (BD+H) samples in the particle size range of 1 µm to 30 µm. 153
Figure 5.47 Particle size distribution of cavitated Fuel 5 (BD+MN) samples in the particle size range of 1 µm to 30 µm. 153
Figure 5.48 Daily change (per 10 hours) in measured absorption at the 425 nm peak of discrete samples for the five test fuels..... 157
Figure 6.1 Normalised laser transmission at 405 nm against cavitation time for Fuel 1 (BDN) at 550, 1,100 and 1,650 bar injection pressures 162
Figure 6.2 Time-dependent spectral attenuation coefficient at 405 nm against cavitation time for Fuel 1 (BDN) at 550, 1,100 and 1,650 bar injection pressures 162
Figure 6.3 Normalised laser transmission at 405 nm against cavitation time for Fuel 1 (BDN) at 825 and 1,650 bar injection pressures 165
Figure 6.4 Time-dependent spectral attenuation coefficient at 405 nm against cavitation time for Fuel 1 (BDN) at 825 and 1,650 bar injection pressures 166
Figure 6.5 Self-normalised laser transmission at 405 nm against cavitation time for Fuel 1 (BDN) at 825 and 1,650 bar injection pressures. Self-normalisation is performed by offsetting the normalised laser transmission to obtain zero as the initial transmission value for both pressure tests 167
Figure 6.6 Self-normalised spectral attenuation coefficient at 405 nm against cavitation time for Fuel 1 (BDN) at 825 and 1,650 bar injection pressures. Self-normalisation is performed by offsetting the time-dependent spectral attenuation signal to obtain zero as the initial attenuation coefficient value for both pressure tests..... 168

Figure 6.7 Self-normalised spectral attenuation coefficient at 405 nm against number of fuel recirculation cycles completed by respective Fuel 1 (BDN) test charges at 825 and 1,650 bar injection pressures.....170
Figure 6.8 Normalised laser transmission signal (top) and self-normalised laser transmission at 405 nm against cavitation time for Fuel 6 (BDA) at 825 and 1,650 bar injection pressures.172
Figure 6.9 Spectral attenuation coefficient (top) and the self-normalised spectral attenuation coefficient at 405 nm against cavitation time for Fuel 6 (BDA) at 825 and 1,650 bar injection pressures.....173
Figure 6.10 Absorption spectra of cavitated Fuel 6 (BDA) samples from 825 bar test (left) and 1,650 bar test.....174
Figure 6.11 Self-normalised spectral attenuation coefficient at 405 nm against number of fuel recirculation cycles completed by respective Fuel 6 (BDA) test charges at 825 and 1,650 bar injection pressures.....176
Figure 7.1 Normalised laser transmission at 405 nm against cavitation duration for Fuel 1 (BDN) and Paraffinic Model Fuel. 182
Figure 7.2 Spectral attenuation coefficient at 405 nm against cavitation duration for Fuel 1 (BDN) and Paraffinic Model Fuel. 183
Figure 7.3 Absorbance spectra of a pure non-cavitated paraffinic model fuel sample in the wavelength range of 190 – 500 nm.....184
Figure 7.4 Normalised laser transmission at 405 nm against cavitation duration for Fuel 1 (BDN) at 1,650 bar injection pressure (173 μm nozzle).....186
Figure 7.5 Spectral attenuation coefficient at 405 nm against cavitation duration for Fuel 1 (BDN) at 1,650 bar injection pressure (173 μm nozzle).....186
Figure 7.6 Fuel 1 (BDN) discrete sample spectra for pure samples in the 350 - 500 nm range 189

Figure 7.7 Fuel 1 (BDN) discrete sample spectra for DRF 520 diluted samples in the 240 – 305 nm range.....189
Figure 8.1 Normalised spectral transmission (at 405 nm) against cavitation time for Fuel 6 (BDA) at ambient, 5 bar and 10 bar receiver pressures.....194
Figure 8.2 Time-dependent spectral attenuation coefficient of Fuel 6 (BDA) at ambient, 5 bar and 10 bar receiver pressures.....195
Figure 8.3 Fuel 6 (BDA) discrete sample spectra from the ambient receiver pressure test ..196
Figure 8.4 Fuel 6 (BDA) discrete sample spectra from the 5 bar receiver pressure test 197
Figure 8.5 Fuel 6 (BDA) discrete sample spectra from the 10 bar receiver pressure test 197
Figure 8.6 Overall change in absorbance of the Fuel 6 (BDA) samples from the ambient, 5 bar and 10 bar receiver pressure tests. 199
Figure 8.7 Fuel 6 (BDA) discrete sample spectra for DRF 520 diluted samples from the ambient receiver pressure test.....200
Figure 8.8 Fuel 6 (BDA) discrete sample spectra for DRF 520 diluted samples from the 5 bar receiver pressure test.....200
Figure 8.9 Fuel 6 (BDA) discrete sample spectra for DRF 520 diluted samples from the 10 bar receiver pressure test.....201
Figure 8.10 Absorption spectra of the three receiver pressure test samples for Fuel 6 (BDA), self-normalised at 245 nm to show the variations in the benzenoid band range 202
Figure 8.11 Normalised spectral transmission signals (at 405 nm) for Fuel 1 (BDN) tests at ambient and 10 bar receiver pressures.....203
Figure 8.12 Time-dependent spectral attenuation coefficients (at 405 nm) for Fuel 1 (BDN) tests at ambient and 10 bar back pressures 204
Figure 8.13 Absolute change in spectral attenuation coefficients (at 405 nm) for Fuel 1 (BDN) tests at ambient and 10 bar back pressures 205

Figure 8.14 Fuel 1 (BDN) discrete sample spectra from the ambient receiver pressure test 205

Figure 8.15 Fuel 1 (BDN) discrete sample spectra from the 10 bar receiver pressure test ..206

Figure 8.16 Fuel 1 (BDN) discrete sample spectra for DRF 520 diluted samples from the ambient receiver pressure test.....207

Figure 8.17 Fuel 1 (BDN) discrete sample spectra for DRF 520 diluted samples from the 10 bar receiver pressure test.....208

Figure 8.18 Absorption spectra of the two receiver pressure test samples for Fuel 1 (BDN), self-normalised at 245 nm to show the variations in the benzenoid band range 208

Figure 9.1 GC x GC chromatogram for Fuel 1 (BDN) pre-cavitation sample. 214

Figure 9.2 Proportions of hydrocarbon classes present in the pre-cavitation samples of each of the five test fuels, obtained through GC x GC analysis. 215

Figure 9.3 Relative change in proportions of the open-chain paraffins in the five test fuels after forty hours of cavitation.....216

Figure 9.4 Relative change in proportions of naphthenes in the five test fuels after forty hours of cavitation 217

Figure 9.5 Relative change in proportions of the alkylated mono-aromatics in the five test fuels after forty hours of cavitation 218

Figure 9.6 Relative change in proportions of the naphthenic mono-aromatics in the five test fuels after forty hours of cavitation.....218

Figure 9.7 Relative change in proportions of the di- and tri(+)-aromatics in the five test fuels after forty hours of cavitation 219

Figure 9.8 Relative change in proportions of the tri (+)-aromatic hydrocarbons in the five test fuels after forty hours of cavitation.....220

Figure 9.9 Relative change in proportion of FAMEs in the five test fuels after forty hours of cavitation.....221

Figure 9.10 Change in fuel components (%wt) for the five test fuels obtained through GC x GC analysis as a result of forty hours of cavitation at 1,650 bar rail pressure 222
Figure 10.1 Diels-Alder reaction for addition of ethene to 1,3-butadiene to give cyclohexene. Hydrogen elimination from cyclohexene can then lead to the formation of single ring aromatics[101] 229
Figure 10.2 Photographs of fuel receiving cylinder with its internal surface coated in a hard-brown lacquer with a polymeric appearance. 231
Figure 11.1 Soot formation mechanism in combustion systems (adapted from Smith[120]).....234
Figure 11.2 Polytropic temperature and pressure profiles for the kinetic modelling of diesel fuel pyrolysis.....238
Figure 11.3 Change in the number of moles of n-paraffins and naphthenes in the model diesel fuel 245
Figure 11.4 Change in the number of moles of mono-aromatic hydrocarbons in the model diesel fuel 246
Figure 11.5 Change in the number of moles of di-aromatic hydrocarbons in the model diesel fuel 246
Figure 11.6 Change in the number of moles of tri (+) aromatic hydrocarbons in the model diesel fuel 247
Figure 11.7 Population change of BINs 1, 2 and 3 with reaction time when pure indene (left) and pure toluene (right) are subjected to polytropic modelling (note the difference in scales for the number of moles on the two graphs).....250
Figure 11.8 Population change of BINs 1, 2 and 3 (log10) with reaction time when pure indene (left) and pure toluene (right) are subjected to polytropic modelling.....250
Figure 11.9 Change in the population of BINs 1 – 10 with residence time, resulting from the polytropic modelling of the surrogate diesel fuel. 252

Figure 11.10 Change in the population (log10) of BINs 1 – 10 with residence time (post 50 μs), resulting from the polytropic modelling of the surrogate diesel fuel.....254
Figure 11.11 Change in the number of moles of n-paraffins and naphthenes in the model diesel fuel with dissolved oxygen 256
Figure 11.12 Change in the number of moles of mono-aromatic hydrocarbons in the model diesel fuel with dissolved oxygen 257
Figure 11.13 Change in the number of moles of di-aromatic hydrocarbons in the model diesel fuel with dissolved oxygen 257
Figure 11.14 Change in the number of moles of tri (+)-aromatic hydrocarbons in the model diesel fuel with dissolved oxygen 258
Figure 11.15 Change in the number of moles of oxygen gas in the model diesel fuel with dissolved oxygen.....259
Figure 11.16 Changes in the amount of hydroxyl radicals during the modelling of surrogate diesel with dissolved oxygen 260
Figure 11.17 Comparison of the changes occurring in the amount of indenyl during the modelling of diesel fuel without dissolved oxygen (Case I) and with dissolved oxygen (Case II).....261
Figure 11.18 Change in the population of BINs 1 – 10 with residence time, resulting from the polytropic modelling of the surrogate diesel fuel with dissolved oxygen. 261
Figure 11.19 Change in the population (log10) of BINs 1 – 10 with residence time, resulting from the polytropic modelling of the surrogate diesel fuel with dissolved oxygen.....264

List of Tables

Table 2.1 Elemental composition of petroleum diesel[28]. ……8

Table 2.2: Approximate proportions of some major crude oil distillates 9

Table 2.3: Diesel additive types and their function[7] 21

Table 2.4: Potential sources of sodium and carboxylic acids.[36] 32

Table 2.5: Moholkar et al. (1999) studied the effects of initial size of pre-existing cavities in the liquid and the intensity and frequency of ultrasound on the behaviour of cavities. 49

Table 2.6: Various parameters and their effects on cavitation formation and/or collapse. 49

Table 2.7: The three regions of cavitation where sonochemical reactions occur as identified by Riesz and Misik[25]. 65

Table 4.1 Table of Fuels analysed in the Investigations 90

Table 4.2 Test matrix for analysis performed on each fuel 90

Table 5.1 Five commercial fuels tested in the fuel composition investigation.....112

Table 5.2 Control variables for the fuel tests 112

Table 6.1 Control variables for the injection pressure dependence tests 161

Table 6.2 Volumetric flowrate measurements for the 176 µm test nozzle, measured at 1,650 bar injection pressure following the completion of the specified pressure tests on Fuel 1 (BDN). The measurements are quoted with the standard deviation over the 8 to 10 repeats. 169

Table 6.3 Volumetric flowrate measurements for the 173 µm test nozzle, measured at 1,650 bar injection pressure following the completion of the specified pressure tests on Fuel 6 (BDA). The measurements are quoted with standard deviation over the 8 to 10 repeats. 175

Table 7.1 Experimental variables for long duration tests 181

Table 8.1 Control variables for pressurised receiver tests 194

Table 10.1 Comparison of the broadband absorbance decrease in wavelength range of 361-365 nm of each fuel with the change in concentration of their tri (+) aromatic content after forty hours of cavitation.....228

Table 11.1 Polytropic temperature and pressure profiles for the kinetics modelling of a collapsing bubble (n = 1.21) 237

Table 11.2 Classes of pseudo-species defined as BINs and their properties. 241

Table 11.3 General composition of the model diesel fuel based on GC analysis of Fuel 1 (BDN) sample 242

Table 11.4 Detailed composition of the model diesel fuel, species names are given as specified in the kinetic model along with their chemical name in parenthesis. 243

Table 11.5 Growth of BIN_1 to BIN_5 species as a result of the polytropic modelling of the surrogate diesel fuel. 253

Table 11.6 Growth of BIN_6 to BIN_{10} species as a result of the polytropic modelling of the surrogate diesel fuel. 254

Table 11.7 Growth of BIN_1 to BIN_5 species as a result of the polytropic modelling of the surrogate diesel fuel with dissolved oxygen. 263

Table 11.8 Growth of BIN_6 to BIN_{10} species as a result of the polytropic modelling of the surrogate diesel fuel with dissolved oxygen. 263

Acknowledgement

I dedicate this thesis to my father (Mansoor Fatmi) - you always encouraged me to achieve the best of my potential and I could always count on your support and guidance for any aspect of my life. I owe my achievements to you. Thank you!

I am indebted to my supervisor, Dr. Russel Lockett for providing me with the opportunity to work on this challenging project. Thank you for giving me the guidance, wisdom and support that I believe has allowed me to grow as a professional. I would like to thank Shell Global Solutions, in particular Mr. R. Price, Mr. R. Williams and Mr. N. Rounthwaite for financially supporting my research.

I want to express my gratitude to the technical services staff at SMCSE labs, Mr. G. Clow, Mr J. Ford, Mr. R. Cherry and Mr. R. Leach, for their exceptional ability to manufacture and maintain the complicated experimental equipments I utilised in this project.

I must thank Dr. O. Kuti for his assisstance in the various stages of my project during his tenure at City, University of London. His help in development of the dilution methodology for spectrometric analysis of fuels was crucial for the success of my research.

A heartiest gratitute to Alberto and Kassandra, who have become my closest friends during my degree. I thank you both for bearing with me during my times of turmoil and for giving me motivation and support when I needed it most. A big thank you to all my friends and colleagues Hamza, Asfak, Umer, Yiannis, Eleni, Antonio, Elina, Kostas, Saeed, Hessam, Israt and Sohaib for the different ways they all helped me in making my time easier and more memorable.

Last but not least, my mother, brother and sisters, I cannot thank you all enough for your unwavering support and encouragement during this challenging period of my life.

Abstract

Recent advancements in the diesel fuel injection equipment (FIE) have resulted in increased reports of internal injector deposits (IIDs) and fuel filter fouling. The nature and deposition location of particulates has led to the belief that the deposits are formed due to pyrolytic reactions resulting from the recirculating cavitating flow that occurs inside the diesel vehicles.

In this study, diesel fuels of varying compositions have been subjected to high-pressure cavitation experiments and the resulting change in their optical and chemical characteristics have been identified. To this end, a purpose built high-pressure hydrodynamic cavitation test-rig was employed to recirculate the diesel fuels under sustained cavitation conditions. An optical setup was utilised to measure the in-situ change in optical extinction coefficient of the fuels at 405 nm. Samples of the cavitated diesel fuels were drawn and subjected to spectroscopic measurements and two-dimensional gas chromatography analysis. Results from the optical characterisation of diesel fuels revealed a consistent change in the fuels' optical properties as they were subjected to cavitation. All tests have indicated a build-up of particulate suspension in the recirculating fuel charges with cavitation duration. Analysis of diesel fuel spectra indicated a breakdown of primary aromatic compounds in the fuels, with indications for the formation of polycyclic aromatic hydrocarbons. Gas chromatography results have revealed a consistent chemical behaviour of naphthenic monocyclic aromatic hydrocarbons in all fuels.

Chemical kinetic modelling of the pyrolysis of diesel fuel vapour cavities emulating the high temperature and pressure conditions generated upon a cavitation bubble collapse have revealed the different reaction pathways for the formation of particulates. Increased potency of naphthenic mono-aromatics towards soot formations has been identified. Although low, other chemical components of the diesel fuels have also been shown to have soot formation tendencies.

The obtained results for the investigation have provided an indication of the chemical effects of hydrodynamic cavitation on diesel fuels that may lead to the formation of soot material similar to the IIDs observed in diesel engines.

Abbreviations

BDA: Base Diesel Aged

BDN: Base Diesel New

BD+H: Base Diesel + 10% Hexadecane

BD+MN: Base Diesel + 10% Methylnaphthalene

C/H: Carbon to Hydrogen Atomic Ratio

CV: Coefficient of Variation

DCA: Deposit Control Additives

DDS: Dodecenyl Succinic

DRF: Dilution Ratio Factor

DRIFTS: Diffuse Reflectance Infra-red Fourier Transform Spectroscopy

ECU: Engine Control Unit

FAME: Fatty Acid Methyl Ester

FIE: Fuel Injection Equipment

FTIR: Fourier Transform Infrared Spectroscopy

GC: Gas Chromatography

GC/MS: Gas Chromatography-Mass Spectroscopy

GCxGC: Two-dimensional Gas Choromatography

GTL: Gas-to-Liquid

HACA: Hydrogen Abstraction Carbon(or Acetylene) Addition

HSDI: High-speed Direct Injection.

HP: High Pressure

IID: Internal Injector Deposit.

LPC: Laser Particle Counter

L/W: Length to Width Ratio

MBSL: Multibubble Sonoluminescence

NOx: Oxides of Nitrogen

NVH: Noise, Vibrations and Harshness.

OEMs: Original Equipment Manufacturers

OH: Hydroxyl Radical

PAH: Polycyclic Aromatic Hydrocarbons

PIB: Poly Isobutylene

PIBSI: Poly Isobutylene Succinimide

RME: Rapeseed Methyl Ester

SBSL: Single-bubble Sonloluminescence

ULSD: Ultra-Low Sulphur Diesel

UV-Vis: Ultraviolet - Visible Light

α(t): Time-dependent Spectral Attenuation Coefficient

λ: Electromagnetic Radiation Wavelength

C_i : Cavitation Number $C_i = \frac{\text{Injection Pressure-Vapour Pressure}}{\text{Injection Pressure-Back Presssure}}$

C_N: Cavitation Number $C_N = \frac{\text{Injection Pressure-Back Pressure}}{\text{Back Pressure-Vapour Presssure}}$

Chapter 1
Introduction

Recent years have witnessed significant advances in diesel engine technologies that have been driven by the tightening emissions regulations and growing competition from the fuel-efficient gasoline engines[1,2]. Most noticeable of these improvements has been the development of high-efficiency common rail fuel injection systems. The common rail system has enabled pressurisation of diesel fuels to higher pressures, where current common rail diesel engine technologies have been able to attain rail pressures of up to 2,500 bar, with some engine manufacturers targeting pressures in excess of 3,000 bar in the next generation of common rail systems[3,4]. Improvements in the rail/ injection pressures have resulted in better atomisation characteristics of fuel sprays, giving rise to air-fuel mixtures of high homogeneity that have provided superior combustion characteristics, and have resulted in lower engine emissions of CO and soot[5,6].

Coupled with the improvements in diesel fuel injection equipment (FIE) are the changes taking place in the properties of diesel fuels, including the development of ultra-low sulphur diesel (ULSD) and increased usage of biodiesel blend components. The use of performance enhancing additives has also become more popular[7,8].

Although the improvements in combustion efficiencies of the new high-speed direct injection (HSDI) diesel engines and the usage of fuel additives have resulted in lower nozzle-tip coking and soot emissions, there have been increased reports of injector system failure. These reports have been linked to deposits, called the internal injector deposits (IIDs). These deposits are found on the internal components of the FIE and fuel filters; and are suggested to adversely affect the injector dynamics, including problems such as needle stick. The IIDs have been

found to be different in structure and composition to the traditional nozzle-tip deposits. Mechanism of formation of the IIDs has been suggested to be different from the nozzle-tip deposits, which are formed through interaction with hot combustion products[5,9,10].

The increased frequency in reports of IIDs causing engine failure has been linked to some of the recent developments in diesel engine technologies. Possible candidates for the issues include the increased rail pressures, tighter FIE tolerances and the use of fuel additives[11,12].

Increased injection pressures are thought to subject diesel fuels to very high thermal and shear stresses. It has been suggested that current fuel metering techniques also expose the fuel to hydrodynamic cavitation in diesel pumps and injectors. Stressing of diesel fuel in this way is believed to result in chemical changes of its components that can lead to the formation of carbonaceous particulates through pyrolysis-type reactions[13–16].

Hydrodynamic cavitation occurs in diesel engines when the highly pressurised fuel flows past constrictions (in pumps, valves etc.) that results in loss of local pressures to pressures below the saturated vapour pressure of the fuel. This results in local boiling of the fuel, creating a two-phase flow of liquid fuel containing pockets of vaporised fuel. As the flow decelerates downstream of the constriction and the static pressure head recovers, the vapour pockets are forced to violently implode. Extremes of temperature and pressure have been suggested to occur inside a collapsing cavitation bubble, creating ‘hot-spots’ where complicated chemical reactions can initiate.[17,18]

In a diesel engine, the effect of hydrodynamic cavitation may be enhanced due to the recirculation of fuel from the high-pressure region of the FIE to the low-pressure fuel tank. The in-vehicle recirculation occurs at various components, including the injectors and the high-pressure pump, where a proportion of the pressurised fuel is returned to the tank via spill-valves. The spill-mechanism is part of the metering techniques used by engine manufacturer to

precisely control the fuel flow-rate. Depending on the engine type and load conditions, the proportion of high-pressure fuel depressurising and returning back to the fuel tank can be 20 – 50 %.[13,19]

Depressurisation of high-pressure fuel past the spill-valves is believed to create favourable conditions for the formation of hydrodynamic cavitation. Considerate proportions of the fuel tank volume can undergo multiple in-vehicle recirculation cycles prior to their injection and the subsequent combustion. The recurrence of cavitating flow can thus subject the fuel to prolonged stressing, which is believed to have a detrimental impact on the properties of the diesel fuel, and is suggested to result in formation of the internal deposits.[15,20]

Experimental results have reported the formation of carbonaceous soot-like particles when liquid hydrocarbons, including diesel fuels, are subjected to acoustic cavitation. These reports have indicated that pyrolysis-like reactions occur in collapsing cavitation bubbles that may eventually result in fuel-borne hydrocarbons to be converted into particulate suspension[17,21–26]. The particulate suspension has been found to have similar physical and chemical characteristics to the diesel FIE and filter deposits found in field vehicles.[16]

Based on the effects observed for acoustic cavitation, it has been hypothesised that subjecting hydrocarbons to hydrodynamic cavitation would also result in similar chemical activity. Very limited research has been conducted on deposit forming tendencies of organic liquids when they are exposed to hydrodynamic cavitation. Lockett and Jeshani (2013)[13] were the first researchers to subject diesel fuels to a recirculating cavitation test-rig; they reported a consumption of mono-aromatic hydrocarbons in the fuels, which were believed to be converted to polyaromatic hydrocarbons (PAHs) and particulates. Lockett and Fatmi (2016)[20] later recirculated diesel fuels at higher injection pressures (1,650 bar) to report similar activity.

The objective of this project was to gain further insight into the effect of hydrodynamic cavitation on diesel fuels. The project aimed to identify the chemical changes occurring in the diesel fuels undergoing cavitation, through employment of a simple optical diagnostic setup. A high-pressure cavitation test-rig, designed to produce intense hydrodynamically cavitating flow, was utilised to continually recirculate diesel fuels for prolonged durations.

It was hypothesised that prolonged exposure of the fuels to hydrodynamic cavitation in the rig would result in particulate formation, which would increase the fuel's optical attenuation coefficient. A simple optical diagnostics method, based on the Beer-Lambert-Bouguer law of optical attenuation, was employed to characterise the in-situ change in optical properties of the diesel fuels being cavitated in the test-rig.

Samples of cavitated diesel fuels were also subjected to spectroscopic analysis. This allowed identification of trends of changing fuel component concentrations as a function of cavitation duration. Two-dimensional gas chromatography was performed on cavitated diesel samples to enable identification of the various hydrocarbon classes present in the fuels, along with the change in their concentrations after being exposed to cavitation.

The work presented here has been divided into twelve chapters. A brief description of each chapter content has been provided below:

Chapter 1 provides a short introduction to the project, including the motivation for this work and the state-of-the-art in research for the effects of hydrodynamic cavitation on diesel fuels.

Chapter 2 gives a review on diesel fuels, the relevant diesel engine technology, cavitation and its chemical effects on organic liquids. The chapter highlights research carried out by various researchers in the field, along with the established understanding of the cavitation phenomenon from theoretical books. A review on the problem of injector deposits and their mechanism of

formation has been conducted. Additionally, research work carried out on chemical kinetics modelling of surrogate diesel and other fuels in pyrolytic conditions has been summarised.

Chapter 3 details the experimental setup, encompassing the high-pressure cavitation, recirculation test-rig and the optical diagnostics setup. Chapter 4 follows with the experimental methodology for the cavitation tests. In this chapter, the dilution methodology for diesel samples subjected to spectra measurements and their repeatability statistics are also provided.

Chapter 5 through to Chapter 8 present results for the effects of different variables on the behaviour of fuels when subjected to hydrodynamic cavitation. The investigations involve:

- subjecting five commercial diesel fuels to sustained cavitation
- cavitation of fuels at variable injection pressures
- cavitation of fuels for long-durations
- investigation of the effect of recovery pressure on the behaviour of fuels under cavitation conditions.

Chapter 9 presents results for the two-dimensional gas chromatography analysis performed on the five commercial diesel samples obtained from the fuel cavitation tests.

Chapter 10 conducts a collective discussion for all the cavitation tests, in conjunction with the gas chromatography results. Major trends observed in the various tests are discussed and possible conclusions are drawn from these trends.

Chapter 11 focuses on the chemical kinetics modelling of a surrogate diesel fuel in conditions similar to those believed to exist in a collapsing cavitation bubble. The chapter describes the formulation of a comprehensive soot mechanism, along with the detailed composition of the surrogate diesel fuel to be modelled. The results of the modelling analysis identify major pathways to the formation of soot particles from the diesel fuel components.

Chapter 12 provides an overall conclusion based on the results of this work; along with recommendations of future work that may be carried out in the field.

Chapter 2
Literature Review

2.1 Diesel Fuel

When Rudolf Diesel first designed his compression-ignition reciprocating engine in 1892, he used crushed coal as the fuel. This fuel did not work and Diesel had to divert his attention towards an alternate fuel type. At that time in the US, crude oil was being refined to produce kerosene (lamp oil) while the remaining by-products were being discarded. Recognising the potential of the liquid petroleum by-products, Diesel made design changes to his engine to incorporate the liquid fuel. A successful prototype engine was completed in 1895. Today, both the engine and the fuel bear his name[27].

The following sections will summarise literatures on the diesel fuel and diesel engine technologies with relation to the subject areas being addressed in this study. This section will elucidate the distillation and refinement processes used for the manufacture of diesel fuel from crude oil, the composition of diesel fuels, the parameters used to quantify their physical and chemical properties, and their performance. In the end, some diesel fuel alternatives will be discussed briefly.

2.1.1 Distillation from Crude Oil and Conversion Processes

In general terms, diesel fuel is any liquid fuel that can be used to power a compression ignition engine. Modern petroleum or crude oil derived diesel is a mixture of hydrocarbons in the middle distillate range, comprising of compounds having carbon numbers of eight to twenty-six.

Crude oil is a natural mixture of hydrocarbons, that may also include compounds of sulphur, nitrogen, oxygen, metals and water. The exact composition of crude oil varies based on its source, however its elemental composition falls in the following range:

Table 2.1 Elemental composition of petroleum diesel[28].

Element	***Percent by weight***
Carbon	83-87
Hydrogen	11-16
Oxygen + Nitrogen	0-4
Sulphur	0-3

Distillation of Crude Oil

The hydrocarbon classes that make up crude oil are generally paraffins, isoparaffins, naphthenes (cycloparaffins) and aromatics. Their proportions are strongly dependent on the origin of the crude oil, and based on the proportions of each class the crude oil can be classified as either paraffin based, naphthene based, aromatic based or mixed base.

The different hydrocarbon compounds that make up the crude oil mixture have a wide range of physical properties; the most important of these properties for its separation is the boiling point. The range of boiling points allow crude oil to be separated into smaller fractions using fractional distillation process.

In a modern oil refinery, two types of distillation processes take place; crude oil is initially distilled into fractions of narrow boiling ranges at atmospheric pressure. During atmospheric distillation, the light components of the crude oil are separated, while the heavy fractions stay as a mixture (called atmospheric residue). These heavy fractions require very high temperatures to evaporate and separate, but overheating of these fractions can lead to thermal decomposition

or breakdown of the molecules. For this reason, the heavy fractions are subjected to a second type distillation at negative pressures, called vacuum distillation.

Table 2.2 shows the major fractions of crude oil that are obtained through fractional distillation. The fractions of crude oil are not separated into very precise chemical compounds. The distillation products have overlapping boiling point ranges, and they need to be refined through further processing.

Table 2.2: Approximate proportions of some major crude oil distillates

Product	***Percent by Volume***
Gasoline	44
Distillate Fuel Oil (includes diesel fuel)	21
Kerosene-type Jet Fuel	9
Residual Fuel Oil	5

Chemical Conversion

Following the distillation process, the quality of the crude oil fractions is needed to be improved (upgraded). This refers to the conversion process of crude oil fractions through removal of sulphur, nitrogen and oxygen containing species, collectively known as the heteroatoms. The presence of heteroatoms has an adverse impact on the storage stability of the fractions (particularly on diesel and fuel oil) and are also linked to emission of harmful combustion products. Nowadays, the most common process of removal of heteroatoms from the crude oil distillates involves reaction with hydrogen in presence of a catalyst, known as catalytic hydrodesulphurisation. During the removal of heteroatoms thorough catalytic hydrodesulphurisation, some side reactions also take place. These include hydrogenation (saturation of aromatics and olefins) and hydrocracking. Saturation of aromatics is important

for improving the cetane number, which serves to increase the ease of ignition; while saturation of olefins increases the storage and oxidative stabilities of the product[29].

Another conversion process that is applied in refineries to convert heavy, less useful fractions (like distillation residue) into lighter more useful fractions (like gasoline and diesel) is called 'cracking'. This process requires high temperature and pressure to cleave the carbon-carbon bond, often in presence of a catalyst. Presence of a catalyst is not necessary for cracking and its use is dependent on the feedstock[29,30].

Catalytic hydrocracking is one of the most common type of cracking method applied in the industry for obtaining diesel-blending components. The feedstocks used to produce these components usually include heavy gas oils, vacuum gasoline, heavy vacuum oil distillates, and other heavy distillate oils. Catalytic hydrocracking involves subjecting the feedstock to a hydrogen atmosphere, which results in a significant increase in the hydrogen content of the products[27,29].

Alongside the cracking of heavy fractions to lighter fractions, hydrocracking also leads to skeletal rearrangement (isomerisation) of n-paraffins to isoparaffins. This process is also called 'dewaxing' of the n-paraffins, the purpose of which is to reduce the freezing point (or enhance the pour point/cold flow properties) of the product. However, isoparaffins tend to have lower cetane numbers as compared to their straight chain counterparts. Achieving a highest possible cetane number and lowest possible freezing point simultaneously is not possible. Therefore, a compromise is achieved by sometimes selectively "dewaxing" the largest chain n-paraffins[29].

2.1.2 Diesel Fuel Components

Diesel fuel is a complex mixture of hydrocarbon species with the main classes being paraffins, naphthenes and aromatics, the latter including alkylated benzenes and polyaromatic hydrocarbons (PAHs). Generally, a straight-run diesel has an approximate hydrocarbon

composition of 72 % - 75 % paraffins and 24 % - 27 % aromatics. The paraffins include n-paraffins, isoparaffins and naphthenes in typical proportions of 20 %, 30 % and 50 % of the total paraffinic content of the diesel fuel, respectively. Of the aromatics, about 90 % are mono-aromatics (benzenes and alkylated benzenes), 7 % are di-aromatics and 3 % tri-aromatics[20]. Some blending components of diesel fuels also include olefins produced during chemical conversion (cracking) of paraffins. This section will outline the general properties of the different hydrocarbon classes.

Paraffins

Paraffins are hydrocarbons that have a general formula of C_nH_{2n+2}, where n is the carbon number (number of carbons atoms) of the molecule. The paraffins are also called saturated hydrocarbons as they have single bonds between all carbon atoms, each carbon atom forms four single bonds, and no hydrogen can be added without breaking a carbon-carbon bond[27].

Paraffins are further divided into subclasses of normal paraffins (n-paraffins) and isoparaffins. N-paraffins are molecules where carbon atoms are linked together to form a chain-like structure, with each carbon atom (except for those at the ends) bonded to two others. Isoparaffins also have a similar carbon backbone, however they also have carbon atoms branching off from the backbone[27].

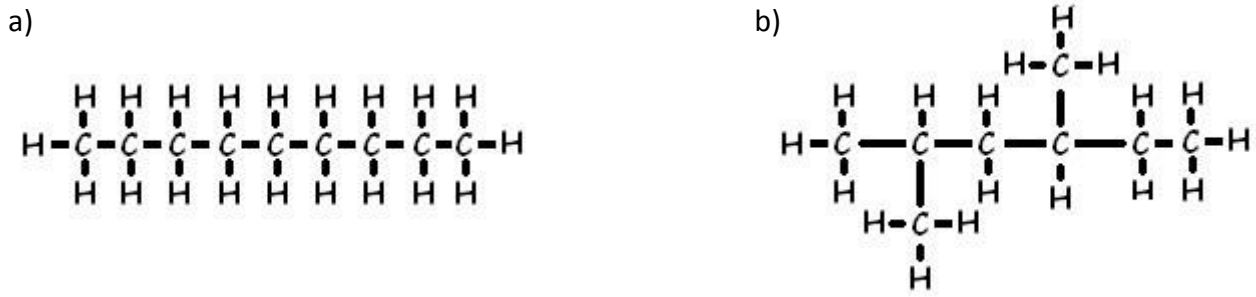

Figure 2.1 Paraffins with the chemical formula C_8H_{18}: a) normal octane b) isooctane or 2,4-dimethylhexane

Normal octane and 2,4-dimethylhexane (isooctane) have the same chemical formula of C_8H_{18}. However, (as demonstrated in Figure 2.1) the structure of the two molecules is different. The difference in structure gives the two molecules different chemical and physical properties. The two molecules with same chemical formula but different molecular structures are called structural isomers.

Naphthenes

Naphthenes are saturated molecules which have carbon atoms arranged in a ring. Diesel fuels consist of naphthenes with rings of five or six carbons atoms. All carbon atoms in the ring have a single bond, which is why they are also classed as paraffins called cyclic paraffins (or cycloparaffins). Naphthenes can have two or more rings fused together, with some carbon atoms shared between the adjacent rings. The general formula for a single ring naphthene is C_nH_{2n}. Figure 2.2 shows two naphthene molecules with a single and a double ring structure[27].

Figure 2.2 Naphthenes with a single and double ring formation a) ethylcyclohexane b) decalin (bicyclodecane)

Olefins

Olefins are similar to paraffins except that the number of hydrogen atoms in their molecules is less; this means that the olefins contain at least one double bond between their carbon atoms.

Presence of a double bond makes them more reactive than paraffins, as the double bond can be broken to add more species; hence they are called unsaturated hydrocarbons. The general formula for an olefin with one double bond is C_nH_{2n}. Like paraffins, olefins can have structural isomers with the same chemical formula but different molecular structures[27].

Olefins are not normally found in crude oil; they are formed during conversion processes such as thermal or hydrocracking of paraffins and naphthenes. Because of their reactive nature and susceptibility to oxidation, olefins are not desirable in diesel fuels, as they reduce the storage stability of the fuel.

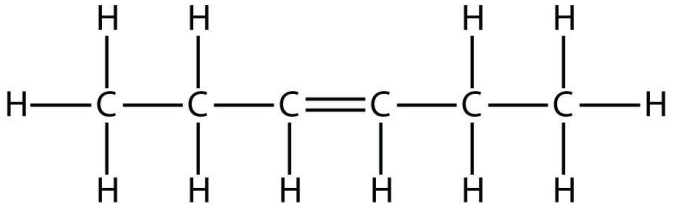

Figure 2.3 A hexene molecule with a double bond between third and fourth carbon atoms.

Aromatics

Aromatic hydrocarbons are cyclic molecules like naphthenes, except that the bond between carbon atoms is an aromatic bond instead of a single bond. An aromatic bond involves delocalised electrons in the pi bond between carbon atoms. Unlike naphthenes, a single aromatic ring structure can only have six carbon atoms[27].

Aromatics are unsaturated; thus, the aromatic bond can be broken to form single bonds between carbon atoms through addition of hydrogen. If an aromatic molecule is partially saturated with hydrogen, it forms a cyclic olefin; when it is completely saturated, it forms a naphthene[27].

A benzene molecule is the simplest aromatic structure with a single ring of six carbons bonded to a hydrogen atom each (Figure 2.4). Some of the hydrogens can be replaced with alkyls to form alkyl benzenes. Aromatics with a single aromatic ring are called monocyclic aromatic or

mono-aromatic aromatic hydrocarbons, which have the general formula of C_nH_{2n-6}. Polycyclic aromatic or poly-aromatic hydrocarbons (PAHs) are compounds with more than one aromatic ring; they have some shared carbon atoms between adjacent rings.

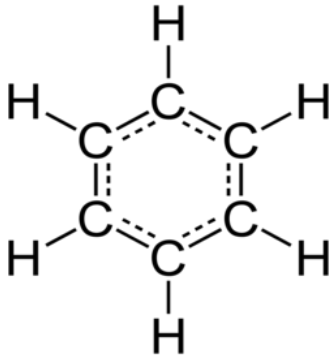

Figure 2.4 A benzene molecule with six carbon atoms. The dotted line represents the aromatic bond.

2.1.3 Diesel Fuel Properties and Performance Parameters

In the early days, a large variety of liquid fuels could be used to power a diesel engine, without the need to give too much consideration to its quality and combustion products. Nowadays, however, diesel fuels are subjected to very stringent regulations and government standards worldwide. In the US, diesel fuel regulation standards are defined by American Society of Testing and Materials (ASTM), while in Europe the corresponding establishment is the European Standards Organisation (CEN). These organisations have developed set of regulations to maintain diesel fuel's chemical, physical and performance specifications; these are the ASTM 975 and EN 590 by ASTM and CEN, respectively. These specifications provide directives for fuel properties such as volatility, cetane number, viscosity, cold flow properties, lubricity, storage stability and sulphur content[30,31]. This section elucidates some of these diesel fuel properties along with other parameters, together with their impact on the fuel performance.

Cetane Number

Cetane number, the most common standard of performance for diesel fuels, is a measure of the ignitability of a fuel, where a high cetane number corresponds to a high ignitability. It also characterises combustion quality, ease of cold starting, duration of white smoke at start-up and intensity of engine knock[30].

Cetane number of a fuel is determined through the Cetane Number test using a reference fuel, blended from varying proportions of hexadecane ('cetane') and heptamethyl nonane that has the same ignition delay as the test fuel. The cetane number is defined precisely as the % hexadecane + 0.15 times the % of heptamethyl nonane contents of the reference fuel blend[8].

The Cetane Number test requires a specially designed test engine that is expensive to acquire and maintain; this makes this method of cetane number determination of fuels very inconvenient. Various alternate tests have been developed to allow estimation of cetane numbers through formulas; two of the most common tests are called cetane index and diesel index. These use specific properties of the test fuel such as its API gravity, and distillation profile as inputs to formulae that determine the indexes. Out of the two indexes, cetane index is a more widely used parameter as it provides a closer match to the Cetane Number test; it is also much less costly and time consuming to obtain.

A cetane index value above 50 indicates that the ignition characteristics of the fuel are good. Values of cetane index below 45 are undesirable and below 40 are unacceptable. When the cetane index falls too low the ignition delay become very long, this results in the bulk of the injected fuel charge igniting simultaneously, causing a violent combustion. Higher cetane index allows ignition to start at several points and gradual spread of flame in the charge. However, if the cetane index is too high the charge can ignite before adequate mixing and thus increasing

emissions. In Europe, the minimum required cetane index for a diesel fuel is 45, while US allows values down to 30.

The hydrocarbon classes that make up the diesel have a profound effect on its cetane index. Generally, alkanes have high, aromatics have low and naphthenes have intermediate cetane indices.

Distillation Properties

An important parameter for determining quality of diesel fuels is the distillation curve. Diesel fuel is a mixture of hydrocarbons that gives the fuel a range of boiling points. To characterise a diesel fuel, its boiling range and sometimes its temperature data related to the amount of distilled fraction are required. The boiling range is determined through a special distillation process, carried out at standard conditions and ambient pressure. A typical diesel distillation curve is shown in Figure 2.5, with a typical boiling point range of 150 °C – 350 °C [8,32].

Diesel fuels have a wide boiling point range, which can be divided into three sections: light fraction, medium fraction and heavy end. Each of these sections can be studied to determine key performance parameters of the fuel in question. The lighter fraction influences the flashpoint of the fuel and the starting ability of the vehicle. The medium fraction affects fuel's density and viscosity. The heavy ends have a significant role in the emissions of the fuel[32].

The heavy end fractions (> T90) contain polyaromatic hydrocarbons, these are responsible for particulate emissions and contribute to the formation of carbonaceous diesel injector deposits as well[32].

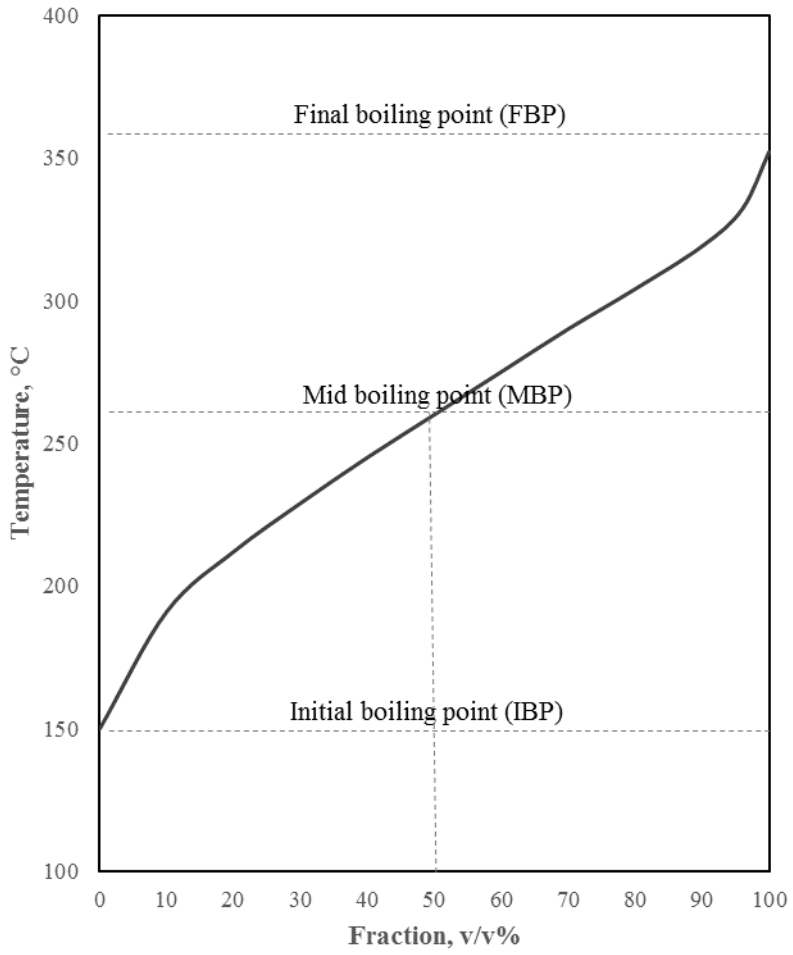

Figure 2.5 Typical distillation curve for diesel fuel. [8]

Viscosity

Viscosity affects the atomisation characteristics and spray patterns when the diesel charge is injected into the cylinder. Fuels with high viscosity form sprays with smaller cone angles with larger droplet sizes. High viscosity values can also result in excessive heat generation in fuel pumps due to viscous shear. On the other hand, very low viscosity values can result in fuel leakage through the tolerances between pump plungers and cylinders[8]. Therefore, diesel fuel viscosity has to be maintained between an upper and a lower limit. ASTM 975 specifies the range of acceptable kinematic viscosity (at 40°C) between 1.9-4.1 mm^2/s, while EN 590 specifies the range between 2.0-4.6 mm^2/s[30,31].

Viscosity is found to be primarily related to the molecular weight of the hydrocarbon molecules and not significantly dependent on the hydrocarbon class. For the same carbon number, naphthenes have slightly higher viscosities than paraffins or aromatics[27].

Sulphur Content

Sulphur content of the diesel fuel is one of the most strictly regulated property by legislation. Sulphur is naturally present in all crude oils as well as all its distillates. During combustion, the sulphur present in the fuel can form acidic species, such as SO_2 and SO_3, which can form sulphates during exhaust emission. These sulphates are part of an engine's particulate emissions, therefore controlling the sulphur content is important in reducing the emission of harmful sulphate pollutants[30].

Acidic sulphur species are also linked to corrosion and wear of engine components; thus, reducing sulphur content can lead to increased engine performance and life. ASTM 975 and EN 590 limit the maximum sulphur content of ultra-low sulphur diesel fuel (ULSD) to 15 parts per million (ppm) and 10 ppm, respectively.

Cold Flow Properties

In winter, some heavy components of diesel fuels can form wax due to their high freezing points. The point at which diesel becomes hazy from formation of wax crystals is known as the cloud point[27]. As the fuel is cooled beyond the cloud point, a point is reached where the wax begins to coat the fuel filter, enough to block the flow of fuel through it. The temperature down to which the filter is not completely blocked and the fuel is still useable is known as the cold filter plugging point (CFPP)[33].

Molecular shapes of n-paraffins and aromatics facilitate them in forming crystal structures more easily than isoparaffins and naphthalenes; thus, the former tend to have higher freezing points. Refineries blend fuels with varying proportions of wax forming components to suit the

weather conditions. Reducing the proportion of components with high freezing points, generally also reduces the cetane number of the diesel fuel, which is why a compromise is required depending on the weather conditions[8].

Storage Stability

All diesel fuels tend to oxidise when exposed to air, heat and moisture for long durations. Presence of unsaturated hydrocarbons such as olefins increases the tendency of the fuel to oxidise, as they are relatively less stable. Certain metals present in the fuels can act as catalysts for oxidation reactions, which further reduces the fuel stability. The oxidation of unstable components can lead to filter plugging, and formation of lacquer and gum-type deposits in fuel injection equipment. This results in poor engine performance and reduced fuel economy[7,27,30].

Over the years, use of cracked products such as olefinic oils and light cycle oils has increased. This makes the stability of fuels an important parameter to address for organisations like ASTM and CEN, along with the engine manufacturers.

Heating Value (Energy Content)

Although not specified by ASTM nor by CEN, this property is of interest to engine manufacturers in terms of thermal efficiency of power production. The heating value can be measured on volumetric basis or weight basis, and the specified units are dependent on the type of measurement[7].

The heating value for diesel is strongly dependent on its composition of hydrocarbon classes. For compounds with the same carbon number, the order of increasing heating value by class is aromatic, naphthene, and paraffin on weight basis. The order is reversed when the same classes are compared on volume basis, with aromatics having the highest heating value. The heating value is usually related to the density of the fuel, with more dense fuels having a higher heating value on volume basis, and the less dense fuels having a higher heating value on weight basis[27].

2.1.4 Additives

As the diesel emissions regulations become increasingly stringent, the petroleum industry struggles to meet and maintain the required diesel quality. Blending of base stocks to obtain high quality in a fuel is a complex procedure. It can, however, be facilitated by introduction of additives of various types[8].

Additives and fuel components are distinctly different from each; in that fuel components add volume to the fuel and fall into hydrocarbon classes, while the additives are added in very small quantities, usually in parts-per-million level, and do not add significant volume to the fuel[7].

There are several commercially available additives that are designed to be used with diesel fuel. Perhaps the most important additive among them are the cetane improvers. Cetane improvers are used to raise cetane numbers and improve ignition quality. Low temperature operability additives are also very important for operators and fuel distributors. These include pour point depressants and cloud point depressants. Cloud point depressants reduce the temperature at which paraffins solidify. In some cases, de-icers may also be used to prevent fuel line freezing[7].

Other diesel fuel additives used include anti-oxidants, lubricity improvers, combustion improvers, cold flow improvers, corrosion inhibitors, detergents, re-odorants and anti-foamants. Functions of some of the important diesel fuel additives are shown in Table 2.3.

Although additives have benefits in improving quality of fuels, they also add to the cost of fuels. Therefore, unless the benefits outweigh the cost, there is no incentive for the oil companies and consumer to use additives. In most cases, the consumer is unaware of the contents on the fuel, and using additives that might already be in the fuel will produce no or little added benefits[8].

Table 2.3: Diesel additive types and their function[7]

Additive Type	***Functions***
Cetane Improvers	*Increased cetane number to give better combustion quality, better starts and reduced white smoke.*
Lubricity Improvers	*Better injector and pump lubrication.*
Detergents/ Dispersants	*Prevent formation and removal of deposits and gums, for clean injectors and better spray patterns.*
Pour Point Depressants	*Low temperature operability*
Cloud Point Depressants	*Reduce waxing temperature of paraffins*
Corrosion Inhibitors/ Metal Deactivators	*Prevent corrosion of fuel transport pipelines. Deactivate copper compounds in fuel to promote longer storage life.*
Anti-Foamants	*Reduce foaming and splashing when filling tanks.*

2.1.5 Alternative Fuels

Reduction in emission of air pollutants from combustion of fuels, combined with the increasingly stringent carbon and greenhouse gas emissions (GHG) regulations has been a major driving force for alternative fuels. Another driving influence, that is gaining focus, is the question of energy security, brought about by depletion of natural energy resources and geopolitical factors.

Some of the diesel fuel alternatives that are being used in or have the potential for commercial applications include: biofuels, synthetic diesel fuels and alcohol-diesel blends. To address their relevance to this study, biofuels and synthetic gas-to-liquid (GTL) diesel fuel will be discussed in detail in the following subsections.

Biodiesel Fuels

In general terms, biodiesel refers to a variety of materials derived from vegetable oils, animal fats, or recycled cooking oils. However, in definition, it is a fuel composed of mono-alkyl esters of long chain fatty acids derived from vegetable oils or animal fats. Some of the common

sources of vegetable oil derived biodiesel include soybean oil, rapeseed/canola oil, palm oil and sunflower oil[27].

Research on sources of biodiesel has been focused on the use alkyl esters due to their superior properties as opposed to the use of pure vegetable oils or partially esterified oils. Use of virgin vegetable oils for diesel applications has been found to lead to a variety of engine problems such as nozzle blockage from deposits, needle stick and lube oil gelling. These problems have been linked to the presence of triglycerides - three fatty acids bonded to a glycerol molecule. A process involving reaction of the triglycerides with an alcohol (usually methanol or ethanol), in presence of a catalyst, is used to separate glycerine from the fatty acid alkyl esters. This process is commonly known as transesterification (see Figure 2.6). The alkyl group in the fatty ester is dependent upon the alcohol used. Use of methanol in the transesterification process results in production of biodiesel that is composed of fatty acid methyl esters (FAME); these have similar chemical and physical properties to a conventional diesel fuel[7,27].

Acronyms are often used to differentiate between biodiesel fuels based on their vegetable oil feedstocks. Some common biodiesel feedstocks and their acronyms are given below:

- RME – Rapeseed Methyl Ester
- SME – Soybean Methyl Ester
- PME - Palm oil Methyl Ester

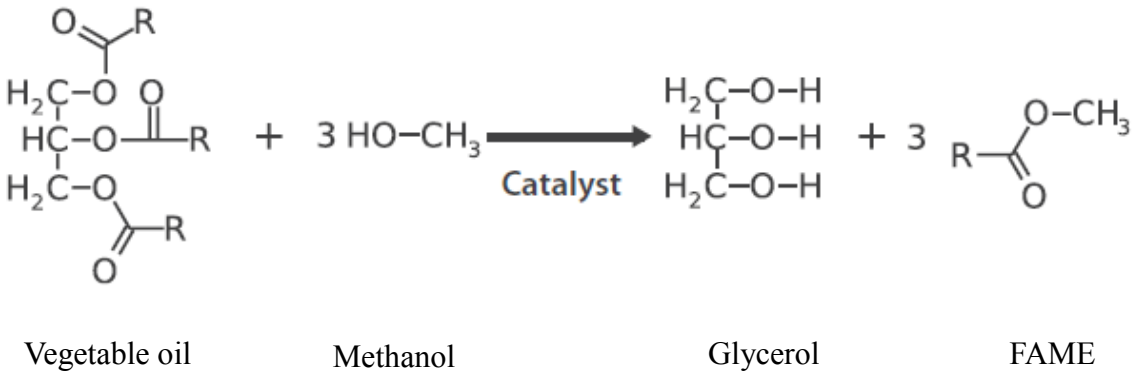

Figure 2.6 Transesterification of vegetable oil to produce FAME and glycerol, using methanol[34]

Physical and chemical properties of the resultant fatty esters strongly depend on the source of the vegetable oil. Depending on the vegetable oil feedstock, the fatty esters can have a mixture of chemical profiles that are designated according to the number of carbon atoms and the number of unsaturated bonds in their molecules. FAMEs obtained from some common vegetable oils, along with their chemical structures, are listed below:

- Methyl palmitate (C16:0)

$$CH_3OOC-(CH_2)_{14}-CH_3$$

- Methyl stearate (C18:0)

$$CH_3OOC-(CH_2)_{16}-CH_3$$

- Methyl oleate (C18:1)

$$CH_3OOC-(CH_2)_7-CH=CH-(CH_2)_7-CH_3$$

- Methyl linoleate (C18:2)

$$CH_3OOC-(CH_2)_7-(CH=CH-CH_2)_2-(CH_2)_3-CH_3$$

- Methyl linolenate (C18:3)

$$CH_3OOC-(CH_2)_7-(CH=CH-CH_2)_3-CH_3$$

Chemical profile of a FAME molecule is designated, in general form, as CX:Y, where X denotes the number of carbon atoms in the molecule originating from the fatty acid source, while Y denotes the number of unsaturated chains/compounds in the molecule.

Although having the ability to be used by itself, biodiesel is usually used as a blend component in conventional diesel. The blends are designated by a capital B followed by biodiesel percentage by volume in the blend; for example, B20 refers to a biodiesel blend containing 20% biodiesel and 80% conventional diesel. A neat biodiesel will be represented as B100.

Biodiesel have low sulphur content and relatively high cetane number. Blends made from biodiesel also seem to improve the lubricity characteristics of the fuel, in fact small proportions of biodiesel (B2) is added to conventional diesel to improve lubricity. Being a renewable energy source, it has the potential of reducing GHG emissions and net CO_2 emissions[7].

Biodiesel (B100) has certain properties that reduce its storage stability. It is hygroscopic, which means that it tends to absorb moisture from the atmosphere. Over long periods of storage, the water content of the biodiesel can increase above the acceptable levels. This increases the risk of corrosion as well as microbial contamination[7].

At higher blend levels, biodiesel can increase NO_x emissions and negatively impact low temperature operability. Concerns regarding the low solvency of biodiesel loosening sediments in fuel tanks have been raised, which can lead to fuel filter plugging[7].

Synthetic Diesel Fuels – Gas-to-Liquid

Conventional diesel fuels are manufactured by refining crude oil. However, other carbon bearing feedstocks can also be utilised to synthesise diesel. Coal and biomass have been used to produce diesel, but the most popular alternate feedstock for diesel fuel synthesis today is natural gas.

The best known synthetic fuel technology is the Fischer-Tropsch (FT) process, which was developed in Germany in the 1920s. FT has been used in production of synthetic diesel fuels from different carbonaceous feedstocks such as coal. FT diesel fuel synthesised from natural gas is known as gas-to-liquid or GTL and the processes used in their manufacture are known as gas-to-liquid technologies[27].

The FT process of synthesising GTL diesel uses catalysts to convert natural gas through a carbon monoxide-hydrogen intermediate into a mixture of hydrocarbons. This yields a high-quality fuel that is almost entirely composed of paraffins and olefins, with virtually no aromatic hydrocarbon content. The olefins present in the fuel are then hydrogenated to convert them to paraffins. The high proportion of paraffins gives GTL diesel a significantly higher cetane number than conventional diesel. GTL diesel has the added benefit of having nearly zero content of sulphur and nitrogen. However, GTL diesel suffers from low lubricity

characteristics, along with poor cold flow properties, which limit its use in cold weather conditions[27].

The limitations can be overcome with proper treatment of GTL fuel using additives to improve its lubricity and cold flow properties. GTL diesel is fully compatible with current diesel technology and can be readily mixed with conventional diesel to produce desirable diesel fuel blends[27].

Recently, GTL technologies have been a subject of interest for some major oil companies including Shell, ExxonMobil and Sasol. So far, GTL diesel has only seen limited commercial use, in form of a blend component for premium diesel fuels, due to its high production costs as compared to its conventional counterparts. However, as the technological advances are made, the costs of GTL diesel production are expected to reduce gradually, while at the same time depletion of natural resources is expected to increase the cost of crude oil derived diesel, making GTL diesel increasingly cost competitive[27].

2.2 Modern Diesel FIE

Development of the high-speed direct injection (HSDI) diesel engines in the late 1970s introduced it as a true alternative power unit and a high-performance, fuel-efficient competitor to the gasoline engine. The superiority of the modern diesel engine was reflected by the increase in market share of diesel passenger cars in the European automotive market to over 50 % in the past decade, while it was just 36 % in 2001[1,2].

The rise in proportion of diesel cars has been attributed to improvements in specific power, torque and NVH (noise, vibrations and harshness), made possible thorough advancements in three key engine component systems in particular. First is the development of common rail fuel injection system with electronic control, which allowed decoupling of injection pressure from engine speed, increase in operating injection pressure and enabled multiple injections along

with flexible injection timings. Secondly, there have been improvements in the turbocharger efficiencies with the introduction of variable geometry turbochargers. Thirdly, more sophisticated electronic controls have increased the performance and response time of engine systems. These enhancements have been driven by the tightening European emissions legislation and CO_2 targets. Similar trends in legislations and increasing popularity of diesel cars are observed in other parts of the world, including the USA and Japan[2].

Enforcement of more stringent gaseous and particulate exhaust emission limits have demanded an increase in diesel fuel combustion efficiencies through better atomisation of diesel fuel. This can be achieved by a reduction in injector nozzle-hole diameters and increase in fuel system operating injection pressures. For this reason, diesel engines in service today have very high injection pressures; Fuel Injection Equipment (FIE) Original Equipment Manufacturers (OEMs) have developed common rail fuel injection systems that have operational injection pressures in excess of 2,500 bar, with near-future technologies aiming for injection pressures up to 3,000 bar[3,4].

2.2.1 Spill Valves and In-Vehicle Fuel Recirculation

Introduction of common rail injection systems has allowed multiple injection events to take place over the speed-load range, which has resulted in better combustion efficiencies and engine noise reduction. It has provided the opportunity for a pilot injection to control combustion noise by modulating the rate of cylinder pressure rise at the start of the combustion. Small pilot injections are a major factor in achieving the desired trade-off between combustion noise and emissions, required to meet the emission standards. It is believed that pressure inside the injector, as well as the injector performance in terms of operating speed to allow short and multiple injections is of more importance for engine performance than the maximum rail pressure[1,35].

Current-generation diesel common rail injectors are hydraulically connected via HP fuel pipes to the HP fuel rail, and electrically wired to the Engine Control Unit (ECU). Regardless of the rail pressure, the injector only injects fuel when there is a voltage supply from the ECU to the injector actuator. The duration of the voltage supply is proportional to the volume of fuel injected into the engine cylinders. Although different in design, the operating principle for the various OEM diesel injectors is the same[35].

The injector technology has undergone refinement for quicker response times to allow shorter injections with higher shot-to-shot repeatability. To increase the response time of injectors for shorter, multiple controlled injections, the needle lift and re-seating is needed to be accelerated. One way the needle speed has been increased is through incorporating a spill mechanism that utilises the HP (high-pressure) fuel to force the needle motion for a quicker needle lift and seal.

The HP fuel in a control chamber located above the control piston applies a downward force which is greater than the upward force applied by the HP fuel on the nozzle needle; this force imbalance keeps the needle seated and no injection occurs. When a voltage is supplied to an actuator, a control valve (also called a spill valve) is opened allowing HP fuel in the control chamber to ‘leak’ into a LP (low-pressure) return line (and back to the fuel tank). The resulting drop in pressure inside the control chamber significantly reduces the downward force on the control piston, allowing the upward force on the nozzle needle to dominate; resultantly, the needle lifts and injection starts. At the end of the injection, the voltage supply is stopped and the spill valve closes to isolate the control chamber from the leak passage. Pressure inside the control chamber increases to match the rail pressure, forcing the control piston downwards, seating the nozzle needle and stopping the fuel injection event.

Throttles at the inlet and outlet of the control chamber determine the rate at which fuel enters or exits the chamber. The rate at which the fuel enters the chamber defines the injector closing speed, whereas the rate at which fuel exits determines the injector opening speed[35].

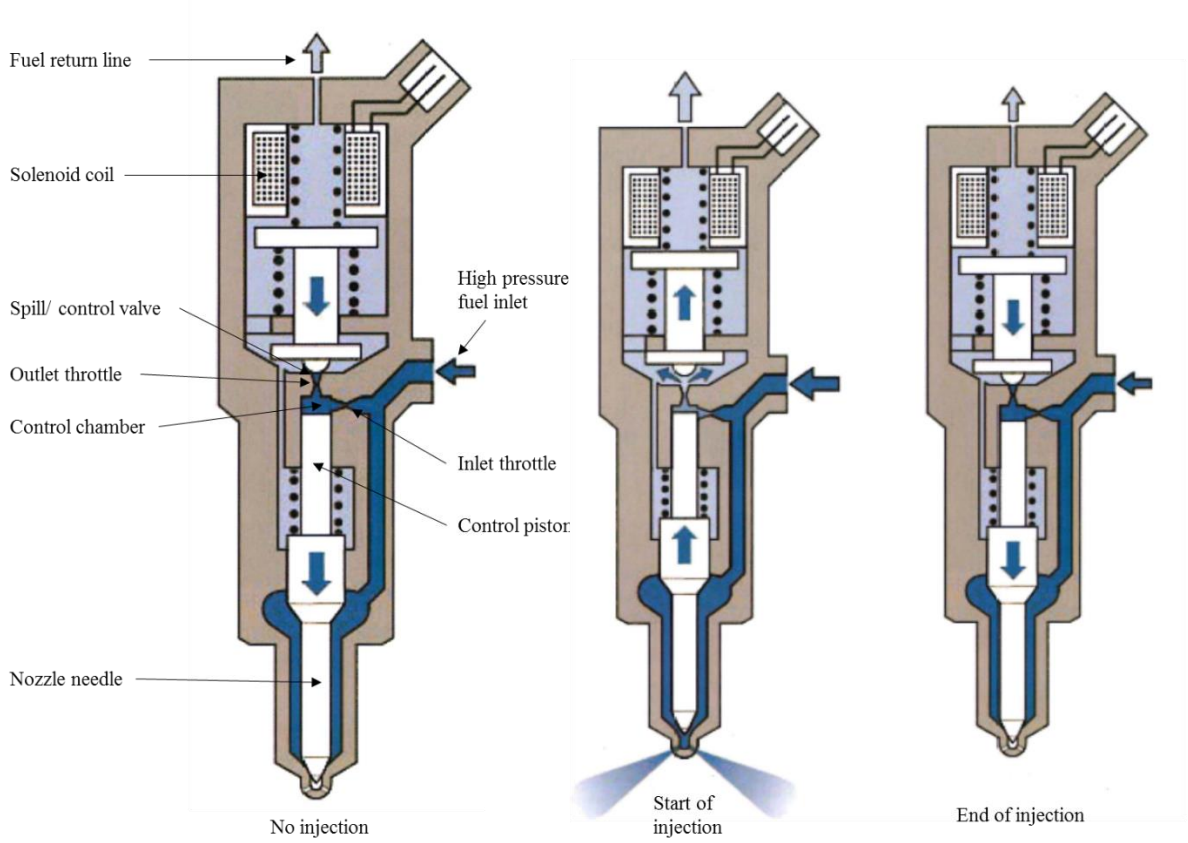

Figure 2.7 Operation of a common rail solenoid injector [19]

Currently, there are two main types of injector technologies in use for diesel common rail injection systems based on their actuation mechanism, the most common being the solenoid controlled injectors followed by the piezoelectric injectors[19]. Both injector types work using the spill mechanism described above. Spill mechanism operates on the principle of HP fuel depressurising and returning to the tank to be pressurised again, creating an in-vehicle recirculating flow of diesel compression and re-expansion[36].

The amount of fuel returning to the tank from the injectors via spill valve varies from injection-to-injection and load-to-load. Engine operating at low/part load can have rail pressures of

around 600 bar and 40 % of the HP fuel being supplied to the diesel injectors can return back to the tank via the spill valve. However, depending on the common rail system, at high loads the rail pressures may reach 1,400 bar to 2,500 bar. At these conditions, the proportion of fuel returning to the tank can be as high as 20 % to 30 % of the total amount supplied to the common rail and the injectors. This return of diesel is a combination of return from the injector spill valve and pressure regulating safety valves in the common rail and the high-pressure pump[13,19]. In some marine applications, the proportion of fuel returned to the tank, after undergoing compression in the common rail, can be up to 50 %[15].

Apart from the high pressures (up to 2,500 bar), the fuel flowing through the common rail injection system is exposed to temperatures up to 200°C, and the bulk return fuel temperatures commonly exceed 100°C [5,15]. The HP fuel in the common rail is released into the low-pressure return line through a control valve. This creates the possibility of HP fuel jetting into LP fuel, generating shear, friction, cavitation and consequently, heat[11]. The return of fuel to the tank and subsequent recirculation through the high-pressure common rail fuel injection system subjects the fuel to repeated thermal stressing.

Flow of diesel through restrictors in the control valves provide favourable geometric conditions for the flow to undergo hydrodynamic cavitation. Cavitation has been shown to accelerate fuel ageing and has been suspected to cause injector deposits.

Cavitation occurs when the HP fuel flows past valve restrictions to a region of low pressure; the acceleration of flow causes drop in local pressures below the vapour pressure of the fuel, creating vapour pockets of the ‘boiling’ fuel. Downstream of the restriction, the flow velocity of the fuel reduces and the pressures recover, resulting in collapse of the vapour cavities.

2.3 Deposits in Diesel FIE

Recent advancements in the high pressure common rail diesel injection systems, including the increase in rail pressures and reduction in flow passage geometries, combined with the in-vehicle fuel recirculation has led to increased reports of injector deposit formations.

Coincident with the changes in diesel FIE are the developments in the fuels used for these compression ignition engines. Today, diesel fuels are subjected to increasingly aggressive refinery processes to reduce their sulphur content. This has reduced the ability of fuels to carry semi-soluble reaction products, necessitating the use of lubricity additives and sometimes corrosion inhibitors. Use of Fatty Acid Methyl Esters (FAME) has gained popularity, leading some marketers to increase concentrations of Deposit Control Additives (DCA) in the fuel to reduce possibilities of nozzle coking from FAME[10]. Fuels that were previously deemed acceptable are being exposed to extreme conditions inside the modern common rail injection systems, creating new chemical pathways for the formation of injector deposits that have different properties to the traditional carbonaceous nozzle deposits[9].

A modern diesel injector is a high precision equipment with high efficiency nozzles designed to ensure precise and repeatable metering of minute fuel quantities. Formation of deposits on the nozzle tip and inside the injector body can have adverse effects on the engine performance and emissions[5].

Injector deposits can be divided into two types based on their deposition location. First are the external injector deposits found in the nozzle holes and on the nozzle tip. The external deposits are responsible for deterioration of fuel atomisation and spray characteristics through blockage of fuel flow passages. Second are the Internal Injector Deposits (IIDs) found on the plunger guide and slots, armature plate and guide and at the nozzle needle. These are found to have a detrimental effect on injector dynamics, causing needle stick and retarded motion of the

injector components. Recently, the impact of the IIDs has become of great significance due to the very tight tolerances within the FIE leaving little room for even small amounts of deposits[5,10].

The external/nozzle-hole deposits are formed due to the exposure of unburnt fuel to high temperature combustion gasses. IID, however, are not likely to have the same mechanisms of formation as there is no possibility of exposure to hot combustion gasses inside the injector body. Use of DCAs has addressed the issue of external/ nozzle-hole deposits, but relatively less work has been done to study, understand and tackle IIDs[10].

2.3.1 Internal Injector Deposits

In the past, deposit formation was attributed to ineffective maintenance of engines and improper care taken to avoid fuel contamination, such as water entrainment or lube oil adulteration. The recent deposits, however, have been observed to be different and have shown indication of being possible precursor molecules[37,38].

Researchers have studied deposits obtained from the fuel injection equipment (FIE) in diesel engines in order to determine their composition, the factors that cause them and ultimately the chemical mechanisms that lead to their formation. Two main types of internal injector deposits have been observed:

- Metal carboxylate salts, particularly sodium
- Organic polymeric amide

A third type of deposit has also been reported, which has an appearance of combustion soot.

Metal carboxylate salts

Studies conducted on internal injector deposits (IID) found in field injectors have reported thin layers of waxy or soapy, white to yellow deposits on nozzle needles, control pistons and spill

valves, primarily in the lowest clearance areas of the injector internals[9,10,36,39]. These deposits are often soluble in water and consist primarily of metal carboxylate salts, particularly sodium carboxylate salts[36]. Sodium carboxylate salts are formed through reaction of sodium with carboxylic acids, and are thought to be the most common IID precursor. Other metallic salts such as potassium or calcium based salts are possible but not widely observed in IID.

While several suspected sources of sodium contamination have been identified, the most likely source (for FAME based fuels) is sodium hydroxide from biodiesel production process. Sodium is also used as a catalyst during the transesterification reaction for production of FAME. Other sources of sodium include: salt driers used at refineries, sea transportation and de-icing agents and sodium nitrite corrosion inhibitor additives. Most common sources of carboxylic acids include dodecenyl succinic (DDS) acid used as a fuel corrosion inhibitor and stearic acid found in monoacid based lubricity improvers which are common in fuels today[9,10,36]. Sources of sodium and carboxylic acids contaminants are summarised in Table 2.4

Table 2.4: Potential sources of sodium and carboxylic acids.[36]

Sources of Sodium			***Sources of Carboxylic Acids***	
NaOH	• *FAME & $NaNO_2$*		*DDS*	• *Corrosion Inhibitor*
$NaNO_2$	• *Corrosion inhibitor*		*Fatty Acids*	• *FAME Production* • *Lubricity Additives*
NaCl	• *Salt dryers* • *Sea transportation* • *De-icing Agent*		*Di Acid*	• *Corrosion Inhibitor*

Organic amide

Another type of deposit that has been observed in the field with increasing frequency is an organic based polymeric amide deposit. It is usually deposited on the inner parts of an injector and has an appearance of a hard, brown transparent lacquer that is insoluble in most laboratory solvents. Unlike the carboxylate salts, these deposits are found to have very little metal ions, and are essentially composed of polymeric fuel-borne material[5,36,40].

Insolubility of deposits make it very difficult to fully understand the chemical structure of the polymeric material. Organic amides typically contain significant concentrations of nitrogen which can be identified using Fourier Transform Infrared Spectroscopy (FTIR) peaks seen at the polymeric amide deposits have been associated with the use of poly isobutylene succinimide (PIBSI) based fuel detergents. When subjected to the high temperature conditions (130-160°C) of the FIE, the succinimide ring becomes unstable. It can then interact with fatty acid based compounds, specifically di-fatty acid to form amides[5,36].

PIBSI family incorporates a multitude of chemical structures that are produced using poly isobutylene (PIB) of any molecular weight distribution. It has been argued that amide deposits result only from low molecular weight PIBSI (low quality PIBSI detergent)[40].

Carbonaceous deposits

Recent reports of injector deposits have been accompanied with reports of severe fuel filter fouling. Fuel filters from field have been described to be covered in black deposits, which were a complex mixture of graphitic carbon, polyaromatics, cycloalkanes, aromatics, straight chain substituted alkanes, and acids[37,38,41]. Inspection of the internal structure of these deposits revealed layers of graphitic-like carbon[16]. Sodium salts were found in limited quantities[42].

Barker et al. (2009) isolated solid material from filter deposits for further analysis using Diffuse Reflectance Infra-red Fourier Transform Spectroscopy (DRIFTS). The resulting spectrum showed, high carbon content, along with fine structure functionality of C=O, C-O and aromatics. GC/MS analysis of these molecules revealed ethoxyethene, acids and alkene substituted benzenes which are all possible soot precursors[38].

Such carbonaceous deposits have also been found on nozzle springs and as visibly suspended fine particles in samples of fuel from fuel tank of a diesel vehicle. The later phenomenon is commonly known in the US as black diesel. The origin of such deposits is difficult to identify, however studies have been conducted showing their resemblance to deposits produced when diesel fuel samples are subjected to cavitation[16].

Fuel is known to undergo cavitation in the diesel FIE; as it flows past restrictions (such as spill valves) local pressures may drop below the saturated vapour pressure of the fuel, causing pockets/bubbles of fuel vapour to form. As these vapour pockets return to ambient pressure they can collapse and create regions of extreme temperature and pressure. The extreme conditions create opportunity for pyrolysis type reactions to occur, which are believed to form the primary soot like deposits[36]. Over a period of time these primary soot-like particles can undergo coagulation to form larger soot particles. If large enough (>4 μm) they will get trapped in the fuel filter, however smaller particles will pass through the filter and get carried to the injectors[16].

2.4 Cavitation

Cavitation refers to the formation of bubbles in a liquid when the local pressure drops below the vapour pressure of the fluid, leading to a two-phase mixture of liquid and vapour/gas. Fundamentally, the liquid to vapour transition can occur by heating the fluid at a constant pressure, known as boiling, or by decreasing the pressure at a constant temperature; this is

known as cavitation. In terms of thermodynamics, cavitation can be classed as local boiling as well, however the difference in the thermodynamics paths that precede the formation of vapour determines the phenomena. Since, in the case of cavitation boiling, vapour density is at least two orders of magnitude smaller than that of liquid, the phase transition is assumed to be an isothermal process[43,44].

Plesset and Prosperetti (1977) have studied bubble dynamics in two situations; first is where the bubble interior consists for the most part of permanent gas and second is where the bubble interior is composed almost entirely of vapour of the surrounding liquid. Difference between the isothermal and isobaric phase change has been defined by subdividing the vapour-bubble dynamics in a subcooled liquid and in a superheated liquid, respectively. The subcooled-liquid case corresponds to that in which the vapour density is so small that the latent heat flow does not affect the motion, instead it is controlled by the inertia of the liquid, and the liquid is described as a cavitating liquid. A superheated liquid may be described as one in which boiling phenomena occur and the vapour-bubble dynamics is controlled by the latent heat flow rather than the liquid inertia[45].

Other than the generation and subsequent growth, cavitation also encompasses the collapse of vapour-cavities. At a given time, *t*, the equilibrium radius, *r*, of a vapour-cavity is dependent on the pressure of the vapour at the cavity wall, p_i, and the bulk liquid pressure away from the cavity, p_∞, as defined by Laplace's Law in the following relation[45]:

$$r(t) = \frac{2\sigma}{p_i(t) - p_\infty(t)} \qquad 2.1$$

Where, σ is the surface tension of the liquid. The cavity is said to be at rest but it is in an unstable equilibrium. In a pure liquid, surface tension is the macroscopic manifestation of the intermolecular forces that hold a liquid together.

As the liquid pressure surrounding the vapour-bubble recovers, the cavity becomes unstable and collapses violently. Cavities collapsing can result in very high energy densities of the order of 1 to 10^{18} kW/m^3 and can generate conditions of very high temperatures and pressures (few thousand Kelvin temperature and few thousand atmospheres pressure) locally, with the overall environment of the bulk liquid being that of ambient conditions[46]. Cavitation damage, white noise, sonoluminescence, chemical reactions, and other features of cavitation are linked to this violent collapse of cavities[45].

Cavitation can be of various forms depending on the topology of the void fractions formed. For example, in case of a cavitating liquid flowing in a nozzle, cavitation can run in form of travelling bubbles (cloud cavitation) and vapour pockets (sheet cavitation) that extend over partial length of the nozzle body, or full length of the nozzle body (super-cavitation)[44,47–50].

Cavitating flows are of interest in high pressure diesel injection systems due to the possibility of high pressure fuel flowing through nozzles and valves, resulting in formation of vapour cavities. However, cavitation can also occur in a static or nearly static liquid depending on the source of perturbations. Gogate et al.[46] list four principal types of cavitation based on the actuation method:

- Acoustic cavitation – caused by pressure variations in liquid using sound waves, usually ultrasound falling in the range of 16 kHz – 100 MHz.
- Hydrodynamic cavitation – caused by pressure variations using the geometry of the system, creating velocity variation. The geometry is used to interchange the liquid pressure and kinetic energy to generate cavities in the flow through orifice, venturi, etc.
- Optic cavitation – caused by photons of high intensity light (laser) that rupture the liquid continuum.

- Particle cavitation – caused by a beam of elementary particles, e.g. a neutron beam, rupturing a liquid.

The focus of this study is towards the impact of hydrodynamic cavitation on diesel fuels. Due to limited literature available on the chemical effects of hydrodynamic cavitation, studies conducted on acoustic cavitation will be reviewed to link the effects of acoustic cavitation to the effects of hydrodynamic cavitation on diesel fuel properties.

2.4.1 Cavitation Bubble Dynamics

Apart from the differences in their actuation method, two-phase mixtures of vapour and liquid can form through various mechanisms. As mentioned *a priori*, the process of vapour formation in a liquid can be divided into two, based on the thermodynamic path that precedes it; namely, boiling or cavitation. During its lifetime, a typical cavitation bubble goes through distinct stages which encompass its formation, growth and subsequent collapse (implosion).

The behaviour of vapour cavities and bubbles has been of great interest in the field of fluid dynamics for a long time. Serious theoretical research on the subject was initiated by Lord Rayleigh in the early twentieth century when he studied the effect of cavitation damage to ship propellers[51].

Theoretical studies on the dynamics of gas-filled spherical bubbles are performed using the Rayleigh-Plesset equation. It is a nonlinear second-order ordinary differential equation that takes the form of:

$$R\ddot{R} + \frac{3}{2}R^2 = \frac{1}{\rho}\left[P_l\left(\frac{\dot{R_l}}{R}\right)^{3\gamma} - P_\infty\right] \qquad 2.2$$

This equation is a spherical case of the extensive Navier-Stokes equation and is used to describe the three-dimensional oscillatory motion of a spherical cavity in infinite liquid. The equation is readily extended to incorporate surface tension and viscosity effects. Like Navier-Stokes

equation, there are no known general solutions to the Rayleigh-Plesset equation and the equations are often solved numerically[52]. It is worth mentioning that the Rayleigh-Plesset equation is only valid up to the point where the bubble wall velocity is below the sonic velocity in the cavitating medium, as the density of the liquid is assumed to be a constant (incompressible).

Nucleation

Nucleation is the term used for weakening of a liquid leading to formation of small voids in the liquid, which can grow to macroscopic bubbles when transported to regions of low pressure.

Weakening of a liquid can occur in two forms. First is when thermal motions within a liquid form temporary, microscopic voids that create nuclei necessary for rupture and growth to macroscopic bubbles. This process is called homogeneous nucleation[44,53].

Second process constitutes to weakness that occurs at a boundary between liquid and solid wall of the container or between liquid and small particles suspended in the liquid. When bubbles form at such sites, it is called heterogeneous nucleation. Heterogeneous nucleation is a more common method of void formation in practical engineering applications[44].

Presence of micron-sized bubbles of contaminant gas can also act as nucleation sites. These bubbles are known to resist being completely dissolved in the liquids such as water. If the nucleation bubble contains the contaminant gas along with the liquid vapour, then the pressure in the bubble is a sum of partial pressures of the gas and vapour. The implication of this is a reduction in the strength of the liquid, hence the bubble will grow larger at pressures greater than the vapour pressure of the liquid[44]. Presence of gas bubbles in a liquid can significantly reduce its tensile strength by providing nucleation sites for cavitation to occur under smaller negative pressures[17].

A liquid's tensile strength is determined by the attractive forces that hold it together. It varies depending on the type and purity of the liquid. A large negative pressure is needed to overcome the liquid's tensile strength. Pressures needed for overcoming tensile strength of pure liquids can be enormous. Pure water requires over a 1,000 atmospheres of negative pressure to surpass its tensile strength[17]. Liquids such as water are found to be able to withstand pressures below their saturated vapour pressure. A liquid in this stretch state is said to be metastable. In terms of density, a negative pressure corresponds to a liquid density reduced below the equilibrium density. The molecules in the liquid in metastable state are further apart from each other, however the mutual attraction allows the system to remain intact. If the density is reduced enough, the intermolecular distances increase too much and the liquid becomes mechanically unstable. This critical density is called the spinodal density, and the corresponding pressure is called the spinodal pressure[53].

Pressure inside a bubble, p_i, of radius, R, that contains only vapour of the surrounding liquid at a uniform temperature, *T*, will be equal to the saturated vapour pressure $p_v(T)$ of the liquid. For the bubble to be in equilibrium condition, the exterior pressure, *p*, will need to be slightly lower than the p_v, due to the surface tension, σ, trying to shrink the bubble. Thus, ($p = pv - 2\sigma/R$) will be less than pv. If the exterior pressure falls below $pv - 2\sigma/R$, consequent to the pressure difference, the bubble will grow, increasing the radius R. If the drop in exterior pressure is large enough such that the bubble size increases to a critical value R_c (where liquid rupture occurs) then the tensile strength of the liquid, Δp_c, can be stated as [44]

$$\Delta p_c = {}^{2\sigma}/_{R_c} \qquad 2.3$$

Bubble Growth

Growth of a cavitation vapour bubble is governed by inertial, thermal and gas diffusion effects. In cavitating flows (hydrodynamic cavitation) inertial effects play the most significant roles due to the small timescales and bubble sizes.

Inertial Effects

The most common occurrence of cavitation is in flowing liquid systems where hydrodynamic effects result in regions of the flow where the pressure falls below the vapour pressure. The pressure drop can occur either as a result of decrease in the overall pressure of the liquid or increase in flow velocity so that the pressure at some point in the flow approaches the vapour pressure.

Growth of an isolated nucleus in such conditions can be considered in flow through a Venturi. As stated previously, a metastable nucleus can withstand pressures below the vapour pressure p_v. The minimum pressure that a nucleus can withstand, before rupture, is called the critical pressure p_c. $p_v - p_c$ is called the static delay to cavitation and it is larger for smaller bubble sizes. A metastable nucleus passing through a Venturi throat experiences a drop in local pressures in the surrounding liquid. If the pressure drop is below the vapour pressure p_v, the nucleus can undergo growth in two ways, depending on the minimum local pressure p_{min} reached.

- If $p_{min} > p_c$, the nucleus grows slightly and then returns to its initial size after passing through the throat.
- If $p_{min} > p_c$, the nucleus becomes unstable and grows to much large size. Due to inertial forces the maximum bubble size is reached after the throat. At this point, the larger bubble is far from equilibrium and recovery of the surrounding liquid pressure results in a violent collapse of the bubble.

This type of nucleus behaviour is typical of a system where the time spent in the low-pressure region is much longer than the characteristic time-scale of a bubble collapse[54].

Thermal Diffusion

If the time scale for the nucleus in low pressure region is so small that heat transfer between the gas and the liquid cannot be achieved, then the transformation is effectively adiabatic. The behaviour of a permanent gas nucleus in such a situation can be analysed by simplification suggested by Plesset and Hsieh[55].

Assume a nucleus of a perfect non-condensable gas. As the nucleus undergoes a pressure drop, its volume increases and temperature decreases by a small amount. This temperature drop in the nucleus creates a thermal boundary layer in the liquid surrounding the nucleus. The temperature gradient induces a heat flux by conduction and heat is transferred from the liquid to the bubble.

The transformation is considered adiabatic if the exchanged heat is much lower than the internal energy of the nucleus. Inversely, if only a small part of the transferred heat is available for raising the temperature of the nucleus then the thermodynamic process is essentially isothermal.[54,55]

When the amount of heat transferred to the nucleus is large, it can cause the nucleus to grow in size to a macroscopic bubble.

Gas Diffusion

In a gas-liquid solution, a nucleus will grow or shrink through gas diffusion depending on the saturation level of the liquid that surrounds it. The diffusive equilibrium between the nucleus and its surrounding liquid is governed by Henry's law

$$C_s = Hp_g \qquad 2.4$$

Where C_s and p_g are the concentration of gas dissolved in liquid (kg/m^3) and partial pressure of the gas in the nucleus/bubble (Pa), respectively. H is the Henry's constant for the corresponding gas in $(s/m)^2$.

As a gas nucleus in equilibrium experiences a drop in pressure, its volume increases and the diffusive balance shifts. Gas diffuses into the nucleus and the C_s decreases. If the nucleus is static in relation to the liquid, then a diffusive equilibrium is reached due to depletion of dissolved gases in the liquid[56].

However, if the liquid is flowing past the bubble, such as the flow of liquid past a gas filled crevice in a hydrodynamic system, then the gas source is renewed by liquid convection and gas transfer continues for considerably longer.

If a nucleus is subjected to pressure oscillations due to oscillating field such as ultrasound of certain frequency, then the size of the nucleus changes with the imposed pressure. If the nucleus reaches diffusive equilibrium corresponding to the mean imposed pressure, then during the compression cycle the internal pressure of the nucleus becomes larger than the mean pressure, resulting in gas diffusion into the liquid. Reverse happens in the rarefaction cycle of the ultrasound wave, where the internal pressure of the nucleus falls below the mean pressure, and gas diffuses into the bubble. On the whole, the rate of diffusion into the bubble is greater due to a slightly bigger exchange surface area during rarefaction cycle, which results in a gradual growth of the nucleus. This phenomenon of cyclic growth of the nucleus is termed as rectified diffusion[18,44,54].

Bubble Collapse (Implosion)

As a nucleus grows to a bubble the surface tension effects become negligible, and the bubble motion is governed by inertia. Under these conditions, the bubble can continue increasing in size even if the surrounding pressure recovers to pressures above the vapour pressure of the

liquid. At this instance, the bubble is said to have stored potential energy, which is converted into kinetic energy during the bubble collapse phase[57].

In a typical cavitating flow, cavitation bubbles can reach sizes which can be of the order of 100 times the original nuclei size, with the partial pressures of their gas content being 10^{-6} times the partial pressures in the originating nuclei.[44] As this bubble moves out of the region of negative pressure, the resulting pressure difference between the contents of the bubble and the surrounding liquid causes the bubble to collapse violently.

Time of collapse of cavitation bubbles was first formulated by Rayleigh in 1917 using the energy conservation principal. The characteristic time for a cavitation bubble of radius R_i in an infinite liquid, at constant pressure P_∞ and density ρ, to collapse is called the Rayleigh time. In this characterisation, the vapour pressure, gas pressure and surface tension are neglected. Rayleigh time for a bubble collapse is defined as follows[52,54,57]

$$t_{collapse} = 0.91468 \cdot R_i \sqrt{\frac{\rho}{P_\infty}} \qquad 2.5$$

The above relation gives a good estimate for large range of bubble radii. Using the above relation, a 1 cm radius bubble in water under 1 bar of external pressure, has a collapse time of about 1 millisecond.

The behaviour of bubble radius *R(t)* and bubble wall velocity $\dot{R}(t)$ are shown in Figure 2.8. It is observed that the collapse velocity $\dot{R}(t)$ tends to infinity towards the end of a collapse. Close to the end of the collapse, the bubble wall velocity can reach sonic velocity in the liquid, which indicates that liquid compressibility must be taken into account in the final stages of the collapse.

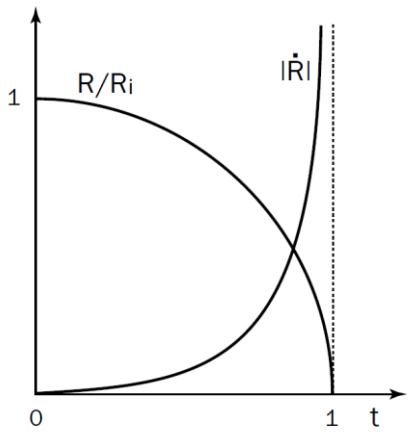

Figure 2.8 Behaviour of $R(t)$ and $\dot{R}(t)$ during bubble collapse.[54]

If the bubble contains a condensable gas, then the dynamics of the bubble during collapse change due to the pressure inside the bubble no longer being constant. Presence of gas in the bubble decelerates the collapse velocity, acting as a damper. Rebounding of bubbles following collapse has been observed where the bubble is seen to rapidly expand, followed by successive collapse and rebound phases. As the bubble rebounds, pressure pulses may be generated which propagate outwards into the liquid. The pressure pulses can be so strong that shockwaves are formed in the liquid. In this stage of the bubble collapse the compressibility of the liquid becomes of further importance. Analytical studies[58] show that these pressure pulses can be about a 100 bar at a distance of about a maximum radius away from the collapsing bubble. Formation of these highly localised shockwaves has been linked to cavitation damage caused to surfaces near a collapsing bubble[44,54].

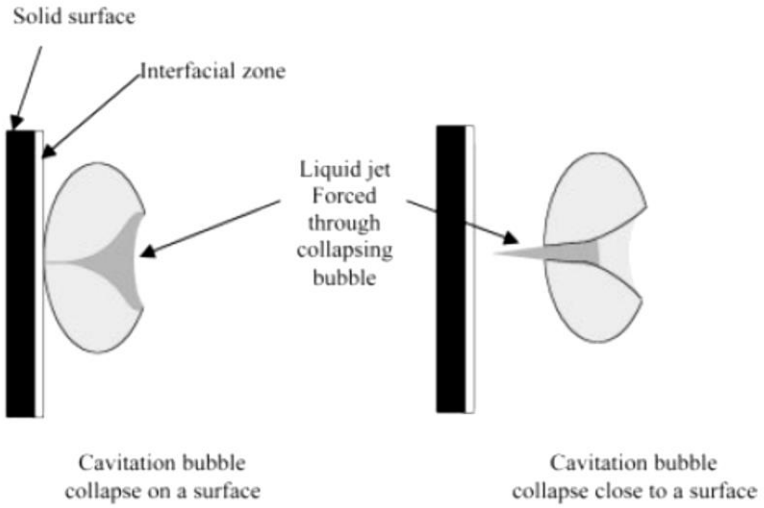

Figure 2.9: Formation of liquid microjets at cavitation bubble collapse near a solid boundary[59].

Another phenomenon linked to cavitation damage is the formation of microjets. Microjets (or re-entrant jets) occur due to an asymmetry such as the presence of a nearby solid boundary. The proximity of the solid boundary alters the sphericity of the bubble-liquid interface, causing one side of the bubble to accelerate inwards more rapidly than the opposite. This results in development of a high-velocity re-entrant microjet of liquid that pierces through the bubble. The direction of the re-entrant microjet is towards the solid boundary. Velocity of the liquid forming the microjet is so high that severe damage is inflicted to the wall solid boundary material[44,54,60]. An estimated velocity of the liquid jet has been given to be around 400 kilometres per hour[17]. Formation of microjets is also possible from perturbations caused to a bubble as a consequence of its proximity to neighbouring bubbles, such as in a cavitation cloud.

Apart from the hydrodynamic erosion caused by shockwaves and microjets, cavitation bubble collapse has also been associated with emission of electromagnetic radiation (sonoluminescence) and cavitation driven chemical reactions (sonochemistry). Some researchers have gone so far as to suggest that cavitation may produce temperatures and pressures conditions suitable for cold nuclear fusion[61,62]. Studies on these phenomena have been conducted as a tool to quantify the extreme temperatures and pressures generated during

cavitation bubble collapse. Some of these studies have been elaborated in the following sections.

2.4.2 Acoustic Cavitation

Acoustic cavitation is defined as the formation and collapse of vapour cavities when a liquid is subjected to pressure variations by an oscillatory acoustic field such as ultrasound. Under the effect of the acoustic field, the molecules of the liquid vibrate about their mean positions. During the compression cycle, the acoustic waves exerts an increased pressure on the liquid causing the average distances between the molecules to be decreased; while during the rarefaction cycle, a negative pressure causes the distances to be increased. If the negative pressure during the rarefaction cycle is sufficiently large enough, such that the average distance between molecules surpasses the critical molecular distance necessary to hold the liquid intact, the liquid breaks down and voids or cavities are created [63].

A liquid is held together by attractive forces, which determines the liquid's tensile strength. In order for cavities to be formed in the liquid, the negative pressure applied in the rarefaction cycle of the acoustic wave has to overcome the tensile strength of the liquid [17].

As mentioned earlier, most pure liquids have enormous tensile strengths and require very large negative pressures to form cavities. However, the presence of trapped gases in crevices of small solid particles significantly reduce the liquid's tensile strength. As a gas filled crevice is exposed to rarefaction cycle of a sound wave, the gas expands until a small bubble is released into the solution.

The bubble irradiated by ultrasound will continue to grow as it absorbs energy from the compression and expansion cycles, where the cavity growth depends on the intensity of ultrasound. At high intensities, the bubble growth is so rapid during the expansion cycle that it does not get time to shrink back during compression.

At low intensities, the bubble size oscillates with the wave cycle. Gas diffuses into and out of the cavity during expansion and compression cycles, respectively. The gas diffusion is slightly more during expansion as compared to compression; the bubble expands a little more than it shrinks, which results in a gradual growth over numerous cycles. This growth process of long-lived bubbles is called rectified diffusion[18,44].

The growing cavity eventually reaches a critical size where it absorbs energy from the ultrasound most efficiently. At this point the cavity can grow very rapidly and become unstable due to its inability to absorb energy efficiently anymore. The unstable cavity collapses as the surrounding liquid rushes in.

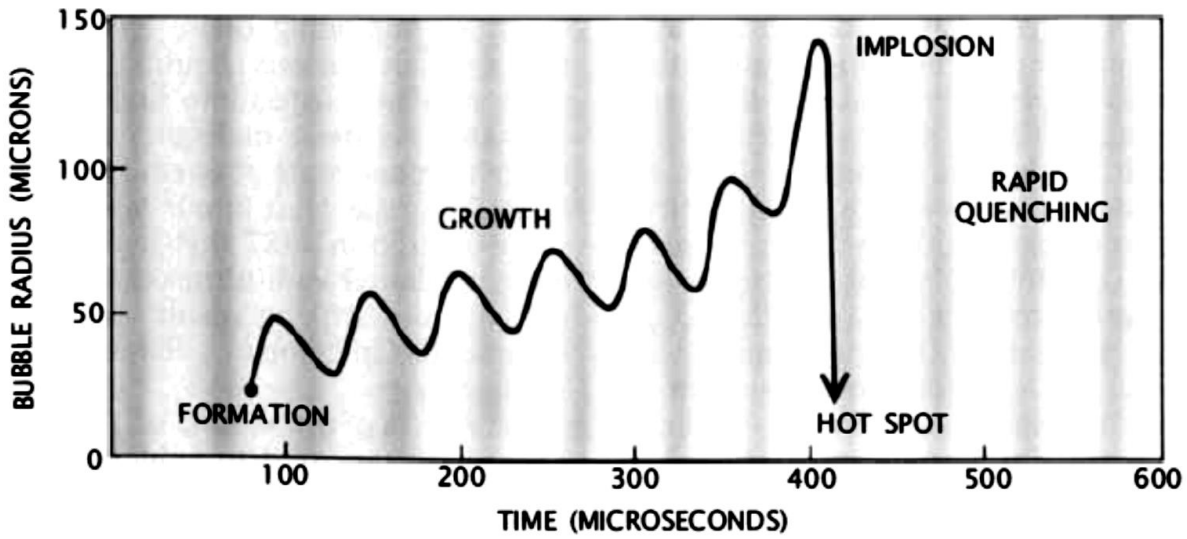

Figure 2.10 A cavity forms and grows in episodes of negative pressure. When it attains critical size it implodes generating intense heat and pressure[17].

Moholkar et al. (1999)[63] used numerical methods and simulations on the Rayleigh-Plesset equation to produce a comparative study of hydrodynamic and acoustic cavitation. A set of parameters were studied to observe their effect on the bubble dynamics in acoustic cavitation; including the intensity of irradiation, frequency of irradiation and the initial cavity radius.

A pressure pulse is produced because of bubble collapse which, in adiabatic conditions, is directly proportional to the ratio of radii at the beginning and at end of the collapse. Therefore, the magnitude of the pressure pulse also increases with intensity.

It was found that increasing the frequency resulted in longer bubble life[63,64]; this was because the time required to collapse a bubble at higher frequencies is longer than the time available during the compression cycle. Similarly, at higher frequencies the rarefaction cycle does not provide enough time for cavitation bubbles to be formed. Therefore, higher intensities are required at high frequencies for bubble formation. Suslick (1989) stated that the critical size of a cavity was related to the frequency of the ultrasound wave, where it will absorb energy most efficiently.[17]

Moholkar et al. (1999) also showed that smaller cavities grew more than the larger cavities (typically about 200 times their original size). Thus, due to the pressure pulse upon collapse being proportional to the ratio of radii of final bubble and initial bubble, the smaller bubbles produced pressure pulses of higher magnitudes.

Table 2.5 below summarises the findings of Moholkar et al. obtained through numerical analysis of various parameters that affect the behaviour of cavitating liquids under acoustic cavitation.

Table 2.5: Moholkar et al. (1999) studied the effects of initial size of pre-existing cavities in the liquid and the intensity and frequency of ultrasound on the behaviour of cavities.

Initial Cavity Size (5 and 10 µm)	• *Smaller cavities grow more (~200 times)* • *Higher pressure pulse for smaller cavities* • *Shorter life spans of smaller bubbles*
Intensity (10 and 120 Wcm^{-2})	• *Max initial radii proportional to intensity* • *Higher pressure pulses at higher intensities* • *Longer life spans at higher intensities*
Frequency (22.7 and 33 kHz)	• *Higher frequencies result in longer life spans* • *No relation to max. bubble size reached* • *Higher frequencies require higher intensities for cavitation production*

Other parameters that affect cavitation in terms of formation of bubbles and their intensity of collapse have also been studied in-depth through numerical and experimental studies. These have been summarised in Table 2.6 below.

Table 2.6: Various parameters and their effects on cavitation formation and/or collapse.

Liquid viscosity	*Higher acoustic pressures required to produce cavitation in viscous liquids due to stronger cohesive forces within the liquid.*
Liquid surface tension	*It is generally thought that cavitation threshold decreases with decreasing liquid surface tension.* *On the contrary the reverse was observed for distilled water with surfactant modified surface tension by Crum (1982).*[66]
Vapour pressure	*Collapse of bubbles in liquids with high vapour pressure is less violent due to the maximum pressure attained during collapse being low*[64]. *Collapse intensity has been shown to increase with the surface area to vapour pressure ratio*[67].

Cavity content	*Greater gas content lowers the cavitation threshold and intensity of collapse due to cushioning.* *Gases with lower isentropic coefficient γ provide higher sonochemical effects, however there is also a strong correlation to the thermal conductivity of the gas which determines the maximum temperature attained in the bubble.*[68,69]
External pressure	*Increase in ambient liquid pressure increases the cavitation threshold and the intensity of bubble collapse. However, it has been observed to decrease the maximum temperature at collapse*[64,69].
Ambient temperature	*Increase in ambient temperature raises the vapour pressure of the liquid which would reduce the maximum pressure and temperature attained during collapse.* *However, optimum temperatures for specific liquids have been identified at which maximum cavitation damage and sonoluminescence has been observed; deviation from these temperatures is shown to reduce the intensity of collapse*[70,71].

Due to the relative simplicity of setting up, conducting and observing experiments on acoustic cavitation as compared to other types of cavitation, it has been the most commonly studied form of cavitation. Acoustic cavitation has been used as a tool to observe conditions created in cavitating media, particularly during the collapse of a cavity.

Suslick et al.[18] investigated the conditions generated inside acoustically driven cavitation bubbles using methods that observed the sonochemistry and sonoluminescence occurring during bubble implosion. Through observation of the electromagnetic emissions and chemical reactions taking place in a cavitating liquid the temperature and pressure conditions being generated by cavitation were estimated.

During collapse (or implosion) of cavities the vapour present within is compressed; as the liquid does work on the vapour the internal energy of the vapour increases, raising the

temperature of the liquid immediately surrounding the bubble and creating a local hot-spot. The temperature of original gaseous content of the cavity can reach up to 5,500 degrees Celsius and the liquid immediately surrounding the cavity can reach 2,100 degrees. The hot-spot is tiny compared to the bulk liquid; as a result, the heat dissipates quickly to the surrounding. The heating and cooling rates during cavitation have been estimated at a billion degrees Celsius per second. At any given time, the bulk liquid is said to remain at the ambient temperature. These extreme conditions have been observed to lead to some rare phenomenon, such as sonoluminescence and sonochemistry, which have been further manipulated to allow detailed understanding and measurement of physical parameters inside a collapsing bubble. [17,64]

Sonoluminescence

Sonoluminescence is the emission of light from gas inside a collapsing/ imploding bubble, that is being driven by an acoustic field. When a cavity implodes, the adiabatic heating of the gas inside the cavity creates a hot-spot, which can cause molecules of the gas to be excited to high energy states. As these molecules return to their ground state, visible light is emitted. The intensity, length and spectral properties of the emitted light pulse are determined by the temperatures achieved at bubble collapse and on the irradiated medium. It has been observed that hydrocarbons irradiated with ultrasound emitted visible light similar in colour to flames produced upon their combustion.[17,18,69]

Early studies on sonoluminescence were conducted on aqueous solutions which produced spectra consisting mainly of a broad and featureless continuum in the visible region. Sonoluminescence from nonaqueous liquids and organic solvents revealed richer spectra, with emissions bands and lines from electronically excited molecules and atoms. Observations of the discrete and identifiable molecular and atomic emissions spectra facilitated the

quantification of physical conditions based on the relative intensities of vibronic and atomic bands.

The study of sonoluminescence has always been classed into two categories. First category involves emission of light from a single, isolated bubble, known as single-bubble sonoluminescence (SBSL); the second category studies the emission of light from a cloud of bubbles in a gassy liquid, known as multibubble sonoluminescence (MBSL).

It is suggested that the conditions generated during SBSL are distinctly different from MBSL. Cavitation in a single, isolated bubble was deemed to be more intense, owing to the sphericity of collapse and lack of disturbance from other bubbles and nearby surfaces. In the case of MBSL, the acoustic pressure applied by the acoustic source, is not uniformly distributed in the cloud of bubbles. Thus, a wide range in the number of photons released per bubbles collapse is observed.

Multi-bubble acoustic cavitation can be generated by irradiating a gassy liquid with ultrasound of typically 20 kHz to 2 MHz at acoustic power of several watts per square centimetre. Due to spatial distribution, the power experienced by each bubble is not uniform. As a result, the luminescing bubbles have different intracavity conditions and produce varying number of photons (light intensity). Observation of discrete emission bands and lines (from non-aqueous liquids) enables one to quantify the effective temperature and pressure generated during multi-bubble sonoluminescence. Suslick et al. (2008) employed a spectroscopic measurement technique similar to the method of pyrometry used to determine thermal conditions of high-temperature sources (e.g., plasmas); it involved comparison of relative intensities of emission lines from electronically excited atoms and molecules. A solution of $Cr(CO)_6$ dissolved in silicone oil saturated with Ar was irradiated with ultrasounds of 20 kHz; upon comparison of emission lines of excited chromium atoms (Cr*) the multi-bubble sonoluminescence

temperatures were found to be 4700 ± 300 K. Temperature measurements of approximately 5000 K have been reported through MBSL emissions from other metal carbonyls including iron and molybdenum carbonyls.[18]

Flint and Suslick (1991)[72] measured MBSL spectra from silicone oil under a continuous Ar sparge. Through comparing the measured spectra to a theoretical emission spectra of the Swan band transition of C_2 it was found that the cavitation temperature was 5075 ± 156 K.

Pressures in multi-bubble cavitation can also be measured by observing the emission lines; in this case, instead of the intensity of lines, the emission line widths are used to determine the pressure. The emission lines can be broadened due to factors that include Doppler broadening, Stark effect and the instrument response, out of which quantification of Stark effect can determine the overall pressure at a given temperature. Quantifying the emission line widths from Cr atoms, during the sonication $Cr(CO)_6$ solution in silicone oil saturated in He and Ar, Suslick et al. estimated the pressure generated at bubble collapse to be 300 ± 30 bar.

Sonoluminescence from a single-bubble (SBSL) presents great obstacles when it comes to quantifying its conditions. Firstly, the volume of the bubble amounts to only a few attoliters, so the concentration of sonochemical products are very low and difficult to analyse. Secondly, the intensity of light emission is usually low which makes the spectroscopic analysis very challenging. However, it was discovered that the radiant power of single-bubble sonoluminescence in H_2SO_4 and H_3PO_4 was tremendously greater than that of any other liquid. Similarly, the sonoluminescence intensity was greatly increased if the gas content of a bubble was composed of noble gases instead of gases such as N_2 or O_2. Thus, Ar bubbles in H_2SO_4 were irradiated with ultrasound and the emission lines obtained were compared with emission lines of electronically excited Ar atoms (Ar*) to determine the generated temperatures. The analysis of relative intensities of Ar* atom emission lines revealed that the temperature of the

bubble, in single-bubble sonoluminescence, could go up to 15,000 K. Emission line from ions formed from the liquid and from dissolved gas in liquid provided the first evidence for the formation of plasma during SBSL. The profile of the emission lines for Ar* in H_2SO_4 sonication was used to estimate the pressure in single-bubble sonoluminescence at above 1000 atm.

Hydrodynamic systems, where cavitating flows occur, have also reported emission of light[73–78]. Konstantinov in 1947 was the first to observe flashes of light in a hydrodynamic system with flow past a cavitating cylindrical obstacle. Jarman and Taylor (1964, 1965)[75,77] observed light being emitted from a water flow system in a Venturi tube. Flashes of light occurred only in a region downstream of the constriction. The intensity of light was found to be several orders of magnitude lower than that of the corresponding sonoluminescence.

Peterson and Anderson (1967)[74] produced cavitation in the free stream of water through a Venturi tube. Light emission was observed from the cavitating liquid when the water was deaerated. Upon introduction of Xenon into the water stream resulted in higher spectral intensities of light. The cavitation collapse region in the flow was observed to have a continuous bluish-white glow with occasional flashes of light.

Leighton et al. (2003)[76] studied cavitation luminescence using a photon-counting technique from flow over a hydrofoil in a cavitation tunnel. Photon-counts were taken as U-shaped cavities were shed from the main cavity. It was suggested that the photon-count increased dramatically as the flow velocity was increased. Farhat et al. (2010)[78] conducted similar experiments on the same cavitation tunnel, this time using a CCD video camera and a photomultiplier PM. Once more, the shedding of cavities from larger cavity ‘sheets’ was observed past the trailing edge of the aerofoil. It was confirmed that the number and brightness of the light flashes increased at higher flow velocities.

Sonochemsitry

The extraordinary conditions generated during acoustic cavitation can be utilised to drive chemical reactions in the cavitating liquid, liquid slurry or at a liquid-solid/gas interface; this is known as sonochemistry.[18]

Acoustic cavitation, as shown, can generate extreme conditions in hot-spots where chemical reactions can occur. This process, known as sonochemistry, can be exploited to quantify temperatures generated during acoustic cavitation. Suslick et al. (2008) used comparative-rate thermometry, a method that involves sonication of a liquid of known composition to enable temperature calculations via the Arrhenius relation through analysis of the products and determination of rate constants for specific kinetic pathways. A solution of volatile metal carbonyls in mixtures of n-alkanes containing an excess of triphenylphosphine was irradiated with acoustic waves which showed that the intracavity reaction zone reached effective temperature of 5,200 ± 650K during multi-bubble cavitation. The results were in agreement with the temperatures estimated using spectroscopic measurements.

Further discussion on the different mechanisms through which sonochemical reactions occur will be provided in the following sub-sections. An attempt to establish an analogy between the chemical effects observed in acoustic cavitation to those observed through hydrodynamic cavitation will be made.

2.4.3 Hydrodynamic Cavitation

Hydrodynamic cavitation is often elucidated using an example of a liquid flowing through an orifice. Bernoulli equation states that the sum of static and dynamic pressures is constant along a streamline. Thus, a reduction in cross-section of the flowing stream increases the velocity head at the expense of the pressure head. During the re-expansion of the flow the fluid stream gets separated at the lower end of the orifice. The static pressure at the *vena contracta* is lower

than the bulk pressure downstream of the flow. As the velocity of the flow is increased the pressure drop across the orifice increases and the pressure at the *vena contracta* decreases. Above a certain velocity, the pressure may drop below the vapour pressure of the liquid, causing partial vaporisation of the cavitating fluid. In fact, due to the presence of dissolved gases, bubble nucleation begins at pressures higher than the vapour pressure of the fluid[53,63].

Cavitation number (C_i or C_N) is a dimensionless parameter that is generally used to characterise hydrodynamic cavitation. It is defined as the ratio of pressure differential between vapour pressure (P_v) and back pressure (P_b) and indicates cavitation propensity. In their work, Jeshani (2013)[50], Giannadakis et al. (2008)[48], Arcoumanis et al. (1999)[79] and others applied cavitation number with the following relation:

$$C_N = \frac{P_i - P_b}{P_b - P_v} \tag{2.6}$$

Where, P_i is the injection pressure. In this case, higher C_N indicates higher cavitation intensity. Other authors, including Brennen (1995)[44], Moholkar et al. (1999)[63], Gogate (2000)[80], Franc and Michel (2004)[54] and Suh and Lee (2008)[81] have used a slightly different definition of cavitation number:

$$C_i = \frac{P_i - P_v}{\left(\rho V^2/2\right)} = \frac{P_i - P_v}{P_i - P_b} \tag{2.7}$$

Where, ρ and V represent liquid density and flow velocity near the orifice, respectively. According to this, the injection pressure downstream of the orifice will fall below the vapour pressure of the liquid when cavitation number is 1 or lower. (Moholkar et al., 1999)

Moholkar et al. (1999) characterises the cavitation number C_i as follows:

1. It is independent of the velocity in the pipe and shows a dependence on the orifice size in the same pipe.

2. It increases linearly with the diameter ratio of orifice to pipe.

3. Cavitation inception occurs at Ci = 1 to 2.5 and its severity increases with decreasing cavitation number.

From observation of equations 2.6 and 2.7 it is understood that the extent of cavitation in hydrodynamic systems is influenced by flow parameters such as the upstream pressure and downstream pressure, and properties of the fluid such as its density and vapour pressure.

Upstream and downstream pressures

The dependence of hydrodynamic cavitation on upstream and downstream pressures has been studied experimentally by Ghassemi and Fasih (2011)[82] through observation of flow in cavitating Venturi tubes. It was suggested that cavitation will always occur given that the upstream pressure is much larger than the downstream pressure in flows where the Reynolds number is below 60,000. Investigation of the downstream to upstream pressure ratio indicated that cavitation inception occurs at pressure ratio of about 0.8; above this value the flow was observed to be cavitation free due to static pressure not dropping enough to reach saturated vapour pressure. At pressures ratios below the cavitation inception point of around 0.8, the flow through the Venturi was choked because of cavitation bubbles blocking the Venturi throat. Oddly, it was reported that the mass flowrate through the tube decreased in the absence of cavitation. This can be a consequence of a decrease in volumetric flowrate as a result of a smaller pressure difference across the tube. However, it is suspected that this behaviour of reduction in mass flowrate is characteristic of such purpose-built cavitating Venturi tubes and not a general trend for other geometries prone to cavitation.

A geometry where the hydrodynamic cavitation is known to occur and is of significance, in terms of engineering, is a diesel injector nozzle. Suh and Lee (2008)[83] investigated the influence of cavitating flow in nozzles of different length to width ratios (L/W) on the diesel

fuel atomisation characteristics. Two two-dimensional rectangular cross-section nozzles and orifice with different L/W ratio were made from acrylic resin to enable optical observations.

In the experiment, it was observed that the fuel flow-rate increased as the injection pressure was increased. For both L/W ratio nozzles the effect of cavitation was seen to increase as the injection pressure was increased.

In cavitating flow tests the fuel injection pressure in the nozzles was increased, and based on the results, the cavitating flow was characterised into three regions; namely, turbulent flow region, cavitating flow region, and hydraulic flip region.

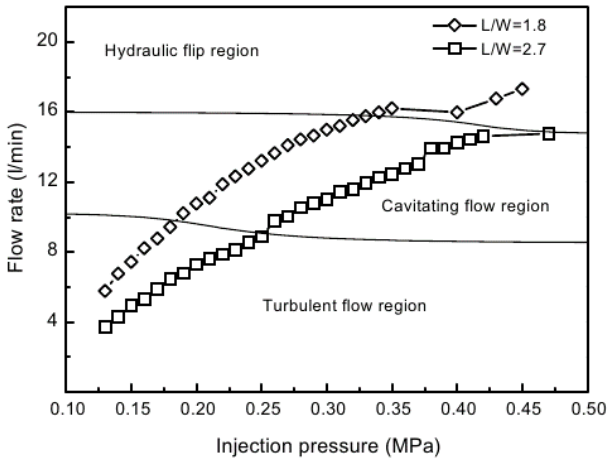

Figure 2.11 Effect of injection pressure on flowrate and cavitating flow characteristics for two nozzles of different L/W ratios.[83]

In the turbulent flow region, the static pressure fell below the saturated pressure of the fuel; as the injection pressure and flow rate were increased, cavitation bubbles started to emerge at the edge of the orifice. In cavitating flow region, the cavitation bubbles reached upstream of the nozzle exit, but collapsed prior to fuel injection; this resulted in wider spray shape and improved fuel atomization. In the hydraulic flip region, the cavitation bubbles were issued from the nozzle exit without being attached to the nozzle wall and the fuel atomisation was found to deteriorate.

There are numerous other experimental and numerical studies that show the positive correlation between injection pressure and cavitation intensity. This correlation has been consistent for varying nozzle geometries and working fluids (e.g. water, diesel, biodiesel etc.) for both real-sized and enlarged nozzles.[79,81,84–87]

Another parameter that affects the cavitation number in equations 2.6 and 2.7, and subsequently the propensity of a hydrodynamic system to cavitate, is the back pressure (or downstream pressure). The effect of back pressure is of importance for applications in the modern diesel FIE where multi-stage injection strategies are employed which involves the main injection event occurring after the combustion has commenced, thus the back pressure gradually increases while the injection (rail) pressure stays constant.

The effect of back pressure or downstream pressure on cavitation has been investigated by Arcoumanis et al. (2000)[87], where a comparative study of flow behaviour of calibration oil in enlarged and real-sized nozzles, at varying injection and back pressures was conducted. The real-size nozzle used for the study was a six-hole vertical sac-type with a nominal hole diameter of 176 μm. The injector was modified to allow flow visualisation in one of the six injector holes. Injection was performed inside an acrylic receiver filled with the test liquid, the pressure of which was controlled using a relief valve.

For back pressure investigation, the injection pressure was set constant at 140 bar while the back pressure was gradually reduced. It was clearly observed that at back pressures below the critical pressure the cavitation bubbles collapsed within the nozzle hole. As the back pressure was reduced the cavitation structures were seen to extend down to the exit of the hole, beyond which the structures were issued from the hole. Initially, a vapour film was seen to form at the top corner of the nozzle inlet; this film became more prominent as the back pressure was reduced. However, as the back pressure was reduced further the film was seen to break down

into smaller bubbles. Another cavitation structure, called ‘string’ cavitation, was observed to enter the nozzle hole as a continuous stream.

The phenomenon of string cavitation has been observed and modelled by other investigators[49,79,88–91], and is related to formation of vortex flow inside the nozzle sac; indeed it has also been named vortex cavitation. The vortex flow results from the interaction of annulus flow and the cross flow, generated from throttling of individual holes by existing nozzle hole cavitation. As a result of this interaction, flow conditions at the vortex core lead to formation of low pressure region, and subsequent formation of cavitation bubbles which coalesce to create vapour string that ‘connect’ adjacent holes[49].

Apart from the string cavitation that connects nozzle holes, a second type of string cavitation has also been observed, more frequently in the VCO (valve covered orifice) nozzles than the mini-sac nozzles; this type is referred to as ‘needle strings’. They appear to originate from the surface of the nozzle needle, extending into a single nozzle hole. They are attributed to formation of strong vortex flow along the axis of the nozzle hole[49].

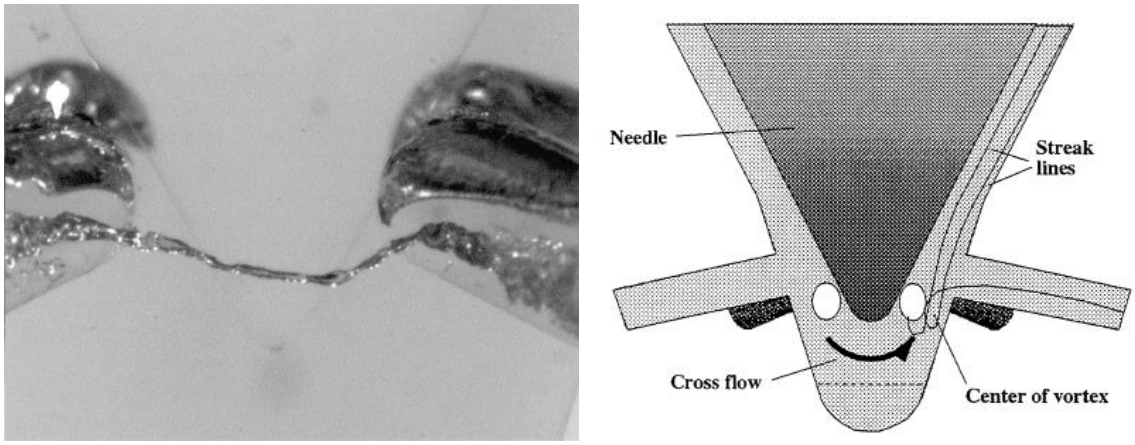

Figure 2.12 Left: An example of string-type cavitation connecting two nozzle holes. Right: schematic of flow inside the sac volume leading to formation of string cavitation[79].

Hysteresis in hydrodynamic cavitation is another phenomenon that is relevant to injection and back pressure ratios. It has been observed by Payri et at.[86] who varied the back pressure at a

constant injection pressure. The experimental study was performed on eight steel drilled plates with varying drilled hole diameters and conicity. Diesel fuel was continuously injected through the nozzle holes into a fuel-filled chamber. The pressure inside the chamber could be modified to vary the back pressure using a back-pressure regulation system. Initially, the back pressure was reduced from a high value to observe the point of cavitation inception, followed by a gradual decrease in back pressure till the cavitation bubbles disappeared. When the back pressure was increased from a low value, the pressure required for cavitation to stop was higher than the pressure at which cavitation began when the back pressure was being decreased from a high value. This difference in back pressures (or injection to back pressure ratios) for cavitation onset and collapse is usually called hysteresis.

Besides the part played in the formation of cavitation, back pressure also influences the collapse of a vapour cavity. Simulations of cavitating flow have shown that as a cavitation bubble flows from a region of low pressure to a region of high pressure it undergoes oscillations, giving rise to multiple pressure pulses. As the back pressure/ recovery pressure is increased the amplitude of oscillations is also increased due to more aggressive collapse and rebound, resulting in higher magnitudes of pressure pulses[63]. The aggression of collapse is important for applications in sonochemistry due to its relevance to the temperature and pressure conditions generated inside the bubble.

Nozzle Geometry

Nozzle geometry, as expected, was found to play a major role in inducing hydrodynamic cavitation. Experimental work and numerical simulations on different nozzle cross-sections and shapes have been conducted; it has been shown that converging tapered nozzles are highly unlikely to demonstrate cavitating flows as compared to cylindrical nozzles at the same flow parameters. Tapered holes are said to greatly modify the pressure distribution, hence the

formation of cavitation within the nozzle hole. They create a smooth pressure gradient along the length of the hole which greatly reduce or even eliminates cavitation regions which would exist for cylindrical nozzles at the same flow conditions [81,84,89,91].

Suh and Lee (2008)[83] compared two L/W ratio nozzles; it was concluded that the longer nozzles required higher injection pressures for cavitating flow to develop.

Effect of the sharpness of nozzle hole inlet on the formation of cavitating flow inside the hole was investigated by Badock et al. (1999)[85]. Nozzles with various degrees of inlet rounding through hydro-grinding were tested. It was reported that the nozzle with a sharp edge cavitated at much lower injection pressures than the hydro-grounded nozzles. The intensity of cavitation decreased with the extent of hydro-grinding. Numerical simulations on the effect of hydro-grinding/ rounding of nozzle inlets was performed by Som et al.[43] were found to be in agreement with the findings of Badock et al[85].

Properties of the fluid

Properties of fluid such as its viscosity and density play a significant role in promoting or damping cavitation. A study comparing diesel and biodiesel flow through nozzles found that biodiesel required higher C_i (or injection pressures) to induce cavitation due to its higher viscosity and density [81].

As in the case of acoustic cavitation, fluids with lower vapour pressures are expected to cavitate less as the drop in local pressure has be to larger to achieve vapour formation. Biodiesel is reported to have lower vapour pressures than diesel fuel, hence larger injection pressures are required to achieve the same intensity of cavitation formation in biodiesel as compared to conventional diesel[43]. There is however a contradictory effect of solvent vapour pressure on the intensity of cavitation collapse. As shown by Suslick et al.[22], upon reducing the volatility

of a solvent being sonicated the rate of sonochemical reactions increases, implying an increase in the intensity of bubble collapse and the maximum temperatures generated upon collapse.

2.5 Effects of Cavitation on Diesel

It is known that cavitation can provide a useful tool for initiating chemical reactions (sonochemistry) due to existence of extreme conditions generated when cavitation bubbles collapse. Sonochemistry might be a recently introduced term, however cavitation has been used in chemistry for much longer. Studies to investigate the chemical effects of cavitation began over 60 years ago[64]. In the recent past, studies have been conducted in various fields including biological effects of cavitation in treatment of cancer cells, increasing yields in organic synthesis, converting environmentally toxic compounds into less harmful substances and sonoluminescence during cavitation bubble collapse [18,46,92,93] .

2.5.1 Cavitation Induced Pyrolysis

There have been limited studies on the chemical effect of cavitation on non-aqueous solutions, particularly the effect of hydrodynamic cavitation. However, a number of investigations have been conducted using ultrasonic cavitation to study the sonochemistry in non-aqueous solutions. Non-aqueous organic solvents are of primary interest in this study, thus the literature mentioned in this section will be focused on them.

Suslick et al.[22] were one of the earliest investigators of the impact of cavitation on organic compounds. They investigated sonochemistry in alkane solvents as they were subjected to acoustic cavitation. It was reported that the primary initiating step as a result of cavitation was the C-C bond cleavage, which resulted in chemistry leading to formation of diatomic hydrogen, methane, acetylene, and smaller 1-alkenes via radical intermediates. These products were found to be consistent with the Rice radical chain mechanism for alkane pyrolysis. On analysis of the sonolysis products it was found that their yield was high relative to yield from low-

temperature pyrolysis, which lead to the conclusion that they were produced by high-temperature pyrolysis (~1,200°C). This agreed with their earlier hypothesis that cavitation bubble collapse generates local transient 'hot-spots' of extreme temperatures and pressures.

Suslick et al.'s findings were supported later by Price and McCollom[24] in 1995 when they sonicated *n*-dodecane as a preliminary study for understanding the effect of cavitation on diesel, as compared to long-term storage stability. It was observed that *n*-dodecane 'cracked' into smaller hydrocarbons and that the rate of formation of these alkanes was similar to those reported by Suslick et al. (1983).

Sonolysis of diesel confirmed similar behaviour for its paraffinic content; the hydrocarbon chains were broken down, and the rate of loss of shorter chains was found to be higher as compared to longer chains, such that it became negligible at ~C20. This was said to be consistent with the pyrolysis mechanism suggested by Suslick et al., with the explanation that longer chain alkanes have lower vapour pressures, thus are less likely to enter the cavitation bubble.

Formation of insoluble sediments was also reported which were formed as a result of alkyl radicals, formed in the cavitation bubbles, diffusing and reacting with other fuel components in the bulk liquid. The deposits were found to contain nitrogen and aromatic components; and had similar ultraviolet and infrared spectra to those produced in other diesel stability studies. Price and McCollom [23,24] concluded that the sonochemical effect of cavitation on diesel followed the same process that lead to gum like deposits forming due to long term storage of diesel but it was greatly accelerated under sonication.

Misik and Riesz[25] conducted an EPR (Electron Paramagnetic Resonance or Electron Spin Resonance) study on the free radicals formed in organic liquids in order to determine the temperatures generated during cavitation. Three regions of cavitation where sonochemical

reactions occur were identified as shown in Table 2.7 and Figure 2.13. Organic liquids including, *n*-dodecane, *n*-decane and toluene, were subjected to acoustic cavitation during the study. EPR spectra of n-dodecane had the dominant signal of radicals produced by hydrogen abstraction and a minor component of radicals produced by homolysis of C-C bonds, defined as the first step in Rice-Herzfeld pyrolysis mechanism. The spectra for *n*-decane bore similar results which confirmed the Rice-Herzfeld pyrolysis mechanism for both alkanes. In case of toluene, benzyl radicals were detected which are formed during the first step of toluene pyrolysis from C-H bond cleavage. The temperature estimated for formation of such radicals from organic compounds was around 5200 ± 500 K, similar to that determined by Suslick et al. (1996).

Table 2.7: The three regions of cavitation where sonochemical reactions occur as identified by Riesz and Misik[25].

Region 1: ***Interior of Imploding Bubbles***	• *Extremely high temperatures and pressures* • *Typical pyrolysis processes occur (Rice-Herzfeld mechanism)*
Region 2: ***Interface between Bubbles and Bulk Solvent***	• *High temperature and pressure gradients* • *Even non-volatile components can undergo pyrolysis*
Region 3: ***Bulk of the Liquid***	• *Liquid at ambient temperature* • *Radicals diffuse from regions 1 and 2 to react with solvent molecules*

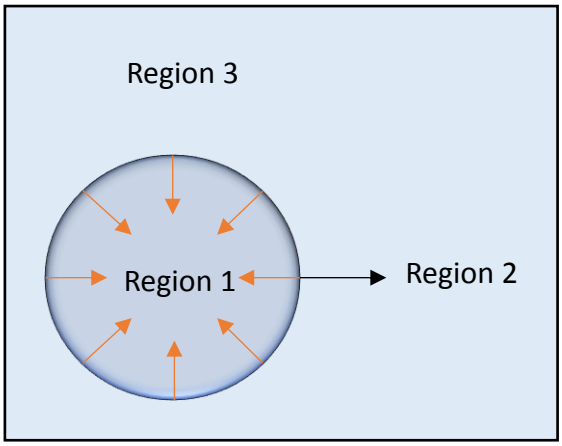

Figure 2.13: Schematic representation of the 3 regions of cavitation where sonochemical reactions occur during bubble collapse.

Hart et al.[26] conducted an extensive study on the chemical effects of acoustic cavitation in water based aqueous solutions of argon and acetylene in varying concentrations. Rapid consumption of acetylene during cavitation bubble collapse was observed. Products of sonolysis included a great number of hydrocarbons with carbon numbers ranging from two to eight and insoluble soot.

Formation of compounds such as benzene, phenylacetylene, styrene and naphthalene was recorded; these products are similar to those found in pyrolysis and combustion of acetylene. All the products were initially formed at a rate proportional to the sonication time, even at small times of 10s; suggesting that they are formed from a single cavitation event and not through subsequent irradiations of initial sonication products.

It was noticed that the concentration of these products varied inversely with the initial concentration of acetylene. This was attributed to the gas in a cavitation bubble having a lower specific heat capacity at lower concentrations of acetylene, thus reaching a higher maximum temperature during the adiabatic compression at bubble collapse. The higher pressures resulted in sonolysis of water vapour that liberated O and OH radicals; these dominate the initiation reactions leading to attack on acetylene molecules and hydrogen abstraction. However,

liberation of H_2 from acetylene was also observed through direct pyrolysis of acetylene; it was suggested that initiation of acetylene decomposition does not necessarily require the presence of O and OH radicals.

Some important precursor particles of higher carbon number products were identified to be C_4H_2, C_4H_3 and C_4H_4. A comparison on the concentration of high carbon number compounds of odd number of carbon atoms and even number of carbon atoms revealed an abundance of even number carbon atom compounds, suggesting coagulation and polymerization reactions as the mechanisms of formation of such species[26].

2.5.2 Hydrodynamic Cavitation and Pyrolytic Effects

The studies mentioned in the previous section demonstrated that the conditions generated during implosion of cavities are suitable to drive pyrolytic sonochemistry[22,24–26]. Diesel subjected to such conditions has also shown formation of insoluble deposits similar to those noticed in long-term storage stability studies[24]. However, all of the above studies have incorporated the use of ultrasound as the source of cavitation. In order to justify the formation of deposits in diesel engines through cavitation induced pyrolysis, the similarities between the conditions generated by hydrodynamic and acoustic cavitation need to be established.

Indeed, some studies have reported conditions generated during the collapse of hydrodynamically generated cavitation to be similar to that generated by acoustic cavitation. Studies mentioned *a priori*[73–78] have shown emission of light from cavitating flows in a hydrodynamic system, a phenomenon known as sonoluminescence in acoustic cavitation.

Moholkar et al.[63] in 1999 reported experimental results from a hydrodynamic cavitation reactor that was used to liberate iodine I_2 from aqueous KI solution through subjecting it to hydrodynamic cavitation past orifice plates. It was suggested that hydrodynamic cavitation

provided an important and more energy efficient tool for driving sonochemical reactions as compared to acoustic cavitation.

Another such study has been conducted by Price et al.[16], who investigated the impact of acoustic cavitation on the hydrocarbons in the middle distillate range (C_8-C_{26}) and compared the results to the deposits noticed in diesel vehicles. The acoustic cavitation experiments tested a range of pure hydrocarbons with varying degrees of saturation and their mixtures. Results showed a clear change in the sonicated hydrocarbon samples, with some polycyclic hydrocarbon samples showing black deposit formation. The deposit forming tendency of the sonicated sample was seen to decrease with addition of alkanes, with the trend becoming prominent as the added paraffinic hydrocarbons became shorter. In comparison, addition of aromatic compounds had little effect on reducing deposit formation, confirming that aromatic compounds have a higher tendency to form deposits compared to paraffinic compounds.

Comparing the effect on hydrocarbons with varying degrees of unsaturation in the molecular structure indicated that deposit forming tendencies increase with the degree of unsaturation. The tendency was found to be linear with the C/H atomic ratio of the hydrocarbon being sonicated.

Nano-sized particulates, formed as a result of sonication were observed. These nano-particulates then agglomerated to form micron-sized particles. The agglomeration process was found to continue for a few days after sonication, during storage. TEM images of the particulates revealed that they were made-up of primary particles that had internal structure of graphitic-like carbon. The particulates were found to be composed of 90% carbon (excluding H) with smaller proportions of oxygen.

Price et al. (2015) then conducted a compositional analysis on deposits obtained from a fuel filter of a diesel vehicles from the field. The morphology and composition of the collected

deposit was found to be the same as that seen in sonicated samples. Through this analysis it was concluded that hydrodynamic cavitation was to be blamed for FIE deposits as cavitation phenomena provides the extreme conditions that are required for hydrocarbon molecules to undergo pyrolysis, just as observed in the sonication experiments.

Lockett and Jeshani[13] (2013) and Jehsani (2013)[50] developed a novel test-rig to study the effects of sustained hydrodynamic cavitation on a model diesel fuel and four commercial diesel fuels. The model fuel had a 98% paraffinic content; two commercial fuels were bought new and the other two were aged. Fuel samples were subjected to hydrodynamic cavitation by injecting through a 5-hole asymmetrical continuous flow nozzle with injection pressures reaching up to 630 bar. Each fuel was recirculated in a loop for 40 hours and a simple in-situ optical setup monitored the change in the fuels' spectral extinction coefficient at 405 nm wavelength.

It was believed that as the fuel undergoes hydrodynamic cavitation, and subsequent pyrolytic reactions take place, some optically active components of the fuel are broken down while other optically active molecules are formed; this results in a change in the fuel's spectral extinction coefficient. The experiments revealed that the spectral extinction coefficient of commercial diesel fuels changed much more than a paraffinic model fuel (98% paraffinic content). The aromatic hydrocarbons in the commercial diesel (~26% v/v) were believed to be the cause of this change, leading to the conclusion that aromatic hydrocarbons are more sensitive to cavitation induced pyrolysis than the paraffinic hydrocarbons, which is in agreement with the conclusion reached by Price et al. (2015).

To separate the thermal effects from cavitation effects, Lockett and Jeshani (2013) subjected the fuels to a hot-water bath at 70°C for 40 hours and then had their spectral extinction coefficients measured. The cavitated fuel samples showed greater deterioration as compared to heated samples, which exemplifies the existence of higher temperature conditions (>>70°C)

during cavitation bubble collapse which could be suitable for sonochemical reactions like pyrolysis.

Lockett et al.[20,94] (2015 and 2016) used a high-pressure fuel recirculation rig to cavitate conventional diesel through a research injector nozzle at three injection pressures of 1,650 bar, 1,100 bar and 550 bar. Spectral transmission of the fuel, recorded as a function cavitation time, showed that the reduction of laser transmission was a function of injection pressure. However, it was suggested that the observed optical behaviour at 405 nm was in fact a function of volumetric flowrate rather than the injection pressure.

It was suggested that the hydrodynamically induced cavitating flow occurring in the nozzle was altering the chemical composition of the circulating diesel fuels; this change was observable in their changing spectral attenuation.

A similar fuel recirculation test-rig has been used by Bouilly et al.[95] (2012) to demonstrate the effect of biodiesel degradation on injector failure times. The tests were conducted at two different injector temperatures; this was designed to model the heating of injectors by the engine block during engine operation. Higher injector temperature resulted in quicker failure, which occurred due to faster deposit formation that led to deterioration of needle actuation and reduction in flowrate.

The rig was designed to maintain fuel at high pressures in a common rail that had a pressure relief valve, allowing fuel to flow back to the tank. The HP pump and the injectors are also shown to have spill ports that returned the leaked HP fuel to the tank for recirculation. Although not mentioned in the investigation, it is highly likely that the flow past the pressure relief valve and the spill ports was cavitating. It is possible that the formation of deposits observed by the authors was a combined effect of sonochemical like effects from cavitating flows and fuel heating in the injectors.

The biodiesel blend (B20) was found to favour deposit formation when compared to low sulphur diesel (B0). It was believed that FAME (Fatty Acid Methyl Esters) in biodiesel was oxidised which caused the deposits. Analysis of the brown lacquered deposits revealed fuel oxidation characteristics, reflecting presence of hydroxyl groups, carboxylic acids and carbonyl groups.

A preliminary study of different fuels indicated that both Ultra Low Sulphur Diesel (ULSD) (B0) and biodiesel blends (Bxx) can cause deposits[38]. It has been further proposed that all hydrocarbon fuels are capable of providing carbonaceous deposits with the variation in deposit formation dependent upon duration and intensity of thermal, oxidative and mechanical stresses[11].

Chapter 3
Experimental Arrangement

Modern common rail direct injection diesel engines operate through injecting high-pressure diesel fuel into the combustion chamber. The pre-injection fuel is maintained at high pressures inside the common rail using a high-pressure pump. Common rail pressures in a modern diesel engine can be up to 2,500 bar.

The high-pressure fuel from the common rail is supplied to an injector that injects the fuel into the combustion chamber through small nozzle holes located at the tip of the injector. The injectors are actuated using an electronically controlled nozzle needle that lifts and seals to start and stop an injection event. Modern diesel injectors utilise a spill mechanism to assist and accelerate the needle lift and reseating motions with the objective of enabling better control of injection duration and injected fuel volume.

The spill mechanism utilises the fuel pressure in the common rail to force the needle motion through throttling of a pressure control chamber located above the control piston. Throttling of the control chamber requires a proportion of the high-pressure fuel supplied to the injector to be ‘leaked’ back to the fuel tank at atmospheric pressure via a spill return line. The amount of fuel leaked back to the tank is a dependent on the engine and injector types, and the engine load; in some applications, the fuel leak can be up to 50% of the fuel supplied to the injector. Apart from the injector spill mechanism, the use of pressure regulating safety valves and fuel metering methods in the diesel FIE (fuel injection equipment) also results in some of the high-pressure fuel returning back to the fuel tank.

The flow of high pressure fuel to the low-pressure return line through restrictions (i.e. throttle hole or control valve) is believed to create conditions suitable for hydrodynamic cavitation to

occur. This occurs because of the fuel accelerating past the restriction, causing the static head of the flow to fall close to or below the saturated vapour pressure of the fuel, resulting in the formation of vapour pockets/ bubbles. As the static pressure recovers downstream of the restriction, the bubbles are forced to collapse.

The bubble collapse is said to generate local hot-spots of extreme physical conditions that are suitable to initiate chemical reactions in the fuel. Indeed, some studies have correlated the deposits found in diesel FIE to the chemical reactions of the fuel resulting from the hydrodynamic cavitation phenomenon[16]. The impact of cavitation is expected to be enhanced when the fuel is recirculated between the engine and the fuel tank, as a consequence of the spill mechanism.

This study is aimed at investigating the effect of recirculating cavitating flow on the chemical stability of diesel fuels over long durations. It is believed that some components of the diesel fuel have higher tendency to form deposits; thus, the investigation will involve testing fuels with varying compositions to gain an insight into the behaviour of the different fuel components when subjected to cavitating flows.

A high-pressure re-circulating flow cavitation rig was designed and built, that employed a continuous flow high-pressure pump and a single hole injector. The design of the rig was based on a lower pressure re-circulation rig described by Lockett and Jeshani (2013)[13]. The experimental test-rig was designed with the purpose of subjecting fuel to sustained hydrodynamic cavitation in an environment similar to that experienced by diesel fuel in the FIE of diesel engines. To accelerate the aging process, the fuel was continuously recirculated, which also models the fuel spill and recirculation in diesel engines.

To characterise the change in properties of the fuel being cavitated thorough the injector nozzle, an optical absorption diagnostic was employed that continuously measured the time-dependent

spectral transmissivity of the fuel, at spectral wavelength of 405 nm. The optical setup was linked to the high-pressure test rig, allowing the recirculating test fuel to be subjected to spectral transmissivity measurements in real-time.

Samples of the test fuel were drawn from the rig at regular intervals for further testing using an ultraviolet-visible spectrophotometer and laser particle counter (LPC). The UV-Vis spectrophotometer was used to obtain absorption spectra, while the LPC measured the particle size distribution in the drawn fuel samples. Some of the cavitated fuel samples were also subjected to a two dimensional - gas chromatography (GC x GC) analysis. The results from the various diagnostics will be discussed in the following chapters.

3.1 High Pressure Cavitation Test Rig

The cavitation test-rig setup (Figure 3.1) consisted of a low-pressure primer pump feeding diesel from a fuel tank through a fuel filter into a fixed displacement high-pressure diesel pump. A diversion was created after the fuel filter to allow the fuel to flow to the high-pressure pump and the optical absorption setup simultaneously. The low-pressure primer pump provided a head of ~1.4 bar to supply the high-pressure pump and the optical setup. After passing through the optical setup the fuel flowed back to the fuel tank.

The Denso Mark-2 high-pressure diesel pump (Part number DCRP200010) was driven by a 7 kW variable speed electric motor. The pump maintained the fuel at pressures up to 1,700 bar in the accumulator/common rail. A conventional pressure gauge connected to a port on the common rail indicated the fuel's pre-injection pressure. The common rail was modified to continuously feed the high-pressure fuel to an upright, permanently opened, purpose-built, single-hole research injector. Details of the injector nozzles are provided later in this section. The fuel pumped through the injector was released into a 0.5 litre receiving cylinder (receiver),

filled with fuel that was maintained at atmospheric pressure. The receiving cylinder assembly was later modified to allow pressurisation of the cylinder up to 10 bar.

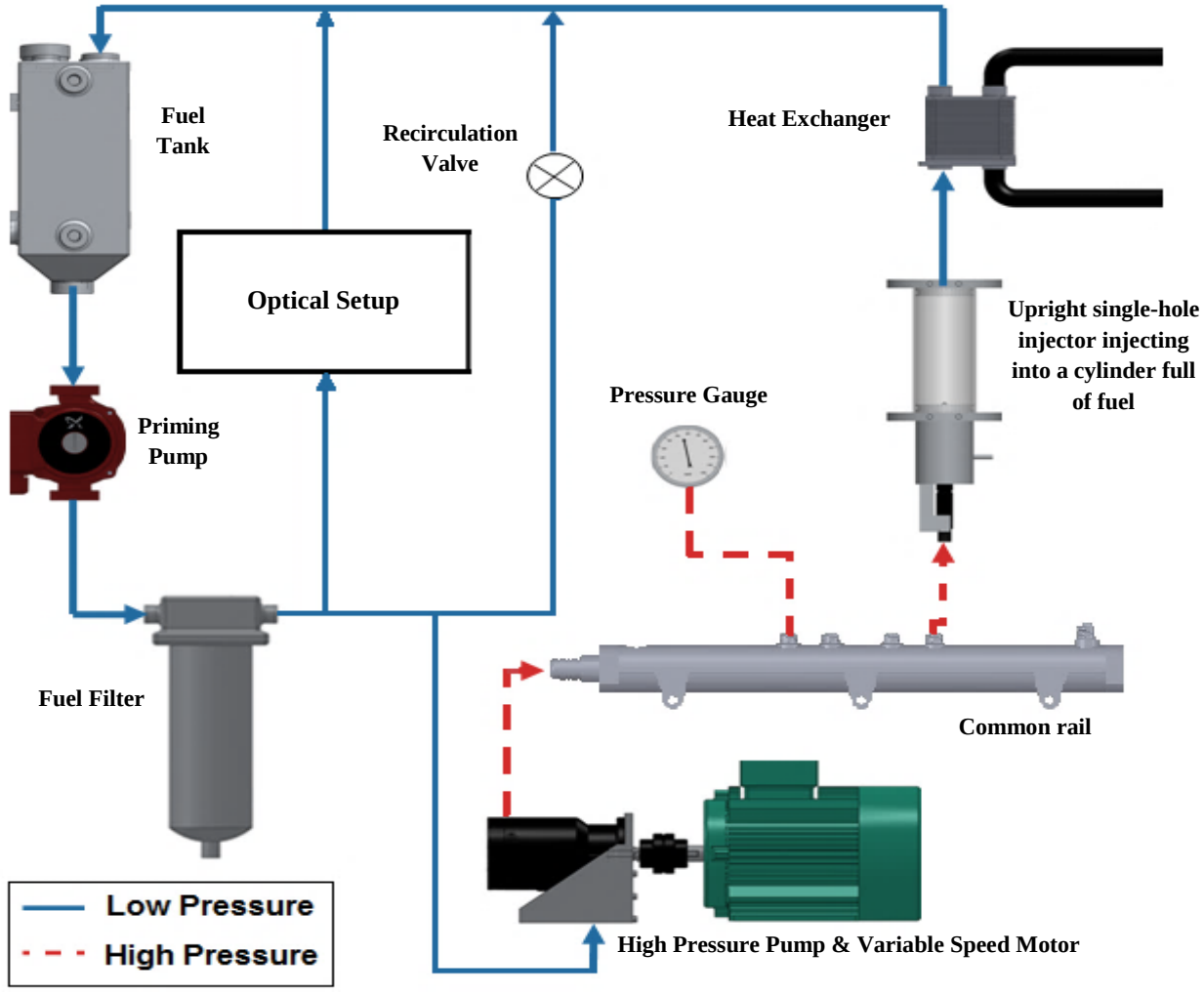

Figure 3.1 Schematic diagram of the high-pressure recirculation cavitation test-rig

The fixed displacement high-pressure pump could provide pressures up to 1,700 bar. Using the Bernoulli relation $\left(v = C_d\sqrt{\frac{2(p_{injection}-p_{back})}{\rho_{fuel}}}\right)$ the flow velocity past the 0.213 mm diameter single-hole nozzle could be estimated to be around 500 m/s ($p_{injection}$ = 1700 bar, p_{back} = 1 bar and averaged ρ_{fuel} = 835 kg/m^3), assuming the nozzle discharge coefficient C_d of 0.8. The volumetric flow rate ($Q = v.A$) of the fuel in the rig was then estimated to be almost 1.1 litres

per minute. The test-rig was refilled with around 3.6 litres of diesel fuel for every test, which meant that at high pressures the fuel charge was circulated around the test-rig once every 3-4 minutes.

The test-rig had the maximum fuel capacity of 3.7 L. However, the rig was never filled to its maximum capacity as a safety precaution to prevent any pipe bursts or leakage. The minimum fuel level for rig operation was just below 2.9 L, at which point the control system was designed to cut-off power to the high-pressure pump. For the purpose of the experiments the test-rig was filled with 3.3 - 3.6 L of fuel; allowing for samples to be drawn-off for further testing while the rig operated, without the fuel level reaching the minimum required level.

The test-rig had three drainage points, which were used to empty the rig of the fuel or to take samples during the rig operation. The three drainage points were located at different vertical positions and the drainage procedure involved starting from the highest point to ensure no diesel remained in the system. The first and highest drainage valve was located below the receiving cylinder, and was employed to drain the receiver. The second drain valve was located under the heat exchanger; it emptied the heat exchanger and the return line from the receiver. The third drain valve, positioned under the fuel filter, drained diesel from the tank, the feed and high-pressure pumps, fuel filter, the optical system and the remaining piping. The third drain valve was also used to draw samples during the test-rig operation, this was chosen for safety reasons considering it was located after the heat exchanger; the temperature of the diesel draining from the other two locations could be extremely high during the rig operation.

3.1.1 Temperature Control System

As a consequence of expansion of the injected fuel in the receiver, the pump's compression energy is converted to the fuel's internal energy, causing a significant rise in its temperature. The release of compression energy from 1,700 bar to ~1 bar was estimated to give a

temperature rise of around 70 °C. Continuous injection of fuel in this manner would produce an indefinite increase in fuel temperature as the fuel is recirculated in the rig. Hence, use of a temperature control system was necessary to prevent the increase in fuel temperatures to levels dangerous for the integrity of the apparatus. Controlling the pre-injection temperature also provided a basis for comparison between the investigations.

A counter-flow shell-and-tube heat exchanger was employed to cool the fuel that was leaving the receiver, before it was returned to the tank for recirculation. A temperature controller managed the rate of cooling water passing through the heat exchanger by monitoring the fuel temperature using a thermocouple. The thermocouple was located at the suction port of the high pressure stage of the high-pressure pump. Pre-injection temperature of the fuel was maintained at 50 °C, allowing fuel temperatures in the receiver to reach ~120 °C.

The temperature controller was setup to control the flowrate of cooling water that was to be supplied with an optimum supply pressure and temperature of ~2 bar and 10 ± 2°C, respectively. At the optimum cooling water supply conditions the temperature controller could maintain the pre-injection fuel temperature at 50 °C with fluctuations of ± 0.3 °C.

3.1.2 Nozzle Description

The injector used was a single-hole nozzle made by Delphi Diesel Systems. The single cylindrical nozzle hole was located at the tip of the nozzle, in line with the centre axis of the nozzle. The needle was removed from the injector assembly in order to obtain the desired continuous flow through the nozzle. The injector was setup vertically upright with the nozzle tip inserted into the bottom of the receiving cylinder as shown in Figure 3.2.

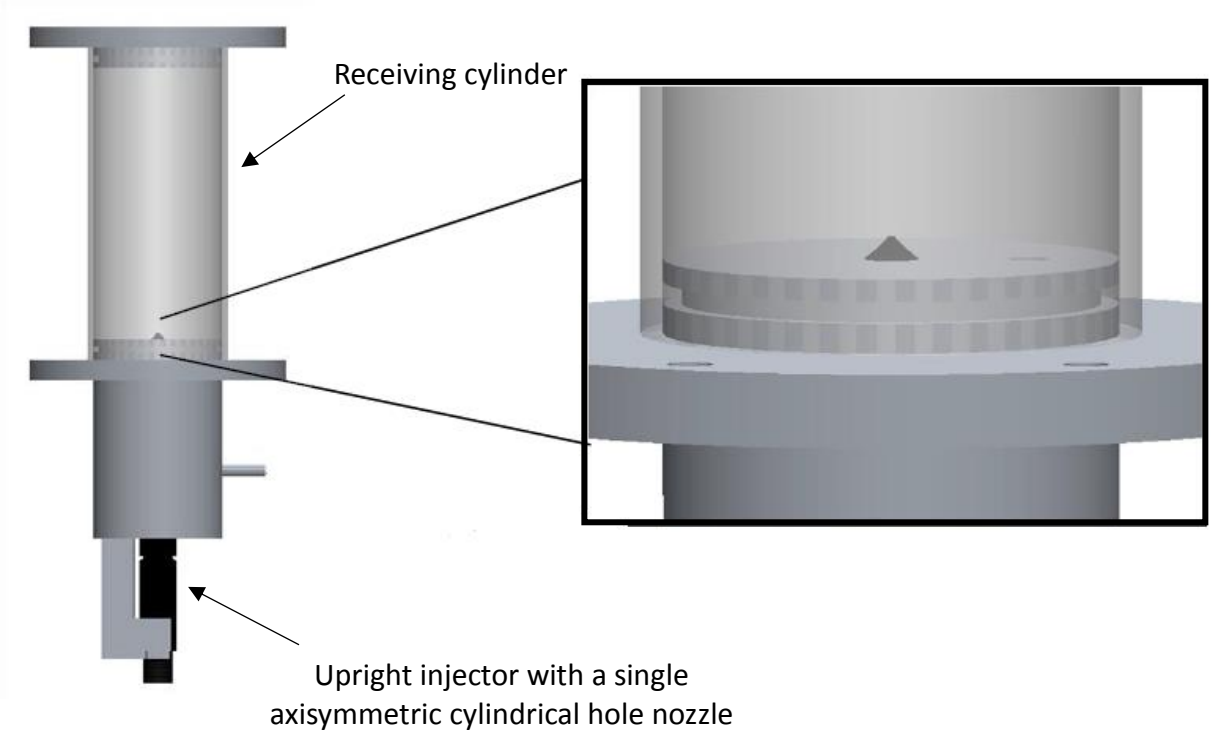

Figure 3.2 Injector and receiving cylinder assembly.

A number of different injector nozzles were used in the cavitation study, varied for tests on the basis of test type and test fuel. The nozzles were divided into two types based on their manufacturing batch, namely the old nozzles and the new nozzles. The two nozzle types were fundamentally different from each other based on their nozzle hole size. Both nozzle types were compatible for assembly with the same injector body.

The old nozzles had the single axisymmetric cylindrical nozzle hole of 213 µm diameter with a 20 % hone, such that the flowrate through the nozzle was 0.3 L/min at 100 bar (C_d ~ 0.8) and approximately 1.1 L/min at 1,650 bar. The new nozzles had an average nozzle hole diameter of 174 µm, with a mean honing level of ~ 13 % ± 2 %. Measurement of flowrates through the new nozzles at 1,650 bar injection pressure gave flowrate values averaging 0.83 L/min, with a subsequent averaged C_d of ~ 0.9.

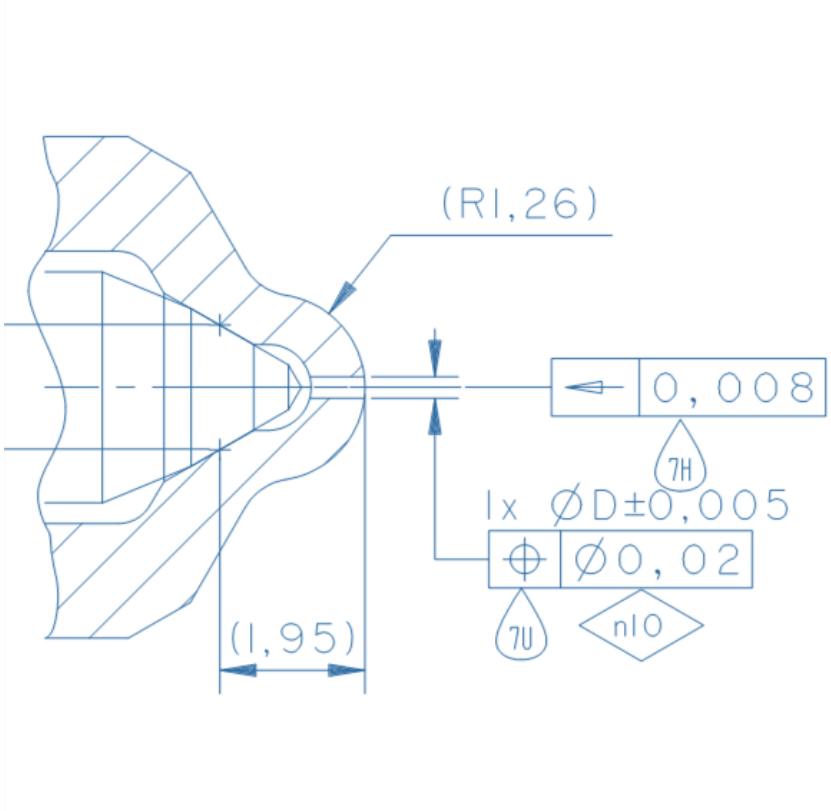

Figure 3.3 Drawing of the 213 µm single-hole old injector nozzle.

3.1.3 Pressurised Receiving Cylinder

As expressed by the definition of cavitation number C_N in equation 2.6, the cavitation intensity and the propensity of a liquid to cavitate is affected by both the injection pressure P_i and the downstream/back pressure P_b. Studies on the effect of downstream pressure have also shown that an increase in P_b can result in more aggressive collapse of cavitation bubbles, resulting in emission of higher intensity pressure pulses[63]. The aggression of bubble collapse has significant implications on the physical conditions generated inside the collapsing bubble that are known to drive the sonochemical-like reactions in the cavitating liquids.

To investigate the effect of downstream pressure on the chemical stability of diesel fuels, the receiving cylinder (or the receiver) assembly was modified to allow pressurisation of the receiver. The 395 mL capacity receiver was originally designed to be able to withstand internal pressures of up to ~20 bar. A pressurising mechanism was required to enable the fuel pressure

inside the receiver to build-up. To this end, the fuel return pipe connected to an exit port on the top of the receiver was replaced with a 10 mm steel tube adjoined to a pressure regulator. A pressure gauge, located between the pressure regulator and the receiver, indicated the gauge pressure of the fluid inside the receiver. A second port on the top of the receiver, which was originally used to bleed the receiver when draining, was used to connect a pressure relief valve that by-passed the pressure regulator and connected to the low-pressure fuel return line to the rig, via the heat exchanger. The modified receiver setup schematic is shown in Figure 3.4.

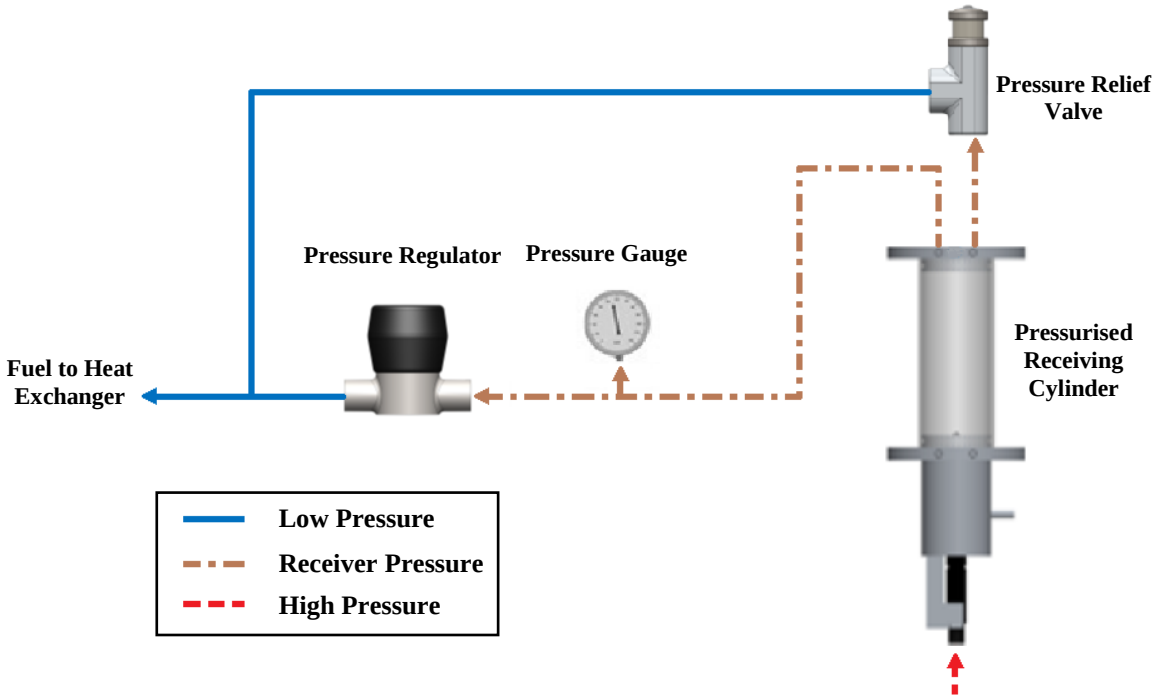

Figure 3.4 Schematic of the pressurised receiving cylinder setup

Using the pressure regulator, the flow of fuel back to the rig was partially choked, leading to build-up of pressure inside the receiver. The spring-loaded poppet valve pressure regulator had the capacity to pressurise the system up to 17 bar, however the receiver was never pressurised above 10 bar to prevent fuel leaks over long term operation of the rig.

3.2 In-situ Laser Transmission Setup

A simple optical diagnostics method, based on the Beer-Lambert-Bouguer law of optical attenuation, was employed in this study to characterise the in-situ changes in properties of the diesel fuel being cavitated in the test-rig. It was hypothesised that as the fuel undergoes degradation during high-pressure recirculating cavitating flow, it would experience changes in its composition and properties. The optical system used for this study aimed to utilise and quantify this change in fuel, in particular its optical properties, through measuring its spectral extinction coefficient.

The optical measurement setup used, included an optical cylinder, a laser diode and two photo-detectors. A proportion of the fuel passing through the fuel filter was supplied to the optical measurement setup. Spectral transmission measurements were performed on the fuel as it flowed through the optical cylinder. The filtered fuel was fed to the optical cylinder from the bottom, after which the fuel flowed into an optical chamber where the optical measurement was performed. Following the optical measurement, the fuel flowed out of the cylinder and returned to the fuel tank.

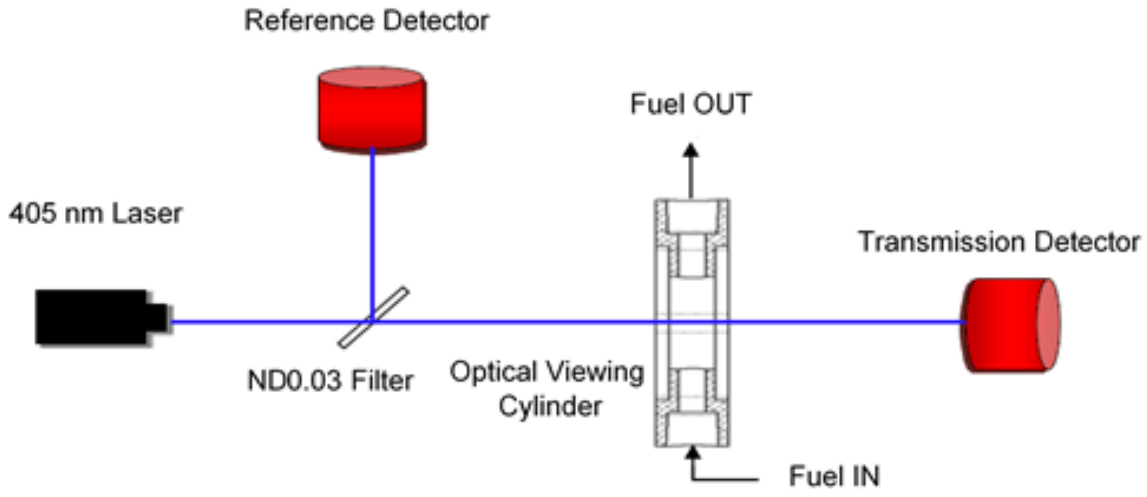

Figure 3.5 Schematic of the laser measurement setup

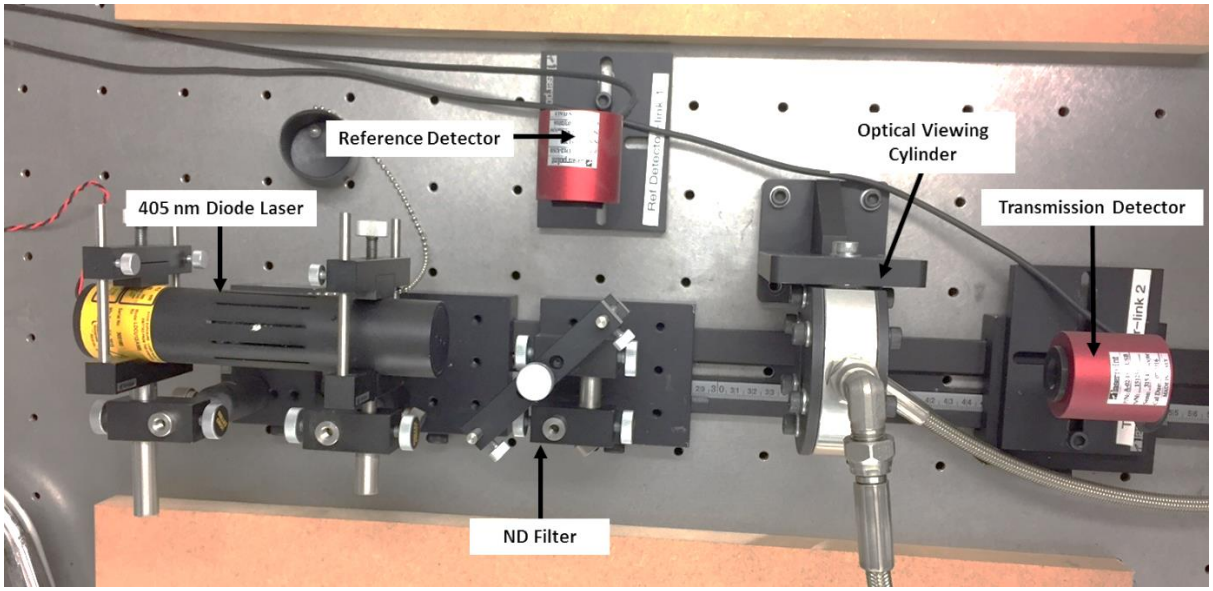

Figure 3.6 Optical measurement setup (top-view)

The optical cylinder consisted of two 6 mm thick optical grade fused silica windows on either end of a 30 mm thick steel cylinder body. The fused silica windows were compressed and sealed in place with the help of two aluminium plates and six M6 screws. The windows enclosed a 10 mm wide, 40 mm diameter optical chamber through which the diesel flowed. This setup provided optical access to the diesel in the optical chamber, allowing spectral transmission measurements to be performed.

The diesel sample present in the 10 mm wide optical chamber was irradiated using a laser diode at the spectral wavelength of 405 nm. Initial experiments were conducted using a 20 mW cw (World Star Tech.) diode laser, this was upgraded to a 35 mW cw (Laser2000) diode laser module for later experiments. The laser light transmitted through the cylinder's fused silica glass windows and the fuel sample to reach a photo-detector that measured its intensity and generated an electrical signal.

The laser from the module passed through a neutral density filter ND0.03 placed at 45° angle of incidence to the laser beam. The ND filter acted as a beam splitter that reflected 10 % of the laser beam onto a reference photo-detector that measured the reference beam intensity. The 90

% laser beam transmitted through the filter irradiated the optical viewing cylinder, following which it was incident on a transmission photo-detector.

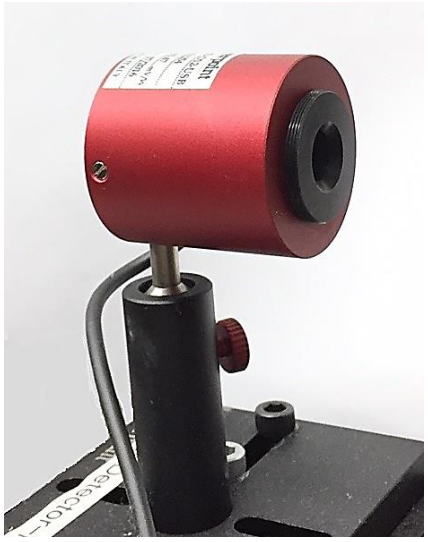

Figure 3.7 Laser Photo-detector

The laser photo-detectors were Laserpoint (A-02-D12-BBF) thermal low power sensors that used thermopile sensors to detect laser power, with a power resolution of 10 µW. The thermopile sensors determine laser power via measuring the relative difference between the temperature inside of the sensors versus the ambient temperature. The detectors had a USB interface that communicated with a computer based software called PC-Link 2 (this was later upgraded to Leonardo). The software logged 30 second averaged laser power measurements from both detectors continuously for over 24 hours.

3.3 Ultraviolet-Visible Spectroscopy

Samples of the test fuel being cavitated in the rig could be drawn from one of the drain ports to perform further analysis. The analysis performed for the purposes of this study included spectra measurements, particle count distribution measurements and 2D gas chromatography.

A Shimadzu UV-1800 UV-Visible spectrophotometer was employed to measure the absorbance and transmittance spectra of the cavitated fuel samples. Similar to the optical setup on the test-rig, the spectrophotometer utilised the Beer-Lambert-Bouguer law of absorbance. Unlike the optical setup on the test-rig, which uses a radiation source of a single wavelength (405 nm diode laser), the spectrophotometer allowed measurements of absorbance and transmittance over a range of wavelengths, from 190 nm to 1,100 nm, this corresponds to near infrared NIR, visible and near ultraviolet regions. It could to do so using a configuration incorporating dual radiation source, namely a halogen lamp and a deuterium lamp. The spectra

measurements could be taken at wavelength resolutions down to 0.01 nm intervals. The spectrometer had a logarithmic absorption measurement range from zero to 4.

The UV-1800 spectrophotometer operated on a double beam – double detector configuration which involved dividing the source light beam into a reference beam and a sample beam. The reference and sample beams passed through a reference and sample cell, respectively, and reached two photodiode detectors. This configuration allowed the spectrophotometer to take a baseline measurement using the reference setup, while the test sample was analysed by the sample setup.

Along with the spectra measurements, the spectrophotometer could perform photometric measurements at a fixed wavelength. The sample and reference liquids were placed in the respective sample compartments in cells or cuvettes of various shapes and sizes. The cuvettes used for this study were Starna Scientific square cells, made from far UV quartz with a sample path length of 10mm.

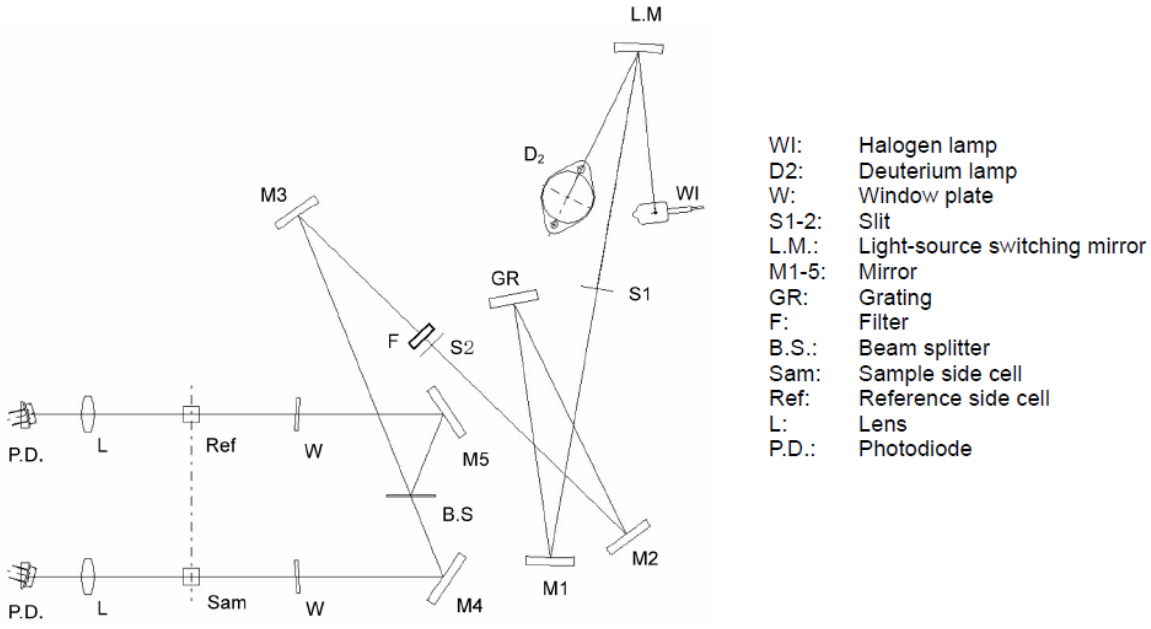

Figure 3.8 The double beam-double detector configuration used on UV-1800 Spectrophotometer[96].

The spectrophotometer could be operated as a standalone system where the results could be stored in a USB storage device or printed; or it could be linked to a computer using a USB interface where a purpose-built software (UV Probe) was utilised to view, process, manipulate and further analyse the absorption or transmission spectra.

3.4 Laser Particle Count

The setup for performing particle counts on cavitated diesel samples involved the use of an off-the-shelf laser particle counter. The Spectrex Laser Particle Counter (Model PC-2200) utilised a diode laser of 650 nm wavelength, which created a laser beam of a defined volume inside the sample liquid. The laser beam was spatially filtered and focused by a lens assembly; meanwhile a scanning mechanism allowed the illuminated volume to rotate at a constant rate to form a cylindrical region to be scanned in the liquid sample.

As the illuminated volume passed over a suspended particle, the light-beam experienced small diffractions, mostly in the near-forward direction. This type of diffraction is known as Fraunhofer diffraction.

After passing through the test sample, the laser light was received by an optical collection system, consisting of a photo-detector assembly. Flashes of laser light incident on the photodetector generated an electrical pulse in a preamplifier connected to the photo-detector. The amplitude and width of this pulse was a function of the size of the particle. If a particle, due to which diffraction occurred, fell within the region where the laser was focused then the pulse generated by the preamplifier was narrow; whereas an out-of-focus particle caused the pulse to be broader. The electric circuits were designed to exclude the broader pulses from the count. As a result of exclusion of these broader pulse signals only the particles present in the defined focused region were counted.

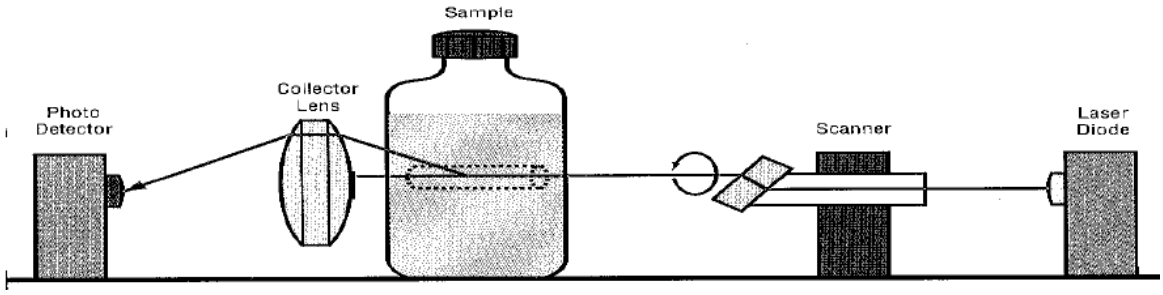

Figure 3.9 Optical schematic of the Laser Particle Counter, highlighting the scanned region inside the sample bottle[97].

Given that the scanning rate of the laser was constant meant that the volume of the liquid scanned could be determined for a definite duration. The laser particle counter then gave the particle count in terms of number of particles per unit volume as counts/mL (counts/cc).

The particle counter had the capacity to measure particle sizes in the diameter range of 1 µm to 100 µm. The size of the particle in the sensitive region was determined by measuring the scattered light and the fraction of that light reaching the photodetector. The amount of light scattered by a particle was a function of the scattering angle and relative index of refraction of the particle. The light collection system collected and averaged light that had been scattered in the near-forward direction at angles ranging from 4° to 19°. Due to the possibility of a particle being at different locations within the depth of field, a variation of ±15 % in the collected light was specified by the manufacturers. The effect of these variations could be reduced by increasing the scan duration and then averaging successive readings.

A USB interface recorded the particle count distributions using a computer software called the Spectrex Supercount. The software displayed the particle sizes in two groups of 16 ranges, first group included particles of 1 µm to 16 µm diameters, and the second group included particles from 17 µm to 100 µm diameters. The software displayed the size ranges of the two groups and their populations as a histogram. A summary report at the end of sample measurement

included additional information such as the mean particle size in the test sample, the standard deviation from the mean particle size, total number of particles per unit volume etc.

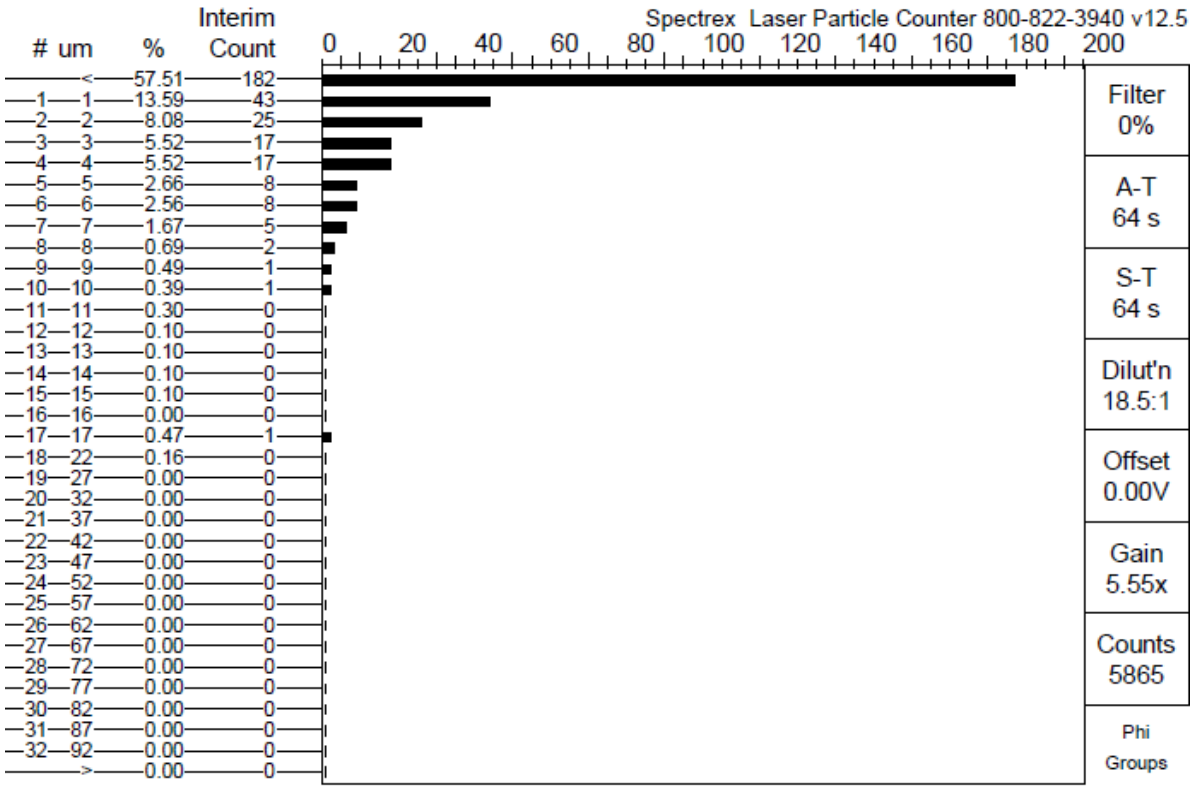

Phi	Size	Total counts /cc	Counts percent	Surface area percent	Volume percent	Mass/bin ppm
10	1-2	4,170.14	71.10%	1.56%	0.29%	0.0003
9	2-4	797.06	13.59%	9.43%	3.60%	0.0035
8	4-8	727.75	12.41%	37.86%	25.36%	0.0247
7	8-16	132.84	2.27%	26.64%	29.45%	0.0287
6	16-31	36.97	0.63%	24.50%	41.29%	0.0403
5	31-63	0.00	0.00%	0.00%	0.00%	0.0000
4	63-128	0.00	0.00%	0.00%	0.00%	0.0000

Total counts: 5,864.76/cc
Total suspended solids: 0.10ppm (mg/liter)
Dilution factor: 18.50:1
Spec. gravity: 0.68
Mean size: 3.36um
Standard dev: 3.03um

Figure 3.10 A sample summary report from the laser particle counter.

Chapter 4
Experimental Methodology

Cavitation experiments involved testing each of the test fuels included in Table 4.1 for a varying test matrix. The fuel recirculation durations for the various tests performed included 40 hour runs over 4 days and 130-140 hour runs over 13-14 days, comprised of 10 hours of testing per day. However, these durations were subject to variations depending on test case and performance of the test-rig components over long durations of operation. The majority of the tests were conducted at injection pressures of 1,650 bar; with some fuels, investigated for injection pressure dependence, also being tested at 550 bar, 825 bar and 1,100 bar injection pressures. Three different types of fuel filter materials were used for the different investigations, with the control filter mesh size being 3 µm. The different filters utilised, based on their construction material, included polypropylene fibre matrix filters, nylon 6 fibre matrix filters and stainless steel wire woven filters. In case of filtration tests, the filter mesh sizes being tested included 3 µm, 5 µm and 10 µm. While the majority of the tests reported in this report were conducted at ambient (~ 1 bar) receiver pressure, an investigation into the effect of back pressure also reports results for 5 bar and 10 bar (absolute) receiver pressures. As described in the previous section, two sets of single-hole nozzles were used for the investigations; the first being the old nozzle with a hole diameter of 213 µm and the second, new set of nozzles, with a nominal hole diameter of 174 µm. Apart from the early injection pressure dependence and long cavitation duration experiments on Fuel 1 (BDN) and the Model Fuel, a separate 174 µm hole-diameter nozzle has been used for each fuel. The old 213 µm hole-diameter nozzle was used for the early injection pressure dependence and long cavitation duration investigations. The control pre-injection temperature of the fuel was set to 55 °C for all cavitation experiments.

Table 4.1 Table of Fuels analysed in the Investigations

Fuel 1 (BDN)	New Conventional Base Diesel
Fuel 2 (B10)	B10 – Fuel 1 (BDN) with 10 % RME
Fuel 3 (B30)	B30 – Fuel 1 (BDN) with 30 % RME
Fuel 4 (BD+H)	Fuel 1 (BDN) with 10 % Hexadecane
Fuel 5 (BD+MN)	Fuel 1 (BDN) with 10 % 1-Methylnaphthalene
Fuel 6 (BDA)	Aged Conventional Base Diesel (not Fuel 1 (BDN))
Paraffinic Fuel	100 % n-Paraffins

Table 4.2 Test matrix for analysis performed on each fuel

Fuel	Fuel Tests	Injection Pressure Dependence Tests	Long Duration Tests	Pressurised Receiver Tests
Fuel 1 (BDN)	✓	✓	✓	✓
Fuel 2 (B10)	✓			
Fuel 3 (B30)	✓			
Fuel 4 (BD+H)	✓			
Fuel 5 (BD+MN)	✓			
Fuel 6 (BDA)		✓		✓
Paraffinic Fuel			✓	

4.1 Fuel Filling, Flushing and Draining Procedures

Prior to the start of each cavitation test, a set of draining, flushing and refilling procedures were followed to prep the high-pressure test-rig. The purpose of these procedures was to ensure minimum test-to-test contamination of fuel under examination. Initially the fuel present in the rig from the previous test was drained out of the rig using the three drainage ports. Flushing procedure involved filling the rig with and recirculating 2.9 L of the test fuel at low injection pressures around the rig and the optical setup, using the high-pressure pump. The recirculation

was carried out for 45 minutes for a single flushing event and the flushing procedure was carried out twice before the start of each test. Following the draining procedure, a small quantity of the fuel remained in the system; the quantity of the residual fuel was estimated to be around 300 mL. The two flushing cycles and the refill together reduced the contamination from the previous test to approximately 0.1 %.

A set procedure was also followed while filling the rig with fuel for flushing procedures or for the cavitation tests. The fuel was poured into the fuel tank and was recirculated using the low-pressure pump for two minutes. The high-pressure pump was then used to recirculate the fuel through the high-pressure assembly at pressures of around 300 bar. This was done to ensure removal of trapped air from the system, which is important for preventing damage to the high-pressure pump.

Detailed procedures for fuel draining, flushing and refilling are included in Appendix E.1.

4.2 In-situ Laser Transmission Setup Calibration

Prolonged cavitating flow was expected to degrade some optically active molecules present in the fuel and produce new optically active molecular species. Formation of carbon-rich species, resulting from long-term cavitation of diesel, was expected to increase the diesel's spectral attenuation, thus, decreasing the intensity of the transmitted laser signal in the optical setup.

The spectral attenuation is effected by the spectral attenuation coefficient of the liquid understudy. According to the Beer-Lambert law of absorptivity the transmitted signal (I_t) is related to the spectral attenuation coefficient (α) through the following relation:

$$\boldsymbol{I_t = I_0\, e^{-\alpha l}} \qquad 4.1$$

here, I_0 and l are spectral flux of light incident on an absorptive sample and the distance the light travels in the sample, respectively.

The spectral attenuation coefficient α is composed of scattering coefficient α_{sc} and absorption coefficient α_{abs}, such that the overall spectral attenuation coefficient $\alpha = \alpha_{sc} + \alpha_{abs}$.[13]

I_t/I_0 is called the transmittance (T) while $(1/T) = \log(I_0/I_t)$ is called the absorbance (Abs).

The laser power incident on the diesel samples I_0 had to pass through the beam splitter (ND0.03 filter at 45° angle of incidence), followed by the fused silica window into the optical cell, that is $I_0 = t_f\ t_{fs} I_{laser}$, where t_f, t_{fs} and I_{laser} are the transmission coefficient through the neutral density ND0.03 filter, the transmission coefficient through the fused silica window and the 405 nm diode laser power, respectively. I_0 can also be expressed in terms of the laser power reflected from the ND filter onto the reference detector I_{ref}, such that $I_0 = \frac{t_{fs}(1-r_f)}{r_f} I_{ref}$, where r_f is the reflectivity of the ND0.03 filter being used as the beam splitter.

The laser power exiting the diesel samples I_t passed through the second fused silica window before reaching the laser power detector. The laser power measured with the detector is denoted by I_P and is related to the laser power leaving the diesel sample I_t by $I_P = t_{fs} I_t$.

The time-dependent spectral attenuation coefficient is then derived from equation 4.1 to be

$$\boldsymbol{\alpha(t) = \frac{\ln \frac{I_{0(t)}}{I_t(t)}}{l} = \frac{\ln \frac{t_{fs}^2 (1 - r_f) I_{ref}(t)}{r_f I_P(t)}}{l}} \qquad 4.2$$

Where l is the optical path length of the laser through the diesel in the optical cell.

The transmission coefficient is defined to be the fraction of light transmitted through the sample, and may be expressed as

$$\boldsymbol{T = \frac{I_t(l)}{I_0}} \qquad 4.3$$

The values for t_{fs}^2 and r_f were determined through a series of calibration tests described in detail by Lockett and Jeshani (2013)[13] and Jeshani (2013)[50], they were found to be 0.945 ± 0.010 and 0.093 ± 0.005, respectively.

The optical extinction arrangement was calibrated before and after the experiments. During the course of the cavitating flow tests and optical extinction measurements, the fused silica windows of the optical cell were checked regularly for external and internal fouling.

The intensity of laser was expected to change over-time due to the diode warming up or other external factors that could contribute to a variation in laser performance. To incorporate the effect of laser performance, a beam splitter was used to split the laser beam into a reference beam and a sample beam. The reference beam was detected by the reference photo-detector, whereas the sample beam, ensuing from the optical cell, was detected by the sample photo-detector.

4.2.1 Spectral Attenuation Data Analysis

The in-situ optical attenuation setup utilised a computer based software that logged 15-second averaged laser power from the two photo-detectors (i.e. transmission and reference detectors). The 15-second averaged laser power signals from the two detectors were used to calculate 15-minute averaged normalised laser transmission signal. Normalisation was carried out by dividing the 15-minute averaged transmission signal $I_P(t)$ by the synchronous 15-minute averaged reference signal $I_{ref}(t)$. This procedure eliminated the effect of variations in the performance of the 405 nm laser module over the course of a test day.

The 15-minute averaged time-dependent transmission $I_P(t)$ and reference $I_{ref}(t)$ signals were used to determine the time-dependent spectral attenuation coefficients $\alpha(t)$ of the fuels using the relation shown in equation 5.2.

4.3 UV-Visible Spectra Measurement Sample Dilution Methodology

30 – 40 ml samples of test fuel were drawn off from the test-rig at regular intervals during each cavitation test, for further analysis on the UV-Visible spectrophotometer and Laser Particle Counter (LPC). Dilution of the pure diesel fuel samples was required to enable precise and accurate measurements for both diagnostic methods. HPLC grade n-heptane was used as the diluent in both cases.

The UV-Visible spectrophotometer had a dynamic absorption measurement range from zero to 4; however, the diesel samples were diluted in order to limit the maximum absorbance to 2.7. Absorbance between zero and 2.7 ensured a proportional response to variation in concentrations.

Diesel fuel has higher spectral absorption in the ultraviolet region as compared to the visible region. Therefore, the diesel sample was diluted to different extent for separate wavelength ranges. To this end, the complete measurement range was divided into three subranges of 350 nm – 500 nm, 240 nm – 305 nm and 190 nm – 405 nm.

For the measurement subrange of 350 nm – 500 nm the diesel fuel samples were tested without any dilution. Dilution ratio factors (DRF) of 520 and 10,000 were used for the measurement subranges of 240 nm – 305 nm and 190 nm – 405 nm, respectively.

The dilution ratios were kept constant for all fuels except for Fuel 5 (BD+MN). The presence of 10 % additional 1-methylnapthalene increased the fuel's absorbance for the complete measurement range. Fuel 5 (BD+MN) was thus diluted to DRF 3,000 and DRF 17,000 for the measurement subranges of 240 nm – 405 nm and 190 nm – 405 nm, respectively. However, it was left undiluted in the measurement subrange of 350 nm - 500 nm.

For all fuels except Fuel 5 (BD+MN), the dilution methodology for DRF 520 involved diluting 5 µl of each diesel sample into 2.6 ml n-heptane. A glass syringe was used to pour the 2.6 ml

of n-heptane into a cuvette, followed by the addition of 5 µl of diesel sample to the cuvette. The cuvette containing the DRF 520 sample was then placed on the spectrometer and the spectra measurement was made. The sample was scanned three times in the wavelength range of 240 nm – 305 nm and the three spectra were averaged to give a mean spectrum for the sample. Similarly, three further DRF 520 samples were produced and scanned, giving a total of four averaged spectra for the four diluted samples of the same diesel fuel sample. The final absorption spectrum for that diesel sample was the mean of the four averaged spectra in the 240 nm – 405 nm range.

One of the four DRF 520 samples was chosen to produce four DRF 10,000 samples. Each DRF 10,000 sample was produced by diluting 140 µl of the DRF 520 sample with 2.6 ml of n-heptane in a cuvette. The diluted samples were then scanned thrice each in the wavelength range of 190 nm – 405 nm and averaged to give four averaged spectra. The final absorption spectrum for that diesel sample was the mean of the four averaged spectra in the 190 nm – 405 nm range. As a measure of precision, the $\frac{Absorbance\ Range\ (\lambda)}{Mean\ Absorbance\ (\lambda)}$ of the four diluted samples for each diesel sample was recorded; it was aimed to be kept < 2 % at each wavelength (λ) for both DRF 520 and DRF 10,000 dilutions.

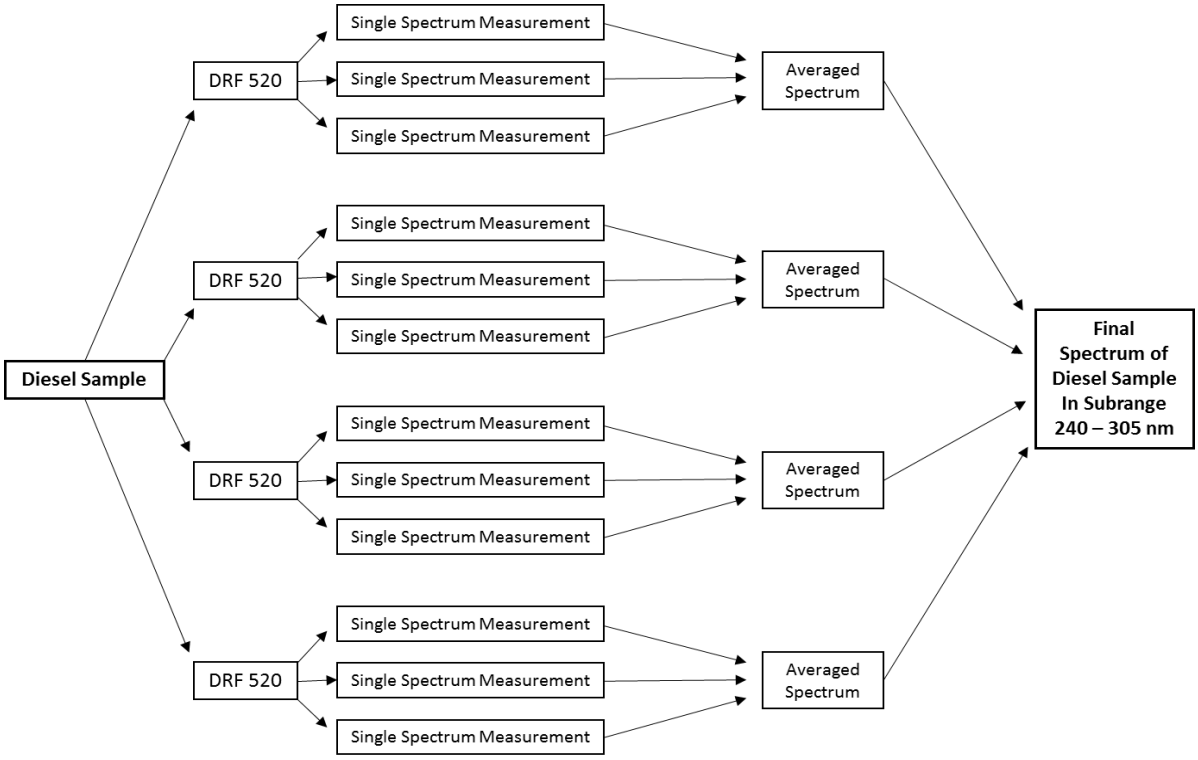

Figure 4.1 Scheme of spectra measurements in the subrange of 240 nm - 305 nm for all fuels except Fuel 5 (BD+MN)

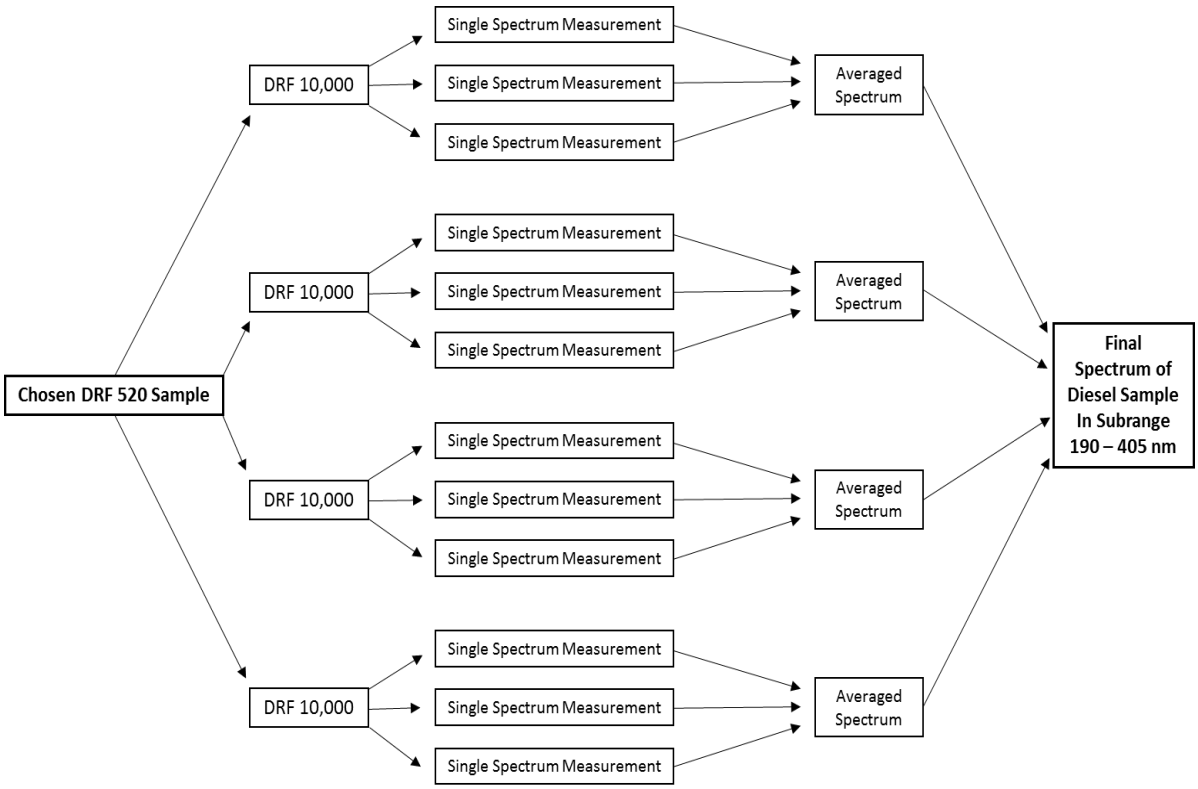

Figure 4.2 Scheme of spectra measurements in the subrange of 190 nm - 405 nm for all fuels except Fuel 5 (BD+MN)

Fuel 5 (BD+MN) dilution methodology involved producing a base solution of DRF 130 which was then further diluted to produce the DRF 3,000 and DRF 17,000 samples. DRF 130 sample was produced in a cuvette by diluting 20 µl of the diesel sample in 2.6 ml of n-heptane. 120 µl of DRF 130 sample was drawn and diluted with 2.6 ml of n-heptane in a separate cuvette to produce the DRF 3,000 sample. Following this procedure, three further DRF 3,000 samples were produced from the base solution. Each DRF 3,000 sample was subjected to three scans on the spectrometer in the wavelength range of 240 nm – 305 nm, followed by averaging to produce the averaged spectrum of the sample. The scanning process was repeated for all DRF 3,000 samples and mean of the four averaged spectra gave the final spectrum of the diesel sample in the 240 nm – 305 nm wavelength range.

Four DRF 17,000 samples were produced by diluting 20 µl of DRF 130 base solution in 2.6 ml of n-heptane. Similar to the previous diluted samples, each DRF 17,000 was scanned on the spectrometer and the resulting scans were averaged to give the final spectrum of the Fuel 5 (BD+MN) sample in the 190 nm - 405 nm wavelength range.

4.3.1 Dilution Repeatability and Statistics

The dilution methodology of diesel samples for spectra measurements was rigorously tested to ensure repeatability and precision. Repeatability tests were conducted on a fresh sample of Fuel 1 (BDN), which was used to prepare 40 diluted samples of DRF 520. The 40 diluted samples were subjected to spectra measurements in the wavelength range of 240 nm – 285 nm. Four out of the 40 diluted samples were randomly chosen and combined to be used for further dilution to DRF 10,000. 40 new samples of DRF 10,000 were then produced and tested in the wavelength range of 195 nm – 250 nm. Mean spectra of the two measurement ranges are presented in Figure 4.3 and Figure 4.4 along with the error bars representing 2σ standard deviation over the 40 samples in each case.

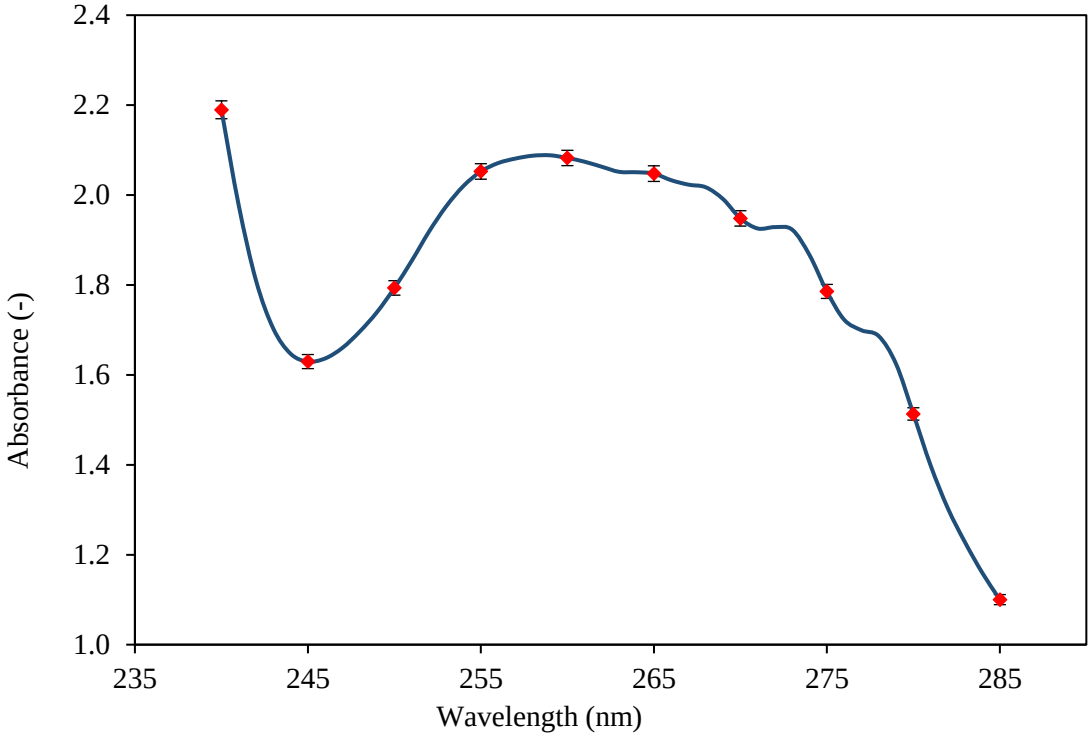

Figure 4.3 Mean spectra of the 40 DRF-520 samples in measurement range of 240 nm - 285 nm. Error bars represent 2σ standard deviation

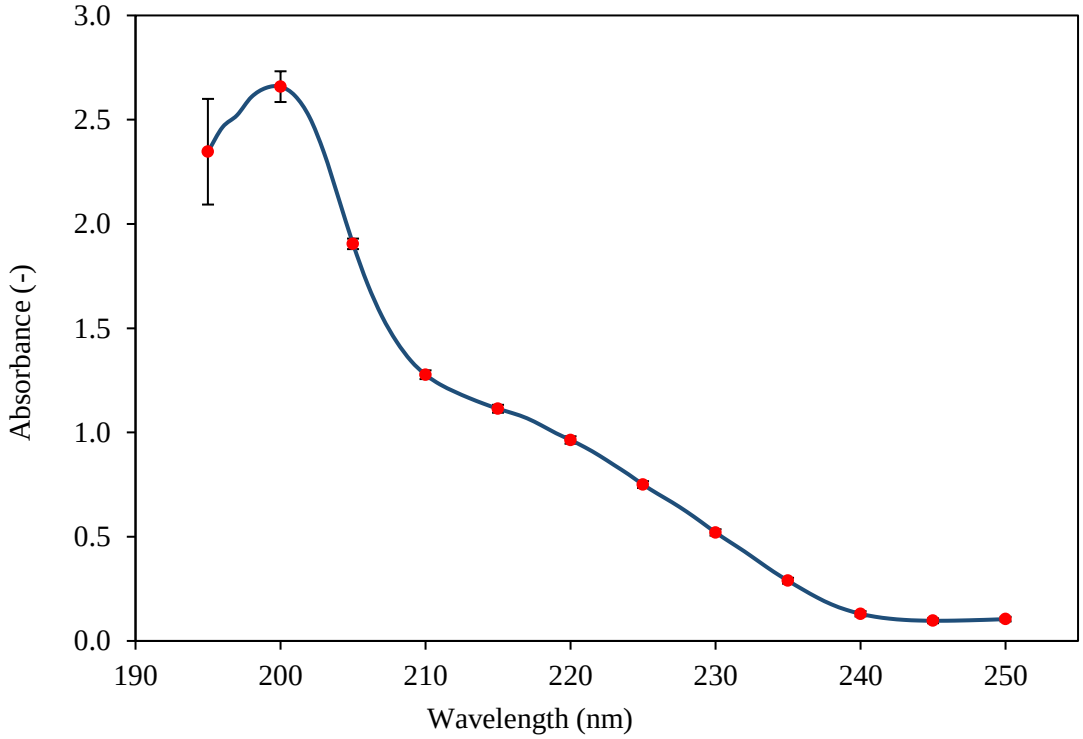

Figure 4.4 Mean spectra of the 40 DRF-10,000 samples in measurement range of 195 nm - 250 nm. Error bars represent 2σ standard deviation

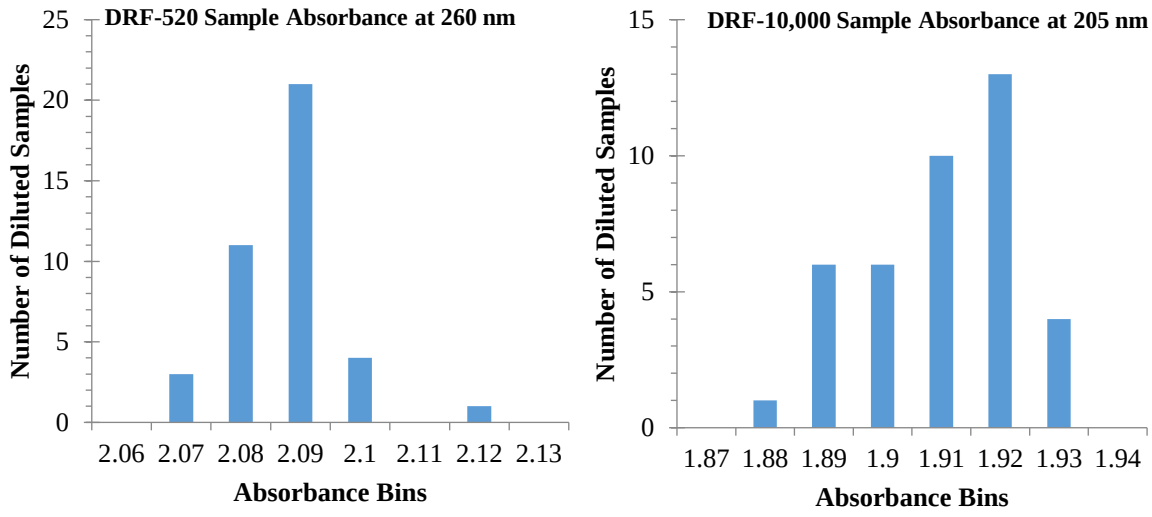

Figure 4.5 Histogram of 40 DRF-520 diluted sample absorbances at 260 nm wavelength (left). Histogram of 40 DRF-10,000 diluted sample absorbances at 205 nm (right).

Figure 4.5 shows histograms of the two measurement ranges at chosen wavelengths. For DRF 520 dilution the histogram was produced at 260 nm where the mean absorbance for the 40 samples was 2.0824. For DRF 10,000 dilution the histogram was produced at 205 nm where the mean absorbance of the 40 samples was 1.9045. Histograms show that the dilution methodology displayed high repeatability, higher for the DRF 520 dilution samples than the DRF 10,000 dilution samples.

Coefficients of variation (CV) were calculated for spectra of the two sets of 40 diluted samples to provide another measure of the dilution repeatability and precision. CV was defined as $\frac{Standard\ Deviation}{Mean}$, where standard deviation was 1σ. CV of the 40 DRF 520 dilution ratio samples was measured to be < 0.5 % for the complete range of 240 nm – 285 nm. CV of the 40 DRF 10,000 samples was measured to be less than 2% in the wavelength range of 200 nm – 230 nm. For wavelengths beyond 230 nm the absorption of the samples was too low, consequently the signal-to-noise ratio was likely to be very low as well, giving rise to higher CV values.

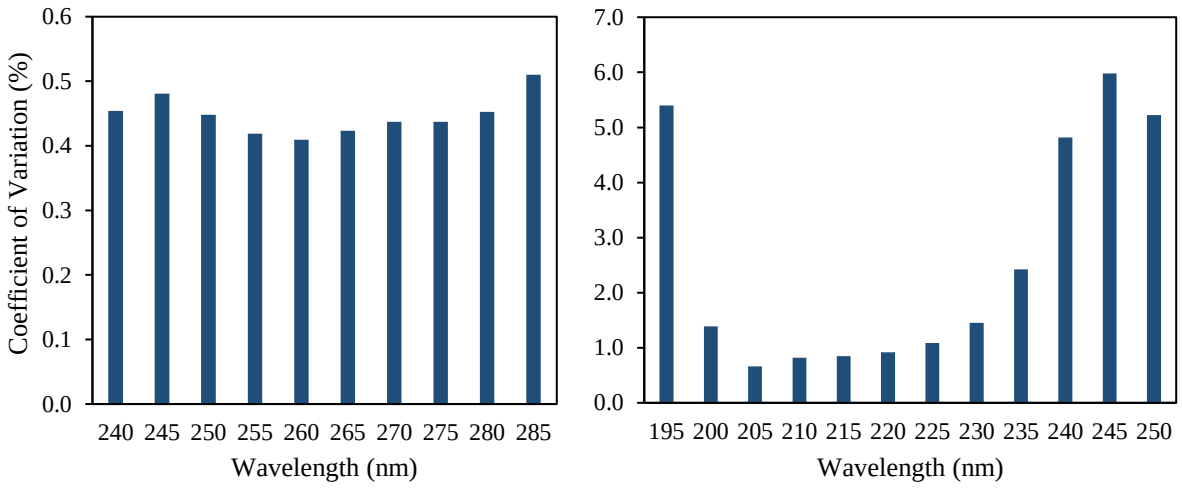

Figure 4.6 Coefficients of Variation of the 40 DRF 520 samples in measurement range of 240 nm - 285 nm (left). Coefficient of Variation of the 40 DRF 10,000 samples in measurement range of 195 - 250 nm (right).

4.4 Author's Note

Dilutions for spectra measurements of the fuel samples were conducted by two investigators, the author and a postdoctoral research fellow, Dr. Kuti. While the majority of the dilutions were conducted by the author, some results included in this work were produced by Dr. Kuti. The results obtained through dilutions performed by Dr. Kuti correspond to the initial set of fuel tests for Fuels 1 – 4.

The above-mentioned repeatability results correspond to the dilutions performed by the author. Dr. Kuti also carried out a similar set of dilution measurements as part of the repeatability tests. The tests were performed following the methodology outlined above, however thirty samples for each of the two dilution ratio factors were produced to obtain the mean distributions. The mean distributions along with the wavelength dependent coefficient of variations (CV) are presented in Figure 4.7, Figure 4.8 and Figure 4.9.

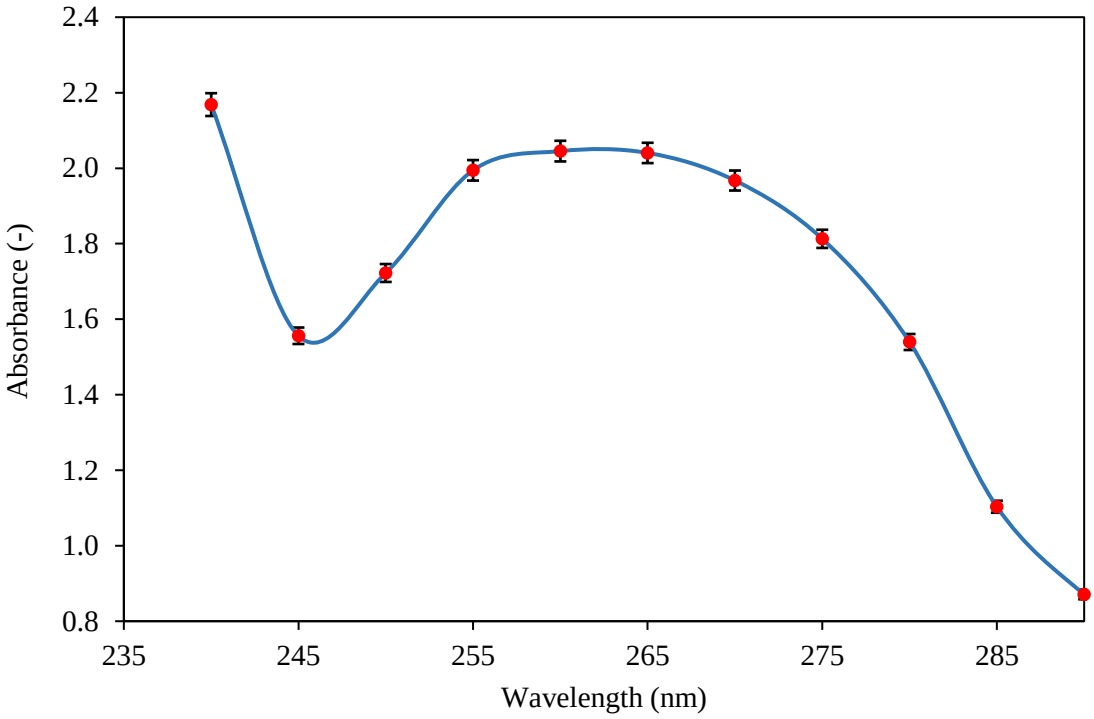

Figure 4.7 Mean spectra of the 30 DRF-520 samples in measurement range of 240 nm - 290 nm. Error bars represent 2σ standard deviation

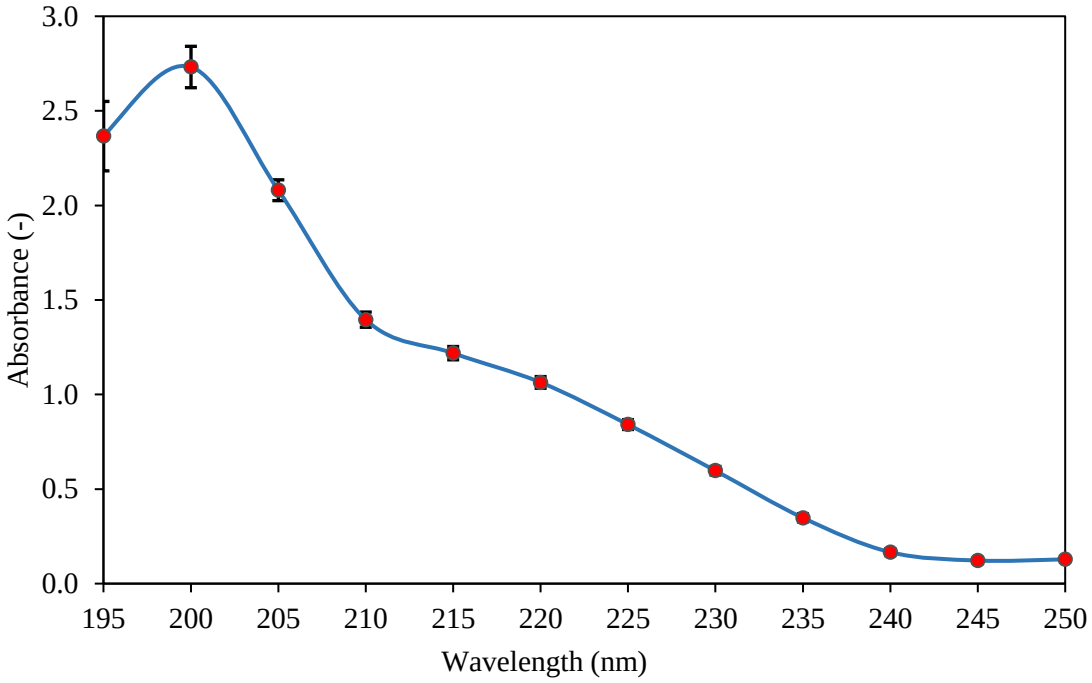

Figure 4.8 Mean spectra of the 30 DRF-10,000 samples in measurement range of 195 nm - 250 nm. Error bars represent 2σ standard deviation

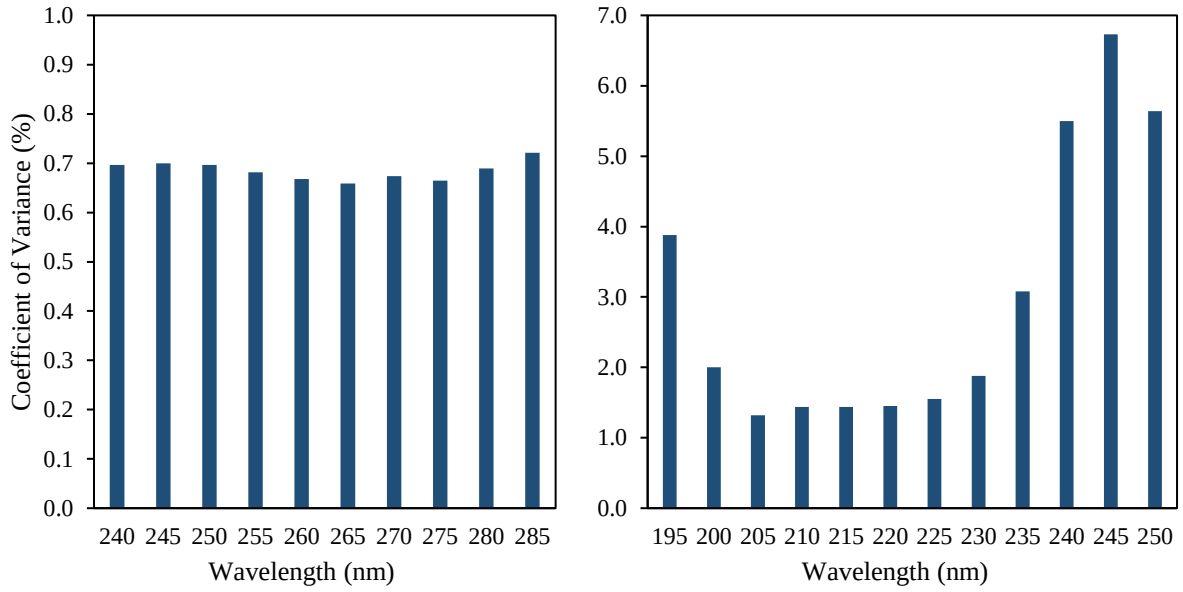

Figure 4.9 Coefficients of Variation for the 30 DRF 520 samples in measurement range of 240 nm - 285 nm by Dr. Kuti (left). Coefficient of Variation for the 30 DRF 10,000 samples in measurement range of 195 - 250 nm by Dr. Kuti (right).

As observed in the bar chart above, the thirty DRF 520 dilutions carried out by Dr. Kuti had the highest coefficient of variation of ~ 0.72 % in the wavelength range on 240 – 285 nm. For the DRF 10,000 dilutions, CV values were found to be less than 2 % in the 200 – 230 nm range. The results for dilutions performed by Dr. Kuti indicated high repeatability, with higher precision in the DRF 520 dilutions than the DRF 10,000 diluted samples.

4.5 Laser Particle Count Dilution Methodology

The Spectrex Laser Particle Counter LPC (PC-2200) detects particle sizes by measuring the laser scattering caused by individual particles. When particles interact or drift too close to one another, the LPC measures them as a single large particle. Therefore, the diesel sample being investigated needs to be diluted to reduce the particle density for accurate measurements. However, there is also a need for setting a maximum dilution limit; this is to limit the proportion of counts from particles present in the diluent itself. Although the diluent used was HPLC grade n-heptane with > 99 % purity, when subjected to the LPC it gives particle counts up to 50 particle counts/cc.

Through preliminary tests and manufacturer's instructions in the user manual, it was decided that the count rate at which the instrument counted particles most accurately was limited in the range of 600 to 1,000 counts/cc of the diluted sample. Therefore, all dilutions were aimed for raw total counts that fell in the that range.

In case of fuel samples that had been circulated and filtered in the rig for long durations, it was often found that their particle count range was below the 600 counts/cc even at very low dilution ratios. For such cases the highest possible particle count, achievable from the available volume of diesel fuel sample, was recorded. Detailed procedure of laser particle count dilution is provided in Appendix E.3.

4.6 Two Dimensional – Gas Chromatography (GC x GC)

Gas chromatography (GC) is a standard analytical technique used in modern chemistry to analyse mixtures. The technique is applicable to mixtures composed of compounds with boiling point ranges from zero to over 700 K, or those which can be heated without decomposition to produce vapour pressure of a few mmHg[98]. GC is a separation technique to analyse individual components based on their chemical or physical properties. The mixture being analysed is dissolved into a mobile phase (carrier gas), which then passes through a column containing the stationary phase. Modern GC columns are made from coiled fused silica capillaries, coated on the inside with the stationary phase (liquid). The carrier gas (usually helium or hydrogen) is pumped from a cylinder to a sample injector, that injects the mixture to be separated and analysed. A pressure controller is used to control the flowrate of the mobile phase – sample mixture through the columns. As the mixture passes through the stationary phase, it separates based on the physio-chemical properties of the sample and the stationary phase. The separated mixture analytes emerge (or elute) from the column with different retention times. The separated analytes eluting from the column are then subjected to a detector, that measures some physical or chemical property to allow their characterisation.

Early gas chromatograms were generated by detecting bulk properties of the separated components, including gas density, flow impedance and gravimetry. Development of the capillary-column technology allowed the possibility of advanced ionisation detection techniques to be implemented, which were considerably more sensitive. Some of the well-known ionisation-based detectors in use nowadays include flame ionisation detectors (FID), electron-capture detector (ECD), photo-ionisation detectors (PID) and alkali flame-thermionic detector (TID). Each of the above-mentioned ionisation-based detectors are suited to providing sensitive chromatograms for selected mixture types.

Despite providing a powerful separation technique, one-dimensional GC techniques are unable to separate highly complex mixtures such as crude oil fractions. In industries, such as the petroleum industry, detailed characterisation of different fuel components is of crucial importance. Here, use of multidimensional separation techniques is required which encompass methods including two-dimensional-GC (or GC x GC) and GC-Mass Spectroscopy (GC/MS).[99]

Among the multidimensional separation techniques, GC x GC is regarded as the most effective method. It involves the use of two columns connected in series to each another; the effluent of the first column (first dimension separation) is subjected to further separation in the second column (second dimension separation). The two columns are orthogonal, or independent of each other, which means that they separate compounds based on different properties; this is achieved using different stationary phase coatings inside the two columns.[99]

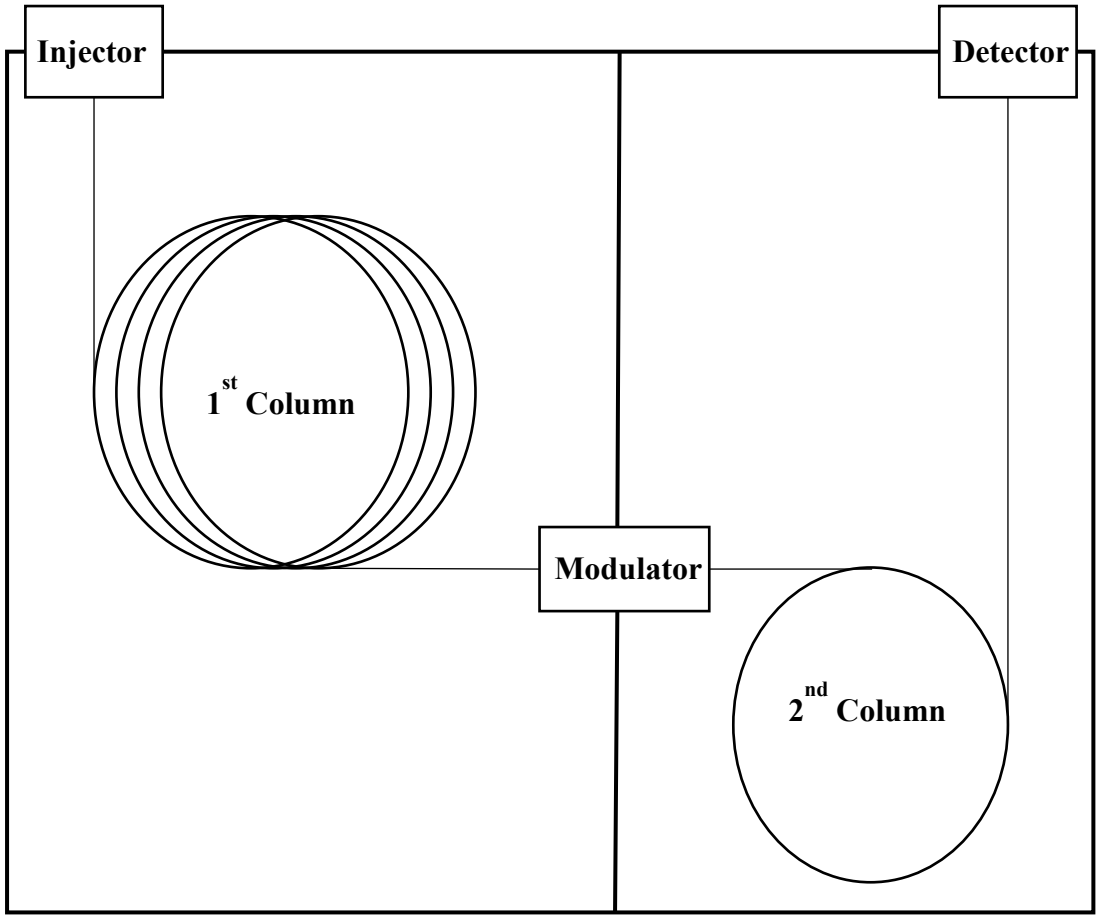

Figure 4.10 Schematic of a GC x GC system, showing the injector, modulator, detector, with the 1st and 2nd separation columns in their respective ovens.

Small fractions of the effluent from the primary column are periodically collected by a modulator, located between the two columns. Each fraction is then injected into the second column for further separation. At the completion of the secondary separation, the next fraction of the collected primary effluent is injected into the secondary column. This continues until all of the initial sample is subjected to both separation columns. Apart from collecting and injecting primary effluent to the secondary column, the modulator ensures that the primary effluent fractions are not injected into the secondary column simultaneously, this ensures that the separation achieved in the first column is maintained. The ability of GC x GC to retain the separation achieved in the first-dimension during secondary separation, and subjecting the

complete initial sample to both columns, is the reason why GC x GC is called a fully comprehensive multidimensional separation technique.[99]

At the outlet of the secondary column, the effluent enters a detector which records a continuous linear signal, which consists of a series of second-dimension chromatograms eluting from the second column. The time taken for secondary separation in much shorter than that for primary separation, resulting in rapid succession of elution from the secondary column.[99]

A one-dimensional gas chromatogram produces a two-dimensional plot of signal intensity in relation to retention time. GC x GC chromatogram is a three-dimensional plot which shows the retention times of the two columns and the signal intensity. The detector at the exit of second column produces a linear signal with series of second dimension chromatograms. Based on the modulation time (time step between injection of consecutive primary effluent fractions into the secondary column), the linear chromatogram is transformed into a three-dimensional representation, as shown in Figure 4.11. The final representation is a contour plot with retention times from the two columns in the X-axis and the Y-axis, while the signal intensity is represented as contours or contour lines, usually viewed from the top. Transformation of the linear signal into a contour plot is generally performed by a computer software. The contour plot can also be viewed as a 3D plot using the software.[99,100]

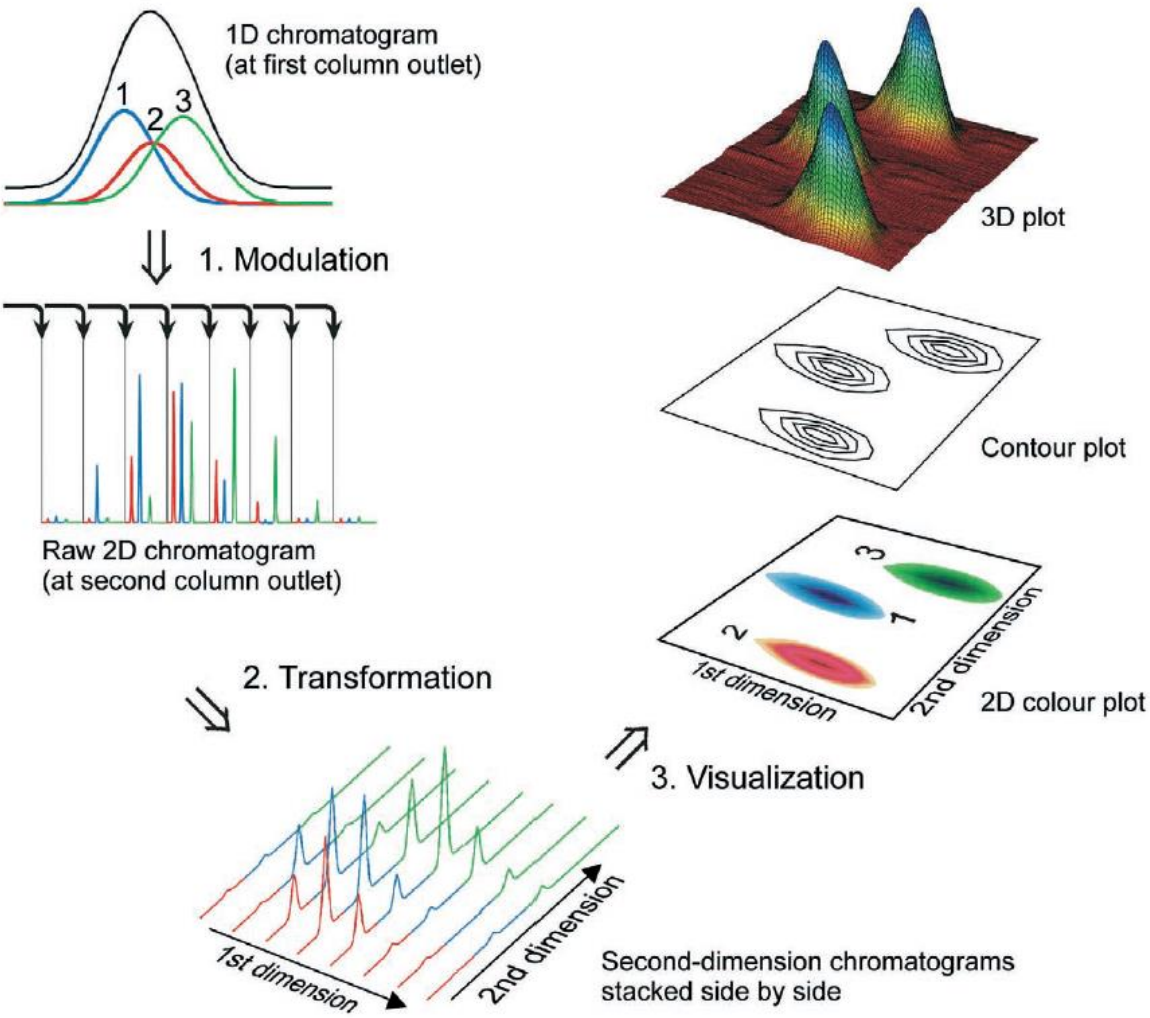

Figure 4.11 GC x GC transformation of continuous linear signal from the detector into a contour plot and a three-dimensional[100].

4.6.1 GC x GC Sample Preparation and Analysis

Diesel fuel samples of Fuels 1-5, collected from the rig during cavitation tests, were subjected to GC x GC analysis to identify the different hydrocarbon classes, i.e. paraffins, aromatics, FAME and residuals. Pre- and post- cavitation samples were tested to identify the changes in composition of the fuels arising from cavitation induced effects.

GC x GC analysis of the fuel samples reported here was carried out at Shell Global Solutions laboratory, using their equipment. The fuel samples were collected, and prepared for shipping to the laboratory by the principal research student. Approximately 5 mL of the fuel samples,

initially drawn for the purpose of uv-visible spectra and particle count measurements, were poured into clean glass vials. Each sample was poured with a new disposable pipette to prevent contamination. The vials were then securely packed to be delivered to Shell laboratory. The GC x GC results were obtained and compiled by scientists at Shell facilities, and were sent back to City, University of London for further processing and manipulation.

Chapter 5
High Pressure Cavitation Tests for Five Fuels

5.1 High Pressure Cavitation Experiments and the Spectral Attenuation Coefficient Measurements

As discussed in the previous sections, cavitation has been linked to the formation of 'hot-spots' of extreme conditions. Subjecting diesel fuel to such conditions inside diesel FIE can initiate pyrolytic reactions. Pyrolysis of diesel fuel components are known to result in formation and growth of carbonaceous soot-like particles. Indication of pyrolytic reactions occurring in the fuel can thus be obtained by analysing the changing composition of cavitated fuels and identifying soot-precursor particles. An indication of soot pre-cursor particle formations can be obtained from the changing spectral properties of the fuel.

Some organic molecules, such as the ones found in diesel fuels, absorb different wavelengths of visible light and ultraviolet radiation to give fuels their colour. These compounds are able to do so owing to the presence of special groups of atoms and electrons (or moieties) called chromophores. A chromophore is a region or functional group in a molecule where the energy difference between two molecular orbitals falls in the visible-light or near ultraviolet spectrum[101,102].

The absorption of radiation by orbitals in the visible-light and ultraviolet regions is called energy transition; this results in promotion of electrons in the σ, π and n-orbitals from ground state to higher energy states.

Absorbance of visible-light and/or ultraviolet radiation by a medium is dependent on the concentration of its chromophoric content. According to the Beer-Lambert law the absorbance (A) of a medium at a given wavelength, λ, is given by the following relation[103]

$$A(\lambda) = \varepsilon(\lambda) l c \qquad \textbf{5.1}$$

Where $\varepsilon(\lambda)$ is the molar absorption coefficient, l is the path length of the radiation in the medium and c is the molar concentration of the absorbing moieties. The relation indicates that for a given moiety (chromophoric molecule) the absorption is directly proportional to its concentration in the medium. Therefore, a change in the concentration of diesel fuel chromophores would result in a proportional change in its spectral absorbance or the spectral absorption coefficient, indicating a change in its chemical composition.

The hydrodynamic cavitation tests involved recirculating a diesel test fuel in the high-pressure cavitation test-rig. An optical diagnostics setup - described in earlier sections – was used to measure 15-second averaged in-situ laser transmission and reference signals during the cavitation tests. For each fuel, the 15-second averaged laser transmission and reference signals were converted to 15-minute averages. The 15-minute averaged continuous transmission signal was then normalised using the synchronous 15-minute averaged reference signal to eliminate the effect of variations in the laser module's performance.

The fuel's transmission was found to be greatly influenced by its temperature. This was observed from the sharp increases in transmission at the beginning of each test day when the fuel warmed up from the ambient temperature to the pre-injection control temperature of 55 °C. The temperature dependence also induced a cyclic pattern in the 15-second averaged raw transmission signal, corresponding to the cooling cycle of the temperature control system. An example of this effect is demonstrated by the solid-line signal in Figure 5.1. As observed from

the graph, each cooling cycle lasted between 2-3 minutes. Maximum oscillations in the laser signal due to fuel heating and cooling were approximately ± 0.03 mW.

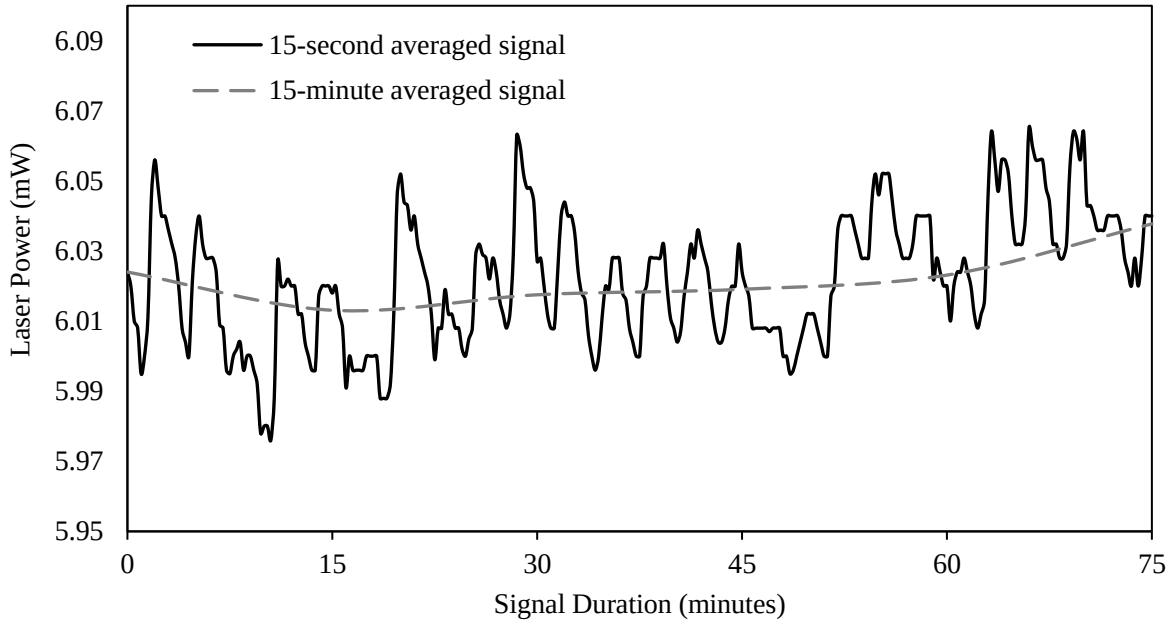

Figure 5.1 Comparison of 15-second averaged raw transmission data with 15-minute averaged correction

However, the cycle period and maximum oscillations in power were subject to variations based on the rate of temperature change of the fuel, which in turn was dependent on the cooling-water supply temperature and pressure, and test-cell air temperatures. To remove the effect of cooling cycle resulting from the normal operation of the temperature control system (i.e. the cooling water supply and heat exchanger) the transmission signal was averaged every 15 minutes. The effects of air temperature and variations in cooling water supply (temperature and pressure) were random and could not be eliminated from the data. The outcome of converting the 15-second averaged transmission signal to 15-minute averaged signal can be seen in the comparison of a recorded data samples shown in Figure 5.1.

Table 5.1 Five commercial fuels tested in the fuel composition investigation

Fuel 1 (BDN)	New Conventional Base Diesel
Fuel 2 (B10)	B10 – Fuel 1 (BDN) with 10 % RME
Fuel 3 (B30)	B30 – Fuel 1 (BDN) with 30 % RME
Fuel 4 (BD+H)	Fuel 1 (BDN) with 10 % Hexadecane
Fuel 5 (BD+MN)	Fuel 1 (BDN) with 10 % 1-Methylnaphthalene

5.2 Fuel Dependence Tests

The fuel dependence tests involved testing of Fuels 1 to 5 at an injection pressure of 1,650 bar for 40 hours each, over a span of 4 days (10 hours per day). The aim of fuel tests was to compare the effect of fuel composition on their behaviour when subjected to high-pressure recirculating cavitating flow. The general composition of the five fuels tested here are included in Table 5.1. Fuel 1 (BDN) was a conventional diesel fuel, while Fuels 2 - 5 were blends of Fuel 1 (BDN) with other components added in the specified proportions. Fuel 1 (BDN) had a composition by weight of 38 % paraffins, 37 % naphthenes, 20 % mono-aromatics, 4.5 % di-aromatics, and less than 0.5 % tri- and poly-aromatics. Each of the five fuels in this investigation was cavitated through a separate injector nozzle with a nominal hole diameter of 174 µm. The experiments were then repeated with a new charge of each fuel, using the same fuel-specific injector nozzle. The control variables for all fuel tests and their repeats are shown in Table 5.2.

Table 5.2 Control variables for the fuel tests

Injection Pressure	1,650 bar
Test Duration	40 hours
Receiver Pressure	1 bar
Pre-Injection Fuel Temperature	55 °C
Filter Type and Size	3 µm Nylon Filter

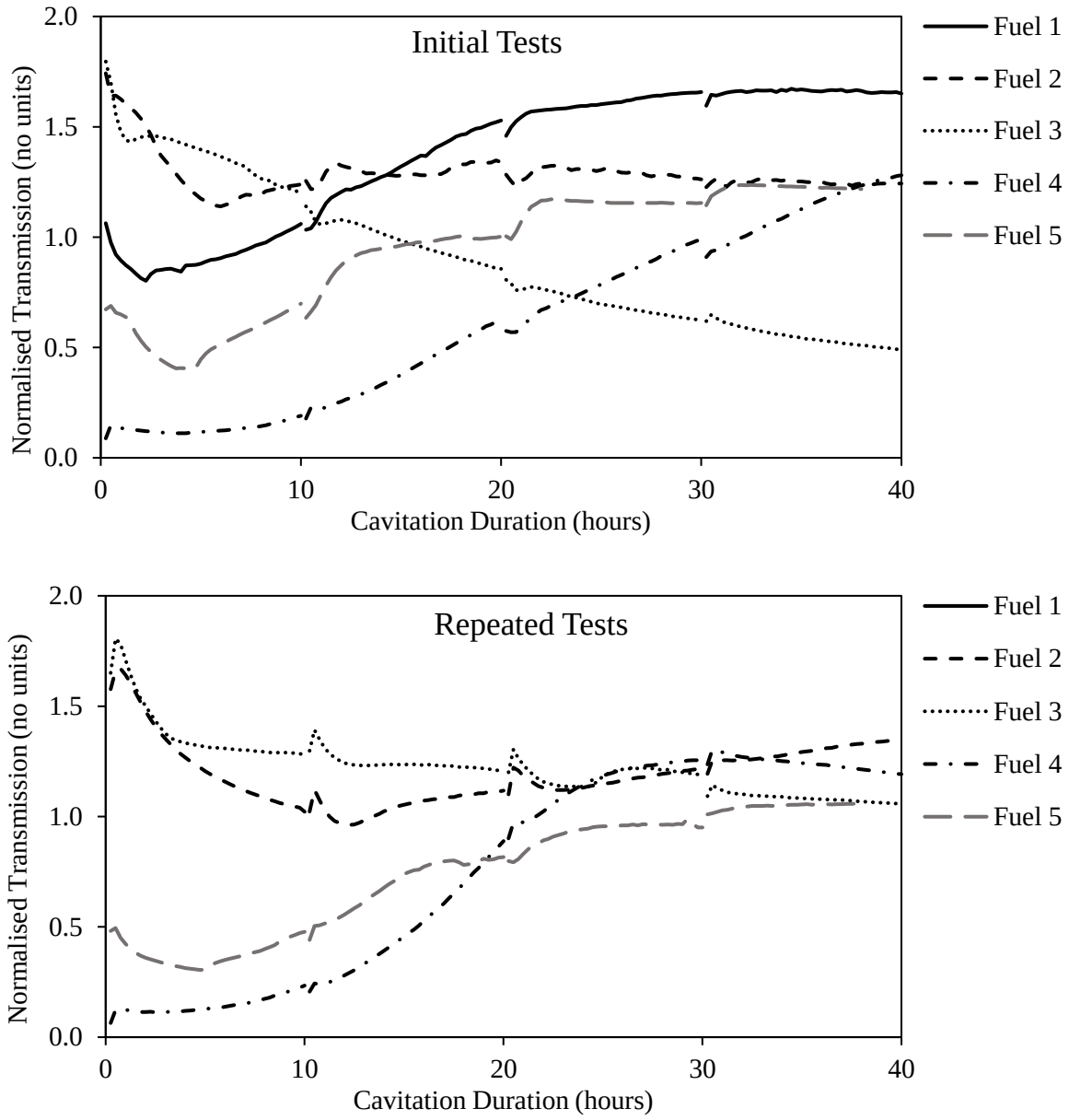

Figure 5.2 Normalised laser transmission at 405 nm against cavitation time for initial (top) and repeated tests on Fuels 1 to 5

Figure 5.2 shows the variations in normalised spectral transmission at 405 nm with cavitation time for the two repeated tests on the five fuels when their samples were subjected to cavitating flows at 1,650 bar for 40 hours. In the initial test, Fuel 1 (BDN) had a pre-cavitation (zero-hour) normalised transmission signal of ~ 1.06, that sharply decreased to a minimum of ~ 0.80 by the 2.25 hour-mark on the first day of testing. The transmission coefficient then gradually

increased till a plateau was reached at the beginning of the final day of testing (at ~ 32 hour-mark), the normalised transmission value at this plateau was ~ 1.66.

During the repeat of Fuel 1 (BDN) test, the pattern of initial decrease, followed by a gentler increase up to an equilibrium value seen in the initial test was observed again. In the repeated test, the pre-cavitation normalised transmission value for Fuel 1 (BDN) was ~ 1.13. The value then decreased to a minimum of ~ 0.67 by the 8 hour-mark; followed by a comparatively gentler rise to a maximum equilibrium value of 1.42 after 35 hours of cavitating flow.

Both biodiesel blends (Fuel 2 (B10) and Fuel 3 (B30)) had a similar initial normalised transmission values of ~ 1.75 ± 0.5 and ~ 1.60 ± 0.05 in the initial and repeated tests, respectively. These values were found to be the highest pre-cavitation normalised transmission values of all five test fuels in their respective test sets. Transmission coefficients of both biodiesel fuels decreased as the fuel underwent recirculating cavitating flow.

In the initial test both fuels experienced a sharp decrease in transmission coefficients. Fuel 2 (B10) reached a minimum transmission value (of ~ 1.14) at approximately 6 hour-mark, followed by a gradual increase to an apparent equilibrium value of ~ 1.26 ± 0.04 after ~ 16 hours of cavitation test, with small fluctuations occurring till the end of the 40-hour test. For Fuel 3 (B30) the sharp initial decrease was followed by a sudden deceleration in the drop at ~ 1.5 hour-mark, beyond this point the transmission coefficient continued to drop at a constant, gentler rate till the end of the 40-hour test, where its final normalised transmission value was ~ 0.49.

In the repeated experiments, the rate of decrease for both biodiesel blends was similar up to the ~ 3 hour-mark, thereafter the decrease in transmission coefficient of Fuel 3 (B30) decelerated sharply to reach a gentler constant gradient, which continued for the remainder of the 40-hour test to reach a final normalised transmission value of ~ 1.06. The transmission coefficient of

Fuel 2 (B10) on the other hand, decreased asymptotically to reach a minimum normalised transmission value of ~ 0.96 around 12.5 hour-mark, beyond this the transmission coefficient gradually increased till the end of the experiment, reaching a final normalised transmission value of ~ 1.35 (40 hours).

Fuel 4 (BD+H) had the lowest pre-cavitation (zero-hour) normalised transmission signal of all five fuels in both sets of experiments (~ 0.09 and ~ 0.06 respectively). This was contradictory to the prior knowledge of paraffins, which suggested that a lack of conjugated pi-bond systems renders paraffins devoid of chromophores, and thus of colour resultant from radiation absorbance in the visible and near-ultraviolet regions. According to this understanding of chromophores, added volumes of hexadecane was expected to increase the spectral transmission coefficient of Fuel 1 (BDN) at 405 nm wavelength rather than decreasing it, as observed in the fuel experiments.

In the two repeated experiments of Fuel 4 (BD+H), the normalised spectral transmission value increased from the minimum starting values with a constant gradient. In the initial experiment, the normalised transmission coefficient continued to rise through the duration of the test and reached a final value of ~ 1.28 (after 40 hours). In the repeated experiment, the transmission coefficient reached a maximum value (~ 1.23) after 30 hours of recirculation flow, this was proceeded by a gradual decrease till the end of the 40-hour test; the final normalised transmission value at the completion was ~ 1.19.

Fuel 5 (BD+MN) showed similar behaviour in the two repeated experiments over the 40-hour durations. At the beginning of the initial and repeated tests, the fuel samples started with a normalised spectral transmission value of ~ 0.67 and ~ 0.50, respectively. The transmission coefficients then decreased to their respective minimum values of ~ 0.40 (after 4.5 hours) and ~ 0.31 (after 4.75 hours), followed by an increasingly gradual rise till the end of the

experiments. At the end of the first test, the normalised transmission value of Fuel 5 (BD+MN) was ~ 1.22, and for the repeated test the value reached ~ 1.06.

The spectral transmission ($I_P(t)$) and reference signals ($I_{ref}(t)$) at 405 nm were processed to calculate the time-dependent spectral attenuation coefficients $\alpha(t)$ for the five fuels. Equation 5.2 shows the relation used to calculate the spectral attenuation coefficient from the measurements taken using the in-situ optical setup.

$$\alpha(t) = \frac{\ln \frac{t_{fs}^2 (1 - r_f) I_{ref}(t)}{r_f I_P(t)}}{l} \qquad 5.2$$

In the equation t_{fs}^2, r_f and l represent the combined transmission coefficients for the two fused-silica optical windows, the reflectivity of the neutral density filter and the optical path length through the test fuel sample, respectively. The derivation of the above relation has been previously detailed in Chapter 4.2.

The variations in the spectral attenuation coefficients of the five fuels with cavitation time for the two repeated experiments are shown in Figure 5.3. Comparison of the variations in the spectral attenuation coefficient of Fuel 1 (BDN) in the two tests showed an increase to a maximum, followed by a decrease to an equilibrium value by the end of the tests. The pattern of variations was the same, albeit the rate of change in attenuation were different. Initial test attained maximum attenuation after 2.25 hours of cavitation whereas the repeated test attained it after 7.25 hours of cavitation. The delay was also observed in the time taken to reach the equilibrium value for the repeated test.

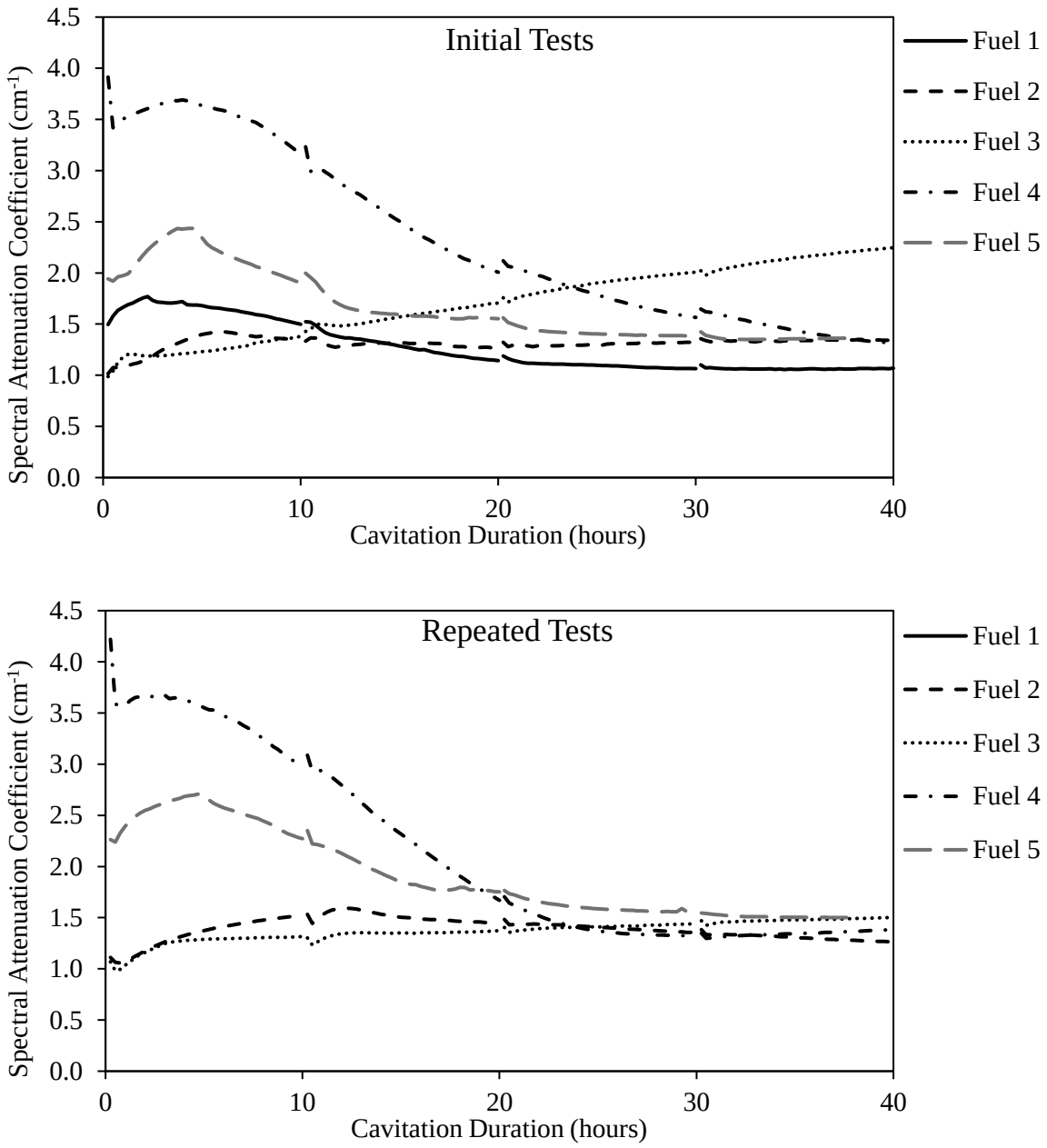

Figure 5.3 Time-dependent spectral attenuation coefficient at 405 nm against cavitation time for initial (top) and repeated tests on Fuels 1 to 5

Comparison of the other fuel tests (Fuels 2 to 5) with their repeated counterparts, indicated a pattern of delayed variations in the spectral attenuation coefficients of the latter. The extent of delay was greater for some fuels such as Fuel 3 (B30). Fuel 3 (B30) experienced a consistent increase in attenuation in both tests, however the gradient of increase in the repeated test was significantly smaller.

Observation of the delayed pattern was suggested to be linked to the conditioning of the injector nozzles. It was believed that the test injector nozzles were getting conditioned during the high-pressure cavitation tests, with their propensity to form cavitating flow getting reduced due to the conditioning.

Each fuel was tested with a separate nozzle; this nozzle was then reused for the repeated test for the same fuel. The nozzles were unused prior to the fuel tests and had an initial honing value of ~ 13 %. The low levels of nozzle honing suggest that their nozzle-hole inlets had sharp edges and the flow passages had rough surfaces, inherent from their manufacturing processes. Nozzles with low levels of honing have been shown to cause greater geometric cavitation, resulting from the larger shear-stress and pressure-gradient formation at the sharper edges of the nozzle-hole inlets. Comparatively, hydro-grinded nozzles and nozzles with rounded inlet edges have been found to display lower intensities of cavitating flow [43,85].

As the test nozzles were subjected to hydrodynamic cavitating flows, the continuous high-pressure flow through the passages would have hydro-honed or conditioned the nozzles. Conditioned nozzles would then have a lower propensity to form geometric cavitation, and a lower intensity of cavitating flow would occur during the repeated experiments at the same injection pressure. The intensity of cavitating flow referred to in this case is not a function of the intensity of bubble collapse in the fuel receiver, rather it is the amount of cavitation bubbles formed in the nozzles that later undergo collapse inside the receiver. Smaller number of cavitation bubbles (lower intensity of cavitating flow) would result in slower rates of chemical changes occurring in the fuel, thus a slower change in the optical properties of the fuels would also be observed.

The variations in the spectral transmission and subsequently, in the spectral attenuation coefficient of the fuels suggest that hydrodynamic cavitation occurring across the nozzle-hole

and inside the receiver altered the chemical composition of the fuels. Sonochemical reaction have been shown to occur in organic liquids during acoustic cavitation bubble collapse[16,21]. Extrapolating these effects to hydrodynamic cavitation suggests that the observed changes occurring in the optical properties of the fuel were resulting from the cavitation bubble collapse in the receiver during flow stagnation.

Discrete samples of the diesel fuel charges being subjected to the high-pressure cavitating flow were drawn from the test-rig at regular intervals during the cavitation tests. Absorbances at 405 nm of the discrete samples were measured using a uv-visible absorption spectrometer. Discrete sample absorbances corresponding to zero hours, 10 hours, 20 hours, 30 hours and 40 hours of cavitation, for all five fuel tests and their repeats, are presented as a function of cavitation duration in Figure 5.4 - Figure 5.8.

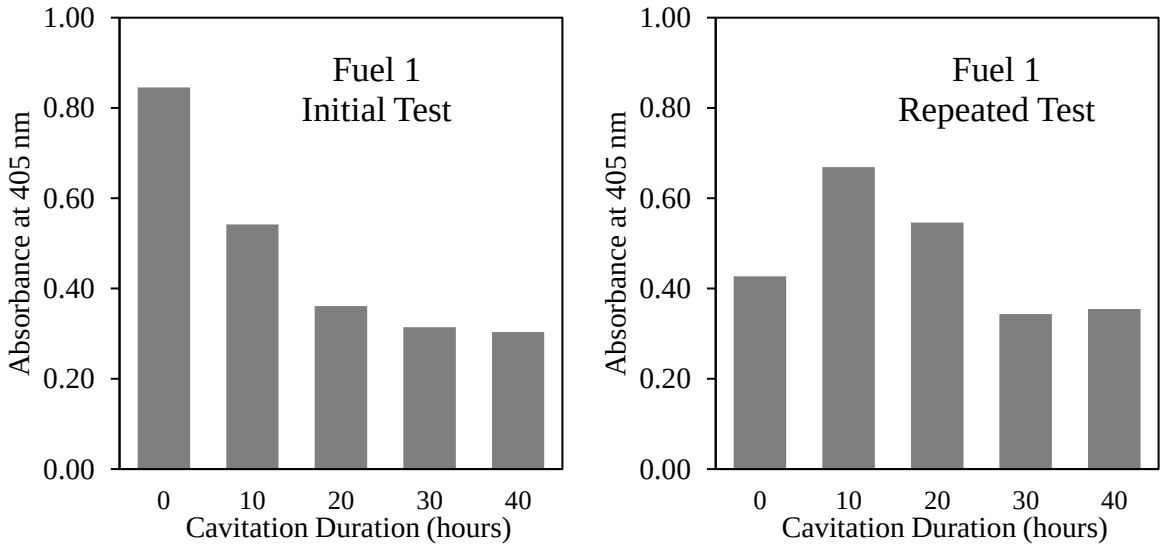

Figure 5.4 Spectral absorbance of Fuel 1 (BDN) samples at 405 nm as a function of cavitation duration for initial (left) and repeated tests

Discrete Fuel 1 (BDN) sample absorbance measurements (at 405 nm) for the initial and repeated cavitation tests are shown in Figure 5.4. For the initial test, the absorbance of the samples was observed to decrease from the zero-hour (pre-cavitation) sample to a minimum

constant value in the 30-hour and 40-hour samples. In the repeated test, the absorbance increased to a maximum value corresponding to the 10-hour sample, following which the absorbance decreased to reach a minimum by 30 hours of cavitation.

The absorbance measurements obtained from the Fuel 1 (BDN) samples of both tests at zero hours, 10 hours, 20 hours, 30 hours and 40 hours were observed to be consistent with the trends seen in the time-dependent spectral attenuation coefficient measurements at 405 nm. It should be noted that the spectral attenuation coefficient measurements were taken when the fuel in the rig was maintained at 55 °C, while the absorbance measurements were conducted on samples kept at ambient laboratory temperature (~20 °C) for maximum 3 days after being drawn from the test-rig.

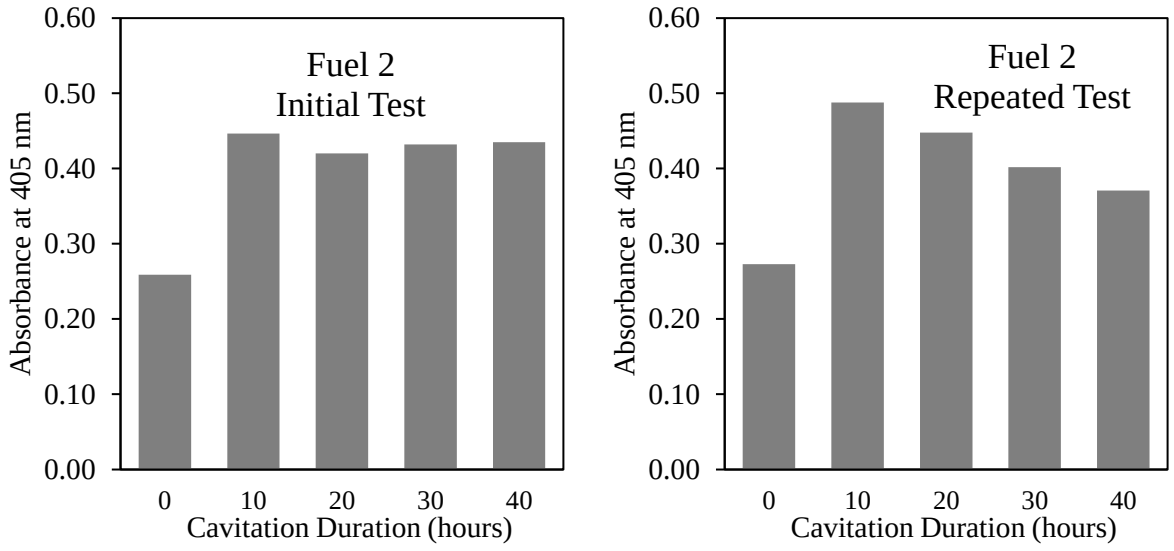

Figure 5.5 Spectral absorbance of Fuel 2 (B10) samples at 405 nm as a function of cavitation duration for initial (left) and repeated tests

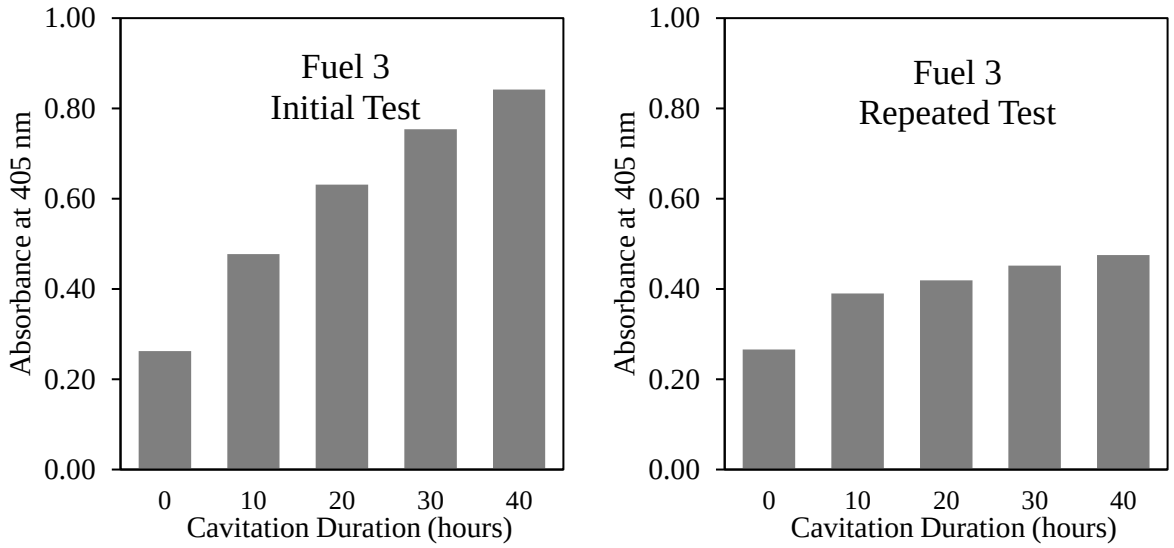

Figure 5.6 Spectral absorbance of Fuel 3 (B30) samples at 405 nm as a function of cavitation duration for initial (left) and repeated tests

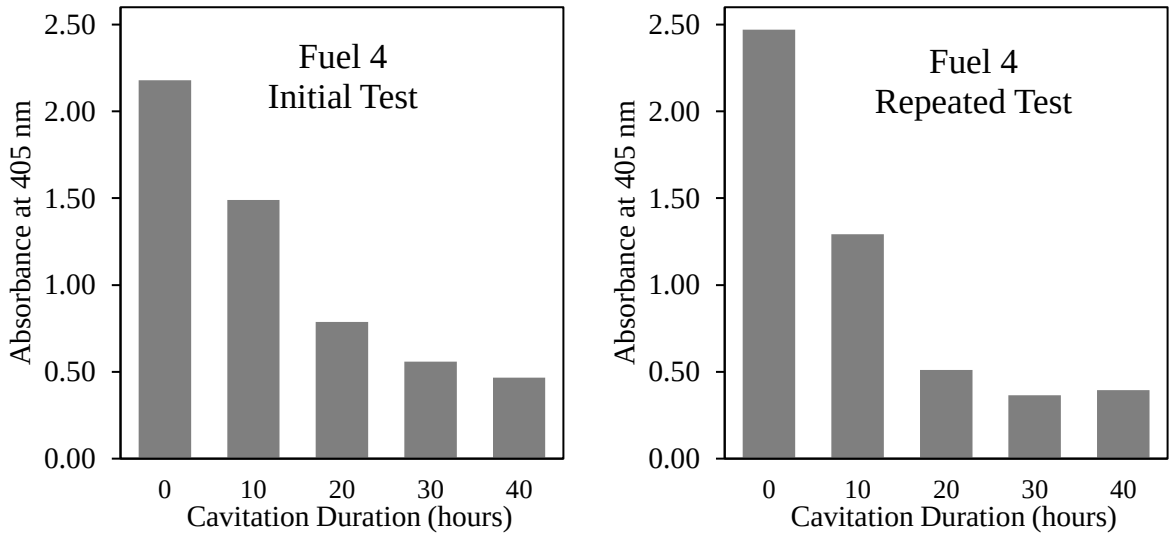

Figure 5.7 Spectral absorbance of Fuel 4 (BD+H) samples at 405 nm as a function of cavitation duration for initial (left) and repeated tests

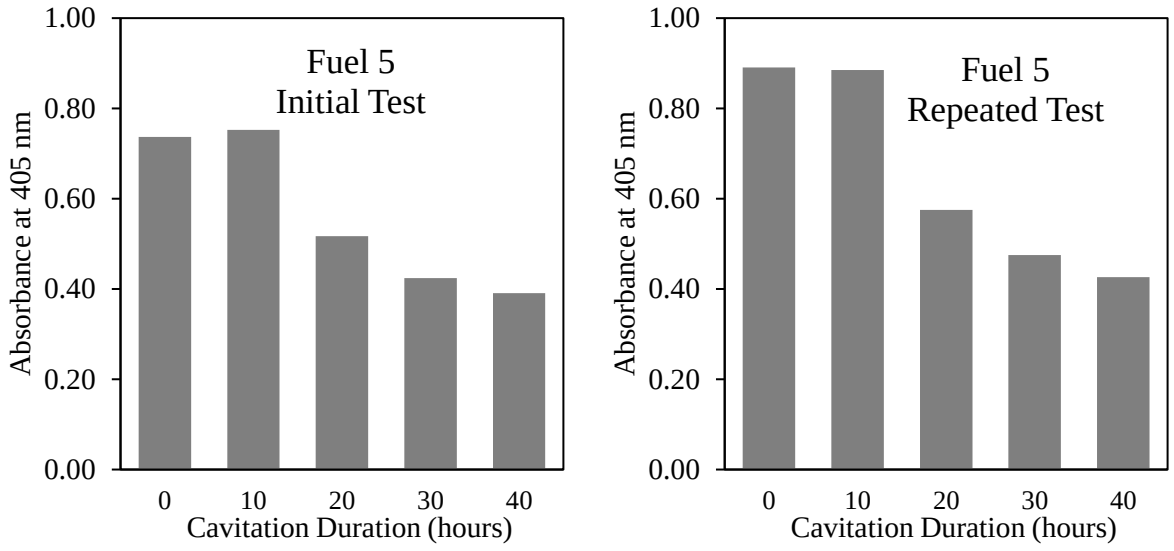

Figure 5.8 Spectral absorbance of Fuel 5 (BD+MN) samples at 405 nm as a function of cavitation duration for initial (left) and repeated tests

The discrete sample spectral absorbances for Fuels 2 to 5 at 405 nm shown in Figure 5.5 - Figure 5.8 all provided an independent confirmation of the trends observed in the time-dependent optical attenuation coefficient measurements of each fuel test, respectively.

The discrete samples used to measure the absorbance at 405 nm were also subjected to spectra measurements on the uv-visible spectrometer. Pure samples of the test fuels were used to obtain spectra measurements in the wavelength range of 350 – 405 nm. Spectra corresponding to the five test fuels from initial and repeated fuel tests are shown in Figure 5.9 and Figure 5.18.

Figure 5.9 shows the spectra measurements for Fuel 1 (BDN) samples collected before and during the cavitation tests. The ‘0 hours’ sample corresponds to the original fuel sample that was drawn from the test-rig following the test-rig filling procedure. The fuel charge was then recirculated in the rig at low-pressures (~ 300 bar) to be filtered through the 3 µm nylon filter for 45 - 60 minutes. At the end of the filtration cycle a ‘0 hours filtered’ fuel sample was drawn for analysis. The remaining fuel charge in the test-rig was then recirculated for the 40 hours of high-pressure (1,650 bar) recirculating cavitating flow. During the 40 hours of cavitation,

samples of the cavitated fuel were drawn at 10-hour intervals (i.e. '10 hours', '20 hours', '30 hours' and '40 hours' samples).

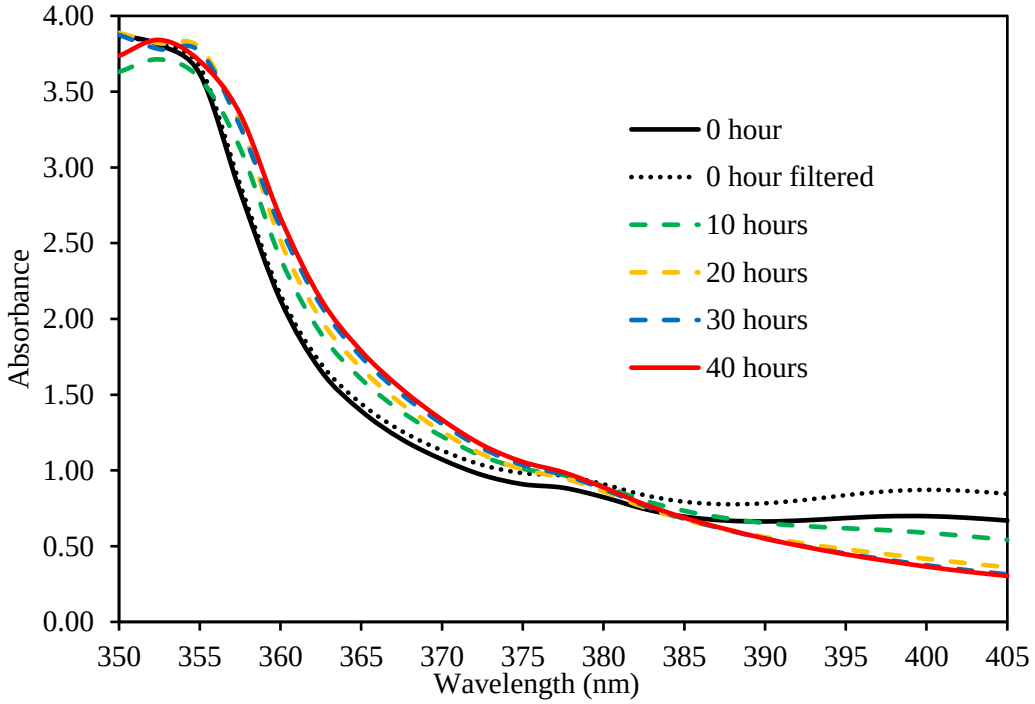

Figure 5.9 Fuel 1 (BDN) discrete sample spectra for pure samples in the 350 – 405 nm range (initial test)

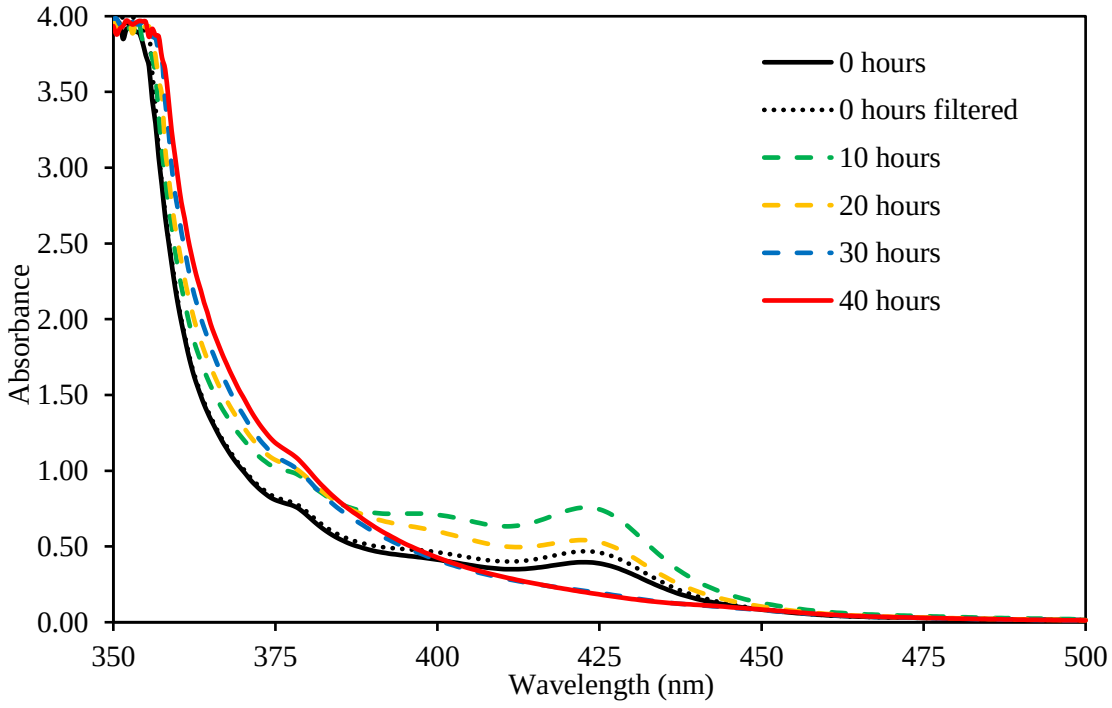

Figure 5.10 Fuel 1 (BDN) discrete sample spectra for pure samples in the 350 – 500 nm range (repeated test)

A non-cavitated Fuel 1 (BDN) sample's absorbance spectrum (Figure 5.9) in the wavelength range of 350 – 405 nm showed high absorbance values at shorter wavelengths, with decreasing absorbance towards higher wavelengths. The spectrum had an absorbance structure peak at ~ 378 nm and another absorbance structure around 405 nm (with a possible peak at ~ 400 nm).

Observing the effect of cavitation on the absorption spectra of Fuel 1 (BDN) showed two effects occurring in the 350 – 405 nm range. The first effect was the broad-band absorbance increase with cavitation time in wavelengths shorter than 375 nm. It is suggested that this broad-band absorbance was caused by the presence of suspended particulates in the fuel charge. An increase in the concentration (or size) of the particulates resulted in an increase in the absorbance of the diesel fuel over the complete range of wavelengths.

The second effect was noticed around 400 nm, where the intensity of an absorbance structure appeared to decrease with cavitation duration. The absorbance of non-cavitated Fuel 1 (BDN) sample was seen to increase after being subjected to the filtration cycle. The absorbance then decreased after 10 hours of cavitation, followed by further decrease after 20 hours and 30 hours of cavitation. After 30 hours of cavitation the absorbance reached a constant minimum, with the 40 hours cavitated sample spectra overlapping the 30 hours sample spectra, around the 400 nm region.

It is suggested that poly-aromatic hydrocarbons (PAHs) of three, four or even non-linear isomers of five ring-structures fused together (e.g. anthracene, phenanthrene, naphthacene, chrysene, pentaphene etc.) have peak absorbances in the wavelength range of 380 – 500 nm. These absorbances are said to be caused by low-energy transitions of $\pi \rightarrow \pi^*$ orbitals in the benzene molecules[101]. The absorbance structure observed in the 425 nm region of the spectra was believed to be a composite of the three, four or five ring PAHs. Decrease in absorbance

intensity of consecutive cavitation samples in Figure 5.9 suggested a decrease in concentration of the said PAHs as a consequence of cavitation.

Fuel samples from the repeated experiments were analysed in an extended wavelength range of 350 – 500 nm. The pattern of change in intensity of the absorbance structure around 400 nm was observed to be different in the case of repeated Fuel 1 (BDN) test shown in Figure 5.10. The pre-cavitation (0-hour) diesel sample had a lower absorbance intensity as compared to the initial test's 0-hour sample. The absorbance intensity of the diesel samples increased as a result of cavitation and appeared to reach a maximum after 10 hours of cavitation, where after the absorbance decreased to reach a constant minimum for the 30-hours and 40-hours samples. The spectra for 30-hours and 40-hours samples were observed to be devoid of the absorbance structure corresponding to the PAHs. The extended spectra measurements of diesel samples revealed the highest absorbance peak at ~ 425 nm wavelength; this peak had the highest absorbance intensity in the absorbance structure and corresponded to the 3 – 5 ring PAHs.

The broad-band absorbance increase, noticed in the initial test for Fuel 1 (BDN), was re-observed for the repeated experiment in the wavelength range below 380 nm, suggesting a gradual build-up of particulate suspension in the diesel sample that was being recirculated in the test-rig.

Figure 5.11 and Figure 5.12 show the absorbance spectra of pure Fuel 2 (B10) samples from the initial and repeated cavitation experiments. In both tests, the pre-cavitation Fuel 2 (B10) samples were observed to have insignificant absorbance structures around the 400 nm range. In the initial test samples, the absorbance at 405 nm appeared to increase to a steady-state maximum value after the first 10 hours of cavitation, with little or no change taking place up to the 40-hours cavitation sample. The repeated-experiment sample spectrum showed the same sharp rise to a maximum value (around 405 nm) in the first 10 hours of the cavitation test; this

was, however, followed by a gradual decrease in absorbance up to the 40-hours sample absorbance.

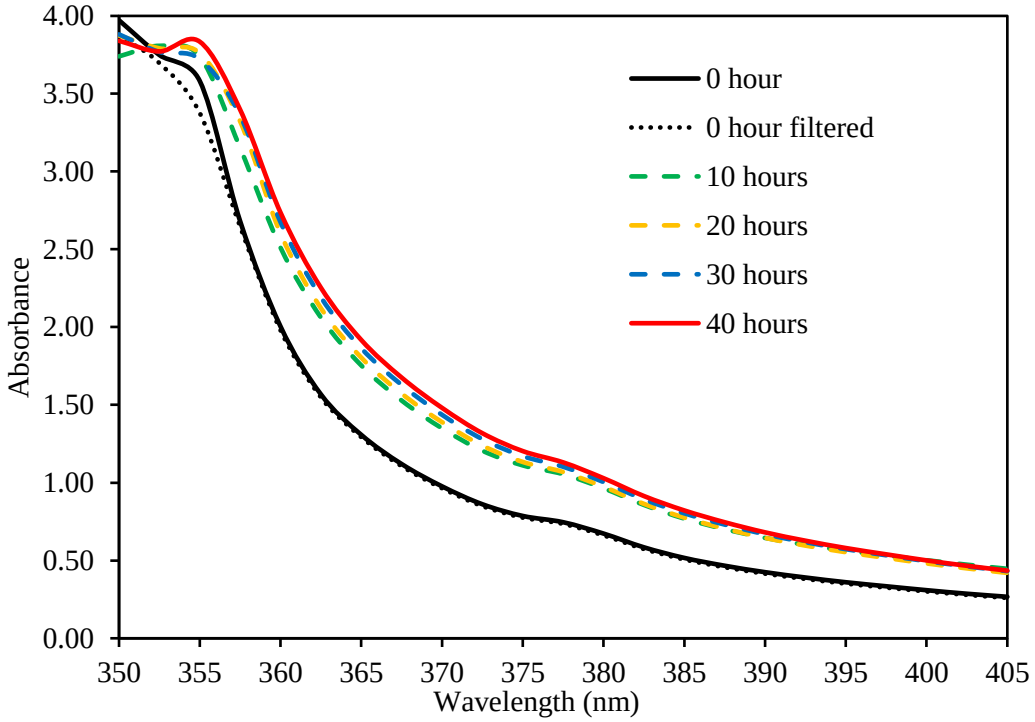

Figure 5.11 Fuel 2 (B10) discrete sample spectra for pure samples in the 350 – 405 nm range (initial test)

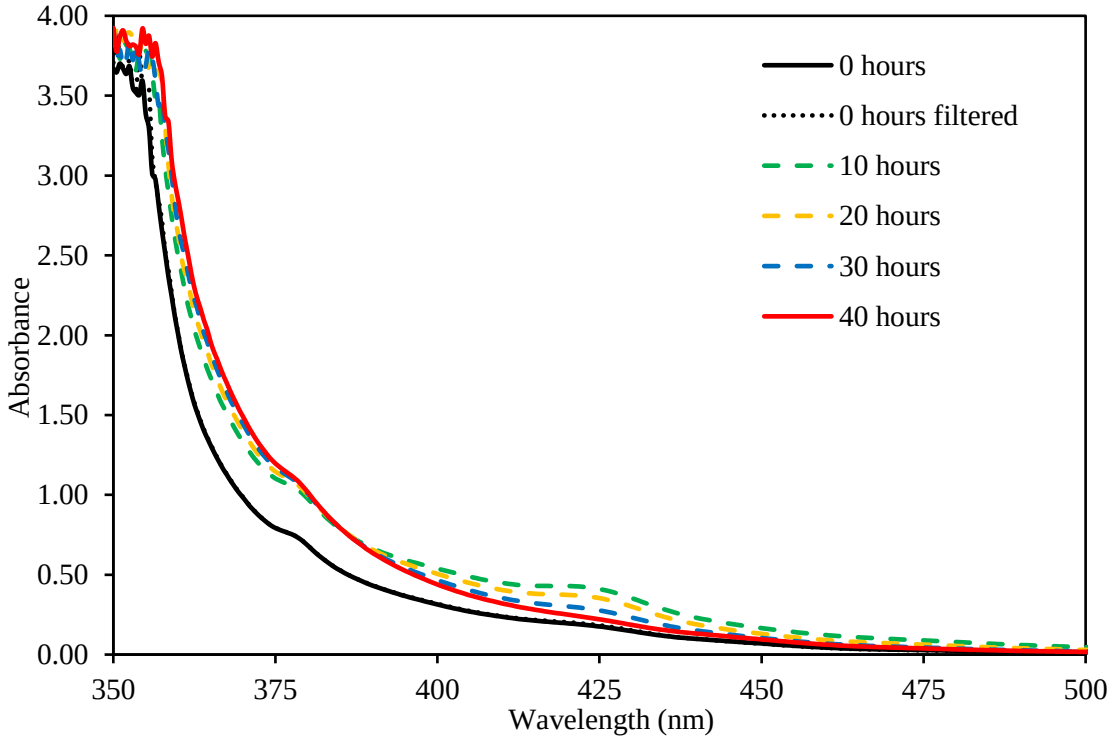

Figure 5.12 Fuel 2 (B10) discrete sample spectra for pure samples in the 350 – 500 nm range (repeated test)

Observing the ~ 425 nm peak in the extended spectra of the repeated-experiment samples (Figure 5.12) showed a small absorbance intensity for pre-cavitation fuel sample; the intensity of absorbance at the peak reached a maximum for 10-hours sample, where after the intensity decreased till the last sample of the test (40-hours). As mentioned earlier, the peak at 425 nm is characteristic of 3 to 5 ring PAHs. The spectrum thus indicated a small initial concentration of the PAHs in the pre-cavitated B10 fuel, the rise in peak absorbance indicated a small increase in concentration of the PAH species followed by their destruction towards the end of the cavitation test.

In both Fuel 2 (B10) tests, a prominent broad-band effect was observed for wavelengths below 375 nm, which is believed to be caused by build-up of particulate suspension in the fuel. It was noticed that the rise in absorption from the suspended particulates was fastest in the first 10 hours of both experiments.

Figure 5.13 and Figure 5.14 show the absorption spectra of the undiluted Fuel 3 (B30) samples from the initial and repeated cavitation experiments. For fuel samples of both tests, the absorption throughout the measurement ranges steadily increased as a function of cavitation time. The rise in absorption was suggested to be the broad-band effect caused by an increase in particulate suspension. The rise in broad-band absorption was the largest during the first 10 hours of both experiments, showing similarities to the behaviour observed for Fuels 1 and 2.

The PAH characteristic absorbance structure with peak at 425 nm was not observed in any sample of the B30 biodiesel fuel. It is suggested that the absence of absorption structures throughout the two spectra was the reason for the extension of the broad-band effect to wavelengths above 375 nm.

The changes observed in the spectral attenuation coefficient and the uv-vis spectra measurements for the two biodiesel blend fuel samples, i.e. Fuel 2 (B10) and Fuel 3 (B30), also

indicate the effect of the breakdown of rapeseed oil methyl esters RME. The hydrodynamic cavitation occurring in the nozzle and the receiver is expected to decompose the RME that would result in formation of species which have varying chromophoric properties. Therefore, the effects of the changing concentrations of such species is expected to be seen in the spectral attenuation coefficient and the uv-vis spectra of the biodiesel fuels.

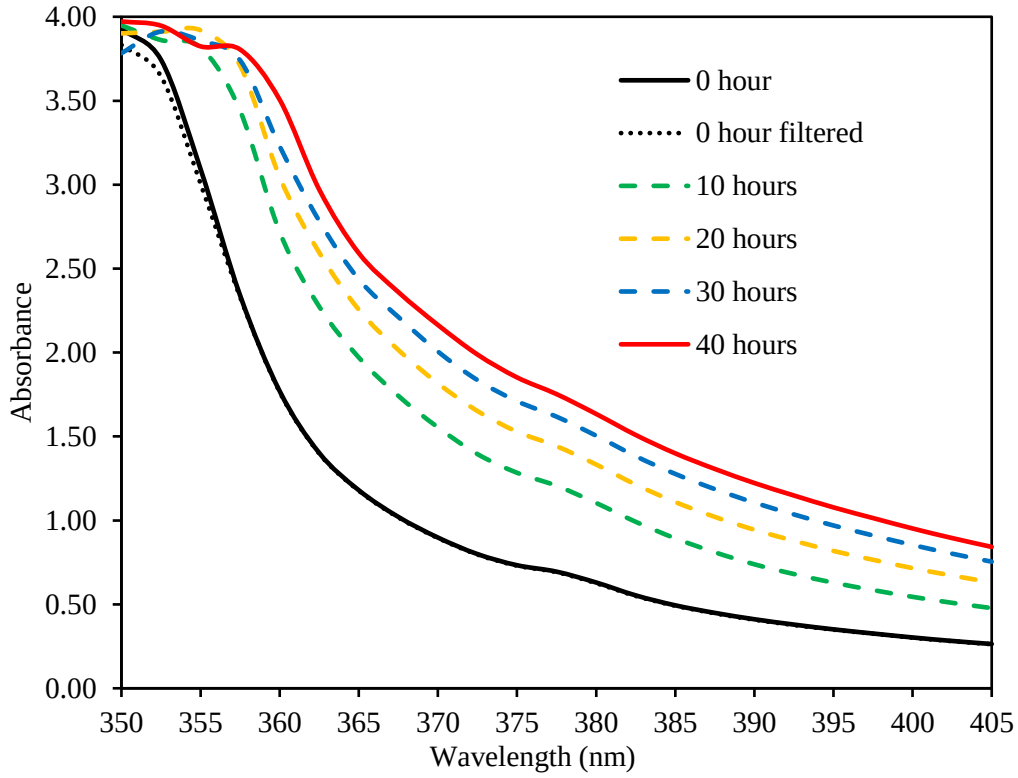

Figure 5.13 Fuel 3 (B30) discrete sample spectra for pure samples in the 350 – 405 nm range (initial test)

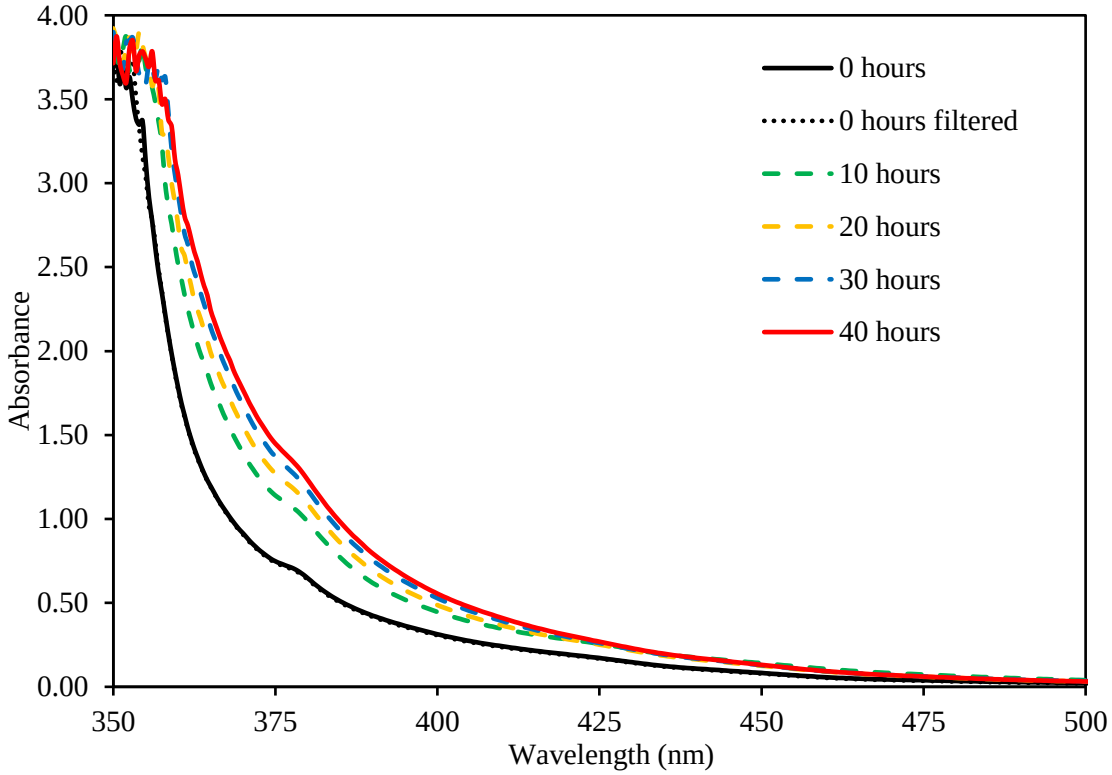

Figure 5.14 Fuel 3 (B30) discrete sample spectra for pure samples in the 350 – 500 nm range (repeated test)

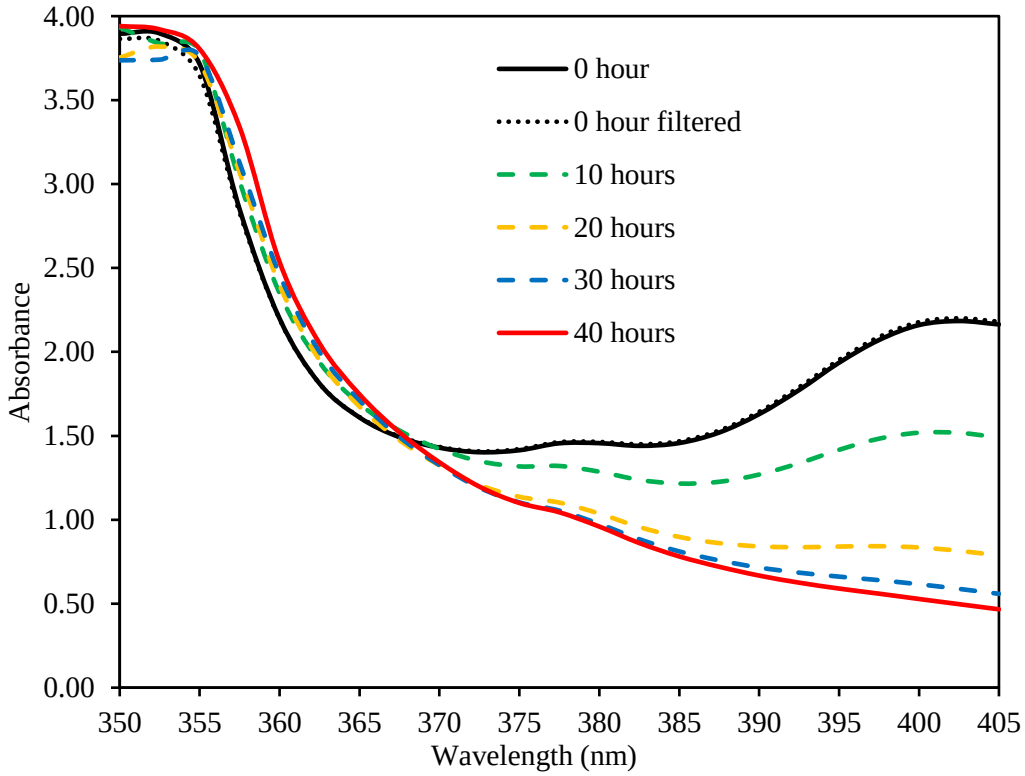

Figure 5.15 Fuel 4 (BD+H) discrete sample spectra for pure samples in the 350 – 405 nm range (initial test)

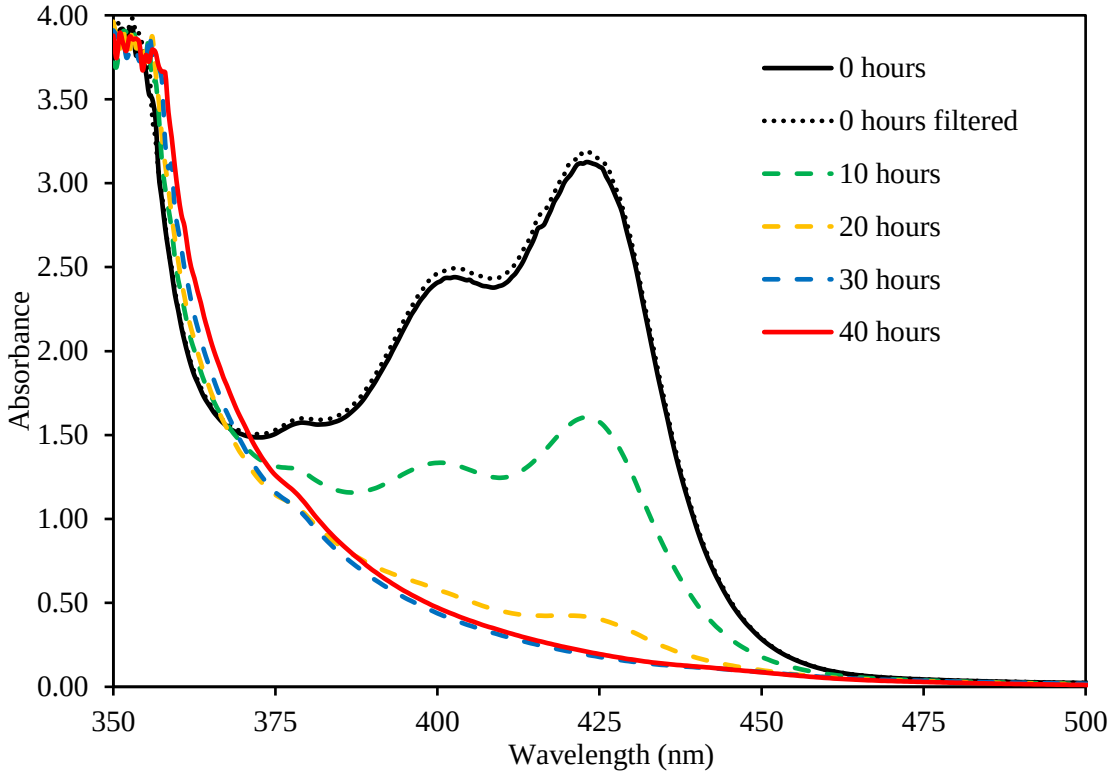

Figure 5.16 Fuel 4 (BD+H) discrete sample spectra for pure samples in the 350 – 500 nm range (repeated test)

Figure 5.15 and Figure 5.16 show the absorption spectra of undiluted Fuel 4 (BD+H) (10 % Hexadecane) samples from the cavitation experiments. In both tests, the pre-cavitation Fuel 4 (BD+H) samples were observed to have a significantly high absorbance values in the 380 – 440 nm range, with the maximum absorbance occurring at the 425 nm peak. During the cavitation tests the absorbance decreased to a minimum, where the absorbance structure appeared to be significantly diminished by the final sample of both tests.

The broad-band effect from particulate build-up was observable in both experimental samples in the wavelengths below 375 nm. The absorbance in the wavelengths below 375 nm appeared to gradually increase over the duration of the cavitation tests.

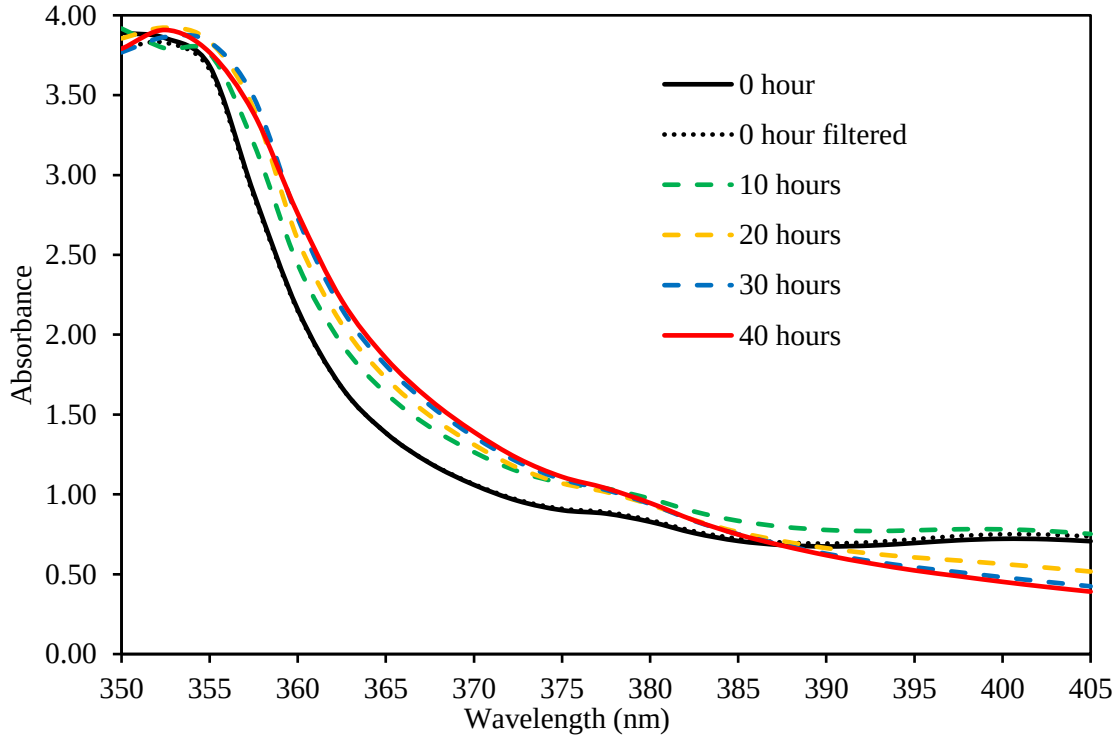

Figure 5.17 Fuel 5 (BD+MN) discrete sample spectra for pure samples in the 350 – 405 nm range (initial test)

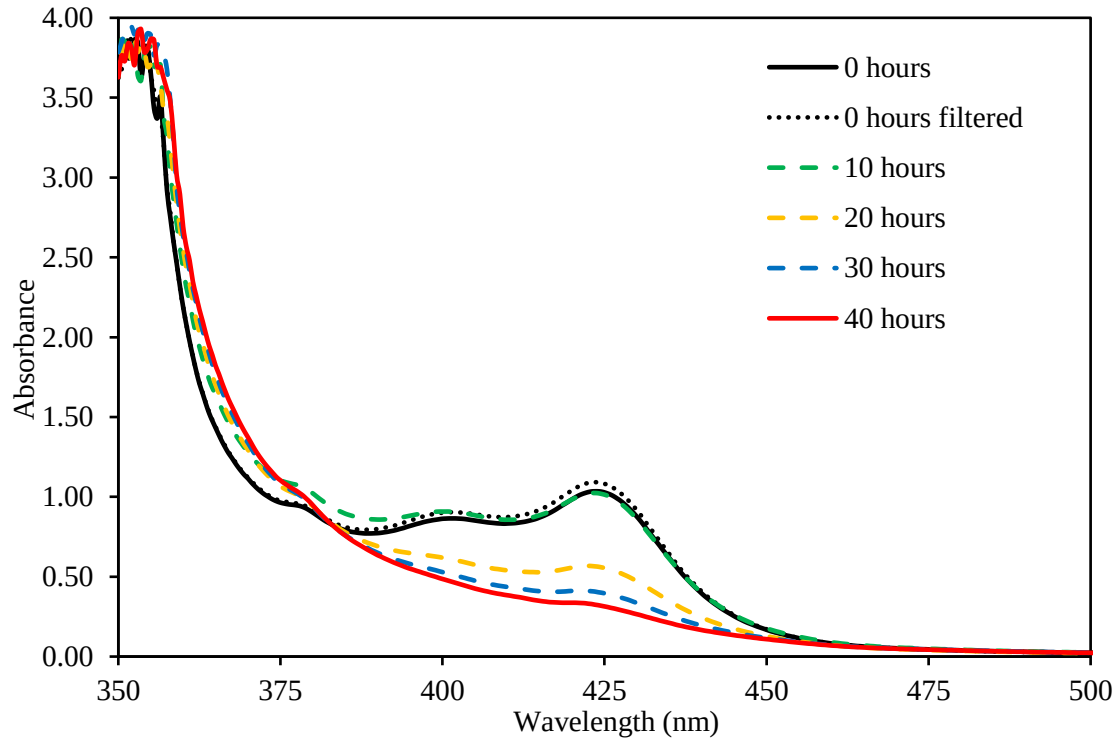

Figure 5.18 Fuel 5 (BD+MN) discrete sample spectra for pure samples in the 350 – 500 nm range (repeated test)

Figure 5.17 and Figure 5.18 show the sample absorbance spectra for Fuel 5 (BD+MN) (10 % 1-Methylnaphthalene) from the initial and repeated cavitation experiments. Pre-cavitation Fuel 5 (BD+MN) samples appeared to show absorbance activity in the 380 – 440 nm range which was diminished due to cavitation during the experiments. However, the process of absorbance decrease in the said wavelength range was not observed going from the 0-hours sample to the 10-hours sample, the absorbances of the two were seen to overlap. A significant drop in absorbance was observed in the following 20-hours samples, followed by progressively smaller decreases in the 30-hours and 40-hours sample absorbances, for both tests.

Below the 375 nm wavelength the sample absorbances show the increasing broad-band absorption trend observed in all previous fuels. Similar to Fuels 1 - 3, the broad-band absorption increase for Fuel 5 (BD+MN) was greatest in the first 10 hours of the experiments.

The discrete diesel fuel samples drawn from the high-pressure test-rig during cavitation experiments were also subjected to spectra measurements in the wavelength range of 240 – 305 nm. The 240 - 305 nm wavelength range is of particular importance due to the absorbance activity of mono-aromatic hydrocarbons in this region. The aromatic absorbance band in this region is called the “benzenoid band” which is characteristic of aromatic hydrocarbons as no similar absorbance structures are found in the spectra of conjugated acyclic polyenes. The benzenoid band corresponds to a low energy $\pi \rightarrow \pi^*$ transition of the benzene ring[101].

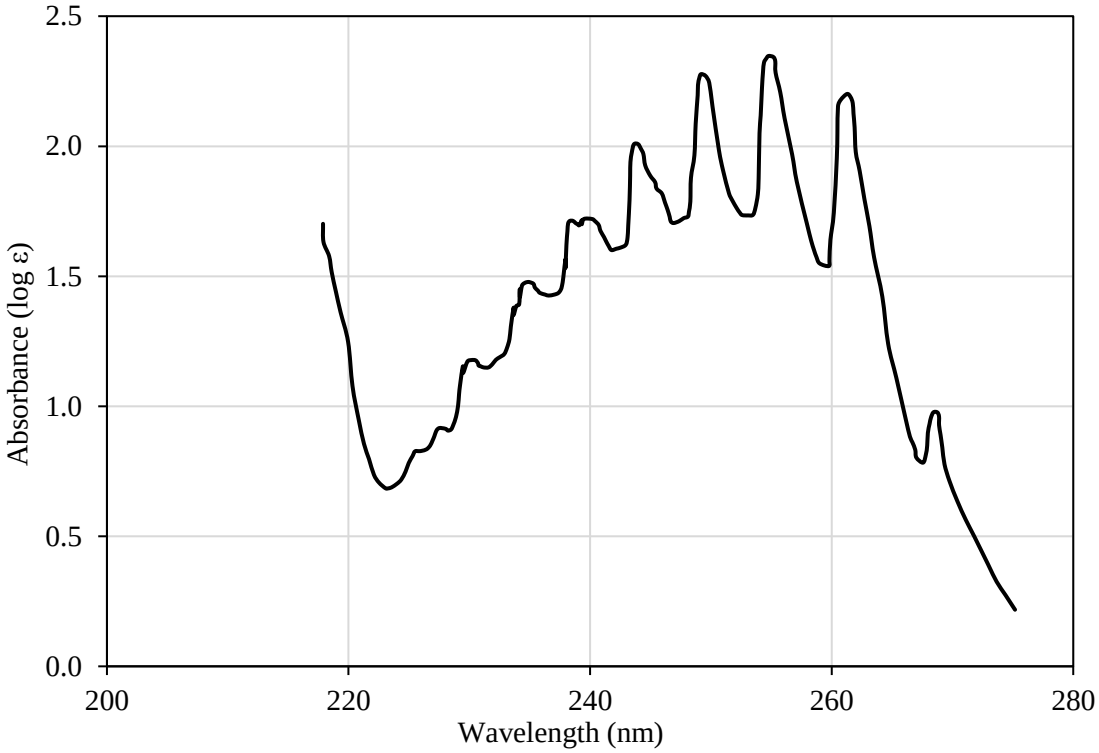

Figure 5.19 Absorbance spectrum of benzene showing the 'benzenoid band' as a series of absorbance peaks in the wavelength range of 220 nm – 270 nm. (adapted from Friedel and Orchin (1951)[104])

The diesel fuel samples were diluted for spectra measurements in the 240 – 305 nm wavelength range. HPLC grade heptane was used as the solvent for dilution of the diesel samples, which were diluted to a dilution ratio factor (DRF) of 520; except for Fuel 5 (BD+MN), which was diluted to DRF 3,000 due to higher absorbance in the range. The dilution methodology has been described in detail in Chapter 4.3.

Figure 5.20 and Figure 5.22 show the spectra measurements in the 240 – 305 nm range for Fuel 1 (BDN) samples from the initial test and the repeated test, respectively. The benzenoid band was observable as a series of peaks in the wavelength range starting from the trough (at 245 nm) up to ~ 280 nm.

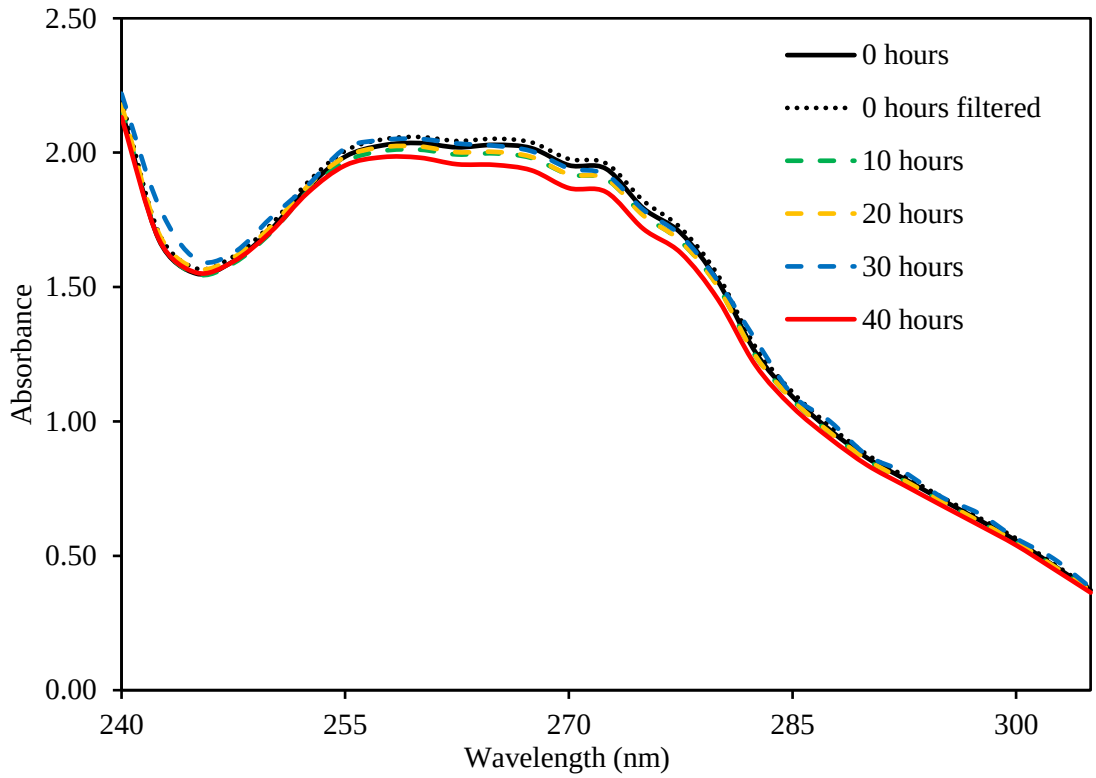

Figure 5.20 Fuel 1 (BDN) discrete sample spectra for DRF 520 diluted samples in the 240 – 305 nm range (initial test)

It was noticed that the benzenoid band in the fuel sample spectra was shifted to longer wavelengths relative to the spectrum of benzene shown in Figure 5.19. The trough observed at 223 nm in benzene spectra was shifted to 245 nm in the diesel sample spectra. It is known that the addition of hydrogen substituents on benzene molecules serves to shift the absorbance band to longer wavelengths. The shift of the trough to 245 nm suggested a presence of naphthenic mono-aromatic hydrocarbons in the fuel samples. An example of a naphthenic mono-aromatic hydrocarbon spectrum is shown in Figure 5.21. Observing the shift of the benzenoid band towards longer wavelengths, it was believed that benzenoid band in the diesel fuel spectra was a composite of alkylated mono-aromatics, naphthenic mono-aromatics and shifted di-aromatic species spectra.

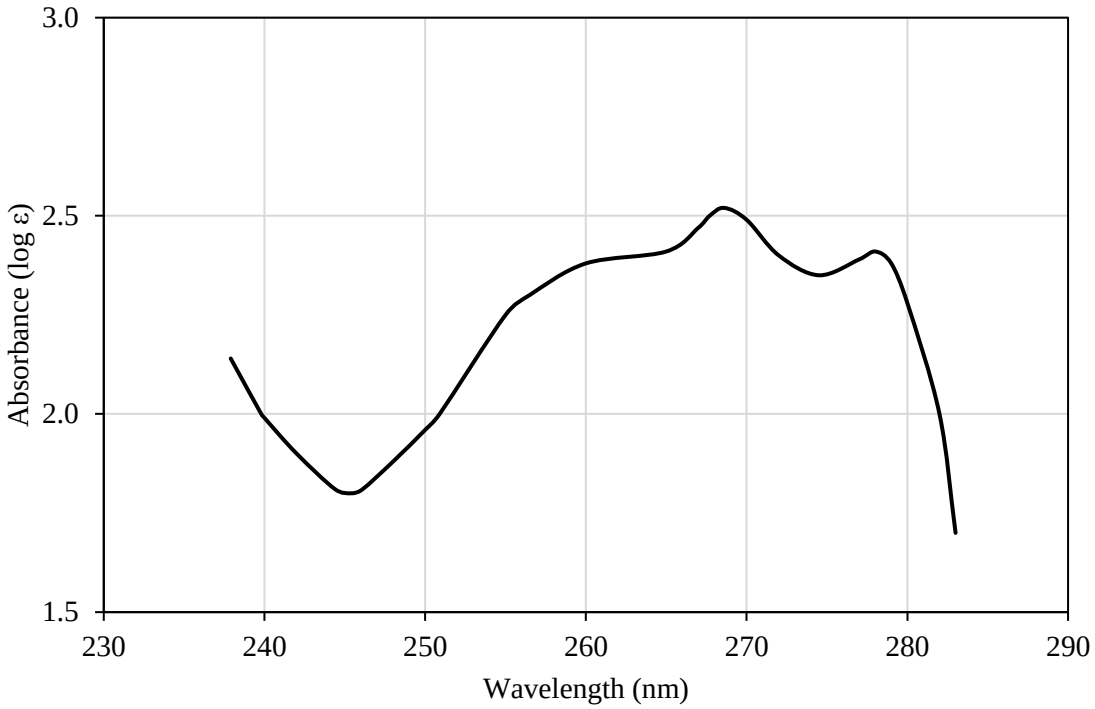

Figure 5.21 Absorbance spectrum showing the 'benzenoid band' of dodecahydrochrysene $C_{18}H_{24}$, a naphthenic mono-aromatic hydrocarbon.

Figure 5.20 shows a gradual decrease in absorbance of Fuel 1 (BDN) samples in the benzenoid band as the cavitation test progressed. The pre-cavitation sample had the highest absorbance, the 10-hours, 20-hours and 30-hours samples had similar absorbances, while the 40-hours sample showed the lowest absorbance in the benzenoid band.

The pattern of gradually decreasing absorbance in the benzenoid band can be made more prominent through normalising the spectra at the 245 nm trough. This is better demonstrated through analysing the spectra in Figure 5.22 and Figure 5.23. Figure 5.23 shows the normalised spectra of Fuel 1 (BDN) repeated test samples. Normalisation was performed by displacing all spectra in order to have same absorbance at the 245 nm trough. Following the normalisation, a clear pattern of progressively decreasing absorbance in the benzenoid band region was observed. The rate of decrease was lowest at the beginning of the experiment and was found to increase as the experiment progressed.

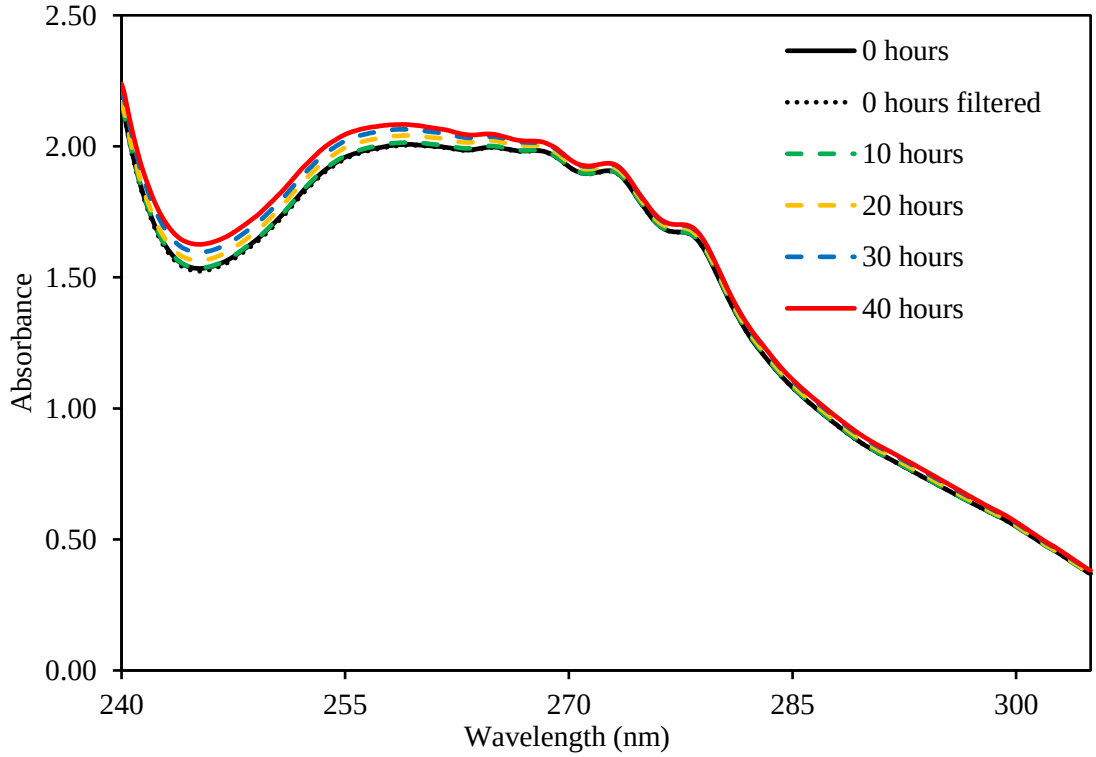

Figure 5.22 Fuel 1 (BDN) discrete sample spectra for DRF 520 diluted samples in the 240 – 305 nm range (repeated test)

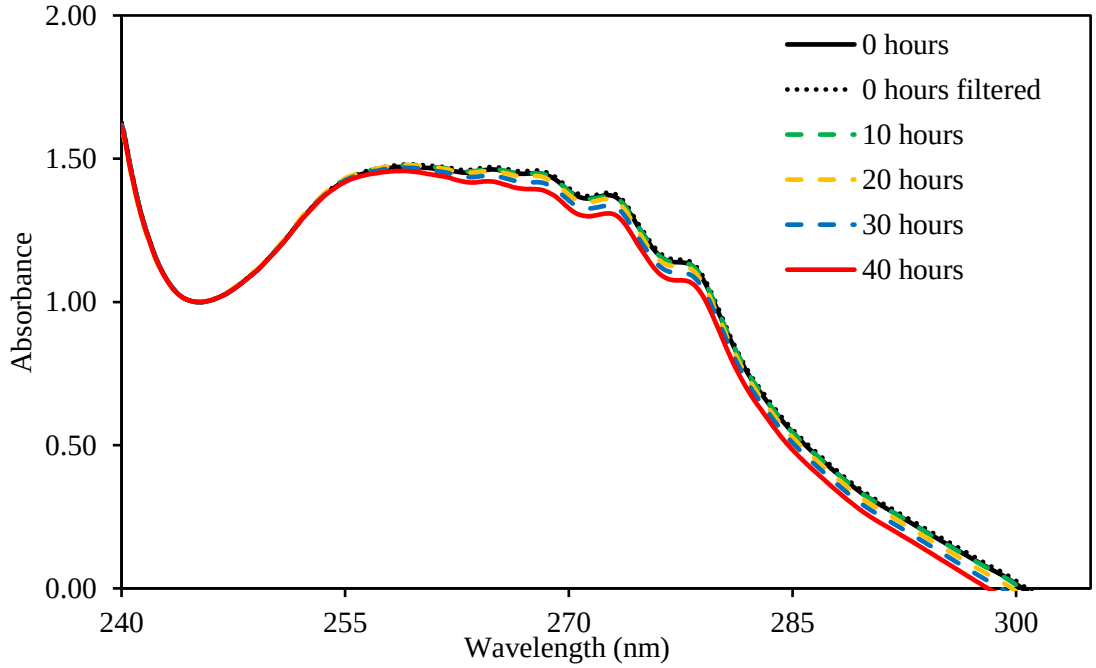

Figure 5.23 Fuel 1 (BDN) repeated test sample spectra normalised at the 245 nm trough to show the 'Benzenoid band'

The increase in absorbance of successive fuel samples around 245 nm wavelength seen in Figure 5.22, shows the same broad-band increase that was previously observed in the spectra at longer wavelengths (in Figure 5.10). The increase in broad-band absorbance was believed to be a result of particulate build-up in the diesel fuel charge being recirculated in the test-rig due to continuous cavitating flow. Normalisation at the 245 nm trough eliminated the broad-band effect to show the change in absorbance in the benzenoid band.

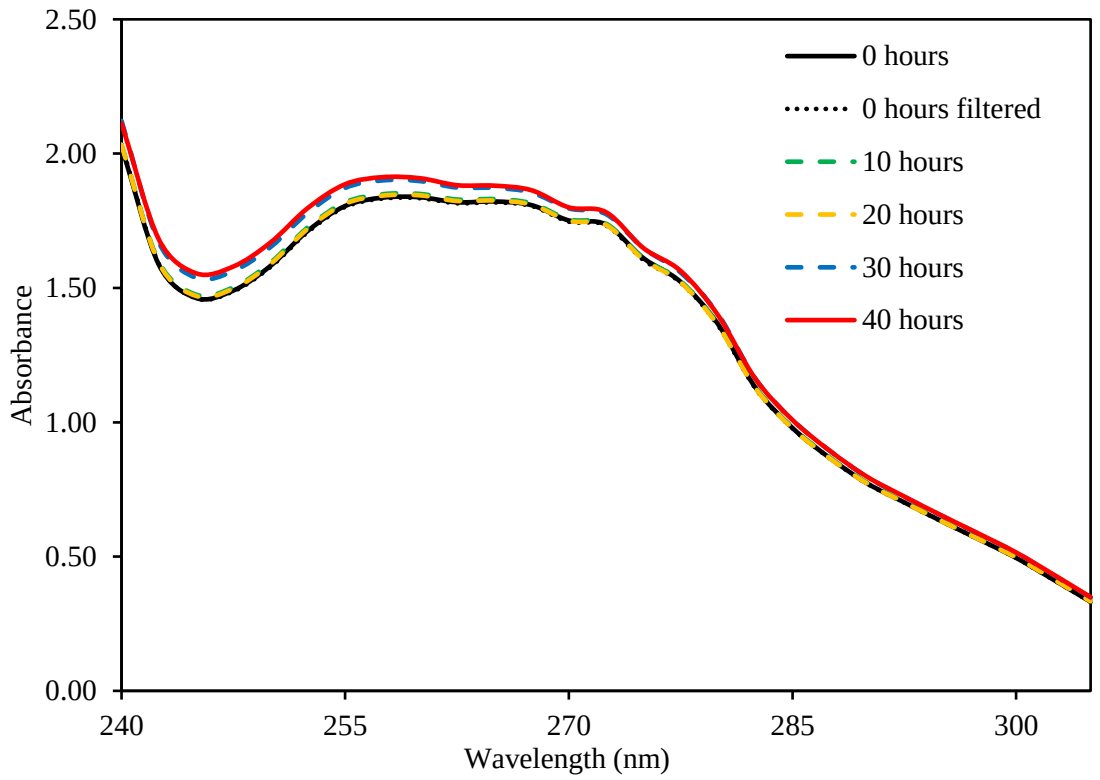

Figure 5.24 Fuel 2 (B10) discrete sample spectra for DRF 520 diluted samples in the 240 – 305 nm range (initial test)

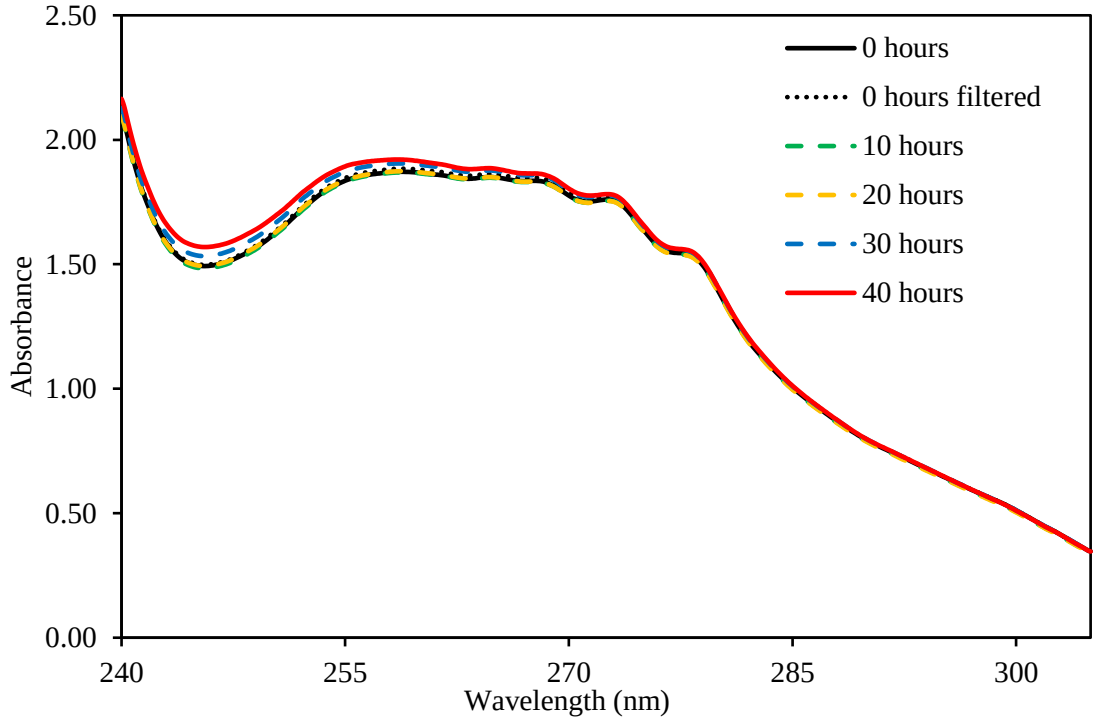

Figure 5.25 Fuel 2 (B10) discrete sample spectra for DRF 520 diluted samples in the 240 – 305 nm range (repeated test)

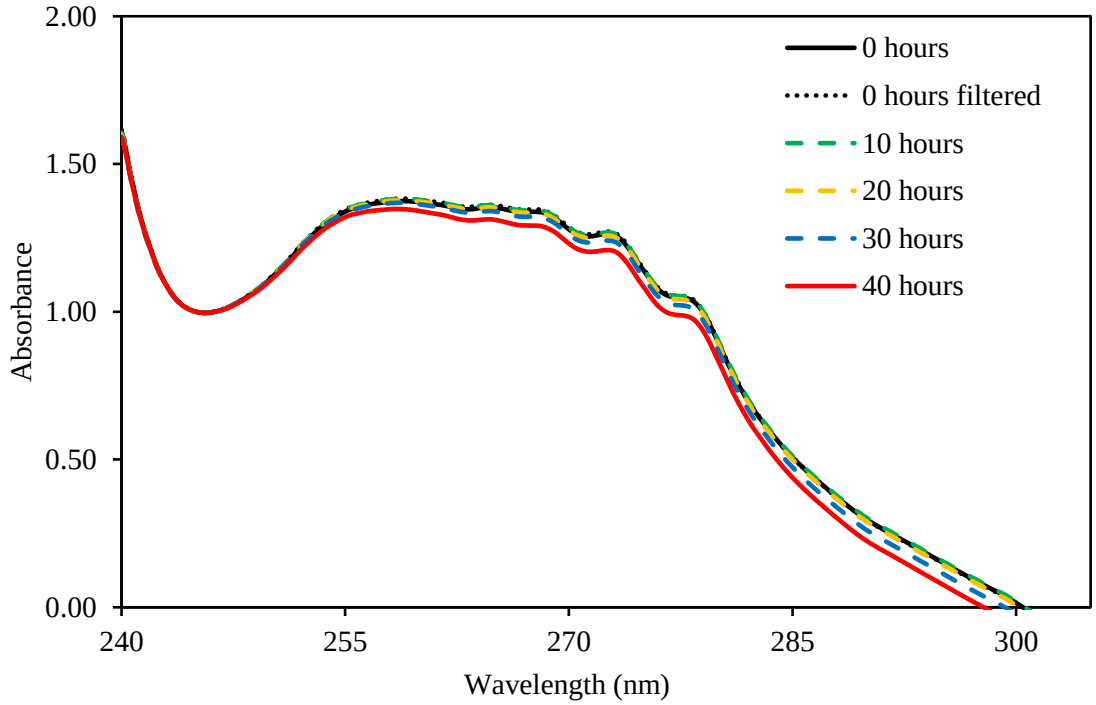

Figure 5.26 Fuel 2 (B10) repeated test sample spectra normalised at the 245 nm trough to show the change in 'Benzenoid band' absorption

Figure 5.24 and Figure 5.25 above show the spectra measurements of Fuel 2 (B10) samples from the cavitation tests. The broad-band absorbance increase in the spectra of both the initial and repeated tests were observed in the vertically displaced troughs at 245 nm. To identify the change in the benzenoid band the repeated test spectra were normalised at 245 nm wavelength; the resulting spectra is displayed in Figure 5.26. A decreasing trend in the absorbance in the benzenoid band was observed, however, the reduction in absorbance was of slightly lower magnitude as compared to the change observed for Fuel 1 (BDN) samples (Figure 5.23).

Figure 5.27 and Figure 5.28 show the spectra for Fuel 3 (B30) cavitation tests samples. In both cases the broad-band effect was very prominent. The increase in absorbance in the broad-band was found to be greater than the conventional diesel (Fuel 1 (BDN)) and B10 (Fuel 2), particularly for the repeated experiment shown in Figure 5.28.

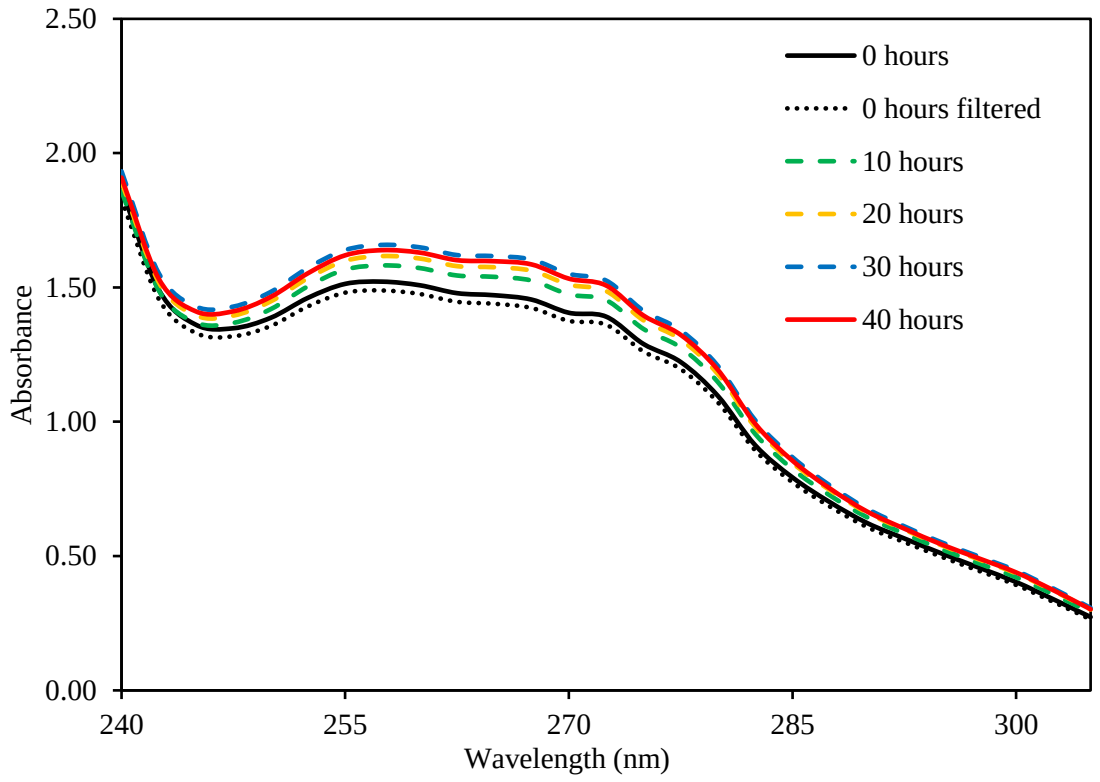

Figure 5.27 Fuel 3 (B30) discrete sample spectra for DRF 520 diluted samples in the 240 – 305 nm range (initial test)

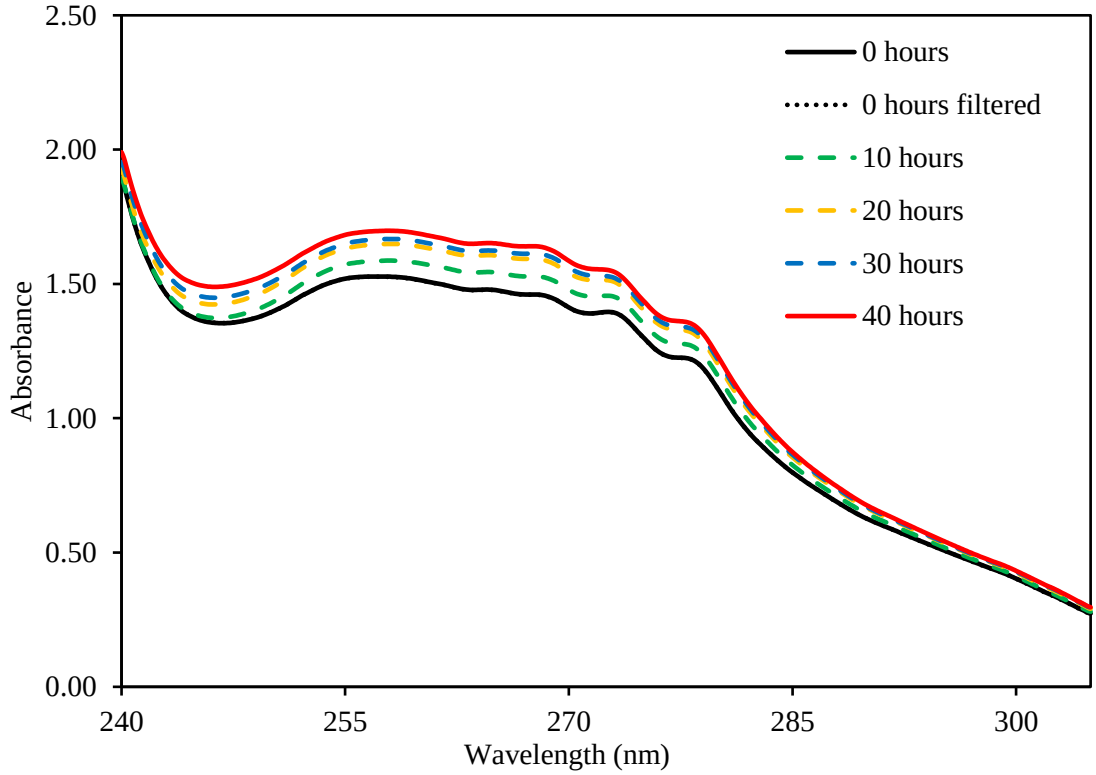

Figure 5.28 Fuel 3 (B30) discrete sample spectra for DRF 520 diluted samples in the 240 – 305 nm range (repeated test)

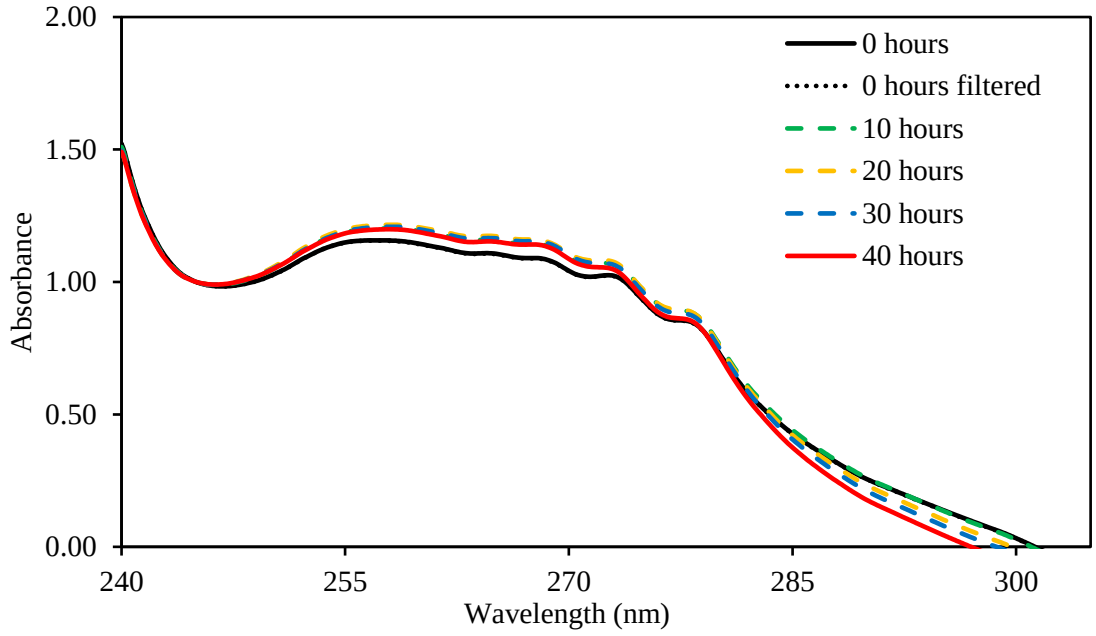

Figure 5.29 Fuel 3 (B30) repeated test sample spectra normalised at the 245 nm trough to show the change in 'Benzenoid band' absorption

Figure 5.29 shows the normalised spectra for the repeated experiment sample of Fuel 3 (B30). It was observed that the absorbance in the benzenoid band increased as a result of cavitation tests, although the increase was not uniform throughout the benzenoid band. The absorbance increase at shorter wavelengths was larger compared to the 270 - 280 nm range, contrary to this, Fuels 1 and 2 displayed larger change in absorbance in the longer wavelengths.

Figure 5.30 and Figure 5.31 show the spectra measurements of Fuel 4 (BD+H) (10 % Hexadecane) samples. Following the trend from Fuels 1-3, Fuel 4 (BD+H) also displayed the broad-band absorbance increase believed to be induced by the build-up of particulate suspension in the test fuel charge. Fuel 4 (BD+H) broad-band increase was found to be significantly larger than the conventional diesel samples.

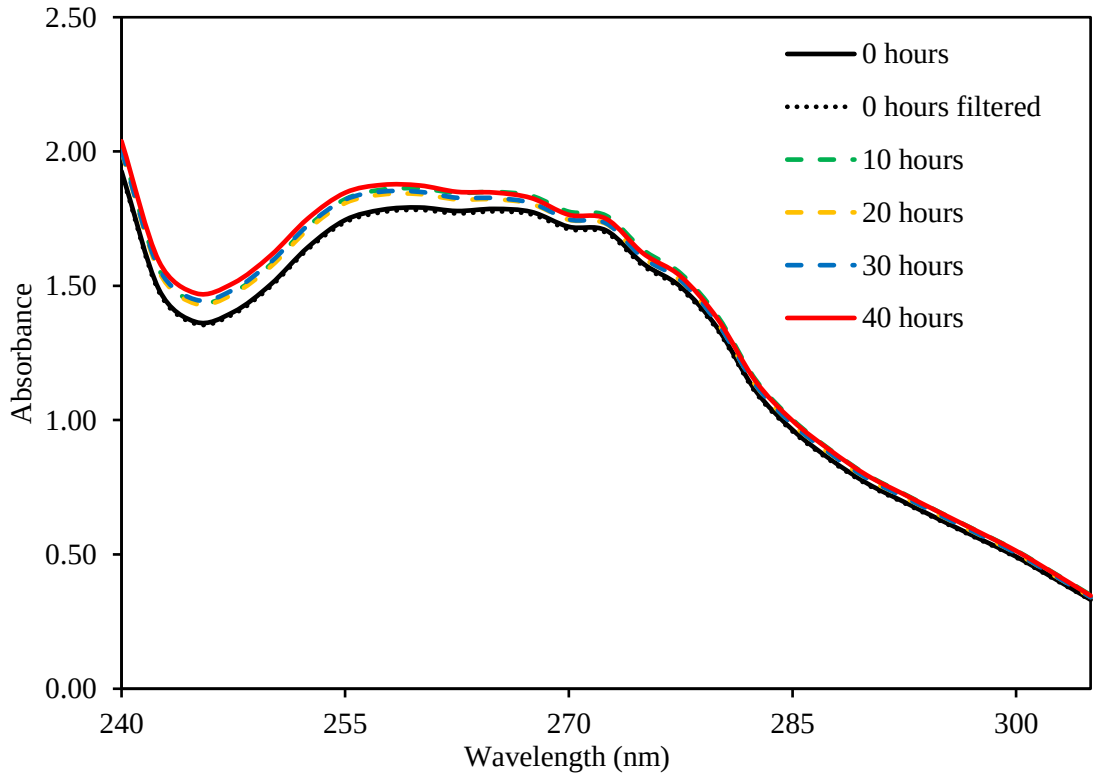

Figure 5.30 Fuel 4 (BD+H) discrete sample spectra for DRF 520 diluted samples in the 240 – 305 nm range (initial test)

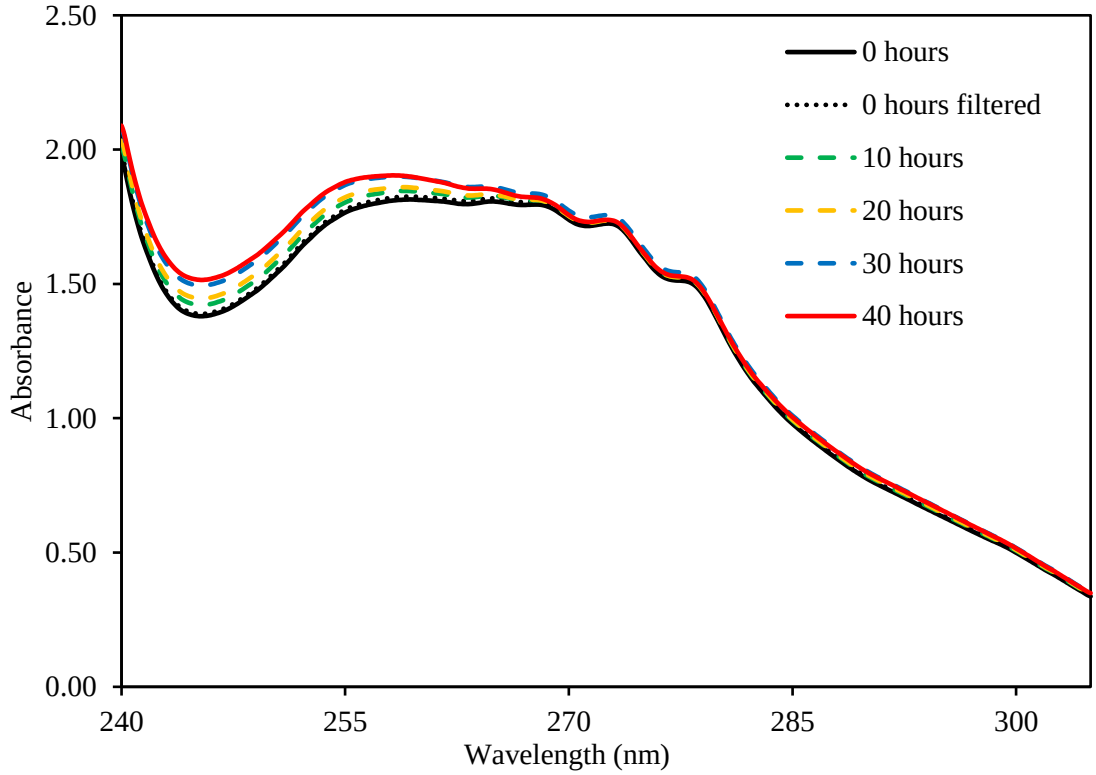

Figure 5.31 Fuel 4 (BD+H) discrete sample spectra for DRF 520 diluted samples in the 240 – 305 nm range (repeated test)

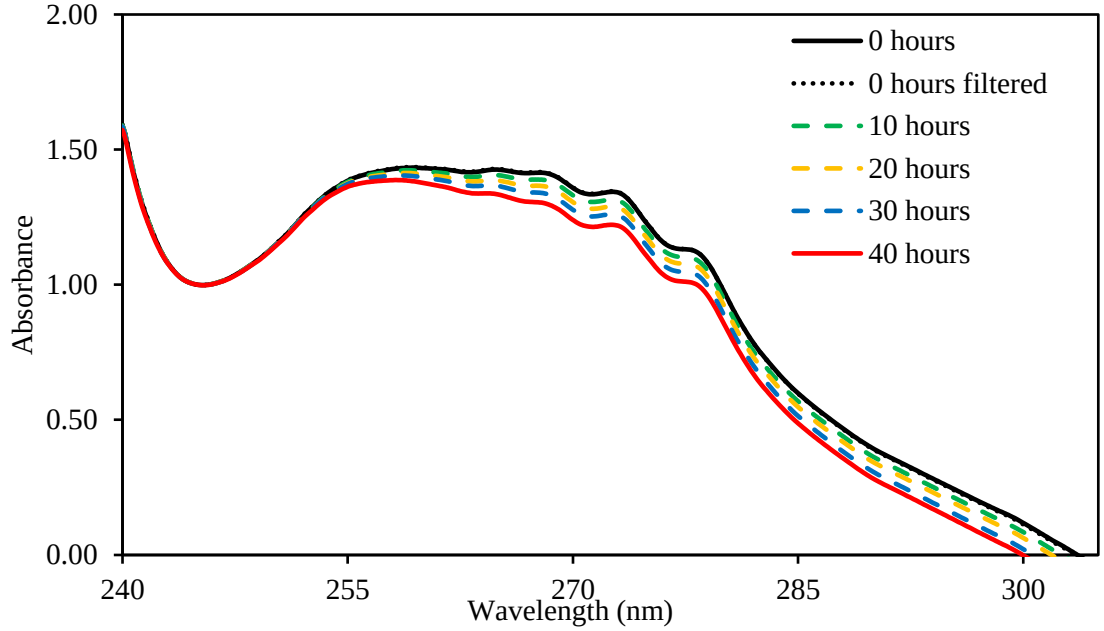

Figure 5.32 Fuel 4 (BD+H) repeated test sample spectra normalised at the 245 nm trough to show the change in 'Benzenoid band' absorption

Normalisation of Fuel 4 (BD+H) repeated test sample spectra (Figure 5.32) shows a clear, decreasing trend in the benzenoid band absorbance over cavitation duration. The change in benzenoid band absorbance was also found to be more prominent than the conventional diesel samples.

Figure 5.33 and Figure 5.34 show the spectra measurements of the Fuel 5 (BD+MN) (10% 1-methylnaphthalene) cavitation experiment samples. Fuel 5 (BD+MN) was found to have significantly higher absorbance in the 240 – 305 nm wavelength range, and was required to be diluted more than Fuels 1 - 4 for spectroscopic measurements. Figure 5.33 and Figure 5.34 were obtained from Fuel 5 (BD+MN) samples diluted to a dilution ratio factor (DRF) of 3,000.

Apart from showing significantly larger absorbances, the spectra of Fuel 5 (BD+MN) samples appeared to be visibly different from the first four fuels, in that the peaks in the benzenoid band region appeared to be modified in shape and shifted towards longer wavelengths. The shift in absorbance towards longer wavelengths is a known characteristic of substituted benzene molecules[101]. However, in this case the spectra show absorption structures matching the spectrum of 1-methylnaphthalene found in literature[104]. Naphthalene molecules also have a characteristic absorbance peak in the benzenoid band region at 314 nm, this was visible in the extended 190 – 405 nm spectra shown later in the section.

Studying the time-dependent change in spectra of the cavitated fuel samples, it was observed that the absorbance of Fuel 5 (BD+MN) samples in the benzenoid band did not vary significantly. Variations in the benzenoid band appeared to be small and random in the initial test samples, while the spectra for the repeated test samples overlapped each other, indicating negligible change. The broad-band absorption increase observed in Fuels 1 - 4 was also found to be minimal or non-existent for Fuel 5 (BD+MN) samples. Although, a minute increase at the 245 nm trough was observed in the repeated test sample spectra.

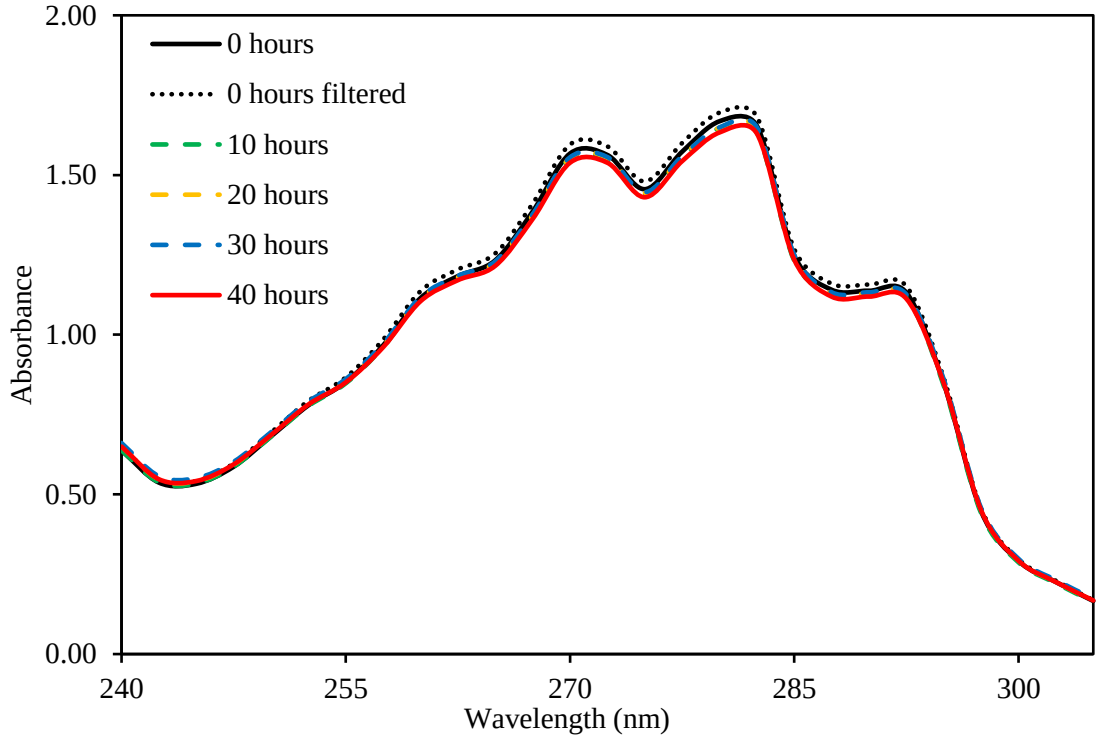

Figure 5.33 Fuel 5 (BD+MN) discrete sample spectra for DRF 3000 diluted samples in the 240 – 305 nm range (initial test)

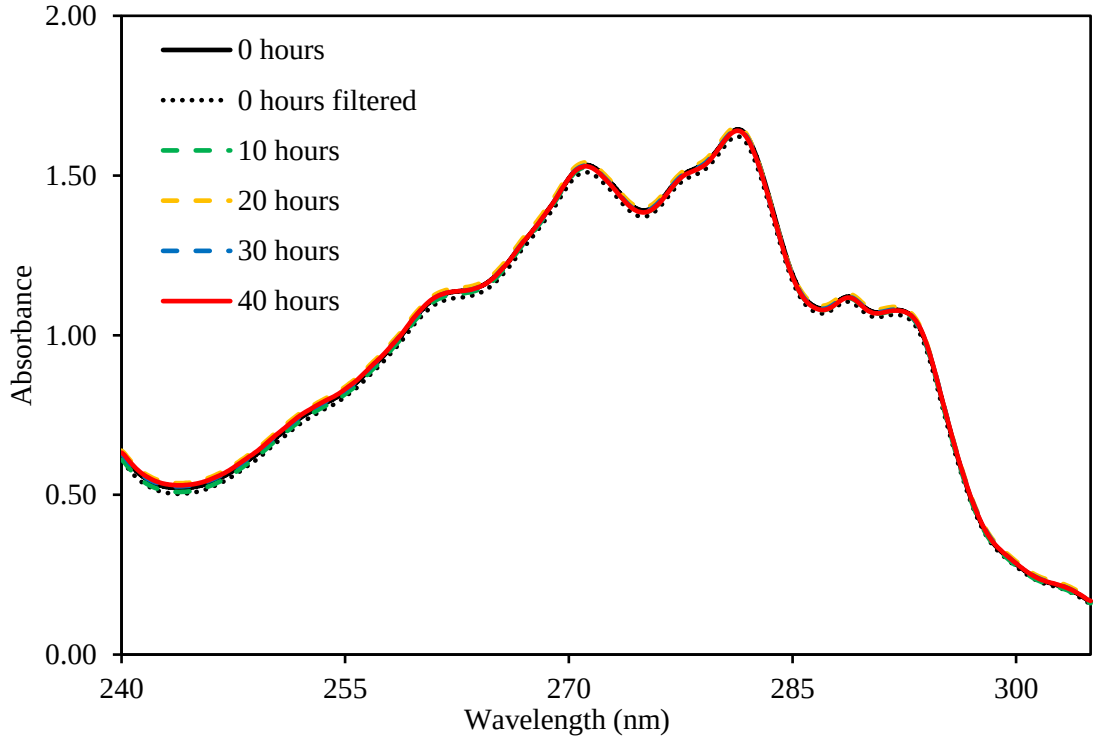

Figure 5.34 Fuel 5 (BD+MN) discrete sample spectra for DRF 3000 diluted samples in the 240 – 305 nm range (repeated tests)

Apart from the benzenoid band shown in Figure 5.20 – Figure 5.34, benzene molecules have a stronger absorption band near 200 nm wavelength. This absorption band is of fairly high intensity and corresponds to excitation of a π electron of the conjugated system to a π* orbital[101].

The discrete diesel samples from fuel cavitation tests were diluted to DRF 10,000 for spectroscopic measurements in the extended wavelength range of 190 nm – 405 nm. Spectra for Fuel 1 (BDN) repeated test samples are shown in Figure 5.35. The two aromatic hydrocarbon absorbance bands around 200 nm (high intensity band) and around 260 nm (benzenoid band) were observable in the spectra. Comparing the time-dependent change in absorbance of the cavitated samples did not reveal any significant trends. The small differences in sample-to-sample absorbances could not be distinguished from the dilution uncertainty, which had a coefficient of variation (CV) of less than 2 % in the 200 – 225 nm wavelength range (from the dilution repeatability statistics provided in Chapter 4.3).

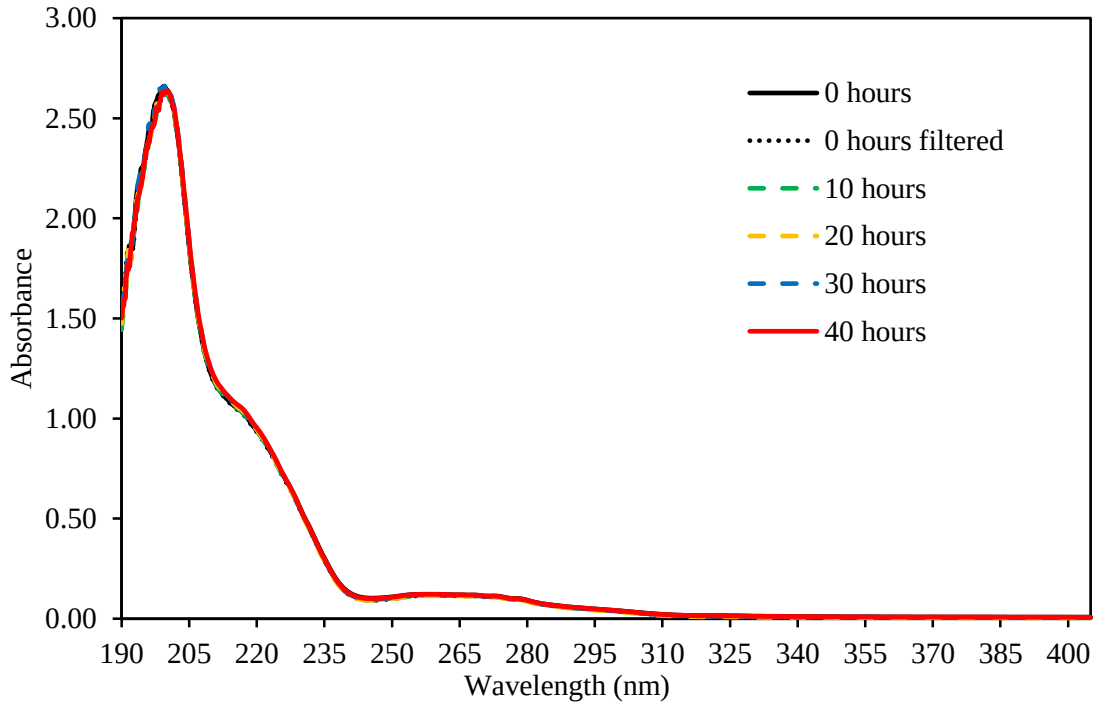

Figure 5.35 Fuel 1 (BDN) discrete sample spectra for DRF 10,000 diluted samples in the 190 – 405 nm range (repeated test)

Figure 5.36 shows the 200 – 230 nm section of the complete Fuel 1 (BDN) spectra in further detail. Some variations in the sample absorbances could be observed in the 'shoulder-like' structure around 210 – 218 nm. The absorbance appeared to increase with cavitation duration, indicating similarities to the broad-band absorbance increase observed in previous spectra measurements due to particulate build-up. However, the differences in absorbance still lie within the dilution uncertainty range of ± 2 %.

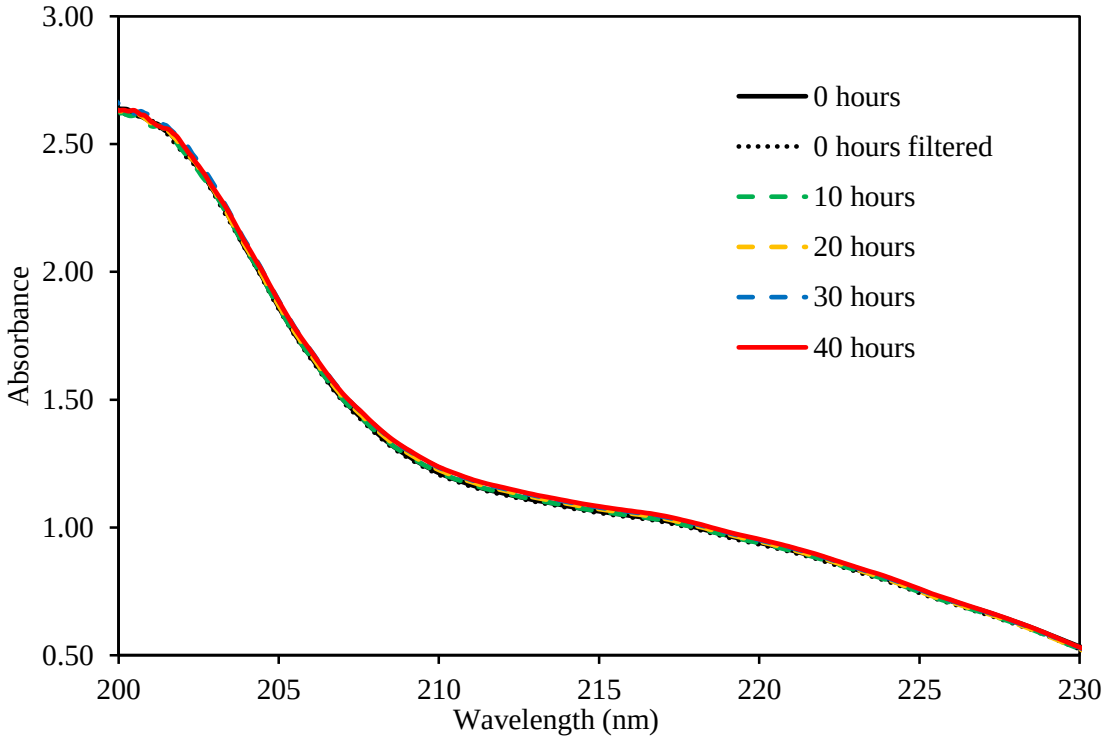

Figure 5.36 Fuel 1 (BDN) repeated test samples in the 200 – 230 nm range (diluted to DRF 10,000)

Spectra measurements of Fuels 2 – 5 in the measurement range of 190 – 405 nm are included in Figure 5.37 – Figure 5.40. For the purpose of fuel-to-fuel comparisons, only the repeated test sample spectra measurements have been shown in this section. The initial test sample spectra for Fuels 1- 5 have been included in Appendix A.1.

All fuels showed absorbance activity in the high-intensity band around 200 nm, corresponding to the $\pi \rightarrow \pi^*$ excitation of the conjugated system in the benzene molecules. The intensity of absorbance in the high-intensity band varied for the different fuels according to the change in

concentration of the mono-aromatics in the fuel samples. Fuel 2 (B10) had lower absorbance in the 200 nm peak relative to Fuel 1 (BDN), a consequence of additional 10 % RME component, indicating insignificant absorbance activity of the RME in the 200 nm region. Absorbance of mono-aromatics in Fuel 3 (B30) was lower still due to 30 % additional RME relative to Fuel 1 (BDN). Fuel 4 (BD+H) had similar absorbance intensity to Fuel 2 (B10) due to 10 % additional hexadecane, which also has no absorbance activity in the 200 nm region.

Fuel 5 (BD+MN) had 10 % additional 1-methylnaphthalene relative to Fuel 1 (BDN), which resulted in higher overall absorbance of the fuel in the complete measurement range. For spectroscopic measurements in the wavelength range of 190 – 405 nm, Fuel 5 (BD+MN) samples were diluted to a dilution ration factor of 17,000. The spectra of the DRF 17,000 samples are shown in Figure 5.40. The absorbance peak at 200 nm had an intensity of ~ 2.1, corresponding to an intensity of ~ 3.8 if corrected to dilution level of Fuels 1 – 4 at DRF 10,000. The absorbance intensity of Fuel 5 (BD+MN) (~ 3.8) was significantly higher that the absorbance intensity of Fuel 1 (BDN) (~ 2.6), indicating absorbance contribution from addition 1-methylnapthalene.

Figure 5.40 shows a stronger absorbance structure with a peak at 224 nm along with a smaller peak at 220 nm. The 224 nm peak is a known absorbance peak of 1-methylnapthalene from the literature[104]. Another region of activity for 1-methylnaphthalene is around 314 nm wavelength, this structure has been shown in more detail in Figure 5.41.

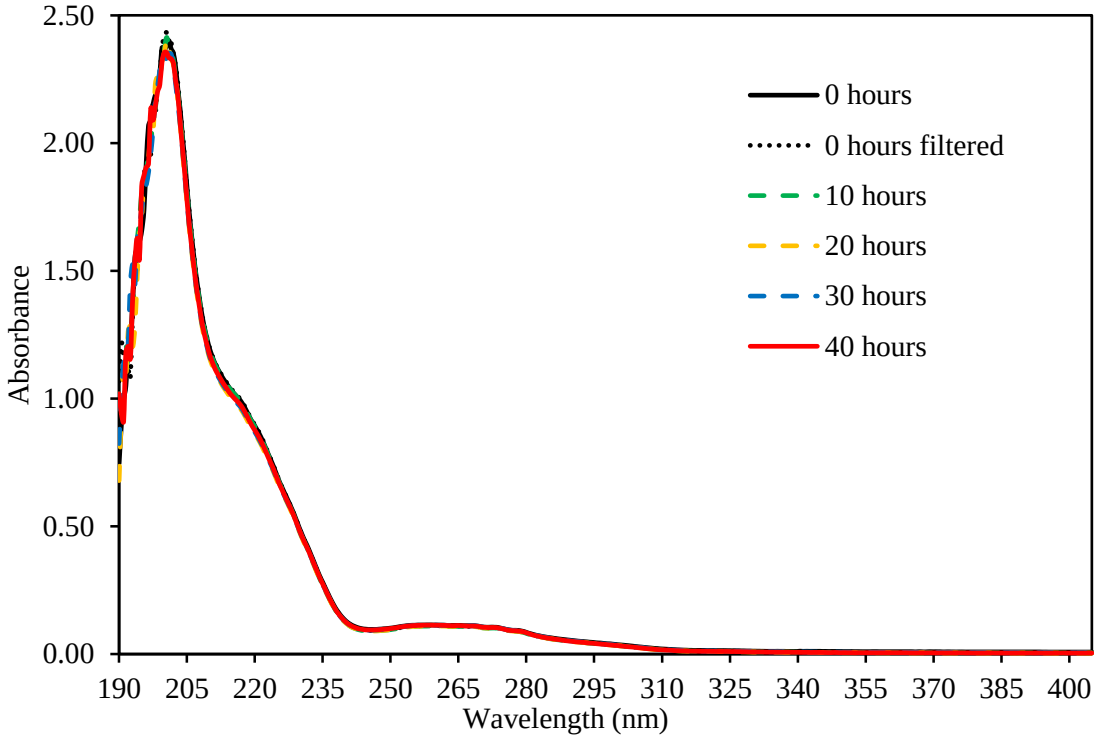

Figure 5.37 Fuel 2 (B10) discrete sample spectra for DRF 10,000 diluted samples in the 190 – 405 nm range (repeated test)

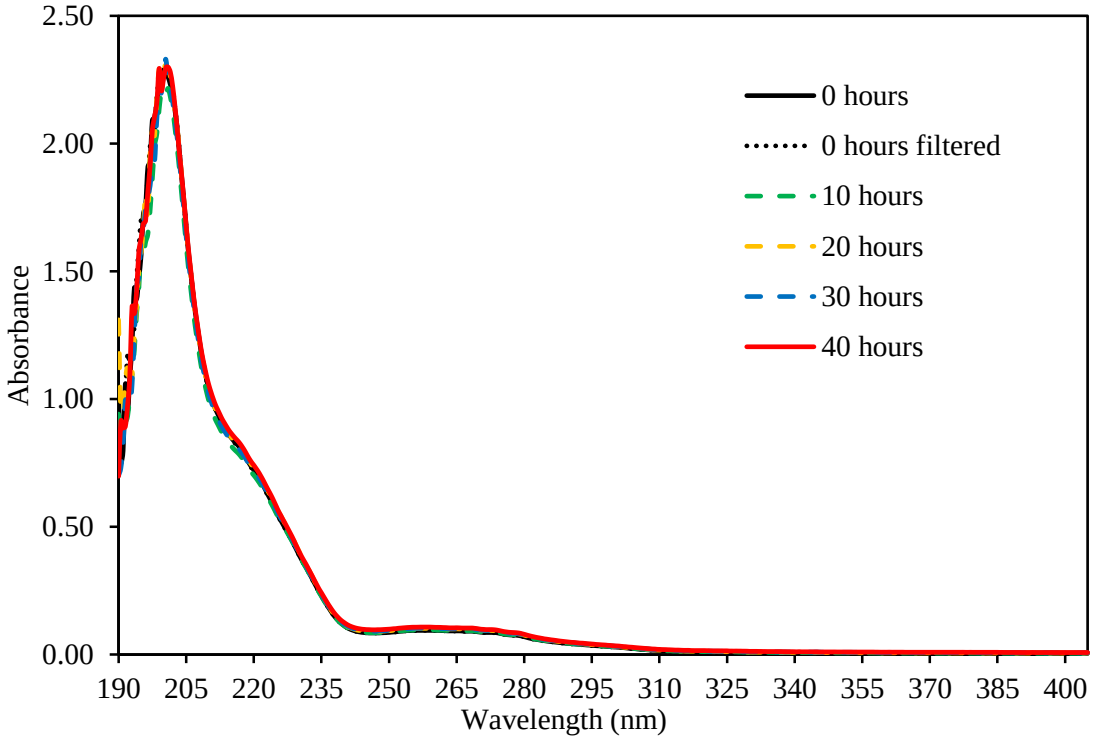

Figure 5.38 Fuel 3 discrete sample spectra for DRF 10,000 diluted samples in the 190 – 405 nm range (repeated test)

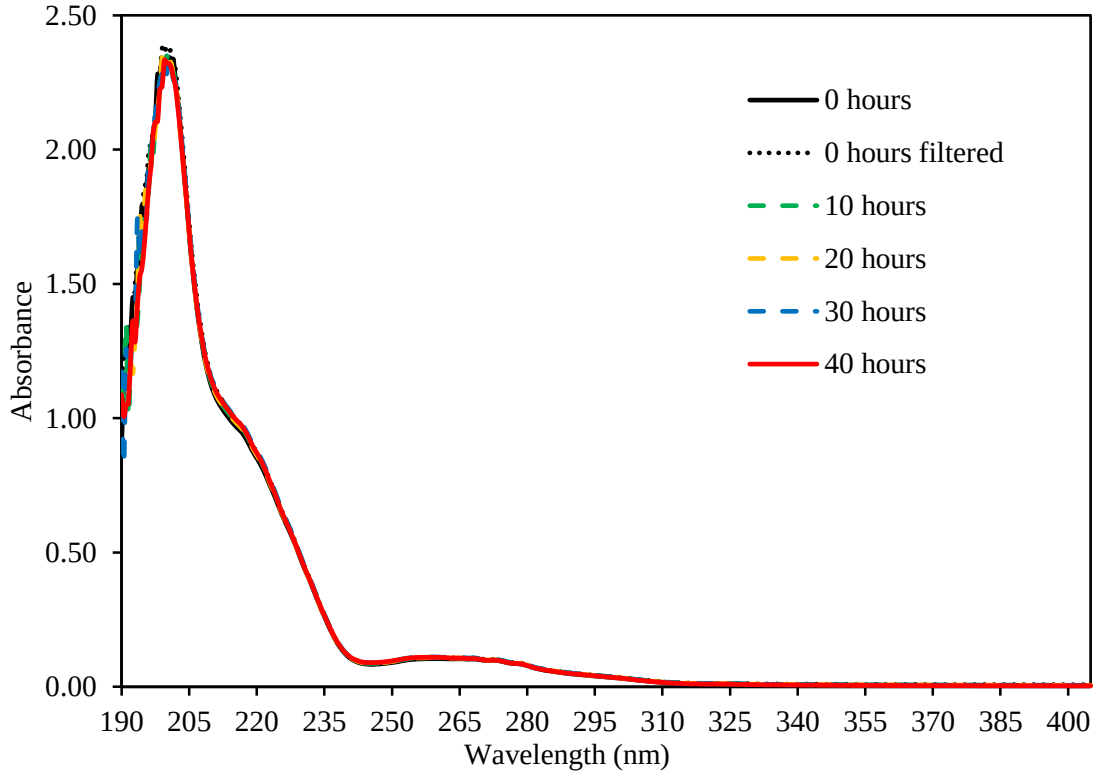

Figure 5.39 Fuel 4 (BD+H) discrete sample spectra for DRF 10,000 diluted samples in the 190 – 405 nm range (repeated test)

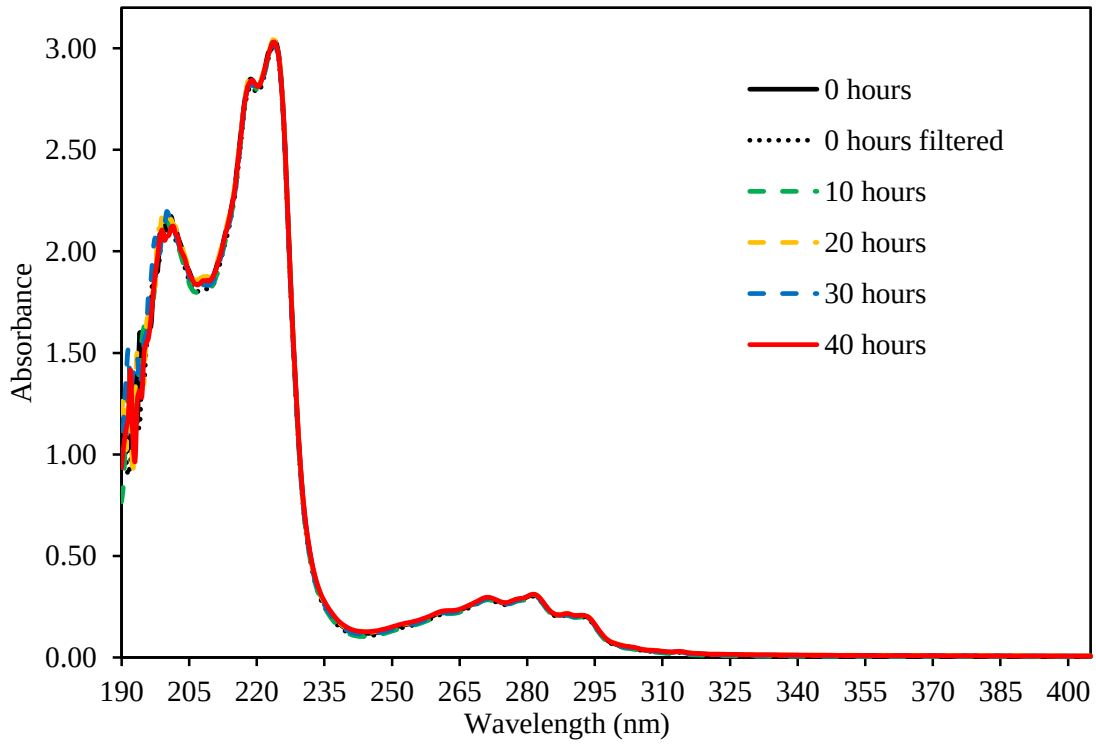

Figure 5.40 Fuel 5 (BD+MN) discrete sample spectra for DRF 17,000 diluted samples in the 190 – 405 nm range (repeated test)

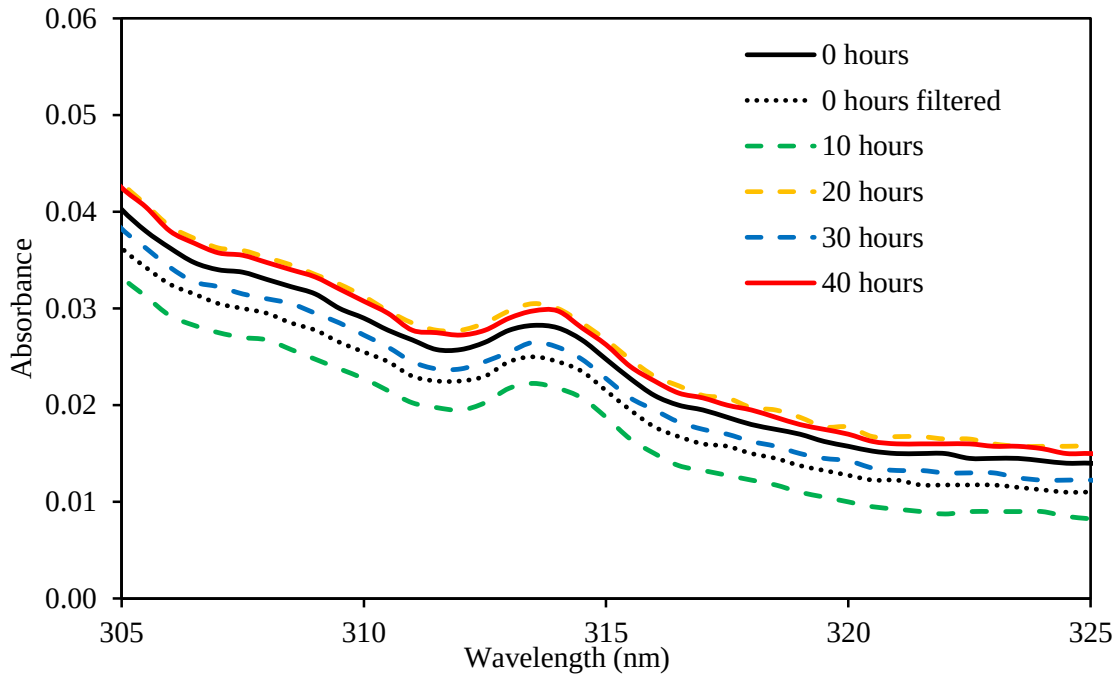

Figure 5.41 Fuel 5 (BD+MN) repeated test sample spectra showing the 314 nm absorbance structure which is a characteristic of 1-methylnaphthalene.

5.3 Particle Count Distributions

The discrete diesel fuel samples collected from the test-rig were subjected to Spectrex Laser Particle Counter (LPC) that determined the particulate size distributions in the diesel samples, resulting from their exposure to hydrodynamic cavitation. This sub-section presents the particle size distribution results for the repeated fuel test samples of Fuels 1 – 5.

The Spectrex LPC was capable of determining concentrations (counts/cc) of particles in the particle size range of 1 µm to 100 µm. Figure 5.42 shows the particle size distributions of Fuel 1 (BDN) samples as a function of cavitation time from the repeated fuel test. The figure shows the population of particles in the complete measurement range of 1 µm to 100 µm. However, it can be observed that the population of particles greater than ~ 15 µm is almost negligible in all samples. Therefore, the plots for the remaining fuels' particle size distributions have been truncated to 30 µm to provide a more detailed analysis of the smaller particle sizes. Figure 5.43

to Figure 5.47 show the particle populations of Fuels 1 – 5 samples in the particle size range of 1 µm to 30 µm.

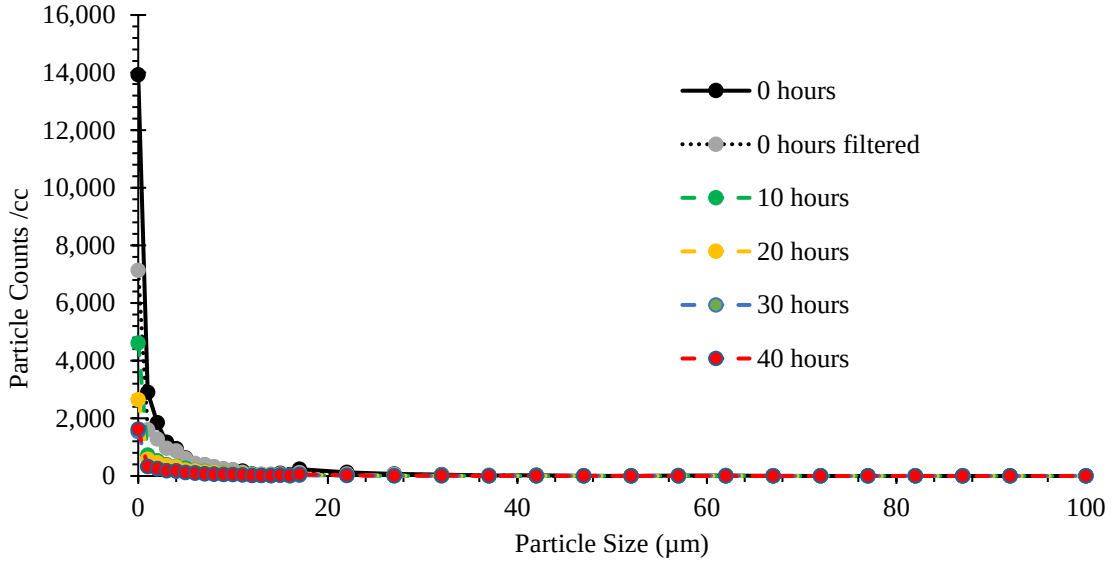

Figure 5.42 Particle size distribution of cavitated Fuel 1 (BDN) samples in the particle size range of 1 µm to 100 µm.

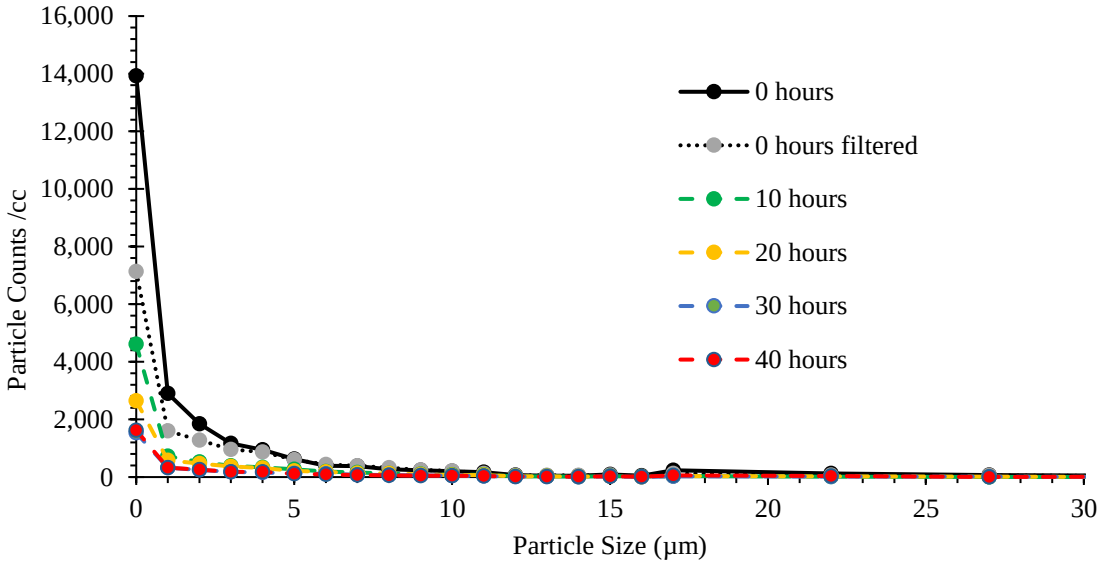

Figure 5.43 Particle size distribution of cavitated Fuel 1 (BDN) samples in the particle size range of 1 µm to 30 µm.

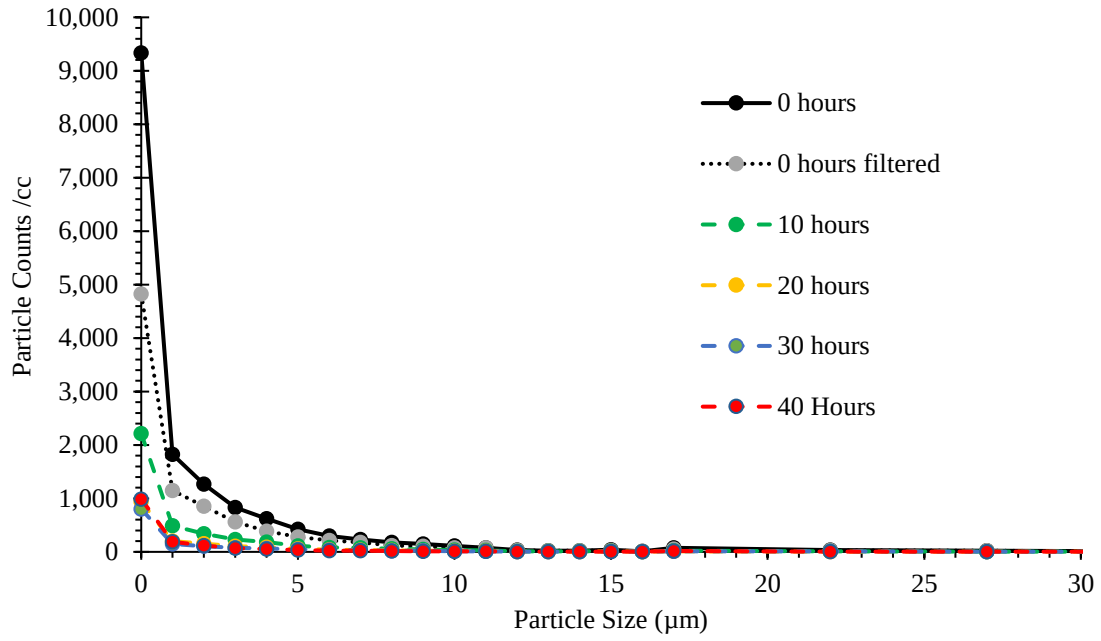

Figure 5.44 Particle size distribution of cavitated Fuel 2 (B10) samples in the particle size range of 1 µm to 30 µm.

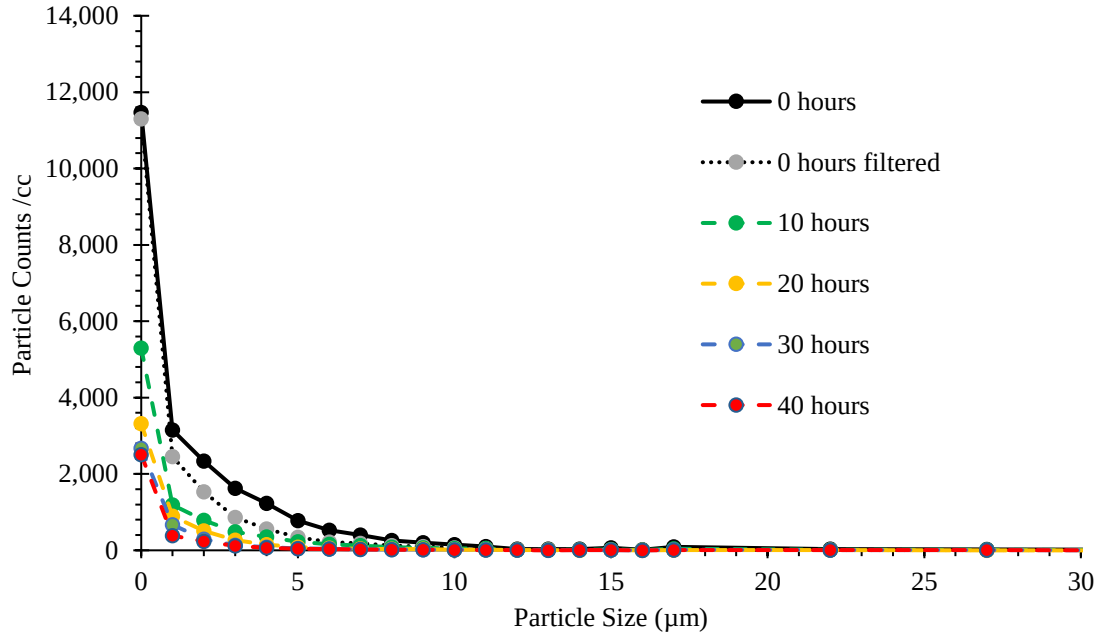

Figure 5.45 Particle size distribution of cavitated Fuel 3 (B30) samples in the particle size range of 1 µm to 30 µm.

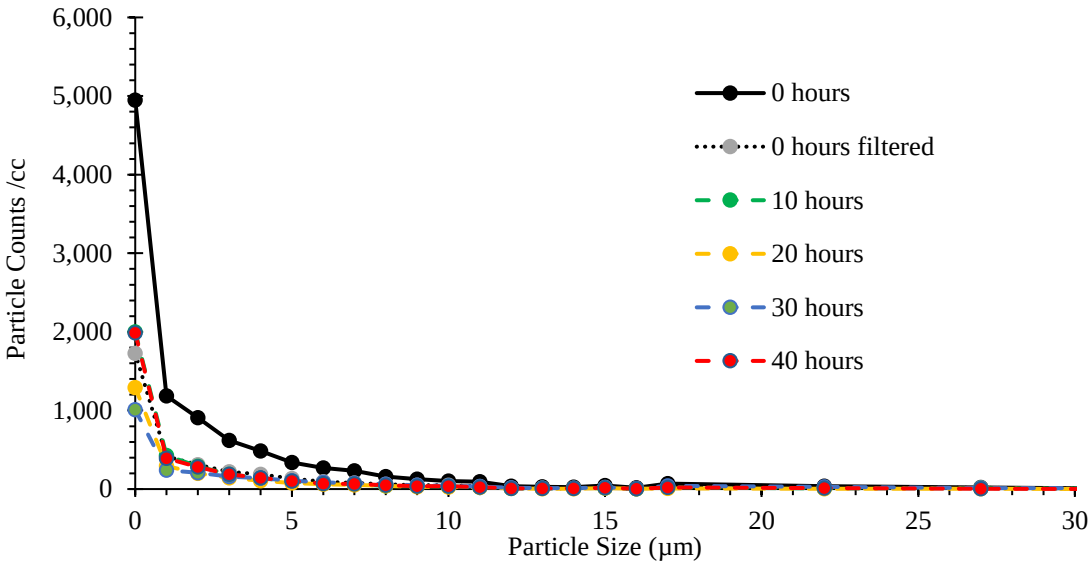

Figure 5.46 Particle size distribution of cavitated Fuel 4 (BD+H) samples in the particle size range of 1 µm to 30 µm.

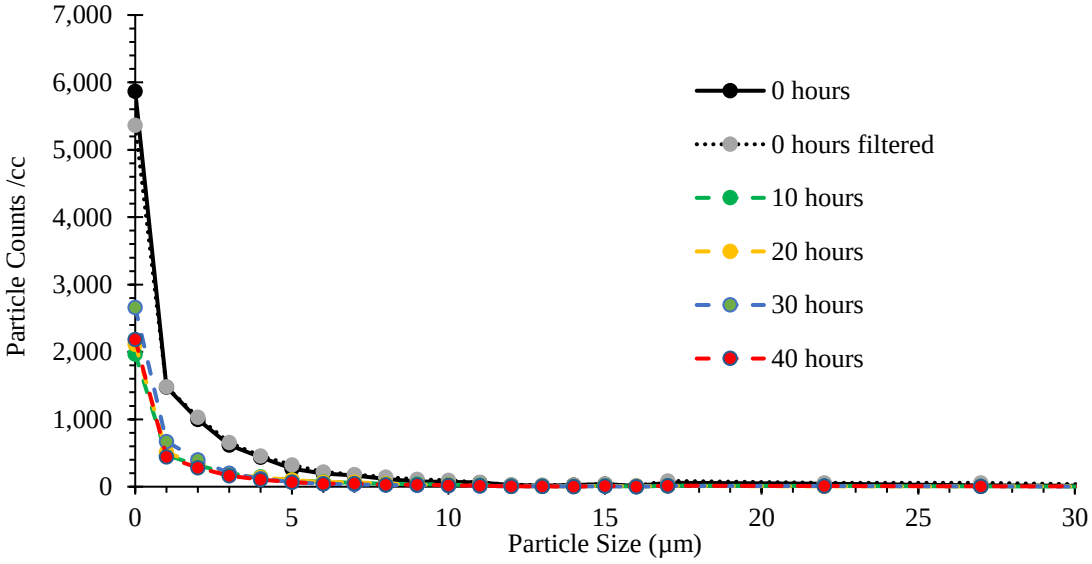

Figure 5.47 Particle size distribution of cavitated Fuel 5 (BD+MN) samples in the particle size range of 1 µm to 30 µm.

Particle size distributions for all fuel samples show a similar trend, where every sample has particle population that asymptotically decreases with particle size, such that there are no significant particle counts for particles greater than ~ 15 µm. Observing the trend as a function of cavitation duration, the size-dependent particle counts decrease significantly after 10 hours of cavitation; the decrease in counts becomes less prominent for the subsequent fuel samples.

It is also observed that for fuel samples taken after the start of high-pressure cavitating flow (i.e. 10 hours, 20 hours, 30 hours and 40 hours samples) the largest particles with significant counts are ~ 4 µm in diameter.

It is believed that the observed trends are a result of fuel filtration by the 3 µm fuel filter being employed in the test-rig. The 3 µm nylon fuel filters used in the test-rig were specified to have a logarithmic particle capture profile, with a capture rate of 99.998 % at 3 µm[105]. Although specified with a 3 µm mesh size, the logarithmic capture profile of the filters allowed trapping of particles down to 0.5 µm. Therefore, the observed trends in particle size distribution results do not signify a breakdown of particulates due to hydrodynamic cavitating flow, rather the particles are being filtered from the fuel over time whereupon their population in the recirculating fuel charge decreases.

The measurement range of the laser particle counter becomes ineffective due to the filter mesh size employed. As the fuel recirculates in the rig, the micron sized particles get filtered out, therefore, the results from the particle counter are not able to provide a correlation between particulate build-up and the hydrodynamic cavitating flow. Due to the mismatch between the measurement range of the laser particle counter and the mesh size of the filter, the results for particle size distributions of the other investigations discussed in this work will not be included.

It should however be noted that the broadband absorbance increase observed in the uv-vis spectra measurements of the fuel samples gives an indication of the build-up of nano-sized particles (< 0.5 nm), which are smaller than the capture range of the fuel filters.

5.4 Combined Discussion of Fuel Tests

The high-pressure cavitation test-rig has been used to investigate the effect of fuel composition on the change in their chemical and optical properties when they are subjected to sustained cavitation. Five commercial fuel blends were used, with Fuel 1 (BDN) being the conventional

diesel fuel and the remaining four fuels being blends of Fuel 1 (BDN) with other components added to it in specified proportions. All fuels have been subjected to 40 hours of recirculating, cavitating flow at 1,650 bar rail-pressure through separate single-hole test nozzles. A simplified spectral attenuation measurement setup and a uv-visible spectrometer have been used to monitor the changes in fuels' properties.

The findings of the time-dependent spectral attenuation coefficient measurements at 405 nm wavelength showed variations for all fuels. It was suggested that the change in optical properties of the fuels indicated chemical compositional changes occurring in the fuels resulting from being subjected to recirculating hydrodynamically cavitating flow past the injector nozzle, into the receiving cylinder. The effects of cavitation bubble collapse have been reported to drive chemical reactions in liquids subjected to acoustic cavitation (sonochemistry); extrapolating these effects to hydrodynamic cavitation would suggest similar chemical activity to occur in the cavitating diesel samples. Changes occurring in the optical properties of the fuels suggest that, as a result of sustained cavitation, their chromophoric systems change significantly; evidently, indicating alterations to their original chemical compositions.

In-situ spectral attenuation measurements on Fuel 1 (BDN) samples (conventional diesel fuel) and Fuel 5 (BD+MN) samples (10 % 1-methylnaphthalene) showed similar trends, where their spectral attenuation coefficients initially increased and then gradually decreased to a steady-state value. Addition of FAME (fatty acid methyl ester) to the conventional diesel changed the trend towards prolonging the duration of the initial increase in spectral attenuation coefficient of the fuels; Fuel 2 (B10) experienced an increase in attenuation for up to the first 12 hours of the cavitation tests, while Fuel 3 (B30) showed a monotonous increase in attenuation throughout the experiments. Fuel 4 (BD+H) (10 % hexadecane) was the only fuel that displayed no significant increase in the attenuation coefficient. It experienced the largest change in

attenuation of all fuels, where its attenuation decreased towards a steady-state minimum in the 40 hours of testing.

Spectral attenuation coefficients of all fuels, except Fuel 3 (B30), appeared to converge towards the end of the cavitation experiments. The converging trend was explained further through analysis of uv-vis spectra measurements of the discrete fuel samples drawn from the test-rig during the cavitation experiments. The absorption band around 425 nm, believed to be resulting from absorption of 3 – 5 ring PAHs, experienced a net decrease in all fuels except Fuel 3 (B30); it should be noted that the broad band increase effect was separated to reach this conclusion. The result of diminished 425 nm band was extended to the 405 nm spectral attenuation measurement wavelength, thus the spectral attenuation coefficients of all fuels appeared to converge by the end of each 40 hour experiment. Fuel 3 (B30) showed no absorption structures in the 425 nm band, instead the increasing broad-band absorption effect dominated its behaviour at all wavelengths, thus a monotonous increase in spectral attenuation coefficient was observed.

The rate of destruction of the 3 – 5 ring polyaromatic hydrocarbons, indicated by the decrease in absorption of the 425 nm band, was different for the different fuels (see Figure 5.48). Fuels 1 and 2 experienced increase in sample absorptions in the early stages of the cavitation experiments, followed by decrease, to indicate destruction of the 425 nm band. Fuels 4 and 5, on the other hand, only showed destruction of the 425 nm band through the course of the cavitation experiments. Fuel 5 (BD+MN) appeared to delay the destruction process in the first 10 hours of the experiment as it experienced a very insignificant change in absorption; alternatively, this behaviour could be explained as the result of the fuel experiencing a rise and fall in absorbance during the first 10 hours, which would not be observable in the sample spectra measurements due to the sampling strategy applied. Figure 5.48 shows that Fuel 4 (BD+H) experienced the largest change in absorption (at 245 nm) of any test fuel on daily basis

(10 hours per day), agreeing with the large changes in time-dependent spectral attenuation observed at 405 nm.

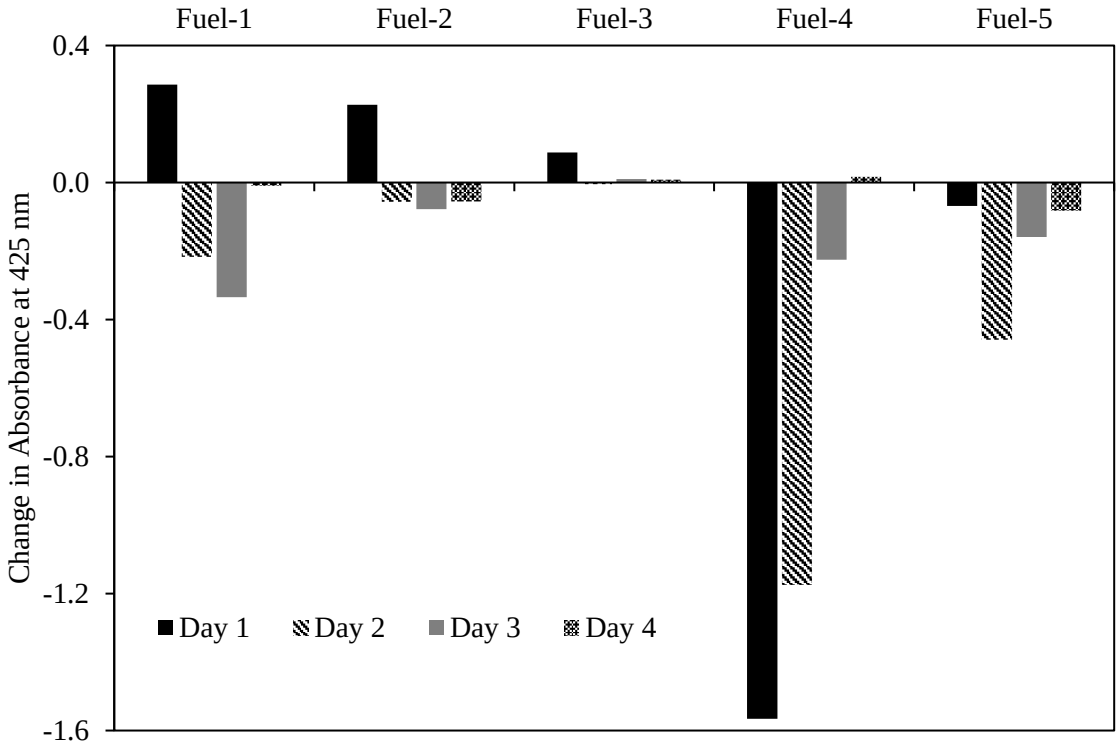

Figure 5.48 Daily change (per 10 hours) in measured absorption at the 425 nm peak of discrete samples for the five test fuels.

Purely paraffinic fuels have been reported to be more stable and show lower optical activity at 405 nm under sustained cavitation conditions. However, this conclusion was not reaffirmed by the behaviour of Fuel 4 (BD+H) seen in these experiments. It is possible that, during cavitation, the paraffinic content of Fuel 4 (BD+H) interacted with other species present in the fuel to give this contradictory result; as opposed to a purely paraffinic fuel, Fuel 4 (BD+H) was also composed of large proportions of aromatics and naphthenes.

It should be noted that the high initial spectral absorbance of Fuel 4 (BD+H) at 405 nm is inconsistent with the prior understanding of chromophoric systems of paraffins. The high absorbance of pre-cavitation Fuel 4 (BD+H) sample around the 405 nm range is needed to be investigated for further explanation.

Spectra measurements in the 240 - 305 nm range showed the benzenoid absorption band, a characteristic absorbance structure of mono-aromatic hydrocarbons. The discrepancy in structure of the benzenoid band observed in the fuel sample spectra to that of a pure benzene spectra suggested a large presence of naphthene substituted mono-aromatic compounds. Normalisation of fuel sample spectra at 245 nm trough, revealed a systematic time-dependent decrease in absorption in the benzenoid band for all fuels, except Fuels 3 and 5.

Fuel 3 (B30) showed a small increase in absorbance, though it is believed that the increase in absorbance was a consequence of interference from absorbance by biodiesel blend components present in the B30 fuel. Standard methyl esters with conjugated trienes are known to show absorbance activity in wavelengths spanning from 250 nm to 300 nm[106]. The absorbance from these methyl esters in the 250 nm – 300 nm range could have masked the decrease in the benzenoid band absorption, or their presence could have altered the chemical activity of mono-aromatics to show a different behaviour from other fuels. At this point, further conclusions can only be drawn after performing chemical analysis of the fuel samples. Fuel 5 (BD+MN) spectra showed a dominating absorption structure corresponding to the benzenoid band of 1-methylnaphthalene; this band experienced no significant change in absorbance over the test durations.

The decrease in absorbance of the benzenoid band for Fuels 1, 2 and 4 indicated a steady destruction/ reduction in concentration of mono-aromatics in the fuels. It is known that hydrodynamic cavitation occurs across the single-hole injector nozzle, creating cavitation vapour that collapse inside the receiving cylinder. The ‘hot-spots’ of extreme temperature and pressure generated at the collapse of such cavities have demonstrated the potential to drive sonochemical-like reactions in the collapsing vapour and the surrounding liquid. In the absence of sufficient oxygen, the fuel components are believed to undergo pyrolytic reactions. It is suggested that the mono-aromatic hydrocarbons undergo pyrolytic reactions to form poly-

aromatic hydrocarbons, along with other highly reactive benzene decomposition products such as acetylene and C_2H radicals. The aromatic hydrocarbons are subjected to hydrogen abstraction and acetylene (C_2H_2) addition reactions, allowing them to form larger PAH molecules, soot precursors and eventually nascent soot particles through various mechanisms, including the well-known HACA (H abstraction, C_2H_2 addition) soot mechanism[26,107–109].

An indication of soot and particulate formation was obtained from the broad band absorption increase observed for all fuels. The trends of increasing broad band absorption were clearly visible in spectra measurements of pure fuel samples at wavelengths smaller than 375 nm. For Fuels 1 – 4 the trends were also observed at the 245 nm trough. Biodiesel blends (Fuels 2 & 3) showed relatively larger increases in broad band absorbance, with the trend becoming more pronounced at larger proportions of the FAME content.

Results presented here have given an indication to the changes occurring in the diesel fuel samples as they were subjected to sustained hydrodynamic cavitation. Fuels of different composition have shown different behaviours, suggesting the various species present in the diesel fuels experienced different effects from cavitating flows. FAME, aromatic and paraffinic contents of the fuels have all been shown to give fuels their varying optical properties. However, it is suspected that the species interact within themselves in complex ways to produce species that change the absorption activity of the fuels over large wavelength ranges in the near ultraviolet and visible regions of the spectrum. Spectroscopic analysis has given some indication towards the changes occurring to the primary aromatics and PAHs, but chemical analysis of the fuel samples is required to affirm these conclusions and provide possible suggestions regarding the mechanisms of these changes. Two-dimensional gas chromatography has been performed on the cavitation test samples of Fuels 1 – 5, the results from the analysis will be presented in Chapter 9 of the thesis.

Chapter 6
Injection Pressure Dependence Tests

The injection pressure dependence tests involved recirculating a test fuel in the high-pressure test-rig for forty-hour experiments at different injection pressures. Three set of tests were conducted to investigate the pressure dependence; these included:

- Tests for Fuel 1 (BDN) at injection pressures of 550 bar, 1,100 bar and 1,650 bar. The injector nozzle used for this set was the old nozzle of 213 µm nozzle diameter, with > 20 % hone. The optical setup for in-situ laser transmission measurements was composed of the old 20 mW, 405 nm laser diode and old laser detectors.
- Tests for Fuel 1 (BDN) at injection pressures of 825 bar and 1,650 bar. The injector nozzle used for this set was the new test nozzle of 176 µm nozzle diameter, with ~13 % hone. The optical setup for in-situ laser transmission measurements was composed of the new 35 mW, 405 nm laser diode and new laser detectors.
- Tests for Fuel 6 (BDA) at injection pressures of 825 bar and 1,650 bar. The injector nozzle used for this set was the new test nozzle of 173 µm nozzle diameter. The optical setup for in-situ laser transmission measurements was composed of the new 35 mW, 405 nm laser diode and new laser detectors.

Table 6.1 Control variables for the injection pressure dependence tests

Test Fuels	Fuel 1 (BDN) or Fuel 6 (BDA)
Test Duration	40 hours
Receiver Pressure	1 bar
Pre-Injection Fuel Temperature	55 °C
Filter Type and Size	3 µm Filter

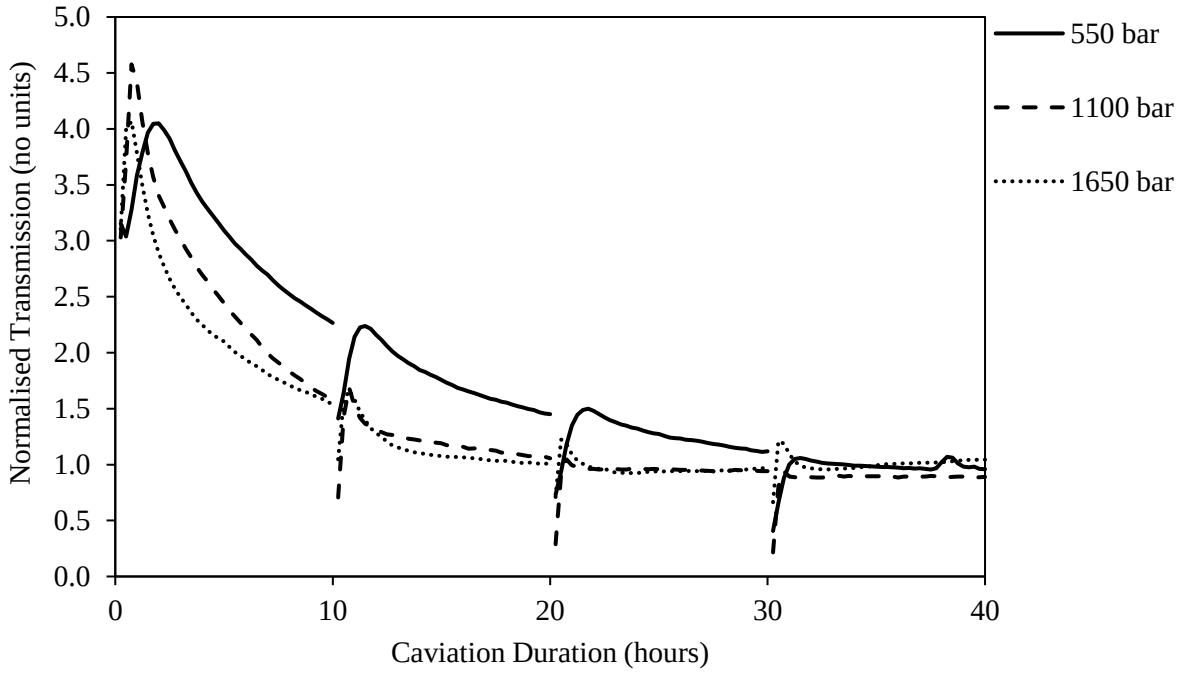

Figure 6.1 Normalised laser transmission at 405 nm against cavitation time for Fuel 1 (BDN) at 550, 1,100 and 1,650 bar injection pressures

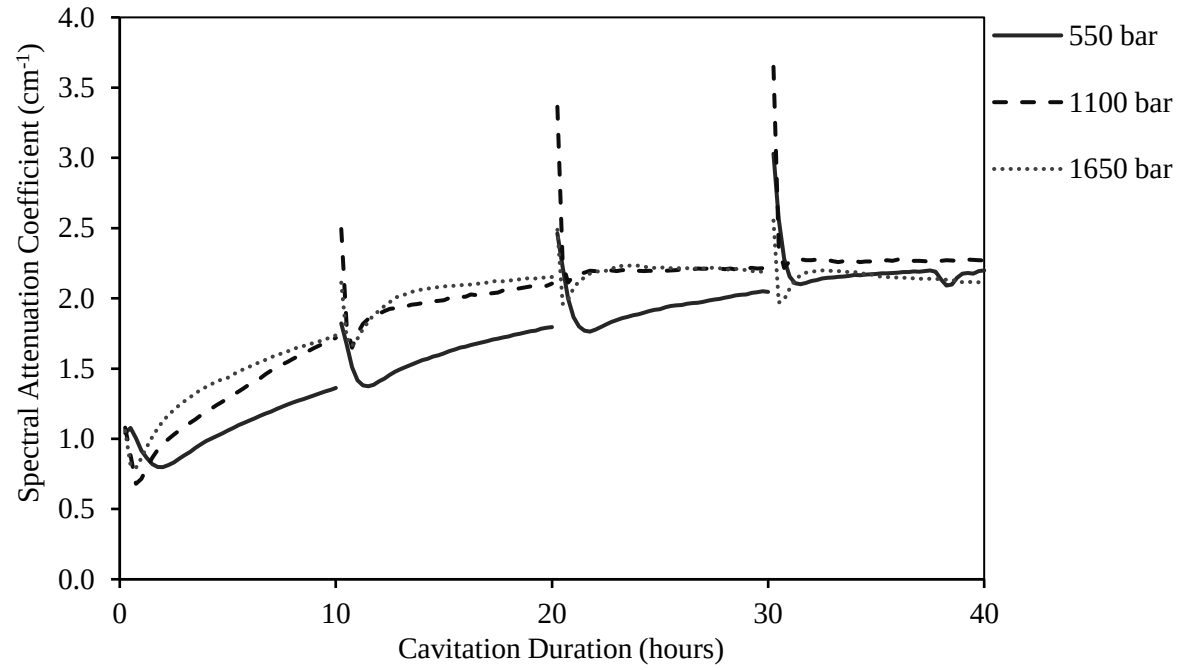

Figure 6.2 Time-dependent spectral attenuation coefficient at 405 nm against cavitation time for Fuel 1 (BDN) at 550, 1,100 and 1,650 bar injection pressures

Figure 6.1 shows the normalised spectral transmission at 405 nm with cavitation time for Fuel 1 (BDN) charges cavitated at injection pressures of 550 bar, 1,100 bar and 1,650 bar. Each of the four 10-hour segments on the figure represents a single day of testing, amounting to a total of 40 hours of testing at each injection pressure.

From Figure 6.1, Fuel 1 (BDN) is observed to have a pre-cavitation (zero hour) normalised spectral transmission of 3.10 ± 0.07. Spectral transmission of Fuel 1 (BDN) is shown to decrease with cavitation time at all injection pressures. In case of 1,100 bar and 1,650 bar injection pressures, the spectral transmission reaches a minimum value. In the case of 1,100 bar the signal appears to reach a minimum steady-state value, whereas at 1,650 bar, it appears to increase after reaching a minimum transmission value.

The rate of decrease in transmission coefficient is observed to increase with increasing injection pressure. Minimum transmission coefficient is reached at 23 hours at 1,650 bar and 30 hours at 1,100 bar, while at 550 bar the same minimum is reached in 40 hours. The minimum spectral transmission value reached for the three injection pressures in around 0.90 ± 0.05. This corresponds to a percentage change in spectral transmission of 71.0 % ± 2.0 %.

Figure 6.2 shows the corresponding changes in the spectral attenuation coefficients at 405 nm with cavitation time for Fuel 1 (BDN) at the three injection pressures. The spectral attenuation coefficients increase with cavitation time irrespective of the injection pressure. The corresponding time-scales to achieve the maximum spectral attenuation coefficient at 1,650 bar, 1,100 bar and 550 bar injection pressures are 23 hours, 30 hours and 40 hours, respectively.

Variations in the spectral transmission and subsequently, in the spectral attenuation coefficient of the fuel suggest that hydrodynamic cavitation occurring across the nozzle-hole and in the receiver, is altering the chemical composition of the fuel. Sonochemical reaction have been shown to occur in organic liquids during acoustic cavitation bubble collapse[16,21]. Extrapolating

these effects to hydrodynamic cavitation suggests that the observed changes in the optical properties of the fuel are resulting from the cavitation bubble collapse occurring in the receiver during flow stagnation.

The high-pressure cavitation test-rig was found to recirculate an approximate 3.0 L volume of diesel charge with an approximate volumetric flowrate of 0.65 L/min at 1,650 bar injection pressure. Hence, the entire 3.0 L charge of diesel sample was recirculated around the rig every 4.6 minutes, corresponding to 13 cycles/hour when the rig was operated at 1,650 bar injection pressure.

The magnitude of maximum variation in the spectral attenuation coefficient of the fuel samples is found to be the same at all three injection pressures. However, these changes occur at different characteristic time-scales, i.e. it takes 23 hours (at 1,650 bar), 30 hours (at 1,100 bar) and 40 hours (at 550 bar) to achieve maximum spectral attenuation respectively.

Assuming a constant nozzle discharge coefficient at all three pressures, the time constants thus correspond to volumetric flowrates of 0.65 L/min (at 1,650 bar), 0.53 L/min (at 1,100 bar) and 0.375 L/min (at 550 bar) respectively. When the test rig is filled with approximately 3.0 L of diesel sample, the time constants correspond to 299 cycles (at 1,650 bar), 318 cycles (at 1,100 bar) and 300 cycles (at 550 bar) of fuel recirculation respectively. The similarity in the number of fuel recirculation cycles completed in order for diesel samples to achieve the maximum attenuation coefficient suggests that the chemical changes occurring in the fuel are dependent on the mass and volumetric flowrate, and are independent of the injection pressure.

The second set of pressure dependence tests on Fuel 1 (BDN) were carried out at two injection pressures of 825 bar and 1,650 bar. The tests on both pressures were conducted using the same injector nozzle of a 176 µm diameter hole; this nozzle was not used for any tests prior to these tests. 1,650 bar pressure test was the first test conducted using the said nozzle, followed by the

825 bar test. It should be noted that the 1,650 bar test results reported here were part of a 140-hour long-duration cavitation test; the complete transmission and spectral attenuation coefficient data for the 140-hour test are included in Appendix B (Figure B.1 and Figure B.2). For the purpose of comparison with the 825 bar test, only the first 40 hours of the long duration test are reported in this section. The 825 bar test was shortened in duration to 38 hours of recirculation instead of 40 hours, due to technical difficulties faced on the fourth day of testing.

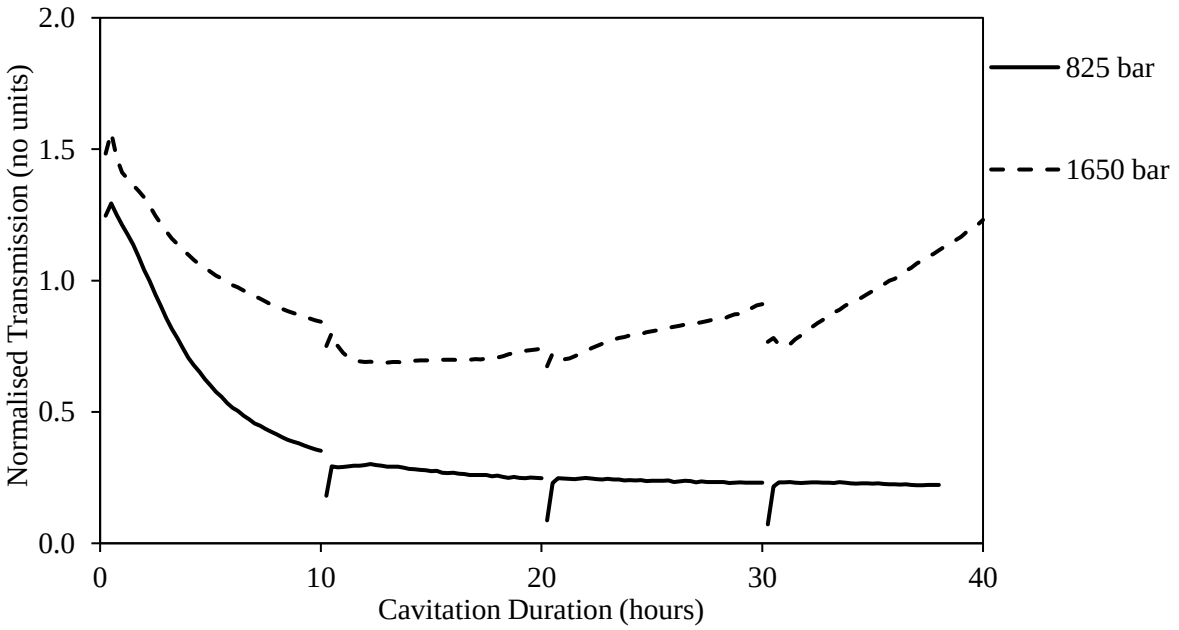

Figure 6.3 Normalised laser transmission at 405 nm against cavitation time for Fuel 1 (BDN) at 825 and 1,650 bar injection pressures

Figure 6.3 shows a comparison of the change in normalised spectral transmission of Fuel 1 (BDN) at 405 nm with cavitation time for the two injection pressures. The normalised spectral transmission is seen to decrease at both pressures in the initial stages of the cavitation tests. Transmission at 1,650 bar pressure then reaches a minimum, where after it increases at an accelerating rate. On the other hand, transmission at 825 bar carries on decreasing at a gradually decreasing rate, up to the end of the test, appearing to almost achieve a steady-state value. The minimum normalised transmission value at 1,650 bar pressure is reached at 12-hour mark.

It is observed that the zero-hour transmission values for the two pressure tests are different, wherein the 1,650 bar normalised transmission value is 1.49 and the 825 bar normalised transmission value is slightly lower at 1.25. The minimum transmission value attained at 1,650 bar injection pressure is also observed to be higher than the minimum value achieved during the 825 bar pressure test. The minimum transmission value attained for 1,650 bar test was 0.69 ± 0.01 while, at the end of testing, fuel at 825 bar injection pressure had a transmission value of 0.22 ± 0.01. The zero-hour and the minimum transmission values correspond to a maximum percentage change in spectral transmission of the fuel of 53.7% and 82.4% for 1,650 bar and 825 bar.

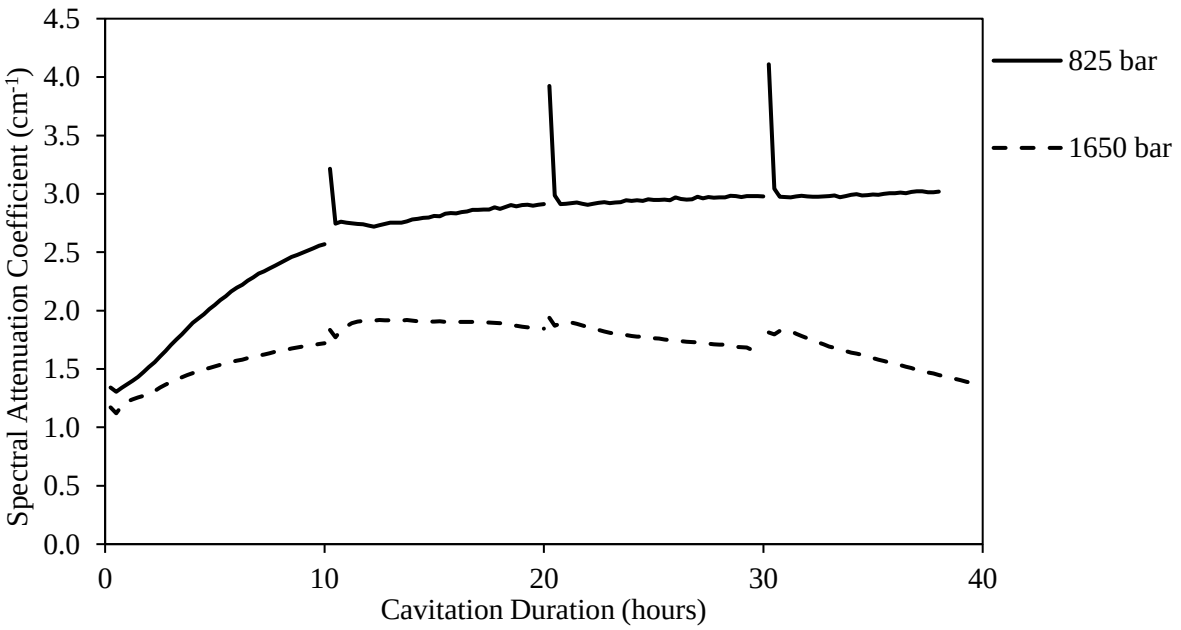

Figure 6.4 Time-dependent spectral attenuation coefficient at 405 nm against cavitation time for Fuel 1 (BDN) at 825 and 1,650 bar injection pressures

Figure 6.4 shows the corresponding variations in the time-dependent spectral attenuation coefficient at 405 nm for the pressure dependence tests of Fuel 1 (BDN) at 825 bar and 1,650 bar injection pressures. Initially, the spectral attenuation coefficient increased at both injection pressures; a maximum was reached for 1,650 bar test while at 825 bar the attenuation coefficient continued to increase at an increasingly slower rate till the end of the experimental

run. Maximum spectral attenuation coefficient at 1,650 bar pressure was reached after 12 hours of cavitation, while at 825 bar the attenuation continued to gradually increased till the end of cavitation test.

To observe the magnitude of change in the fuel's spectral transmission signals at the two injection pressures, self-normalisation of the signals was performed. Figure 6.5 shows the self-normalised spectral transmission signals against cavitation time for pressure dependence tests on Fuel 1 (BDN) at 1,650 bar and 825 bar. Self-normalisation was performed by offsetting the normalised spectral transmission signal, such that the zero-hour normalised spectral transmission for both tests was zero. The plot then showed the magnitude of normalised transmission change due to cavitation relative to the transmission value of pre-cavitated fuel.

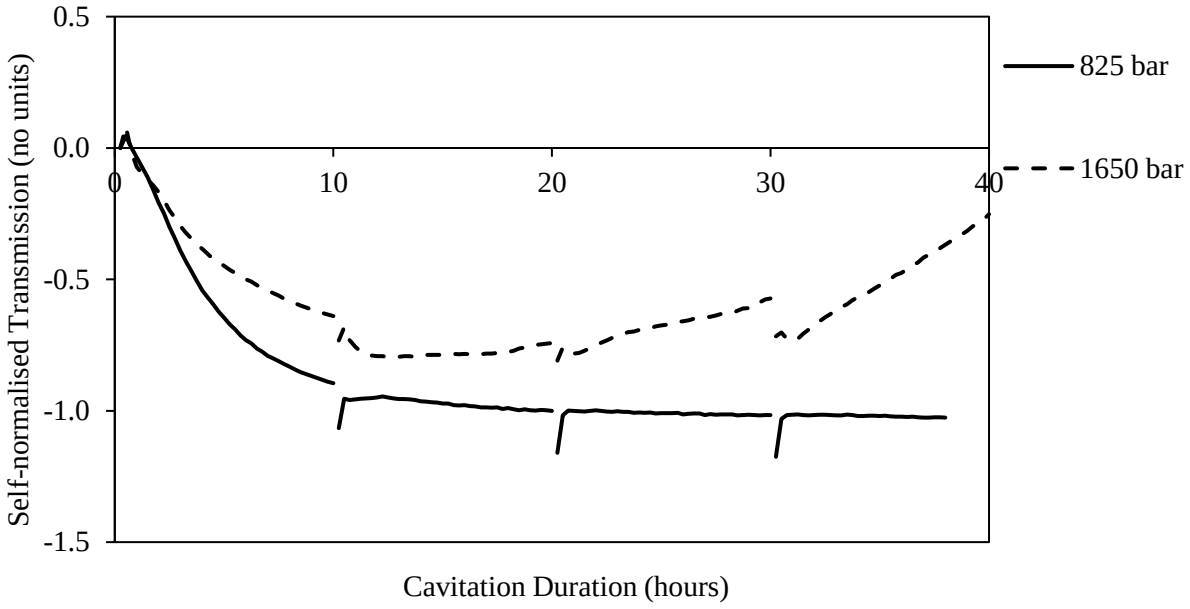

Figure 6.5 Self-normalised laser transmission at 405 nm against cavitation time for Fuel 1 (BDN) at 825 and 1,650 bar injection pressures. Self-normalisation is performed by offsetting the normalised laser transmission to obtain zero as the initial transmission value for both pressure tests

Figure 6.6 shows the corresponding self-normalised spectral attenuation coefficient against cavitation time for the 825 bar and 1,650 bar injection pressure tests. Self-normalisation offsets

the time-dependent spectral attenuation coefficient in Figure 6.4 to display the relative change in spectral attenuation coefficient due to cavitation at the two injection pressures.

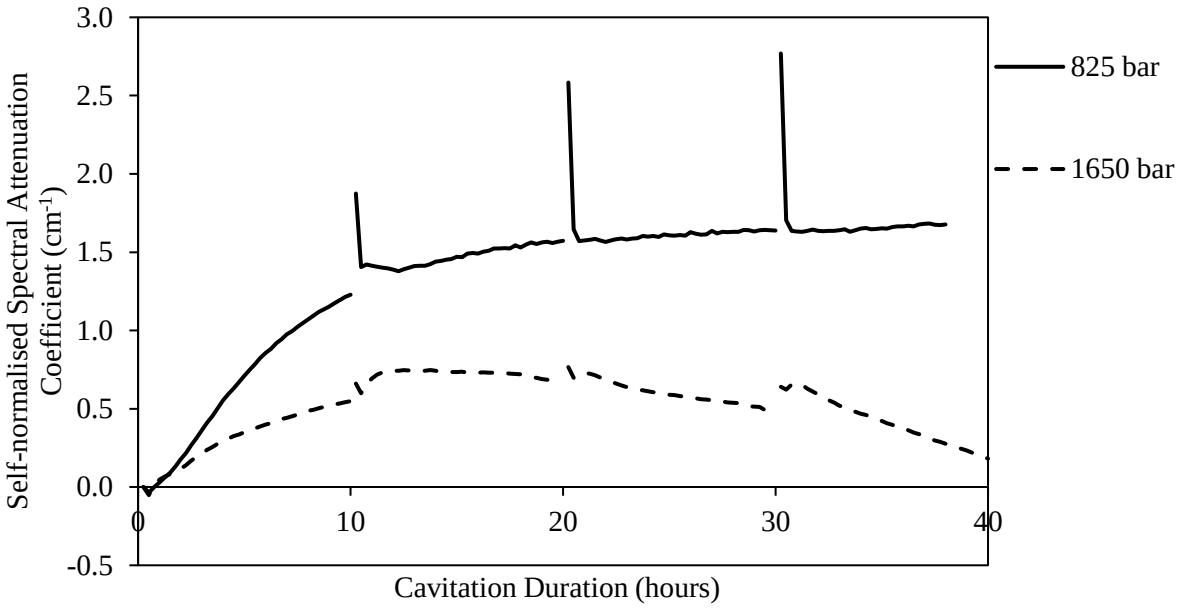

Figure 6.6 Self-normalised spectral attenuation coefficient at 405 nm against cavitation time for Fuel 1 (BDN) at 825 and 1,650 bar injection pressures. Self-normalisation is performed by offsetting the time-dependent spectral attenuation signal to obtain zero as the initial attenuation coefficient value for both pressure tests

As mentioned earlier, the injector nozzle was used for 140 hours during the 1,650 bar test before being used for the 825 bar test. It is expected that the discharge coefficient of an injector nozzle will change over time due to conditioning of the nozzle through hydro-grinding of internal surfaces and smoothening of sharp edges. This might also result in variations in the cavitation characteristics of the flow through the nozzle. Sharper nozzle inlet edges have been shown to lead to more intense geometric cavitating flow formation as opposed to hydro-grinded and rounded nozzle inlets[43,85]. The unused and unconditioned nozzle would have produced cavitating flow of higher intensity during the 1,650 bar test. By the end of the 140-hour test at 1,650 bar, the cavitation characteristics of the nozzle would have been changed as a result of hydro-grinding. This would explain the more gradual change in the attenuation coefficient of

the diesel sample at 825 bar, relative to the changes occurring in the first 40 hours of the 1,650 bar test.

To better characterise the dependence of variations in chemical and optical properties of the diesel fuel to the volumetric flowrate of diesel in the test-rig, measurements of volumetric flowrate through the test nozzle were taken at the end of each test. All flowrate measurements were conducted at injection pressures of 1,650 bar, and the fuel was allowed to reach the test temperature of 55 °C prior to the start of the measurement procedure. The readings were then used to estimate the flowrate at the test injection pressure assuming a constant discharge coefficient. Flowrate measurements after the two pressure dependence tests are quoted in Table 6.2; these measurements are averages of 8 to 10 repeated measurements.

Table 6.2 Volumetric flowrate measurements for the 176 µm test nozzle, measured at 1,650 bar injection pressure following the completion of the specified pressure tests on Fuel 1 (BDN). The measurements are quoted with the standard deviation over the 8 to 10 repeats.

After 1,650 bar test	After 825 bar test
0.936 ± 0.003 L/min	0.933 ± 0.005 L/min

The measured volumetric flowrates for the test nozzle after the two tests indicate a negligible decrease. It can thus be assumed that the discharge coefficient of the nozzle remains the same for the two tests. Assuming the discharge coefficient remains constant at 825 bar injection pressure, the variation on self-normalised spectral attenuation coefficient can then be calculated as a function of the number of fuel recirculation cycles completed by the approximated 3.6 L charge of diesel sample over the course of the two tests; this is shown in Figure 6.7.

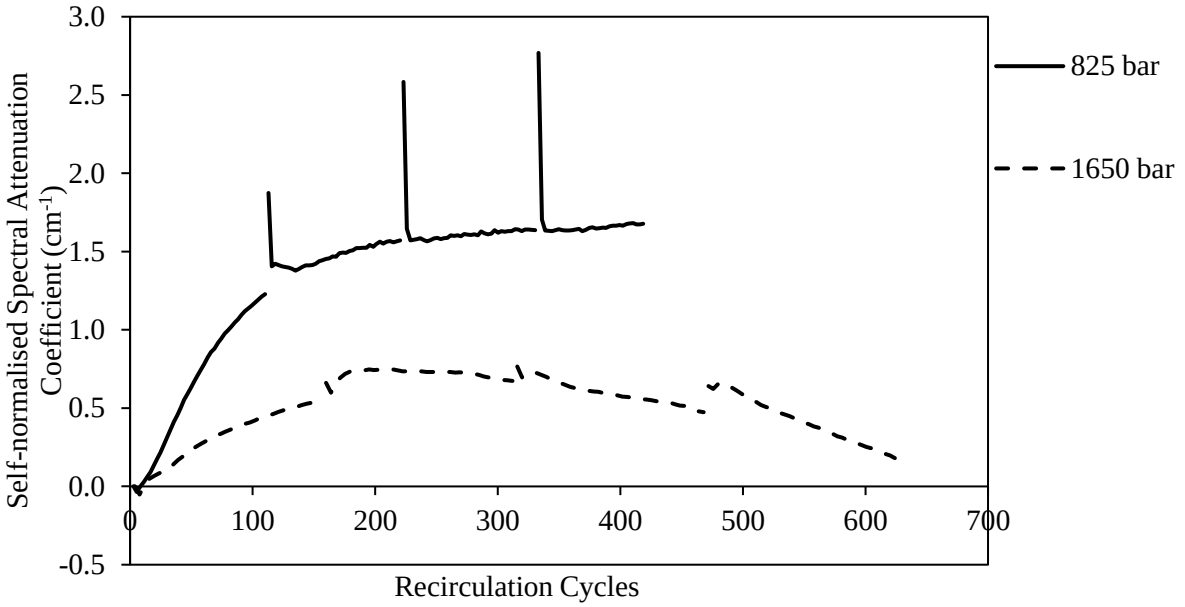

Figure 6.7 Self-normalised spectral attenuation coefficient at 405 nm against number of fuel recirculation cycles completed by respective Fuel 1 (BDN) test charges at 825 and 1,650 bar injection pressures

Comparison of the two upstream pressure tests as a function of recirculation cycles in Figure 6.7 shows that the diesel sample at 1,650 bar completed around 624 cycles by the end of the 40 hours, while the sample at 825 bar completed 418 cycles in the 38-hour test. It is observable that the maximum attenuation reached for each injection pressure differ, wherein 1,650 bar pressure test attains a maximum after ~200 cycles, while at 825 bar the attenuation continues to rise till the completion of the 418 cycles (38 hours).

The results indicate that upstream pressure affects the rate of change in diesel sample's chemical composition (aside from impacting the volumetric flowrate). At higher injection pressure (~200 cycles, 1,650 bar) number of cycles completed to reach the maximum attenuation is less than half of that at lower injection pressure (>418 cycles, 850 bar).

Investigations on nozzle flows have shown a positive correlation between injection pressure and hydrodynamic cavitation intensity; the larger injection pressures produce larger pressure gradients that result in larger vapour formations[79,81,83–85]. Higher intensity cavitation results in formation of larger cavitation structures (such as cavitation sheets or cavitation clouds) that

produce flows of larger vapour-volume fractions. Collapse of these structures is expected to produce larger concentrations of 'hot-spots' of extreme pressures and temperatures in the liquid medium, where sonochemical-like reactions are known to occur. Therefore, the results obtained from the injection pressure tests (Fuel 1 (BDN) at 825 bar and 1,650 bar) suggest an agreement with the findings of these reports.

The third set of pressure dependence tests was performed on Fuel 6 (BDA) at two injection pressures of 825 bar and 1,650 bar. The tests on both pressures were conducted using the same injector nozzle of a 173 µm diameter hole; this nozzle was used for other investigations with Fuel 6 (BDA) prior to these tests. Chronologically, 825 bar injection pressure test was conducted prior to the 1,650 bar test. Before the 825 bar test, the injector nozzle had been used for 100 hours of recirculating cavitating flow tests; whereas, at the start of 1,650 bar test the nozzle had been used for 220 hours of recirculating flow tests.

Figure 6.8 shows the normalised spectral transmission and the emanating self-normalised spectral transmission signal against cavitation time at the two test pressures for Fuel 6 (BDA). Self-normalisation was performed as in the case of Fuel 1 (BDN) pressure dependence tests mentioned earlier in the section. The spectral attenuation coefficient and the corresponding self-normalised spectral attenuation coefficient against cavitation time is shown in Figure 6.9.

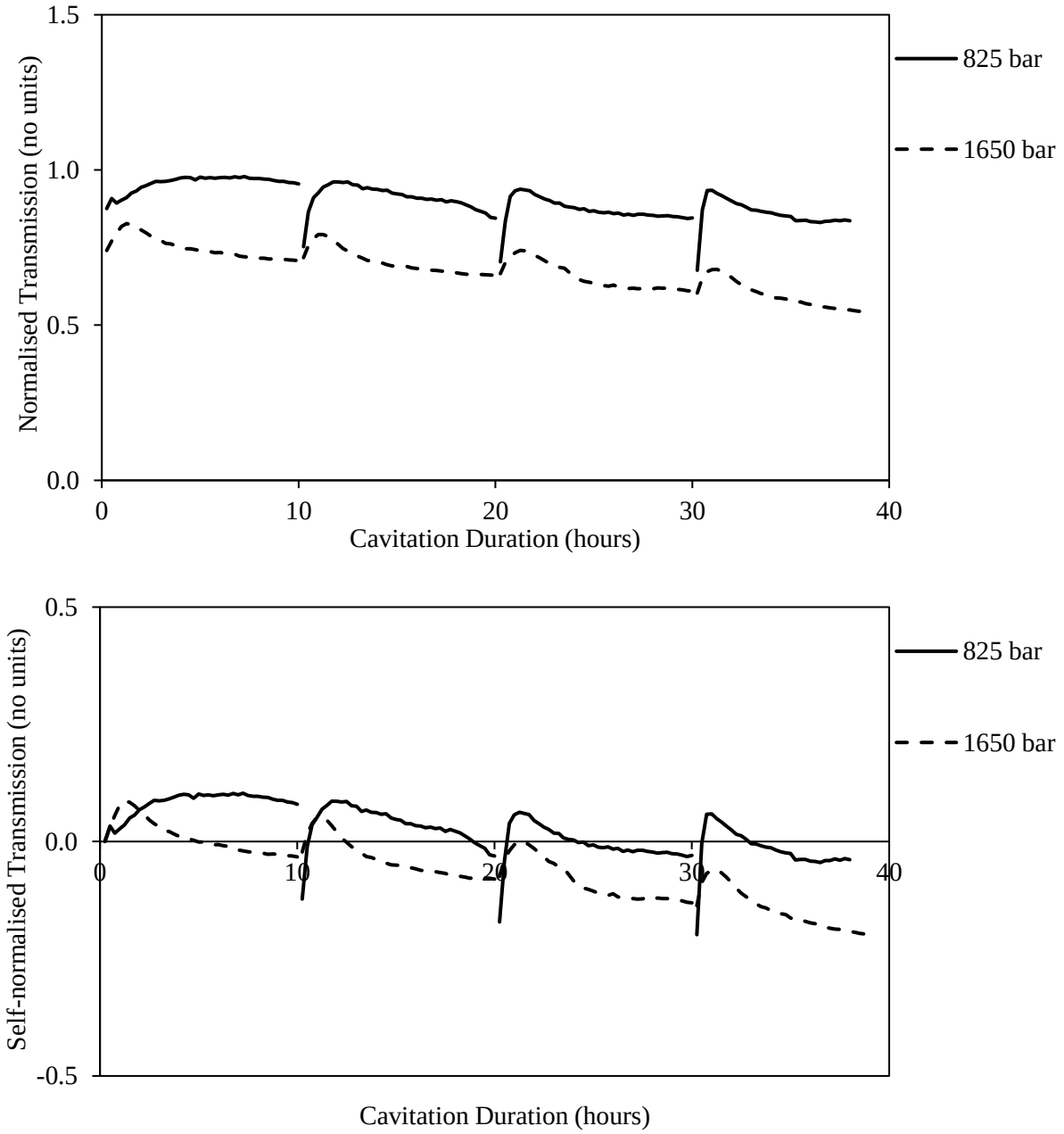

Figure 6.8 Normalised laser transmission signal (top) and self-normalised laser transmission at 405 nm against cavitation time for Fuel 6 (BDA) at 825 and 1,650 bar injection pressures

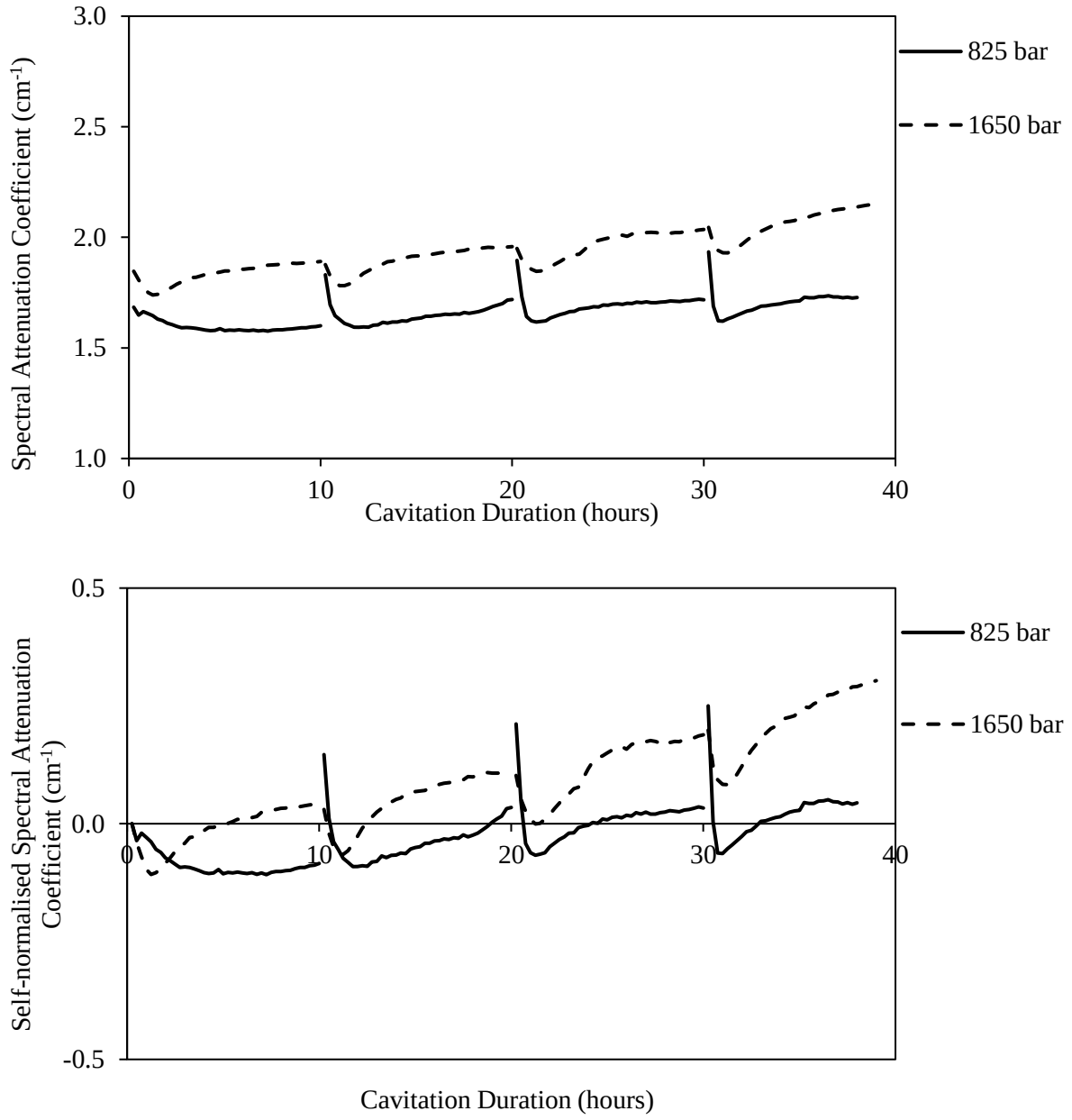

Figure 6.9 Spectral attenuation coefficient (top) and the self-normalised spectral attenuation coefficient at 405 nm against cavitation time for Fuel 6 (BDA) at 825 and 1,650 bar injection pressures

Comparing the change in spectral attenuation coefficient of Fuel 6 (BDA) with cavitation time in Figure 6.9, it is observed that initially the attenuation at both pressures decreases to a minimum, followed by a gradual increase for the remainder of the cavitation test duration. The maximum decrease in attenuation was found to be around 0.11 cm^{-1} for both 1,650 bar and 825 bar tests. The minimum attenuation was achieved during the first day of cavitation for both

tests; the characteristic time taken to achieve minimum attenuation was around 1.5 hours for 1,650 bar and 4.7 hours for 825 bar.

Decrease to a minimum attenuation was followed by a monolithic increase that continued till the end of both tests. The rise in attenuation was faster at 1,650 bar injection pressure, wherein the highest self-normalised attenuation signal achieved by the end of the experiment was +0.30 cm^{-1}. The highest self-normalised attenuation achieved by the end of 825 bar injection pressure test was +0.05 cm^{-1}.

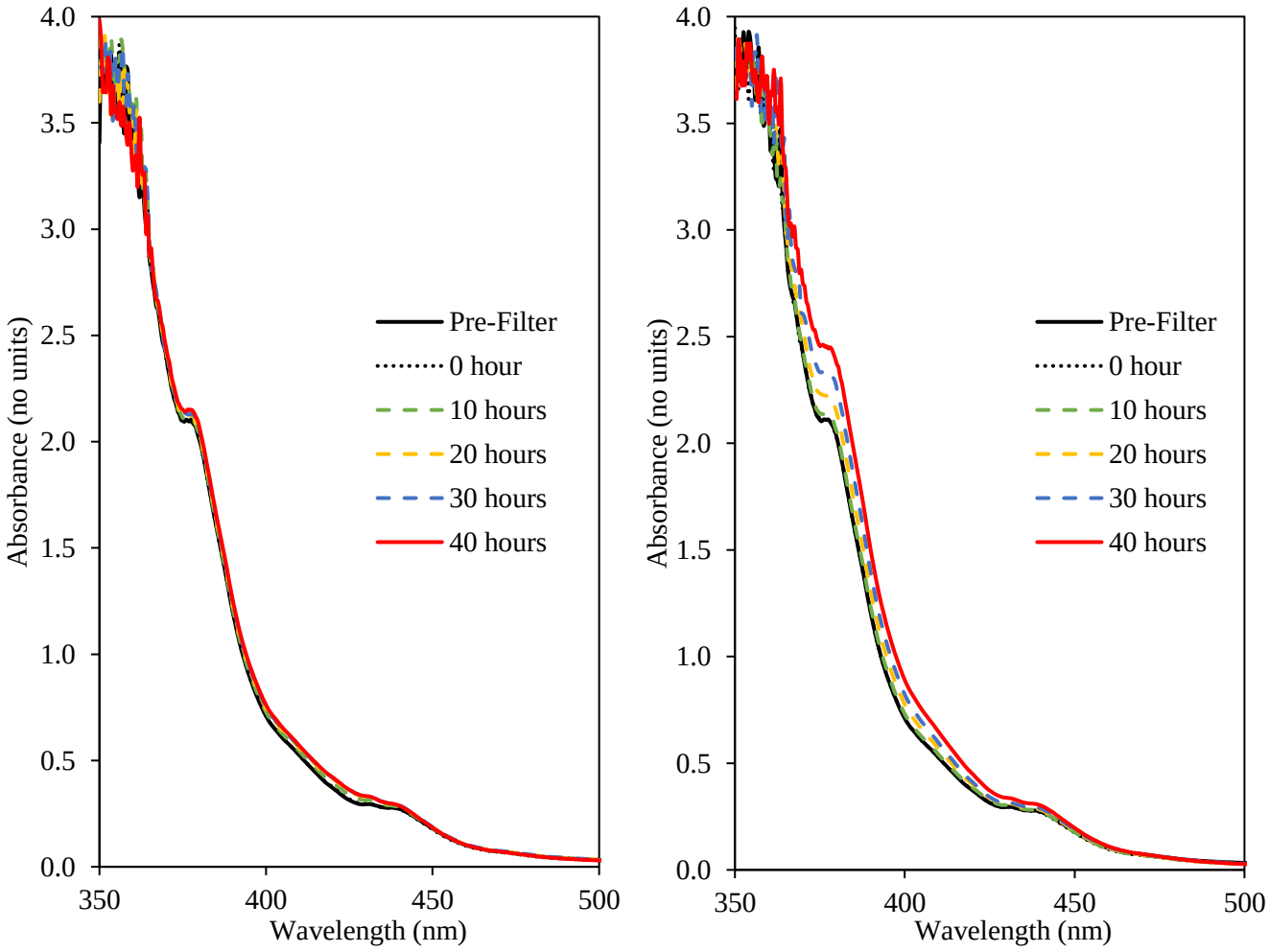

Figure 6.10 Absorption spectra of cavitated Fuel 6 (BDA) samples from 825 bar test (left) and 1,650 bar test.

The monolithic increase of the sample attenuation coefficients over-time is explained by the uv-visible spectra measurements of the samples shown in Figure 6.10. A broad-band increase in absorption of the diesel samples was observed over-time with no absorption structures at 405 nm wavelength at both injection pressures. The broad-band absorbance is caused by absorbance of the suspended particulates is the diesel samples that coagulate overtime, forming larger particulates, thorough mechanisms similar to those observed by Price et al. (2015)[16]. The rate of increase in the broad-band absorbance is distinctly higher for the higher injection pressure test samples, indicating a positive correlation between the injection pressure and particulate formation and coagulation rates.

Volumetric flowrate measurements for the test injector nozzle were performed for characterisation of the variations in diesel sample's properties based on the number of recirculation cycles completed in the test durations. Table 6.3 provides the volumetric flowrates for the nozzle at 1,650 bar injector pressure measured at the end of the specified pressure tests.

Table 6.3 Volumetric flowrate measurements for the 173 µm test nozzle, measured at 1,650 bar injection pressure following the completion of the specified pressure tests on Fuel 6 (BDA). The measurements are quoted with standard deviation over the 8 to 10 repeats.

After 825 bar test	After 1,650 bar test
0.883 ± 0.004 L/min	0.793 ± 0.005 L/min

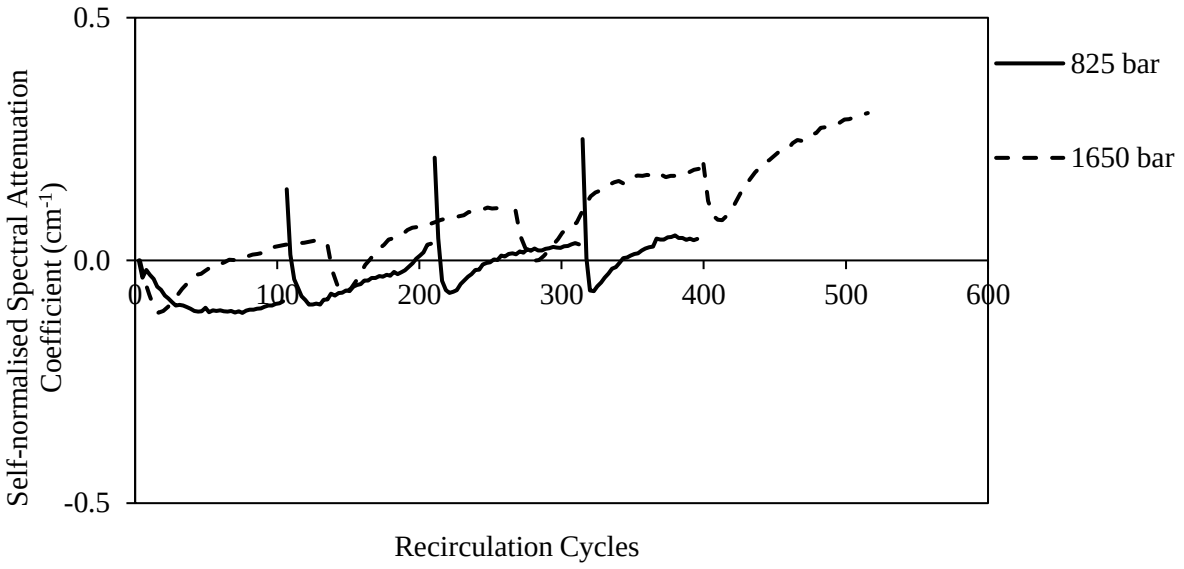

Figure 6.11 Self-normalised spectral attenuation coefficient at 405 nm against number of fuel recirculation cycles completed by respective Fuel 6 (BDA) test charges at 825 and 1,650 bar injection pressures

The volumetric flowrate measurements were then used to obtain the recirculation cycle dependent self-normalised spectral attenuation coefficient, shown in Figure 6.11. The tests were able to achieve a total of 515 and 395 recirculation cycles during the 1,650 bar and 825 bar tests respectively. It can be observed that the apparent minimum attenuation at 1,650 bar injection pressure was achieved after ~20 cycles of recirculation, while it took ~52 cycles to achieve the minimum at 825 bar. This indicates that the changes occurring in the diesel samples as a result of cavitation are independent of the volumetric flowrate of the test charges in the test-rig and are, instead, dependent on the intensity of cavitation as a function of injection pressure.

6.1 Combined Discussion of Pressure Dependence Tests

The high-pressure cavitation test-rig has been used to investigate the effect of injection pressure on the change in chemical and optical properties of Fuels 1 (BDN) and 6 (BDA). Both fuels are conventional diesel fuels, albeit they have been derived from different crude-oil stocks. Fuel 6 (BDA) was aged for over 6 years while Fuel 1 (BDN) was part of a newer batch of fuels.

It is known that the composition of diesel fuels is strongly dependent on the crude-oil it is distilled from, therefore Fuels 1 and 6 are expected to have different chemical and physical properties, regardless of their storage age.

The pressure dependence tests reported in this section have been performed using two types of injector nozzles. The old injector nozzle was the 213 μm single-hole nozzle that has been pre-conditioned from extensive usage with various fuels prior to its use in the pressure dependence tests. This nozzle had initial honing value of 20 %, however this value was expected to be higher for the test discussed in this section, due to excessive usage. The new injector nozzles were smaller in nozzle-hole size (176 μm and 173 μm) and were previously either used for a limited number of tests with a single fuel type or not at all; their honing values were ~ 13 %. It is reasonable to expect that unused nozzle will initially generate high intensity cavitating flow; and over time the flow passages inside the nozzles will get conditioned, reducing their propensity to geometrically cavitate.

Comparison for the influence of nozzle type on the rate of change in Fuel 1's chemical and optical properties can be made from comparison of the 1,650 bar injection pressure tests with the old and the new nozzles. Comparison based on the volumetric flowrate (or number of recirculation cycles) is more appropriate as opposed to cavitation duration due to difference is nozzle hole sizes. Time constants for the fuel samples indicated that it took ~299 and ~200 recirculation cycles for tests with the old nozzle and the new nozzle to achieve maximum spectral attenuation coefficients (at 1,650 bar), respectively. This suggests that the cavitation occurring in the smaller diameter new nozzle (176 μm) was of higher intensity as compared to the larger diameter old nozzle (213 μm), even after eliminating the differences in the flowrate of the two nozzles. It should be noted that the test with old nozzle had a smaller volume of fuel charge in the test rig (3.0 L as opposed to 3.6 L), however having a smaller volume is expected

to have a quicker overall change in fuel properties, therefore the conclusion is not likely to change based on the results reported here.

The results for the old 213 µm nozzle (> 20 % hone) showed only a volumetric flowrate dependence, whereas the results for the new 176 µm nozzle (~13 % hone) also showed an injection pressure dependence. The difference in results from the two nozzles was believed to be caused by the effect of their hole size and honing on the nature of cavitating flow forming in the nozzle. The lower level of honing for the new nozzle was believed to increase its propensity of forming geometric cavitation, while also making it more sensitive to changes in injection pressure.

The two conventional diesel fuels (Fuel 1 (BDN) and 6) tested using smaller (176 µm and 173 µm) nozzles have both indicated a faster rate of change in fuel's spectral attenuation coefficient at higher injection pressures. The rate of change for the two fuels was found to be independent of the volumetric/ mass flowrate of fuels in the recirculation rig.

Spectra measurements of Fuel 1 (BDN) were found to include an absorbance structure around 405 nm wavelength (see Chapter 5). This absorbance band was observed to increase in absorbance, followed by a gradual decrease. The rate of change in the absorbance of the band in the two injection pressure dependence tests revealed that the change occurred at a faster rate during the 1,650 bar test. Maximum attenuation coefficient for Fuel 1 (BDN) was achieved after ~ 200 recirculation cycles at 1,650 bar whereas at 825 bar, the maximum attenuation was not achieved even after ~ 400 recirculation cycles.

Spectra measurements of Fuel 6 (BDA) samples showed an absence of absorbance structures at 405 nm wavelength; instead the spectra indicated a monolithic increase in broad-band absorption of the fuel samples with cavitation time, this was believed to occur as a result of particulate formation and growth. The constant formation of particulates in the fuel charges

resulted in a continuous increase in spectral attenuation of the fuel during the cavitation tests. A difference in the number of recirculation cycles completed by the Fuel 6 (BDA) samples at the two test injection pressures to achieve maximum attenuation coefficient was observed. The rate was change was found to be higher at higher injection pressures. The results showed an accelerated rate of change in optical properties of the fuel at elevated injection pressures, not as a consequence of higher volumetric/mass flowrate but as a result of higher intensity of cavitating flow forming in the test nozzles.

Comparison of the two set of injection pressure dependence tests on Fuel 1 (BDN) have shown that only a flowrate dependence exists for the tests with the larger (213 μm) nozzle while an injection pressure dependence exists for the tests with smaller nozzles. A correlation between the injection pressure and nozzle-hole diameter (and honing levels) on the intensity of cavitation formed has been suggested. However, based on the two set of experiments the relationship is not quantifiable. Experiments using varying nozzle-hole sizes at different injection pressures are required to be conducted to determine the minimum nozzle-hole diameter needed for injection pressure dependence to occur.

Chapter 7
Long Duration Tests

The long duration tests involved recirculating two test fuels in the high-pressure test-rig for over 100 hours of cavitating flow at 1,650 bar rail pressure. The conventional diesel (Fuel 1 (BDN)) and the paraffinic model diesel were the two fuels to be tested in the long duration investigation. Fuel 1 (BDN) was tested twice; once, using the old 213 µm hole injector nozzle, and then again using one of the new 173 µm hole injector nozzles. The paraffinic model fuel was only tested using the old 213 µm hole injector nozzle. In-situ spectral transmission measurement setup used for the old injector nozzle tests employed the old 20 mW laser module, while the Fuel 1 (BDN) test conducted using the new injector nozzle utilised the 35 mW laser module. The experimental variables for the long duration investigation are listed in Table 7.1 below.

Table 7.1 Experimental variables for long duration tests

Test Fuels	• Fuel 1 (BDN) • Paraffinic Fuel
Test Durations	104 - 140 hours 8 hours per day (paraffinic model fuel) 10 hours per day (Fuel 1 (BDN))
Injection Pressure	1,650 bar
Pre-Injection Fuel Temperature	55 °C
Filter Size	3 µm Filter

Figure 7.1 shows the normalised spectral transmission of Fuel 1 (BDN) and the paraffinic model fuel over the duration of the prolonged cavitation tests. Fuel 1 (BDN) test was conducted for 130 hours over 13 days (10 hours per day), and the paraffinic model fuel test was conducted for 104 hours over 13 days (8 hours per day).

Observing the variation in spectral transmission of the two fuels, it was found that the paraffinic model fuel had significantly higher initial spectral transmission signal relative to Fuel 1 (BDN). This was expected as the paraffinic fuel had a composition of 100 % n-paraffins, which are devoid of conjugated pi-bond system chromophores. The absence of chromophores in the n-paraffins makes them very clear under visible light, giving the paraffinic fuel high spectral transmissivity at the 405 nm measurement wavelength. Fuel 1 (BDN), on the other hand, was a complex mixture of compounds, including chromophores that enabled it to absorb radiation in the visible light region.

The paraffinic fuel experienced a gradual decrease in spectral transmission as it was subjected to recirculating hydrodynamic cavitating flow. The change in spectral transmission of the model fuel was observed to be a constant-rate decrease without any indication of reaching a steady-state value. The change of spectral transmission for Fuel 1 (BDN) displayed the behaviour that had been observed in other Fuel 1 (BDN) experiments, mentioned in previous sections. As observed earlier, the transmissivity of Fuel 1 (BDN) initially dropped to a minimum value followed by an asymptotic rise to a steady-state value.

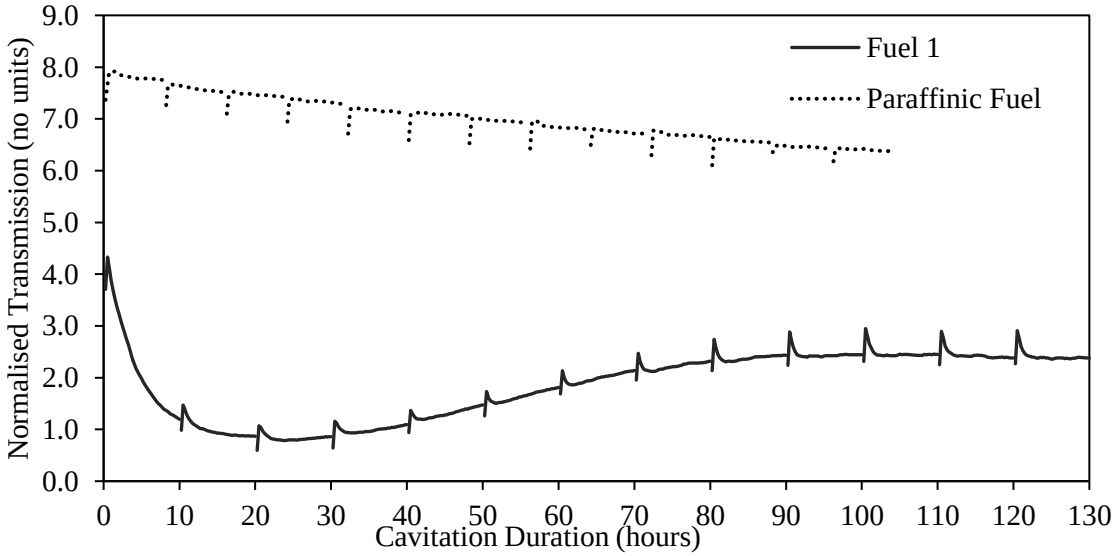

Figure 7.1 Normalised laser transmission at 405 nm against cavitation duration for Fuel 1 (BDN) and Paraffinic Model Fuel.

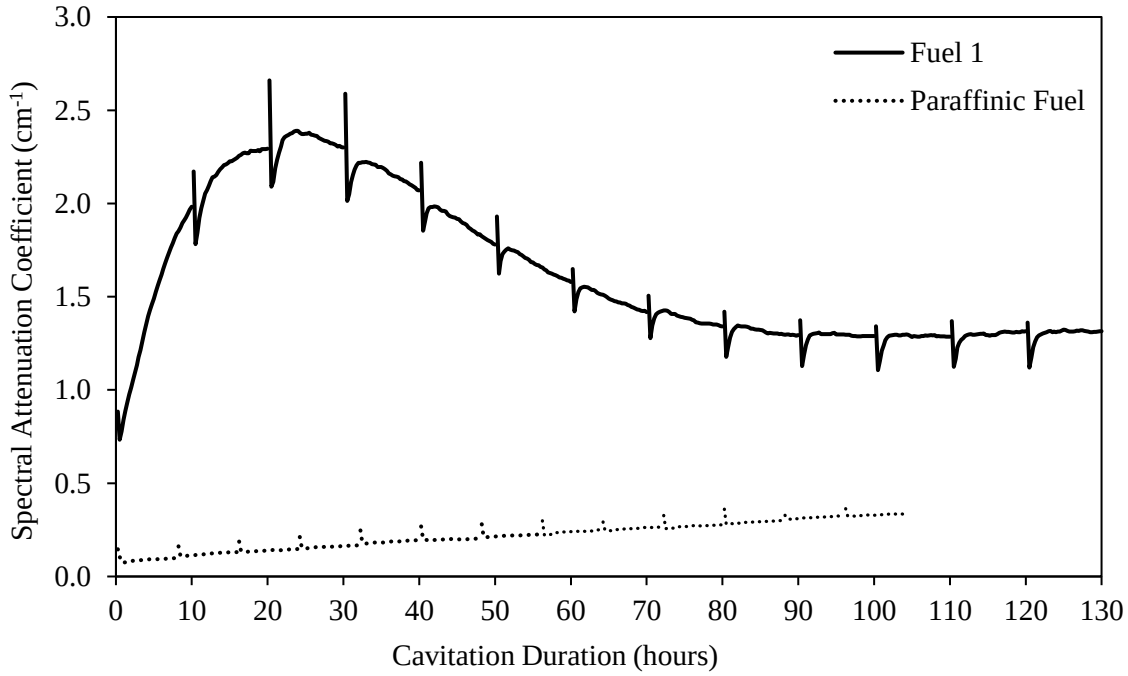

Figure 7.2 Spectral attenuation coefficient at 405 nm against cavitation duration for Fuel 1 (BDN) and Paraffinic Model Fuel.

Figure 7.2 shows the corresponding time-dependent spectral attenuation coefficients of Fuel 1 (BDN) and the paraffinic model fuel at 405 nm during the long duration high-pressure cavitation tests. As observed from the transmission coefficient variations (Figure 7.1), the paraffinic fuel had a very low initial spectral attenuation coefficient value that experienced a gradual increase over the course of the 104-hour experiment from ~ 0.10 to ~ 0.34 cm^{-1} – an increase in attenuation of ~ 240 %. The monolithic increase in attenuation of the model fuel indicated the build-up of particulates in the circulating fuel charge. The build-up of particulates was previously observed to increase the broadband absorbance of fuels. The trend observed at 405 nm for the model fuel was found to have similarities with the monotonous rise in attenuation of Fuel 3 (B30) observed during the fuel tests. The trend for Fuel 3 (B30) was suggested to be enhanced by the absence of absorbance structures around 425 nm in the spectra measurements, which were believed to indicate presence of three to five ring poly-aromatic hydrocarbon species. Similarity of model fuel's behaviour to Fuel 3 (B30) at 405 nm also

suggested an absence of absorbance structures at 425 nm in the spectra of the paraffinic model fuel. UV-visible spectra measurement of an undiluted non-cavitated paraffinic model fuel sample shown in Figure 7.3, confirmed the absence of absorbance structures around 425 nm.

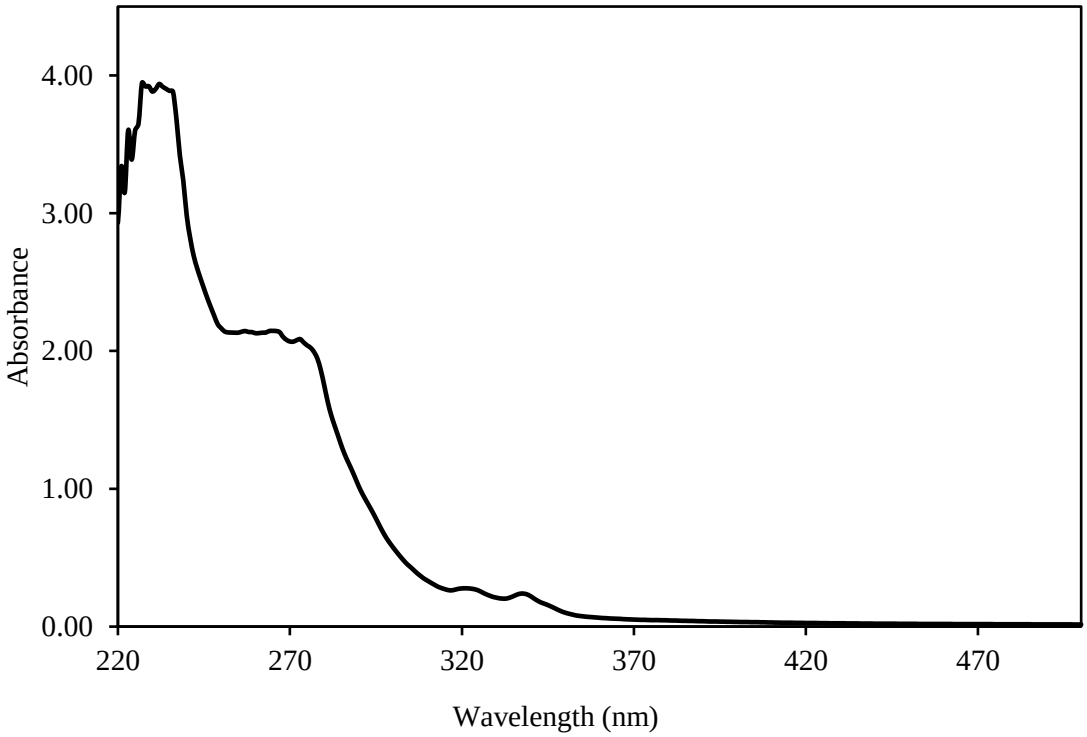

Figure 7.3 Absorbance spectra of a pure non-cavitated paraffinic model fuel sample in the wavelength range of 190 – 500 nm

Variation in time-dependent spectral attenuation coefficient of Fuel 1 (BDN) showed a sharp increase in absorbance of the fuel that reached a maximum value after ~ 25 hours of cavitation. The rise in attenuation corresponded to an increase of ~ 220 %. Following the rise to maximum, the attenuation coefficient decreased asymptotically to reach a steady-state value after ~ 100 hours. The steady-state value corresponded to an overall change in the fuel's attenuation coefficient of ~ 77 % (increase from the pre-cavitation value).

The difference in behaviour of the two fuels, subjected to hydrodynamic cavitation under similar conditions was found to be significant. Paraffinic fuel showed very little optical activity at 405 nm, this was contrasted by the large variations observed for Fuel 1 (BDN). As discussed

earlier, changing optical activity of fuels is indicative of chemical reactions that lead to formation/ destruction of chromophores. The difference in optical/ chemical behaviour was attributed to the compositional differences of the two fuels. It was suggested that the 100% n-paraffins present in the model fuel increased its chemical stability, while the presence of naphthenes and particularly the ~ 25 % aromatic hydrocarbons in Fuel 1 (BDN) made it more susceptible to chemical changes when subjected to cavitation. It is well known that pyrolysis-like reactions, capable of occurring at cavitation bubble collapse, can cause C-C and C-H bond cleavage, followed by molecular recombination that may form poly-aromatic hydrocarbons PAHs (among other species), and eventually lead to the formation of carbonaceous nano-particles[16]. It is believed that the mechanisms of PAH formation, beginning with paraffinic hydrocarbons have rates relative lower than that of the cyclic species such as aromatic hydrocarbons; this argument was supported by the observation of slower changes occurring in the spectral attenuation of the paraffinic model fuel. Chemical modelling of various hydrocarbon fuels in pyrolytic conditions can be performed to further justify this conclusion.

The long duration experiment of Fuel 1 (BDN) was repeated with an unused injector nozzle of a smaller nozzle-hole diameter (173 μm). The time-dependent normalised spectral transmission and the corresponding spectral attenuation coefficient of the fuel, during the repeated test, are shown in Figure 7.4 and Figure 7.5, respectively.

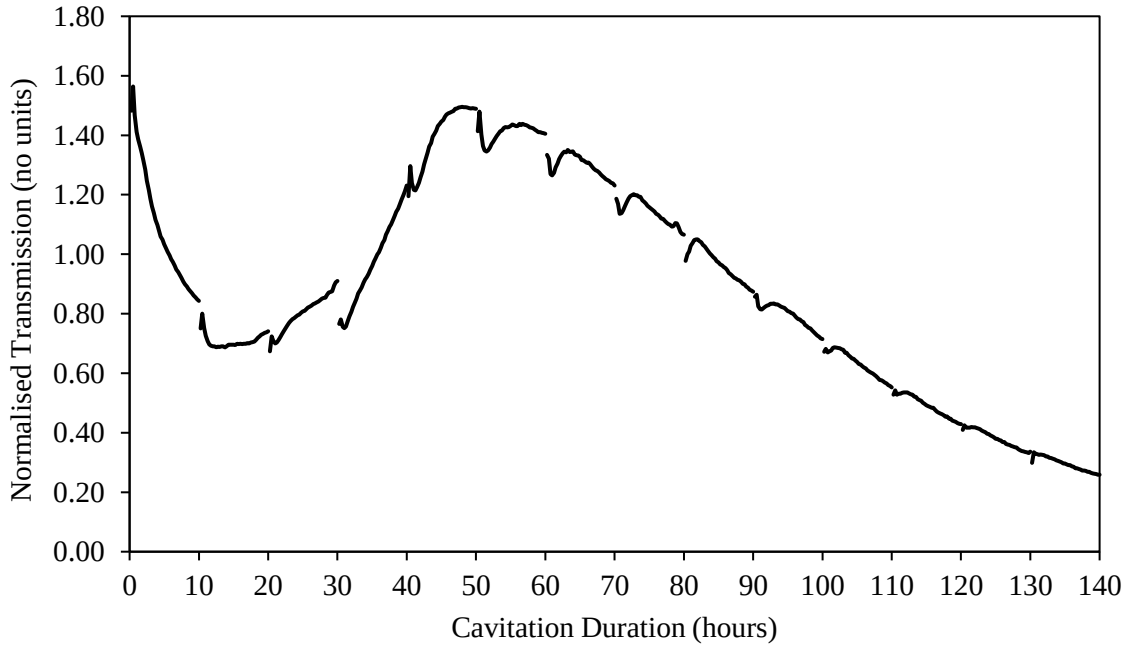

Figure 7.4 Normalised laser transmission at 405 nm against cavitation duration for Fuel 1 (BDN) at 1,650 bar injection pressure (173 µm nozzle).

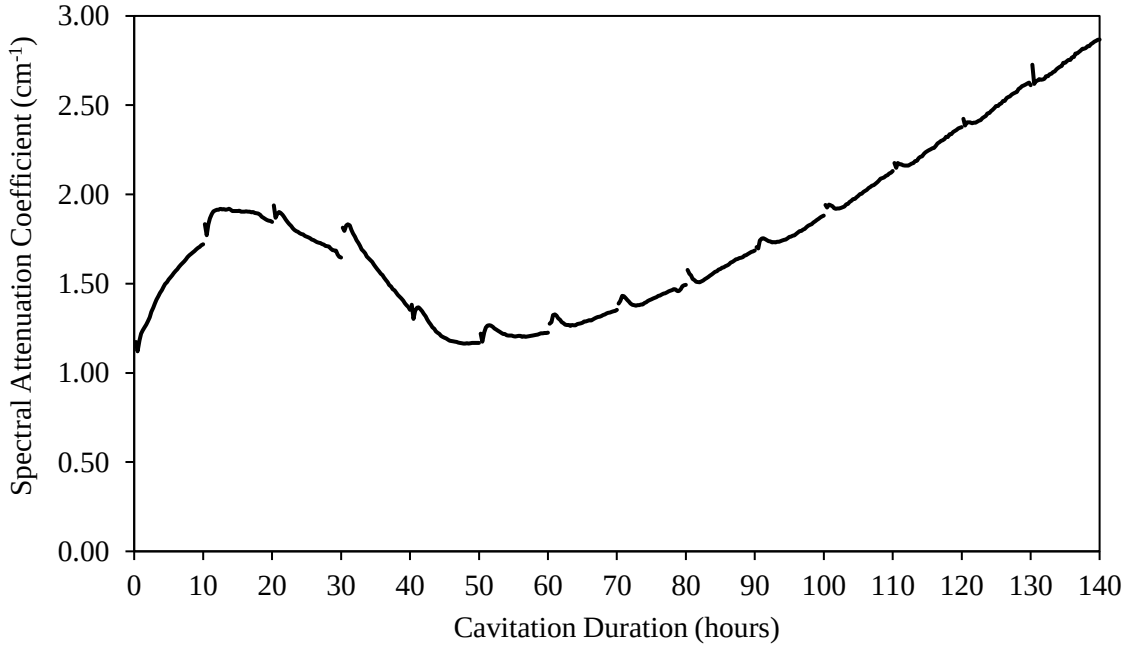

Figure 7.5 Spectral attenuation coefficient at 405 nm against cavitation duration for Fuel 1 (BDN) at 1,650 bar injection pressure (173 µm nozzle).

Variations in the spectral attenuation coefficient of Fuel 1 (BDN) over the 140-hour experiment show an initial increase to a maximum, followed by a decrease to a minimum, which is subsequently followed by a steady increase in attenuation till the end of the experiment. The initial maximum attenuation was achieved after ~ 12 hours of cavitation, and the minimum was achieved after ~ 48 hours.

Comparison of the 173 μm nozzle test results with the earlier 213 μm nozzle test showed similarities in trends of the two experiments. Both tests indicated an initial rise in attenuation coefficient of the fuel when subjected to the 1,650 bar injection pressure cavitating flow. The rise was followed by a decrease in attenuation to a steady-state value during the earlier test, whereas in the case of 173 μm nozzle test, the attenuation dropped to a minimum, whereafter it steadily increased for the remainder of the experiment.

The difference in time-scales to achieve maximum attenuation for the two tests indicated an effect of nozzle hole diameter on the cavitating flow characteristics of the diesel fuel. The use of smaller nozzle indicated a faster rate of change in the diesel fuel properties, which suggests that the intensity of hydrodynamic cavitation at a fixed injection pressure was larger for the smaller diameter nozzle.

The effect was believed to be further intensified by the age and honing levels of the nozzles. The 213 μm nozzle (> 20% hone) had been used for numerous cavitation tests prior to its use for the long duration test, thus it was believed that the internal flow passages of the nozzle had been smoothened over time. The 173 μm nozzle (~ 13 % hone), on-the-other-hand, was previously unused, which suggests that its internal surfaces and passages would still have had roughness and sharp edges inherent from its manufacturing processes. Nozzles with sharp edges and higher surface roughness have been shown to produce cavitating flows of higher intensities. Therefore, it would be correct to assume that the 173 μm nozzle produced cavitating

flows of higher intensities than the 213 μm nozzle, due not only to its smaller nozzle size but also because of the rougher internal flow passages. The higher intensity cavitating flow would then magnify the chemical effects and result in faster changes in fuel properties, as observed from the experimental results.

Increase in the attenuation of the fuel to a maximum and the subsequent decrease, was observed in both experiments; however, while the 213 μm nozzle test appeared to reach a constant minimum value, the 173 μm nozzle test showed a steady rise in attenuation till the completion of the test. The approximately linear rise in attenuation was believed to be the effect of particulate formation in the circulating fuel charge, this was deemed to be similar to the effect observed for the paraffinic model fuel during its long duration experiment.

Build-up of particulate suspension in a fuel is believed to change its broadband absorbance characteristics. This has been observed from the uv-visible spectra measurements of Fuels 1 – 5 in the fuel tests. In order to relate the linear rise in attenuation to particulate build-up, Fuel 1 (BDN) samples, drawn from the test-rig during the 140-hour test, were subjected to uv-vis absorption spectra measurements.

Figure 7.6 and Figure 7.7 show spectra measurements of the 10-hourly discrete fuel samples drawn from the test-rig during the 140-hour Fuel 1 (BDN) cavitation test. Figure 7.6 shows the spectra measurements of pure fuel samples in the wavelength range of 350 – 500 nm. Increase in absorbance around the 425 nm structure was observed for the 10^{th} hour sample. This absorbance then decreased; and the lowest absorbance in the 425 nm absorbance structure was reached by the 50^{th} hour sample, where the absorbance peaks appeared to be destroyed. Beyond the 50^{th} hour sample, spectra absorbance appeared to steadily increase up to the last sample of the test. The absorbance increase observed between the 50^{th} and the 140^{th} hour samples is referred to as the broadband absorbance increase, indicative of the particulate suspension

building-up in the fuel samples. The broadband effect was observable in wavelengths below 375 nm from the beginning of the experiment; this was due to the lack of absorbance structures in that region.

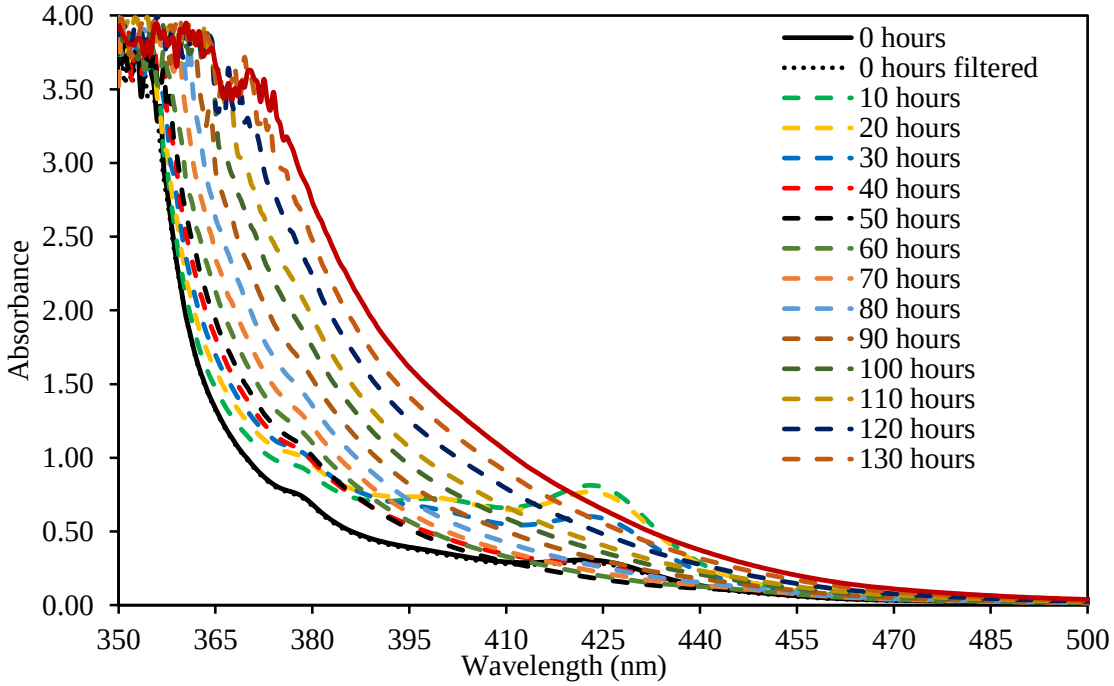

Figure 7.6 Fuel 1 (BDN) discrete sample spectra for pure samples in the 350 - 500 nm range

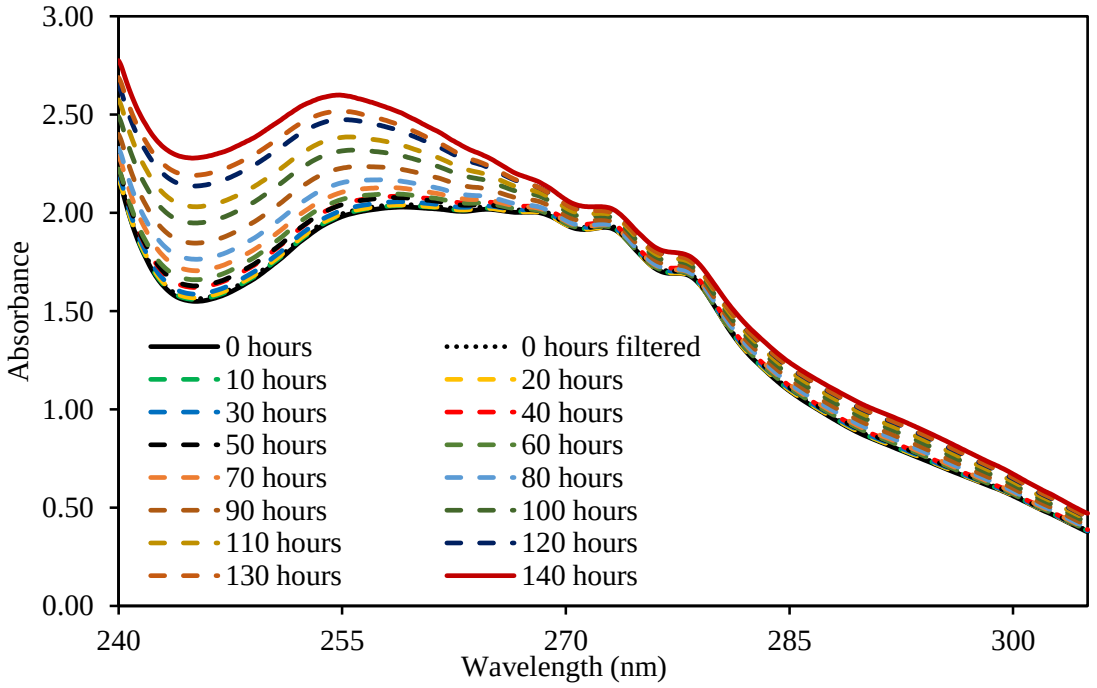

Figure 7.7 Fuel 1 (BDN) discrete sample spectra for DRF 520 diluted samples in the 240 – 305 nm range

Figure 7.7 shows the absorbance spectra of diluted Fuel 1 (BDN) samples (DRF 520) in the measurement range of 240 – 305 nm. The systematic increase in absorbance around the 245 nm trough provided another indication of the broadband absorbance increase. The benzenoid band, characteristic of mono-aromatic hydrocarbons, showed a smaller increase in absorbance as compared to the broadband absorbance increase. However, the small increase in benzenoid band region was believed to be a combined effect of the mono-aromatic species and the particulate suspension absorbances. Eliminating the broadband absorbance increase - by normalising the spectra at 245 nm - would clearly indicate a systematic decrease in absorbance of mono-aromatic hydrocarbons, thus suggesting a decrease in their concentration in the fuel samples resulting from the cavitation.

Experiments of conventional diesel fuel and the n-paraffin based model fuel have been conducted that have provided an insight into the behaviour of certain diesel fuel components when they are subjected to hydrodynamic cavitating flow. Examination of the in-situ time-dependent laser attenuation coefficients of the two fuels has shown that the paraffinic model fuel experienced little change in optical properties during the cavitation tests. In contrast, the conventional diesel (Fuel 1 (BDN)) displayed large variations in its spectral attenuation. It has been suggested that the difference in optical activity of the two fuels was resultant from the presence of cyclic species such as naphthenes and aromatic hydrocarbons in the conventional diesel, which were known to be absent from the model fuel. The presence of naphthenes and aromatic hydrocarbons in conventional diesel fuel were believed to undergo chemical changes during cavitation bubble collapse, which were reflected in the varying spectral attenuation coefficient of the fuel. The chemical changes were driven by pyrolytic reactions that are known to form PAHs from primary aromatic species.

UV-visible spectra measurements of cavitated Fuel 1 (BDN) samples showed a continuous decay in absorbance of the benzenoid band as a function of cavitation time. The decay indicated

a systematic reduction in concentration of the mono-aromatic species in the recirculating fuel, which were believed to undergo chemical changes that could result in formation of PAHs and soot through pyrolysis-like reactions.

Spectra measurements of Fuel 1 (BDN) samples also provided an indication towards formation of particulates in the recirculating diesel fuel. This was inferred from the prominent broadband absorbance increases that were observable in large regions of the spectra. Build-up of particulate suspension was also observed in the paraffinic model fuel during its long duration cavitation experiment. The particulate build-up was blamed for the gradual rise in absorbance of the model fuel (at 405 nm) over the duration of the cavitation test.

Chapter 8
Pressurised Receiver Tests

Pressurised receiver tests were designed to investigate the effect of downstream/ recovery pressure on the cavitation characteristics of diesel fuel flow. The motivation for this investigation came through visualisation of flow inside the receiving cylinder, which was performed for a separate investigation. To allow flow visualisation inside the receiver, the high-pressure test-rig receiver assembly was modified, the aluminium receiving cylinder was replaced with a fused silica receiving cylinder. Visualisation of fuel flow in the receiver of the high-pressure test-rig showed that a large number of cavitation bubbles, being formed in the injector nozzle, were pushed out into the receiver. These cavities of vapour and gas mixture were then observed to collapse inside the receiver upon flow stagnation and pressure recovery. It was thus proposed that through pressurisation of the receiving cylinder the recovery pressure of the hydrodynamic cavitation system could be controlled. The effect of receiver pressure on the cavitation characteristics could then be quantified through monitoring the variations in the optical properties of the circulating test fuel.

The investigation required modification of the high-pressure test-rig setup to allow pressurisation of the fuel receiving cylinder - downstream of the injector nozzle. The receiver was pressurised with the help of a pressure regulator, while a pressure gauge was employed to indicate the pressure inside the cylinder. Modifications to the receiving cylinder assembly have been shown in Figure 3.4 (Chapter 3).

The test fuels used for the receiver pressure investigation were Fuel 6 (BDA) (the aged conventional diesel fuel) and Fuel 1 (BDN). Fuel 6 (BDA) was tested at three receiver pressures – ambient pressure, 5 bar and 10 bar (absolute pressures); while Fuel 1 was tested at two

receiver pressures – ambient and 10 bar. The injection pressure was kept constant at 1,650 bar for all tests. Two separate injector nozzles were used for the two fuel that had a 173 µm single nozzle-hole. The experimental control variables for the pressurised receiver tests are included in Table 8.1 below.

Table 8.1 Control variables for pressurised receiver tests

Test Fuels	Fuel 6 (BDA) and Fuel 1 (BDN)
Test Duration	40 hours
Injection Pressure	1,650 bar
Pre-Injection Fuel Temperature	55 °C
Filter Type and Size	3 µm Nylon Filter

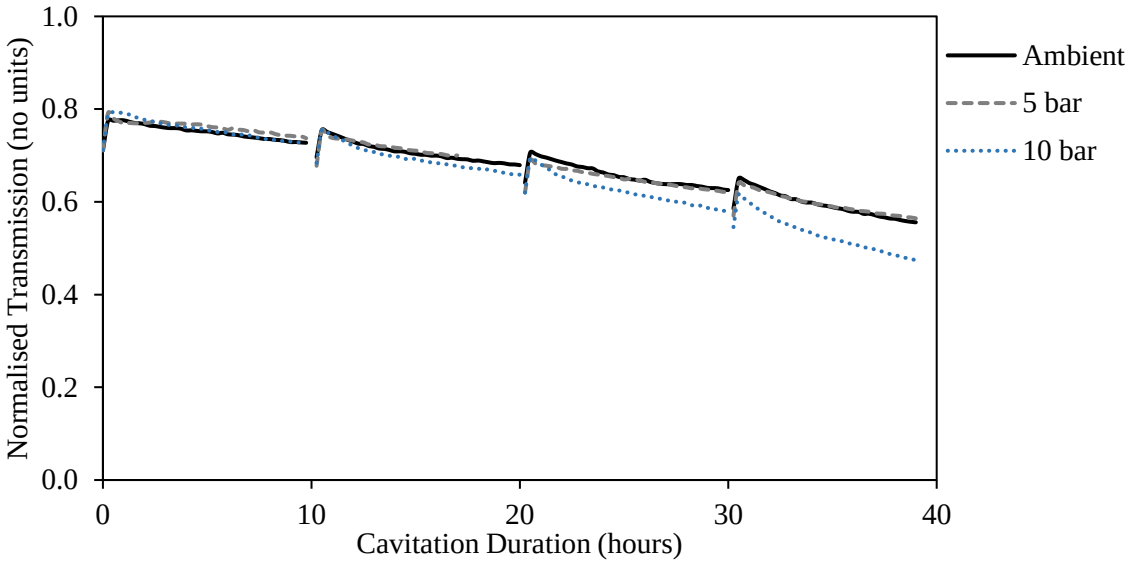

Figure 8.1 Normalised spectral transmission (at 405 nm) against cavitation time for Fuel 6 (BDA) at ambient, 5 bar and 10 bar receiver pressures.

Figure 8.1 shows the normalised spectral transmission signals of Fuel 6 (BDA) samples tested at the three receiving cylinder pressures. The spectral transmission signal for Fuel 6 (BDA) at 405 nm was observed to decrease over the duration of all cavitation tests. The initial normalised spectral transmission signals of the fuel samples were found to be ~ 0.7. The rates of

transmission signal decay were found to be almost identical at ambient and 5 bar receiver pressures. Comparatively, the rate of decrease in spectral transmission at 10 bar receiver pressure was found to be higher.

Figure 8.2 shows the time-dependent spectral attenuation coefficient of Fuel 6 (BDA) samples for the three receiver pressure tests. It was observed that the initial spectral attenuation value of the three test samples were similar. As the cavitation tests progressed the attenuation coefficient of the fuel charges at all receiver pressures gradually increased. As observed from the variations in the spectral transmission signal, the rate of increase in attenuation of the fuel at ambient and 5 bar receiver pressures was found to be very similar; whereas, the rate of increase in attenuation was found to be higher at 10 bar receiver pressure.

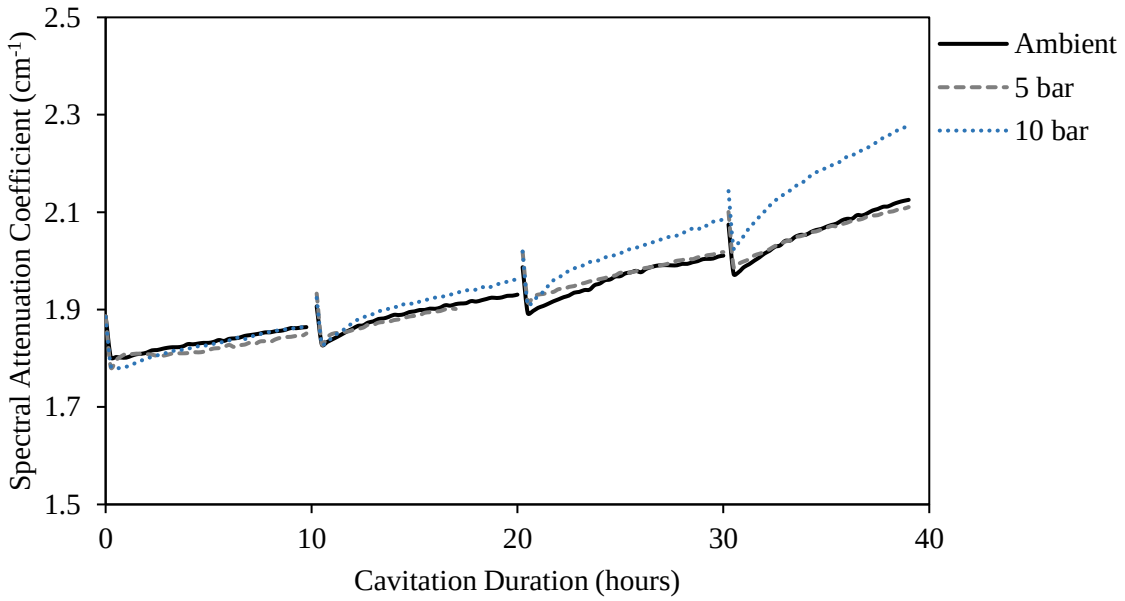

Figure 8.2 Time-dependent spectral attenuation coefficient of Fuel 6 (BDA) at ambient, 5 bar and 10 bar receiver pressures.

The faster change in attenuation coefficient of the fuel at 10 bar injection pressure indicates a positive correlation between the receiver pressure and the rate of chemical activity in the diesel fuel. However, the similarity in behaviour of the fuel samples at ambient and 5 bar pressures

suggests presence of a threshold receiver pressure beyond which the rate of chemical activity of the fuel increases.

Discrete fuel samples collected during the receiver pressure tests were subjected uv-vis spectra measurements. Pure diesel samples were subjected to the spectra measurements in the wavelength range of 350 – 500 nm, these spectra are shown in Figure 8.3, Figure 8.4 and Figure 8.5, corresponding to the ambient, 5 bar and 10 bar receiver pressures respectively.

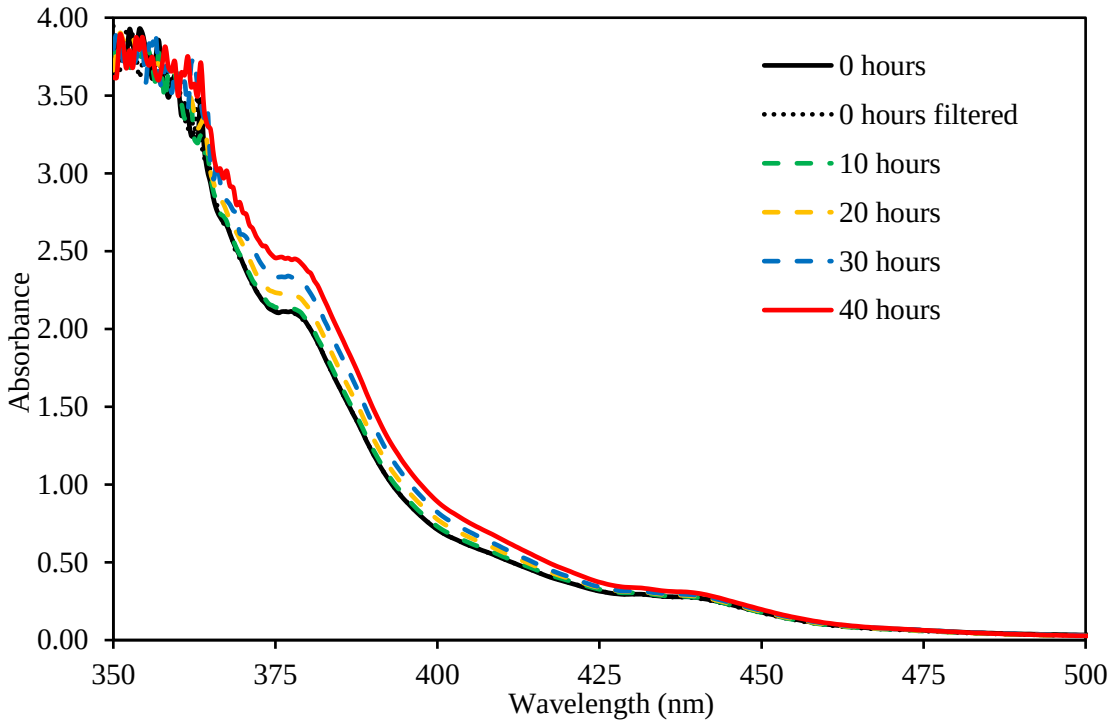

Figure 8.3 Fuel 6 (BDA) discrete sample spectra from the ambient receiver pressure test

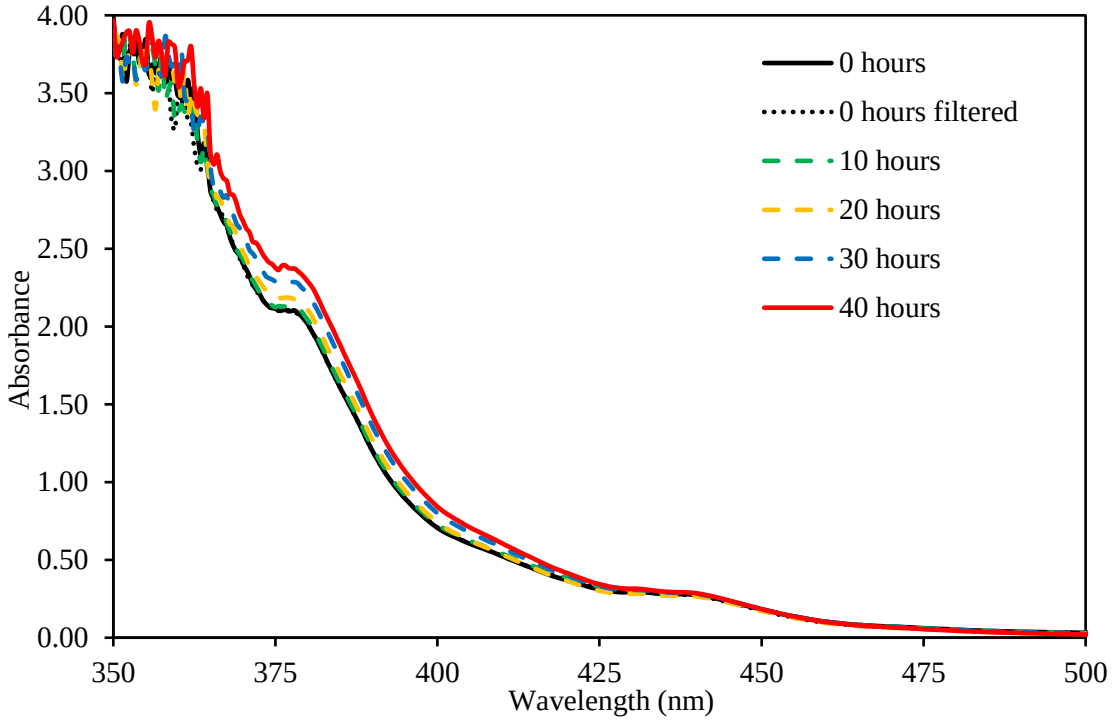

Figure 8.4 Fuel 6 (BDA) discrete sample spectra from the 5 bar receiver pressure test

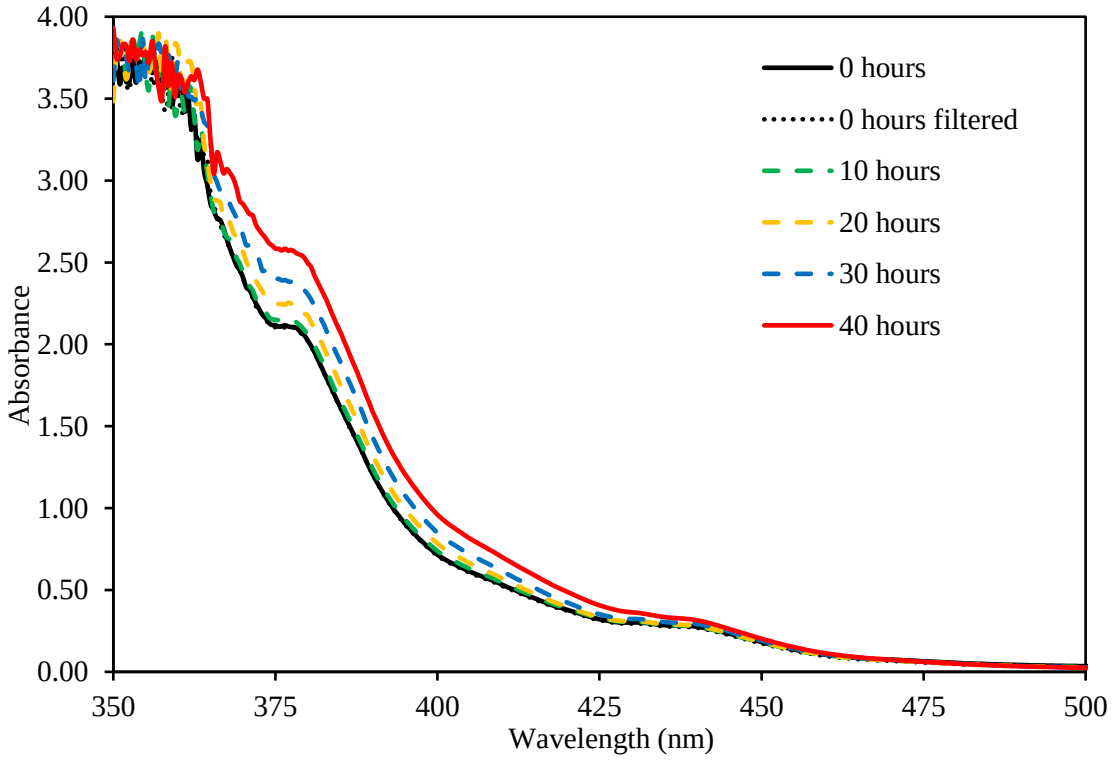

Figure 8.5 Fuel 6 (BDA) discrete sample spectra from the 10 bar receiver pressure test

Spectra of the aged conventional diesel (Fuel 6 (BDA)) showed subtle differences from the conventional diesel fuel (Fuel 1 (BDN)) discussed in earlier sections. Fuel 6 (BDA) showed a higher absorbance in the 375 nm 'shoulder-like' absorbance structure; the structure also appeared to be broader than the one observed for Fuel 1 (BDN). Over the course of the cavitation test, the shoulder-like structure in Fuel 1 (BDN) appeared to diminish, whereas the structure was found to endure during the Fuel 6 (BDA) cavitation tests. Another difference between the two fuels was found in the position of the 425 nm band (from Fuel 1 (BDN)); in Fuel 6 (BDA) the 425 nm band was shifted to longer wavelengths (~ 440 nm).

In addition to the position of the absorbance structure, its behaviour under cavitation was also found to differ between the two fuels. In Fuel 1 (BDN), the absorbance band increased in absorbance followed by its destruction. In Fuel 6 (BDA), the structure appeared to experience a very slight increase throughout the cavitation tests. The differences in spectra and behaviour of the two fuels are most likely inherent from the difference in their feedstocks.

The variation in absorbance of Fuel 6 (BDA) samples bore similarities to the broadband absorbance increase, which is suggested to be an indication of the particulate build-up in the fuel samples. The broadband increase was observable for wavelengths below ~ 435 nm.

Comparison of Fuel 6 (BDA) absorbance spectra from the ambient and the 5 bar receiver pressure test samples showed similarities in behaviour. In fact, analysis of the overall change in absorbance of fuel samples showed a slightly larger increase in absorbance for ambient pressure test samples compared to the 5 bar test samples. At 10 bar receiver pressures, the rate of increase in absorbance was observed to be the largest, whereby the final test sample (40 hours) showed the largest overall increase in absorbance compared to the lower receiver pressure test samples. Figure 8.6 shows the overall change in absorbance of the Fuel 6 (BDA) samples from the three receiver pressure tests.

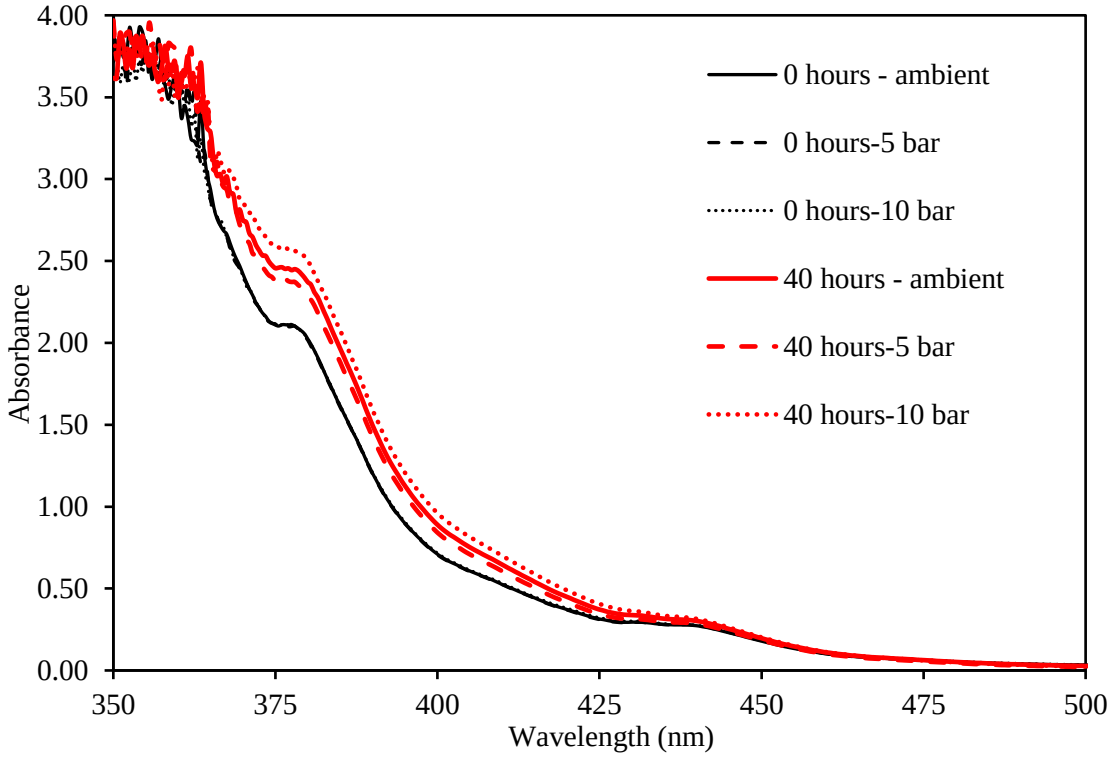

Figure 8.6 Overall change in absorbance of the Fuel 6 (BDA) samples from the ambient, 5 bar and 10 bar receiver pressure tests.

The discrete diesel samples collected during the receiver pressure tests were diluted to a dilution ratio factor (DRF) of 520 and subjected to spectra measurements in the wavelength range of 240 – 305 nm. Figure 8.7, Figure 8.8 and Figure 8.9 show the absorption spectra of the Fuel 6 (BDA) samples from the ambient, 5 bar and 10 bar receiver pressure tests, respectively.

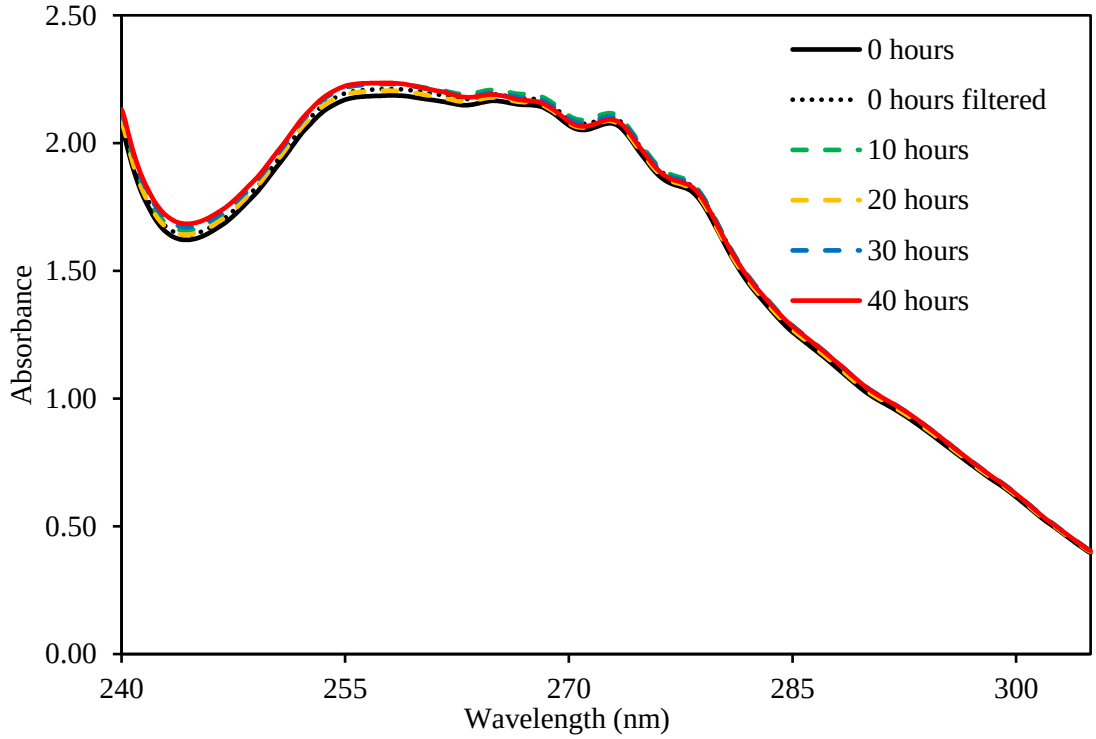

Figure 8.7 Fuel 6 (BDA) discrete sample spectra for DRF 520 diluted samples from the ambient receiver pressure test

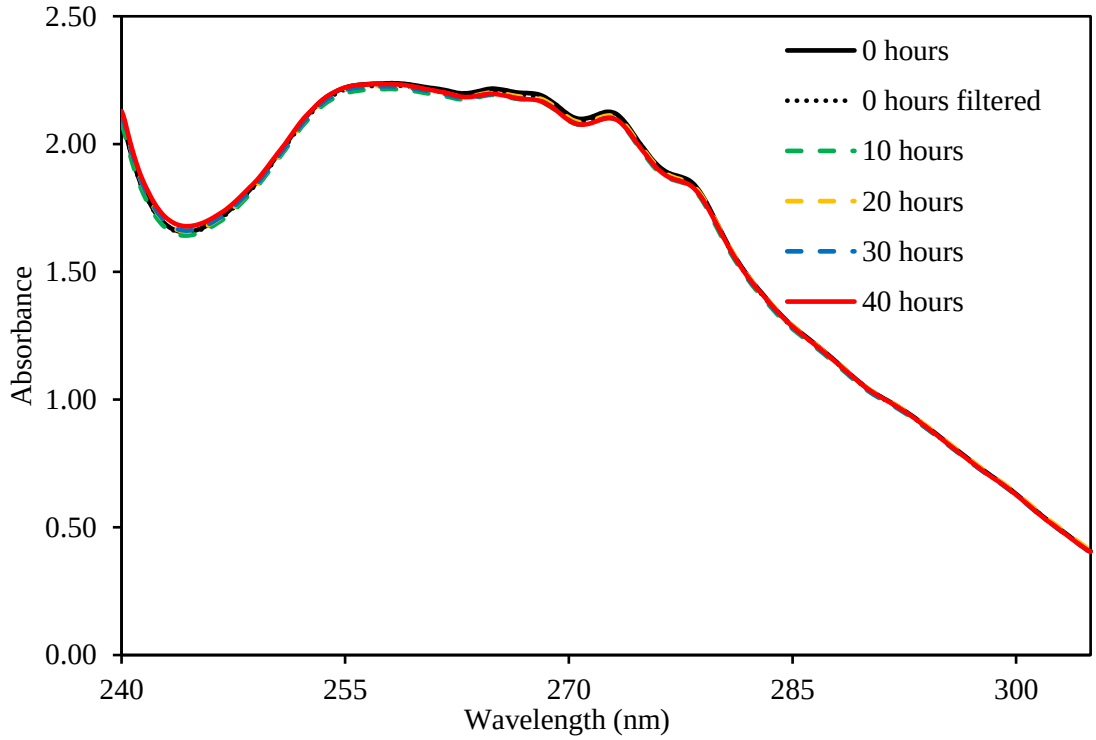

Figure 8.8 Fuel 6 (BDA) discrete sample spectra for DRF 520 diluted samples from the 5 bar receiver pressure test

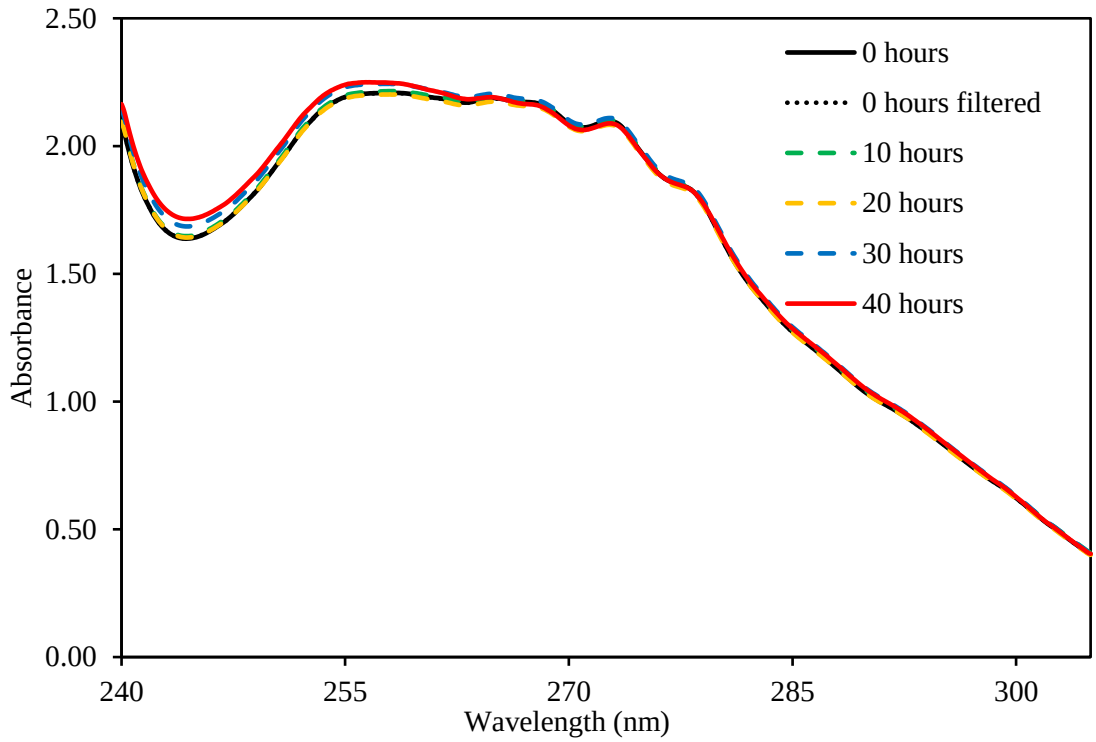

Figure 8.9 Fuel 6 (BDA) discrete sample spectra for DRF 520 diluted samples from the 10 bar receiver pressure test

The 240 – 305 nm measurement range is of significance in this project due to the presence of the benzenoid band, which corresponds to the absorption from primary aromatic hydrocarbon species in diesel fuels. The benzenoid band refers to a series of absorbance peaks in the ~ 250 – 280 nm range.

Variations in absorbance in this band are a combination of the changes occurring in the broadband absorbance and the benzenoid band absorbance. In order to isolate and observe the changes occurring in the benzenoid band, the spectra were self-normalised at the 245 nm trough. Normalisation was performed through offsetting the spectra, such that the absorbance of all samples at 245 nm was equal to 1.0. This allowed separation of the broadband absorbance effect from the benzenoid band absorbance changes. The self-normalised spectra of the sample at the three receiver pressures are shown in Figure 8.10.

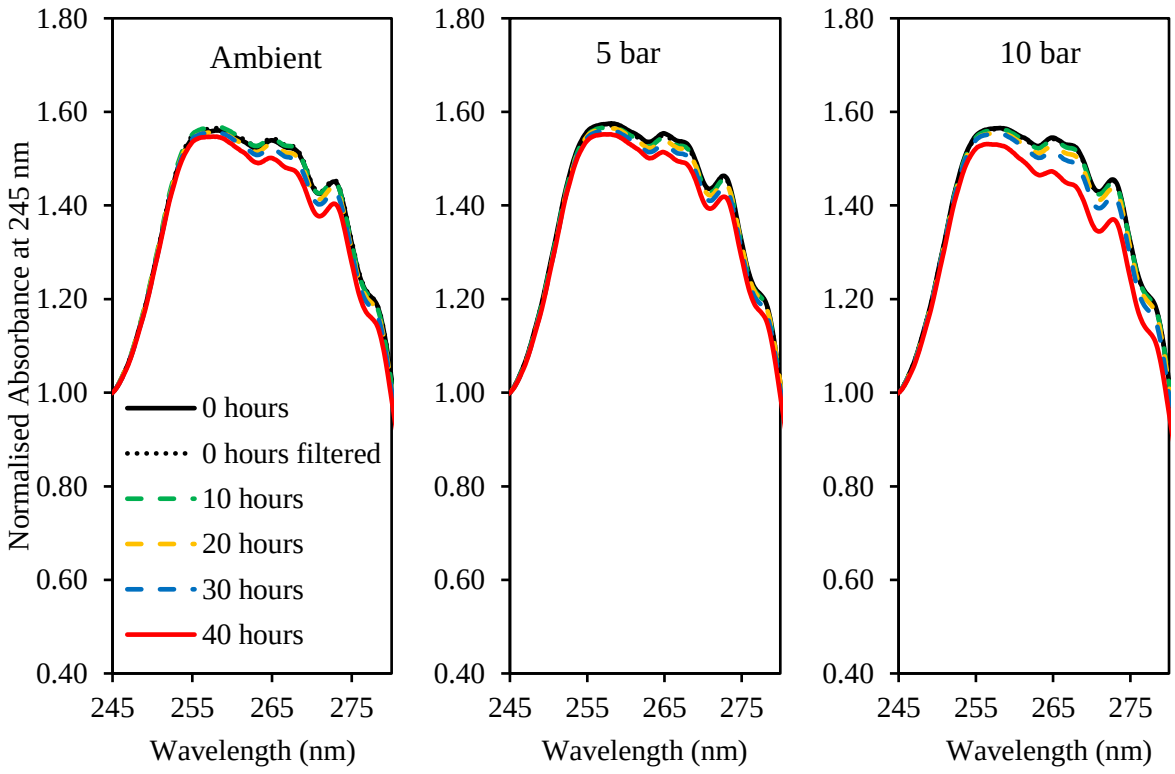

Figure 8.10 Absorption spectra of the three receiver pressure test samples for Fuel 6 (BDA), self-normalised at 245 nm to show the variations in the benzenoid band range

The benzenoid band spectra of Fuel 6 (BDA) samples for the three receiver pressure tests have all shown a time-dependent decrease in absorption of the cavitated samples. The decreasing absorption in the benzenoid band signifies a decreasing concentration of primary aromatic species in the fuel resulting from the cavitation induced chemical activity. The overall decrease in absorbance of the diesel samples (after 40 hours of cavitation) at ambient and 5 bar receiver pressures appeared to be very similar in magnitude. Comparatively, the decrease in absorption for the 10 bar receiver pressure test samples was visibly larger, indicating a greater decrease in the concentration of primary aromatic hydrocarbons present in Fuel 6 (BDA) at higher receiver pressures.

The pressurised receiver tests were repeated at ambient and 10 bar receiver pressures using Fuel 1 (BDN) (conventional diesel from a different feedstock). The resultant time-dependent

normalised spectral transmission signals and attenuation coefficients of the fuel at 405 nm have been shown Figure 8.11 and Figure 8.12, respectively.

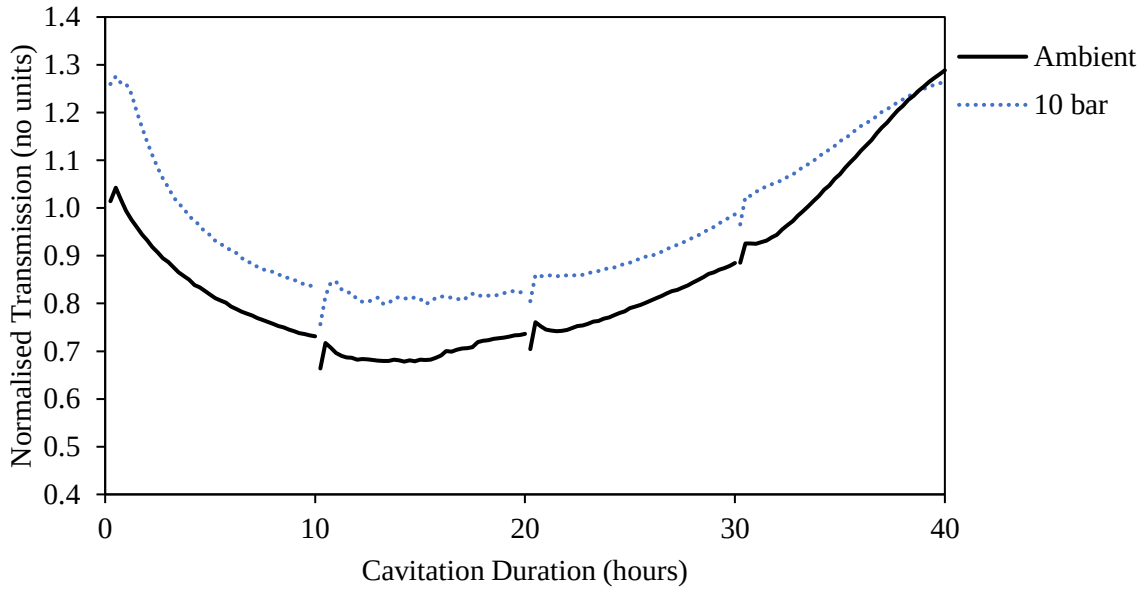

Figure 8.11 Normalised spectral transmission signals (at 405 nm) for Fuel 1 (BDN) tests at ambient and 10 bar receiver pressures

Variation in the normalised spectral transmission signal of Fuel 1 (BDN) showed that at both receiver pressures, the transmission coefficients followed the same trend. Transmission initially decreased to a minimum value, thereafter it increased till the end of the experiments. The rate of increase in transmission towards the end of the experiments was found to be different for the two tests, wherein the transmission signal experienced a faster increase at ambient receiver pressure. An offset in the initial normalised transmission value was observed between the two tests. Fuel 1 (BDN) at ambient receiver pressure was found to have lower pre-cavitation transmission value.

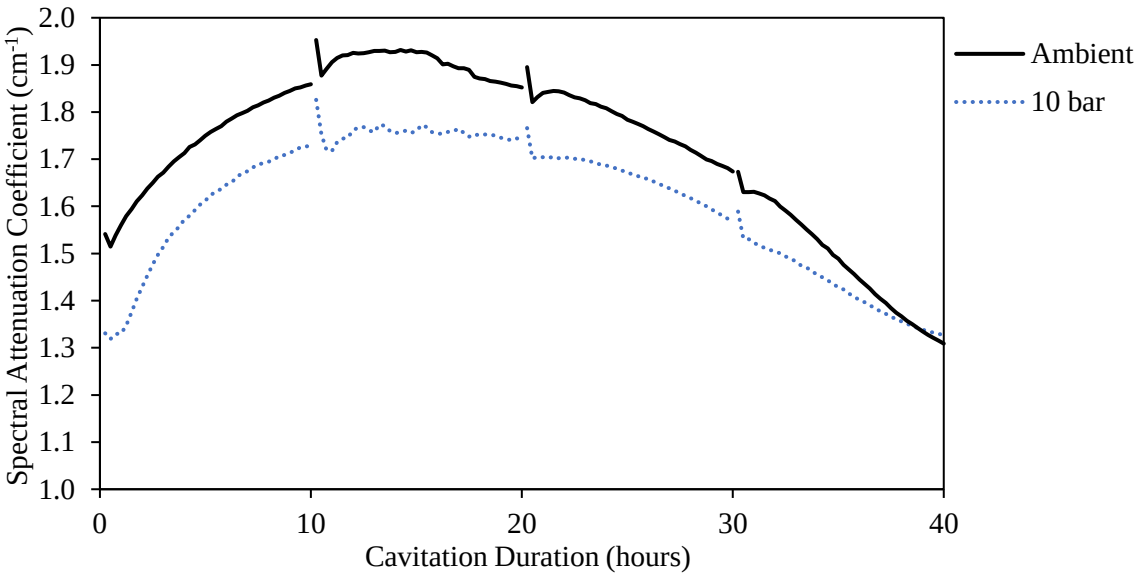

Figure 8.12 Time-dependent spectral attenuation coefficients (at 405 nm) for Fuel 1 (BDN) tests at ambient and 10 bar back pressures

Figure 8.12 shows the corresponding time-dependent change in spectral attenuation coefficients of the two receiver pressure dependence tests. Fuel 1 (BDN) was found to have different initial (pre-cavitation) spectral attenuation coefficients at the start of the two receiver pressure tests. The spectral attenuation coefficients were observed to increase with cavitation time to a maximum value. The two tests attained maximum attenuation in similar time scales, after approximately 15 hours of cavitating flow. Thereafter, the attenuation coefficients of the two fuel samples decreased, with the rate of decrease being faster at ambient receiver pressure.

Absolute changes in spectral attenuation coefficients were calculated for the two tests as a function of cavitation time - shown in Figure 8.13. Fuel sample in the 10 bar receiver pressure test was found to undergo slightly larger increase in attenuation, with the rate of initial increase also being greater at this pressure. In the decreasing attenuation phase, fuel sample at ambient pressure experienced a larger decrease at a faster rate than that at 10 bar pressure.

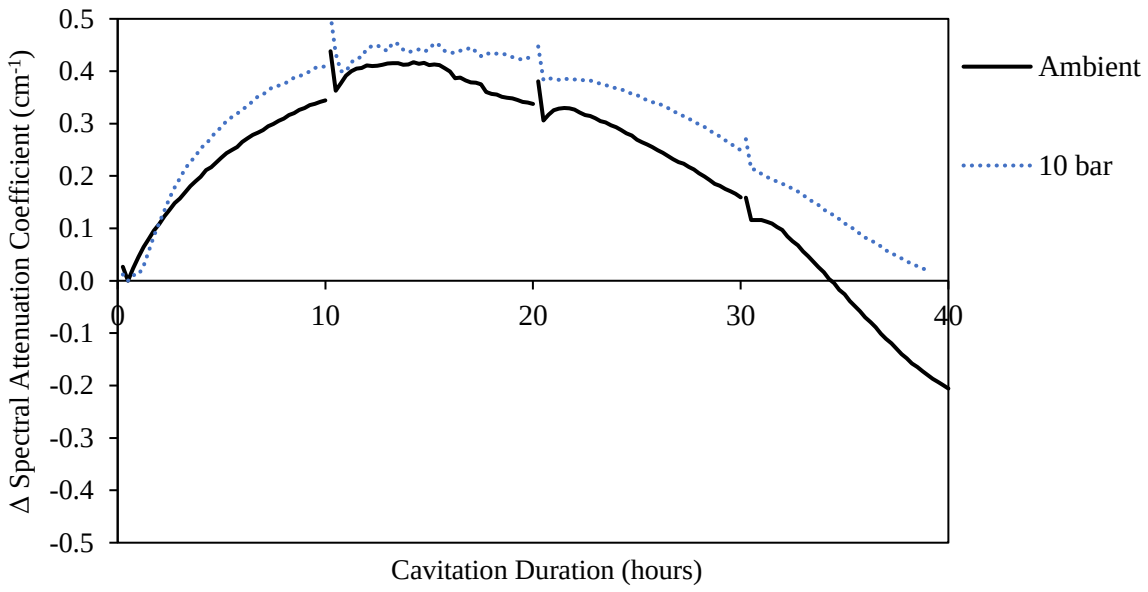

Figure 8.13 Absolute change in spectral attenuation coefficients (at 405 nm) for Fuel 1 (BDN) tests at ambient and 10 bar back pressures

Discrete fuel samples were collected during the two tests and were subjected to uv-vis spectra measurements. Figure 8.14 and Figure 8.15 show the spectra measurements of pure diesel samples in the wavelength range of 350 nm to 500 nm, for the ambient and the 10 bar back pressure tests, respectively.

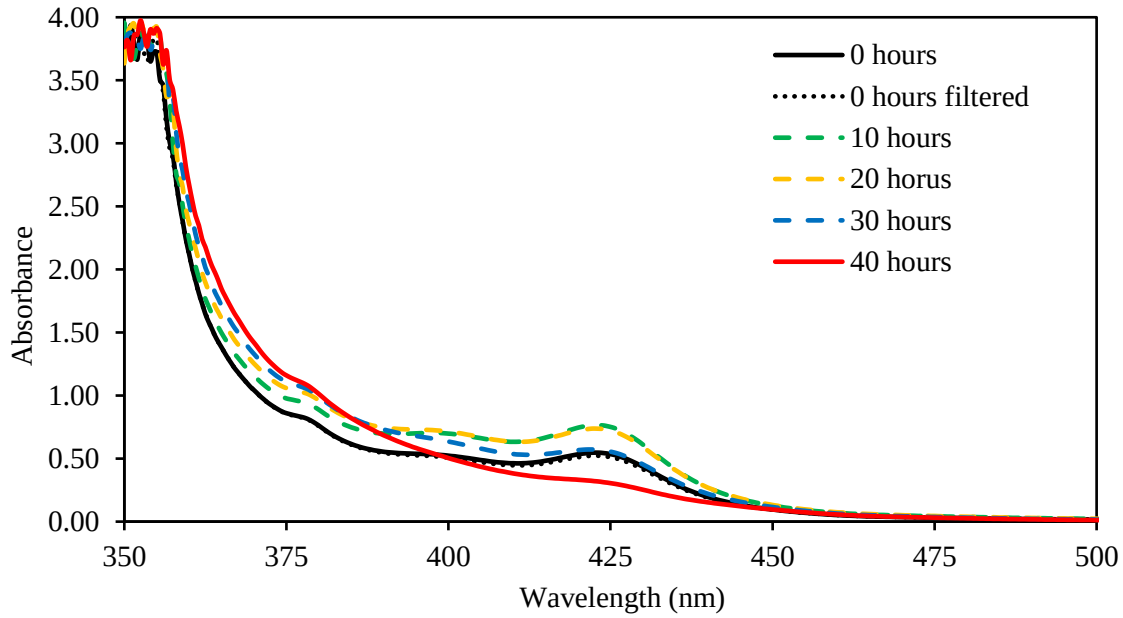

Figure 8.14 Fuel 1 (BDN) discrete sample spectra from the ambient receiver pressure test

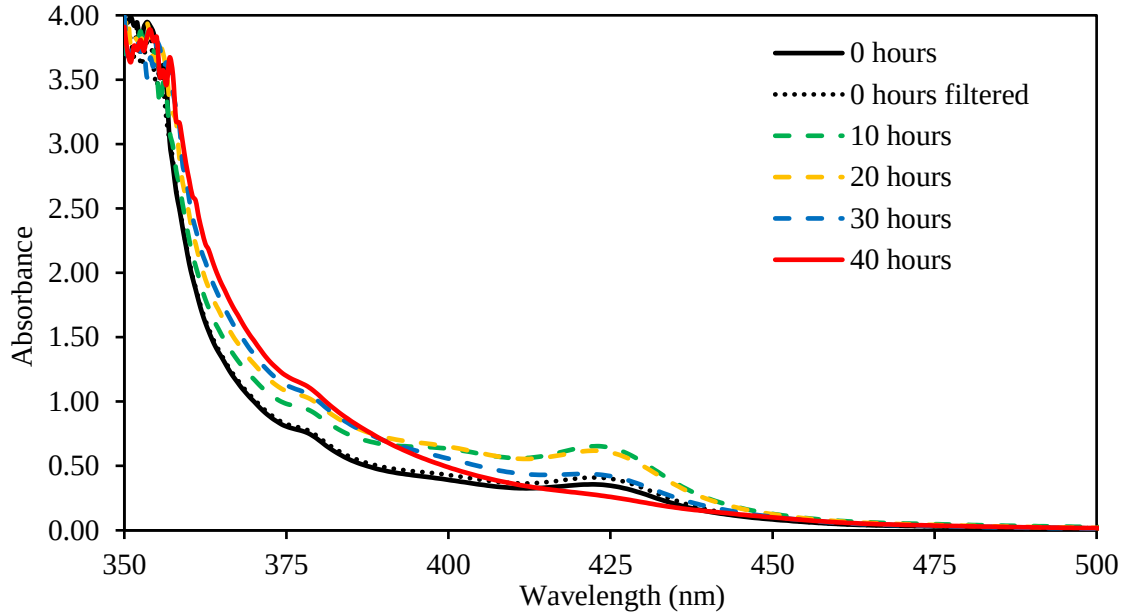

Figure 8.15 Fuel 1 (BDN) discrete sample spectra from the 10 bar receiver pressure test

The spectra measurements for both experiments showed an increase in absorbance in the 425 nm structure, followed by its decay till the end of each 40 hour test. Maximum absorbance in the 425 nm structure was observed to be attained between the 10 and 20 hours samples. This observation agreed with the in-situ laser attenuation coefficient measurements that showed that the highest absorbance coefficients were reached around 15 hours of cavitation.

The 0 hours sample for the 10 bar experiment appeared to show a lower absorbance as compared to the ambient test sample. This was also a confirmation for the lower initial attenuation coefficient observed in the in-situ measurement for the 10 bar experiment.

Absorbance measurements for wavelengths below 375 nm showed the broadband absorbance increase for both receiver pressures. Broadband absorbance increase has been suggested to be an effect of particulate suspension build-up in cavitated diesel fuels. The overall broadband absorbance increase was observed to be comparatively larger for the 10 bar receiver pressure test, suggesting a larger build-up of particulates in the diesel sample over the 40 hours of cavitating flow at the higher receiver pressure.

The discrete diesel samples were diluted to DRF 520 and subjected to spectra measurements in the wavelength range of 240 nm to 305 nm. Figure 8.16 and Figure 8.17 show the absorption spectra of Fuel 1 (BDN) samples from the ambient and 10 bar receiver pressure tests, respectively.

The 240 – 305 nm spectra range shows the benzenoid band which corresponds to the absorbance of primary aromatic species. The range can also be used to observe the broadband effect. In Fuel 1 (BDN) spectra below, the broadband effect was observable at the 245 nm trough, where the 10 hourly absorbance was seen to increase throughout the experiments. To isolate the behaviour of the benzenoid band from the broadband effect, the spectra were self-normalised at the 245 nm trough. The self-normalised spectra of the two Fuel 1 (BDN) tests have been presented in Figure 8.18.

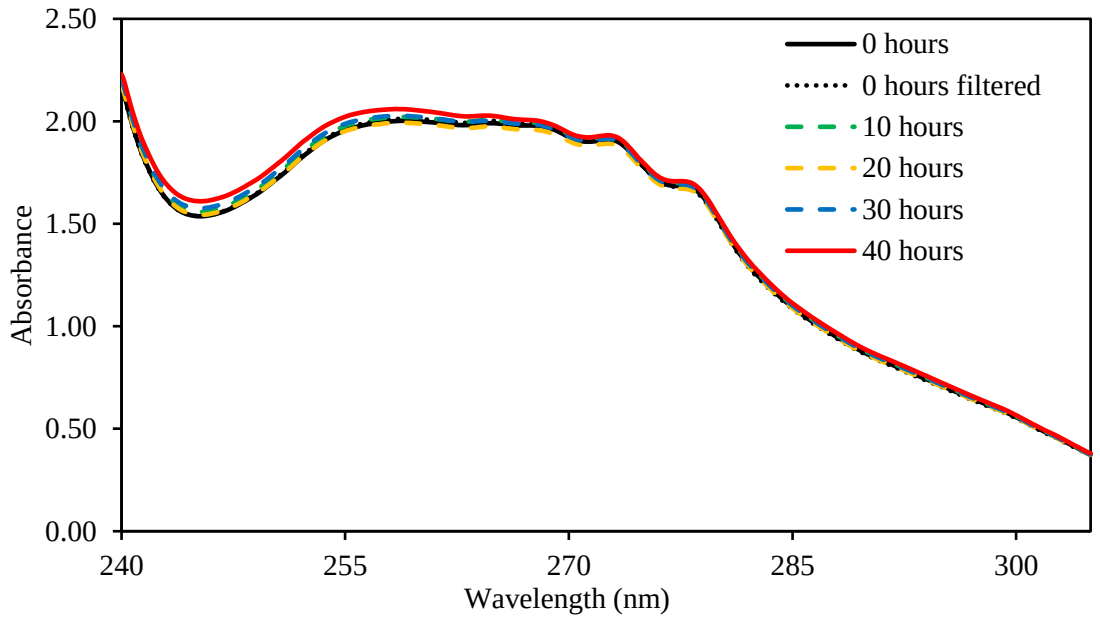

Figure 8.16 Fuel 1 (BDN) discrete sample spectra for DRF 520 diluted samples from the ambient receiver pressure test

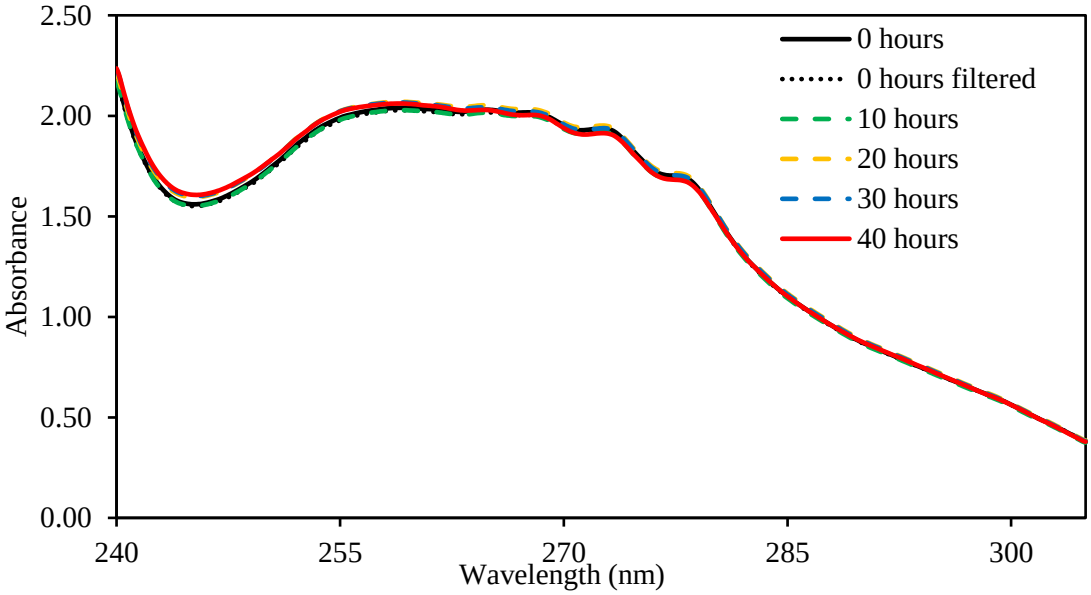

Figure 8.17 Fuel 1 (BDN) discrete sample spectra for DRF 520 diluted samples from the 10 bar receiver pressure test

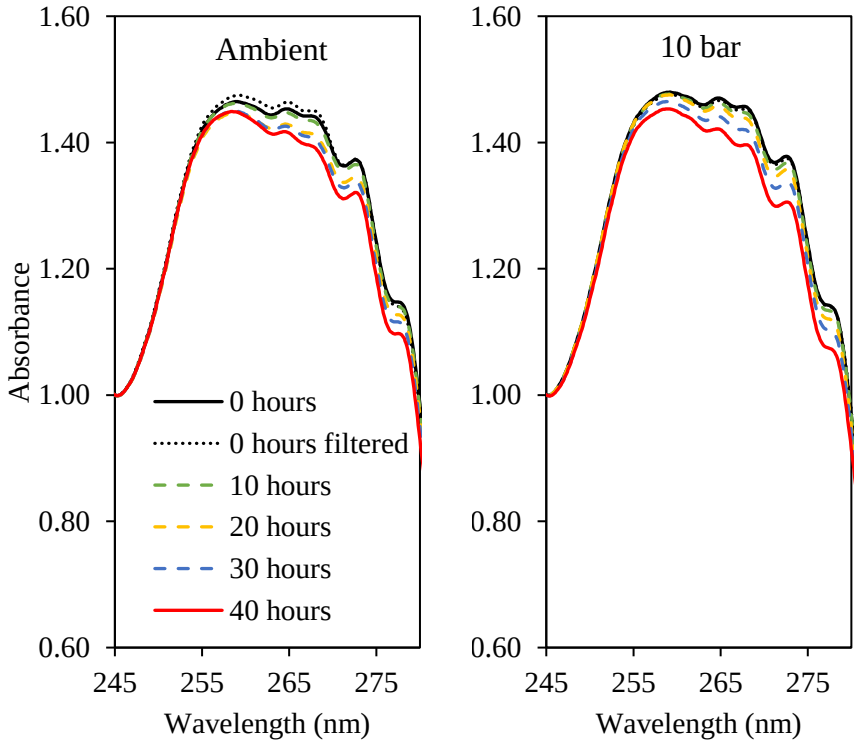

Figure 8.18 Absorption spectra of the two receiver pressure test samples for Fuel 1 (BDN), self-normalised at 245 nm to show the variations in the benzenoid band range

Comparison of the variations in benzenoid bands of the two tests showed that both fuel samples experienced a systematic decrease in absorbance as a function of cavitation time. This suggested an overall consumption of the primary aromatic species in the fuel samples due to the sustained cavitating flow. The overall (40 hour) decrease in absorbance was found to be larger for the 10 bar receiver pressure test as compared to the ambient receiver pressure test.

8.1 Combined Discussion for Receiver Pressure Tests

The results for receiver pressure dependence tests on Fuel 6 (BDA), both from variations in the time-dependent spectral attenuation coefficient and the uv-vis spectra have shown a positive correlation between the receiver pressure and the rate of change in diesel fuel's optical properties. The results have indicated presence of a threshold receiver pressure below which the effect of receiver pressure does not show any significant changes in the fuel's properties.

Fuel 1 (BDN) receiver pressure tests showed varying effects; in the spectral attenuation coefficient measurements at 405 nm, the fuel at 10 bar was found to increase its attenuation at a faster rate in the early stages of the experiments, whereas the rate of the subsequent decrease in attenuation was found to be larger at ambient pressure. The difference in behaviours of the two conventional diesel fuels – Fuel 1 (BDN) and Fuel 6 (BDA) – could be a consequence of the difference in their composition (inherent from their feedstocks). Fuel 6 (BDA) did not display the increase and subsequent decrease in attenuation at 405 nm as observed for Fuel 1 (BDN), instead a steady increase in attenuation was observed which was likened to the broadband absorbance increase noticeable in all diesel fuels tested in this study. Fuel 1 (BDN) displayed the increasing and decreasing attenuation behaviour due to the presence of the 425 nm absorbance structure found in its spectra. It might be correct to suggest that in the absence of the 425 nm absorbance structure, Fuel 1 (BDN) would display the same monolithic increase as Fuel 6 (BDA); this has been observed to occur in later stages of the prolonged cavitation experiments when the 425 nm structure of Fuel 1 (BDN) was diminished (Chapter 7).

Spectra measurements of Fuel 1 (BDN) showed a positive correlation between the broadband increase and the receiver pressure. The receiver pressure correlation was also observable in the consumption rate of primary aromatic species, suggested from faster decrease in the benzenoid band absorbance at higher receiver pressure. These findings were in agreement with the observations for Fuel 6 (BDA).

It is known that hydrodynamic cavitation occurs as the fuel flows past the injector nozzle; this occurs as a result of flow acceleration in the nozzle-hole, leading to a significant decrease in local pressures that can initiate separation of the dissolved gases from the solution or even local boiling of the liquid fuel. A large number of the cavitation bubbles, composed of gas and fuel vapour mixture, may then be ejected from the nozzle-exit into the stagnated fuel receiver. Upon pressure recovery in the receiver, the cavities are forced to collapse violently. The recovery pressure from the surrounding liquid drives the cavity wall during its implosion. Simulations of cavitation bubble collapse have reported that higher recovery pressures result in more aggressive bubble collapse, generating higher temperatures and high magnitude pressure pulses[63].

In this investigation, the recovery pressure was emulated by the fuel receiver pressure. It was believed that an increase in the receiver pressure and the intensity of the subsequent cavitation bubble collapse, may lead to an acceleration in the chemical activity of the diesel fuel. The implications of more aggressive chemical reactions would be reflected in a faster change in the optical properties of the diesel fuel. The results presented in this section confirm the aforementioned statement. However, it has been suggested that a threshold receiver pressure condition applies, below which the effects of increasing the receiver pressure are not noticeable. The optical behaviour of the fuels has also been found to be strongly dependent on their composition; the different hydrocarbon classes constituting to the fuel's composition may

act in significantly different ways and the activity of certain classes might not indicate a recovery pressure dependence.

Chapter 9
Two-Dimensional Gas Chromatography Results

Two-dimensional gas chromatography (or GC x GC) analysis was performed on the repeated fuel tests samples for Fuels 1 – 5. The fuel tests involved recirculating each fuel for 40 hours in the high-pressure test-rig (at 1,650 bar). The results for the time-dependent spectral attenuation coefficients and the uv-vis spectra of the fuels have been presented in Chapter 5. The discrete samples of the cavitated fuels collected during the cavitation tests were sent-off to Shell Global Solutions laboratory for the GC x GC analysis. The chromatograms were obtained and compiled by Shell scientists before they were sent back to City, University of London for further analysis.

In the analysis presented here, relative change in proportions of various hydrocarbon groups present in the fuels have been determined. The calculation of these changes was performed through subtracting the GC results of the 40 hours cavitated fuel sample from the results of pre-cavitation fuel sample of each of the five test fuels. The hydrocarbon groups included in the analysis were paraffins, naphthalenes, mono-aromatics, naphthenic mono-aromatics, di-aromatics and tri-aromatics.

Two-dimensional chromatograms obtained from the GC x GC analysis showed the various species present in the fuel samples through plotting their first-dimension retention time on the x-axis, second-dimension retention time on the y-axis and their signal intensities as coloured peaks. Identification of individual species from the chromatograms was very complex, therefore the species were grouped into the various hydrocarbon classes and arranged according to their carbon number. The hydrocarbon classes included n-paraffins, branched

paraffins, naphthenes, mono-aromatics, naphthenic mono-aromatics, di-aromatics, tri-aromatics, FAMEs and residuals.

Figure 9.1 shows an example of a GC chromatogram of a conventional diesel fuel, marked with estimated regions of the various hydrocarbons classes. Proportions of the different hydrocarbon classes and subclasses were quantified from the peak intensities and their area.

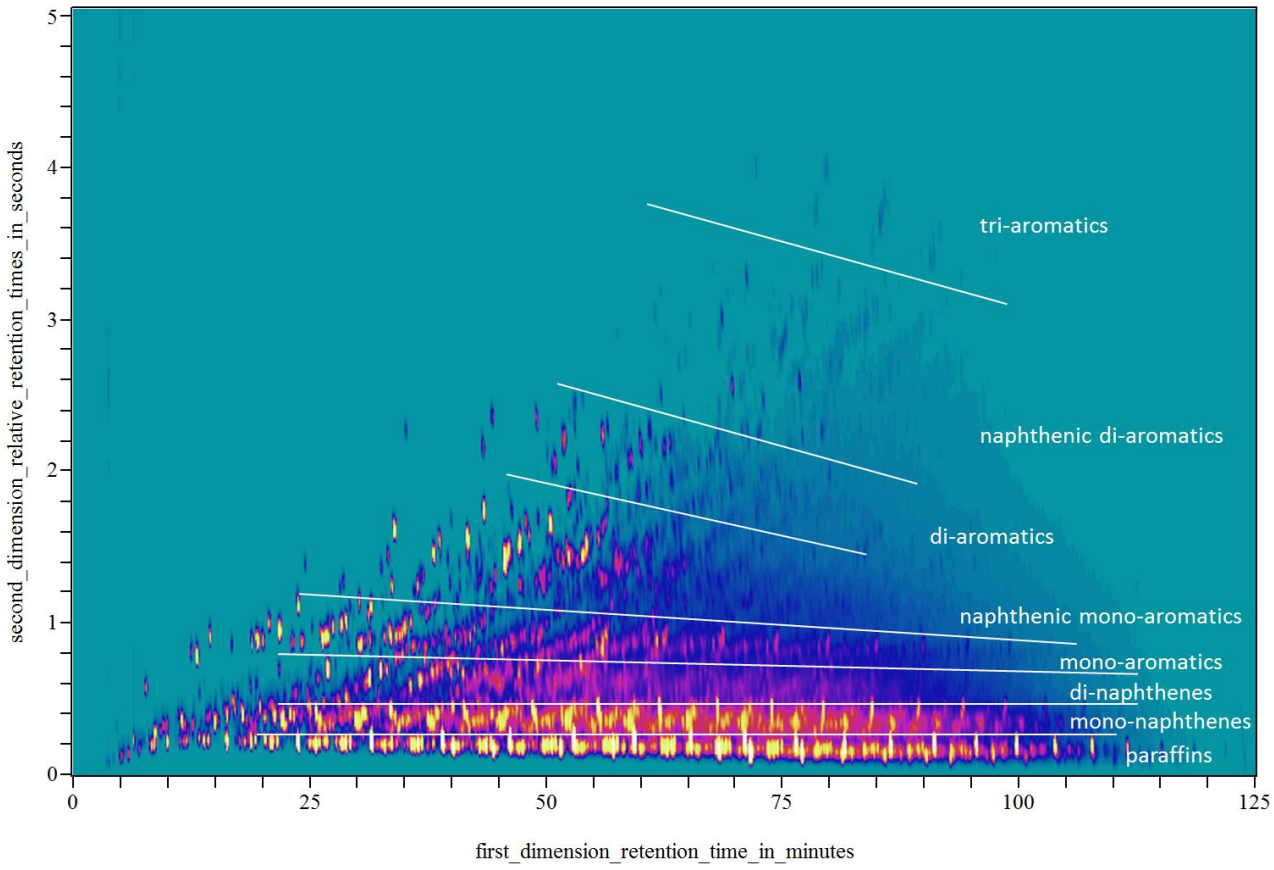

Figure 9.1 GC x GC chromatogram for Fuel 1 (BDN) pre-cavitation sample.

Classification and quantification of the various hydrocarbon classes in the five test fuels was performed by Shell scientists. Composition of these hydrocarbon classes in pre-cavitation (0 hours) samples of each of the five fuels is shown in Figure 9.2. Notice that the open-chain paraffins (including n- and branched paraffins) have been identified separately from their cyclic counterparts (naphthenes). Together the two sub-classes of paraffins account for the largest

proportion of each test diesel fuel. The mono-aromatics have also been sub-divided into two classes of alkylated mono-aromatics and naphthenic mono-aromatics.

The pre-cavitation conventional diesel fuel (Fuel 1 (BDN)) had ~ 38% open-chain paraffins, ~ 37% naphthenes, ~ 11% alkylated mono-aromatics, ~ 9% naphthenic mono-aromatics and ~ 5% di- and tri-aromatics. Figure 9.2 indicates the presence of 10% and 30% FAME in Fuel 2 (B10) and Fuel 3 (B30), respectively. Fuel 4 (BD+H) composition indicates the presence of 10% additional hexadecane in its increased paraffinic composition; while Fuel 5 (BD+MN) shows the increased proportion of di- and tri-aromatics resultant from the additional 10% methylnaphthalene.

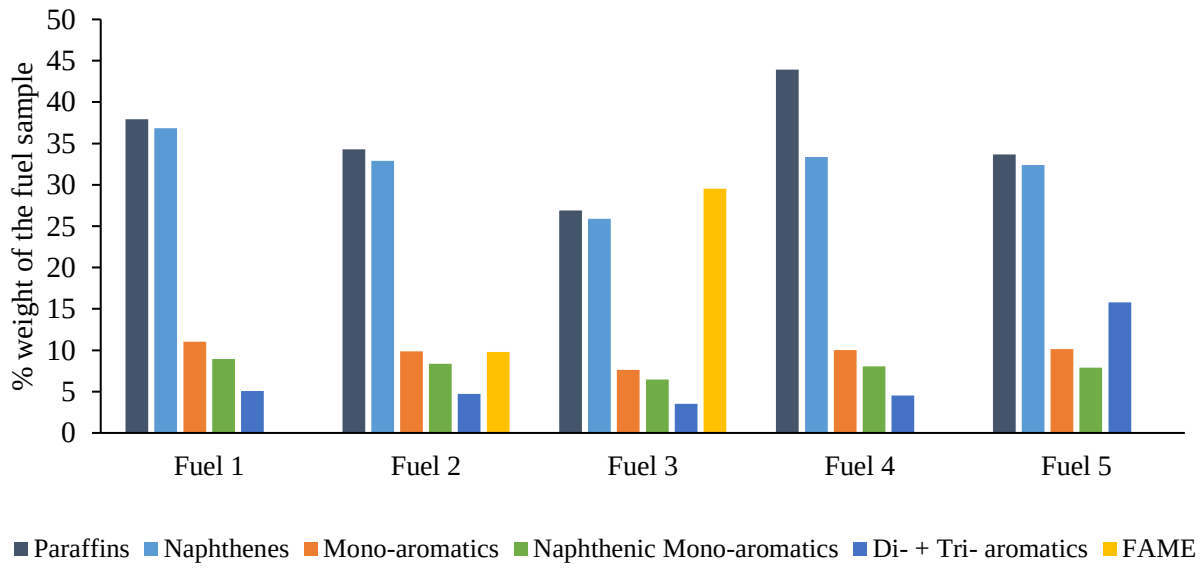

Figure 9.2 Proportions of hydrocarbon classes present in the pre-cavitation samples of each of the five test fuels, obtained through GC x GC analysis.

9.1 Paraffins

Figure 9.3 shows relative change in proportions of the open-chain paraffins of the five fuels after forty hours of cavitating flow at 1,650 bar injection pressure. A small decrease was observed for Fuel 1 (BDN) (~ 0.05 %wt) and Fuel 4 (BD+H) (~ 0.15 %wt). The remaining three fuels showed larger increases in paraffinic composition, with Fuel 2 (B10) showing the

largest increase (~ 1.40 %wt) and Fuel 5 (BD+MN) showing the smallest increase (~ 0.40 %wt). The biodiesel blends (Fuel 2 (B10) and Fuel 3 (B30)) appeared to have larger increases in open-chain paraffin concentrations than the other fuel blends. Addition of 10 % hexadecane appeared to be countered through an overall reduction in paraffins for Fuel 4 (BD+H) after cavitation.

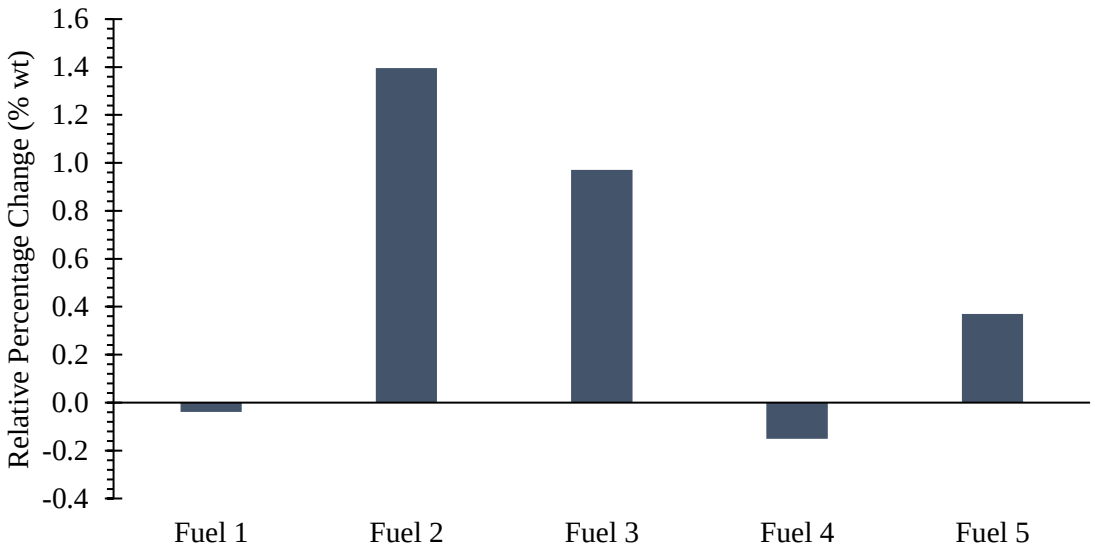

Figure 9.3 Relative change in proportions of the open-chain paraffins in the five test fuels after forty hours of cavitation

Figure 9.4 shows the relative change in naphthenes for the five fuels subjected to cavitation. The relative changes were calculated from the GC analysis results. All fuels except Fuel 1 (BDN) showed an increase in concentration of naphthenes, wherein Fuel 2 (B10) showed the largest increase (~ 1.30 %wt) and Fuel 4 (BD+H) showed the smallest increase (0.50 %wt). Fuel 1 (BDN) displayed a small decrease in naphthenic concentration of ~ 0.14 %wt. As was the case for open-chain paraffins, the biodiesel blends were observed to show the largest increase in concentration of naphthenes as well.

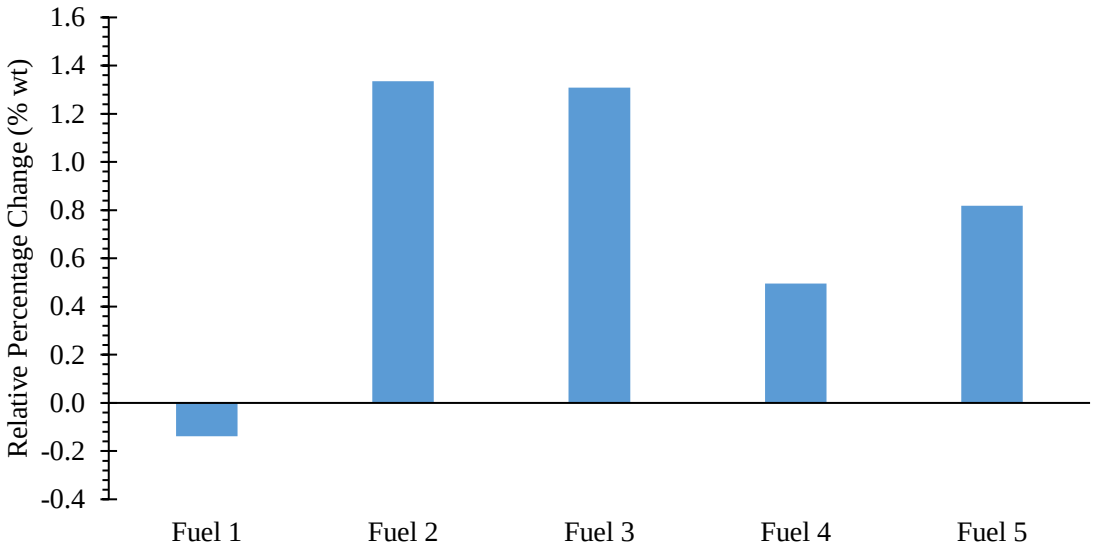

Figure 9.4 Relative change in proportions of naphthenes in the five test fuels after forty hours of cavitation

The changes indicate that chemical reactions occurring in the fuels result in either formation of paraffins or their destruction. An increase in concentration implies formation of paraffins while a decrease in concentration means destruction of the paraffinic species. The relative changes in the two paraffin-subclasses show that most diesel fuel blends experienced an increase in concentration of paraffins after cavitation, with the exception of the conventional diesel (Fuel 1 (BDN)).

9.2 Mono-Aromatics

Figure 9.5 shows the relative change in proportion of the alkylated mono-aromatic species in each of the five cavitated fuel samples compared to their original samples. Fuels 1, 3 and 4 showed an increase, while Fuels 2 and 5 showed a decrease in concentration of the mono-aromatics. Fuels 1 and 3 had the largest relative increase of ~ 1.50 %wt each. Fuel 5 (BD+MN) showed the largest decrease in alkylated mono-aromatics of ~ 1.86 %wt.

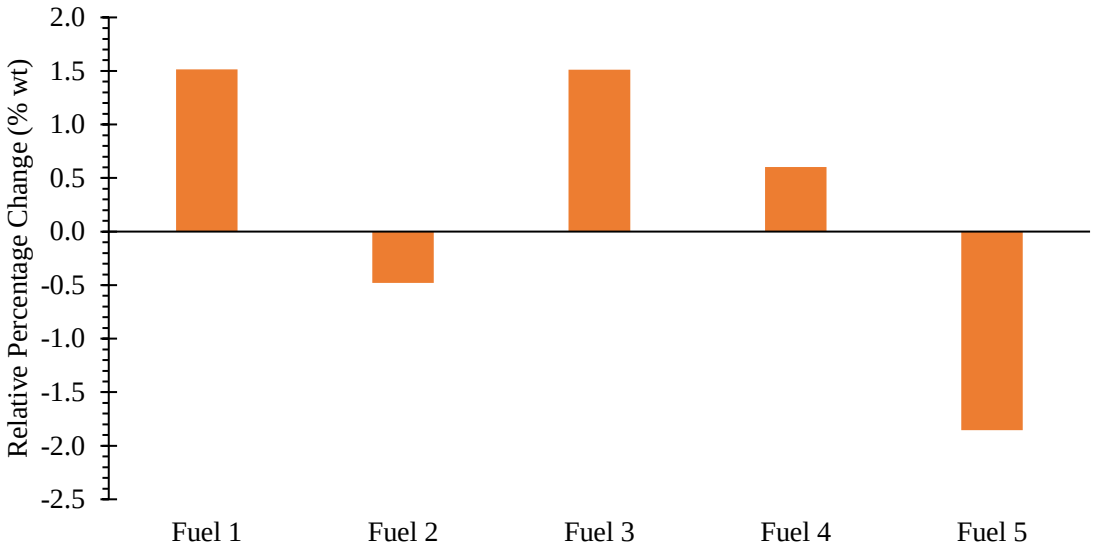

Figure 9.5 Relative change in proportions of the alkylated mono-aromatics in the five test fuels after forty hours of cavitation

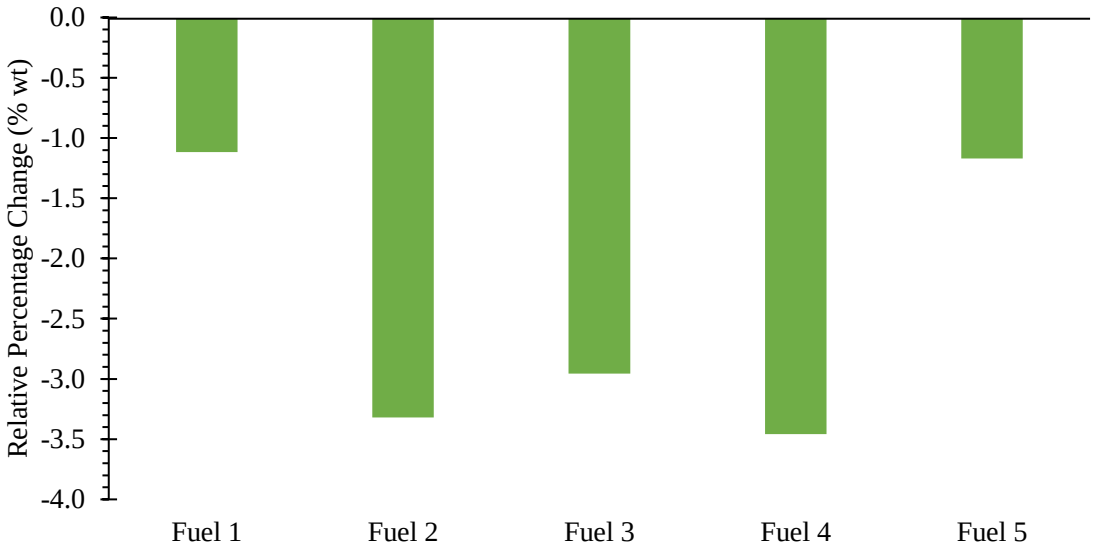

Figure 9.6 Relative change in proportions of the naphthenic mono-aromatics in the five test fuels after forty hours of cavitation

Figure 9.6 shows the relative change in concentration of naphthenic mono-aromatics in each test fuel as a result of cavitation. All fuels showed a trend of decreasing naphthenic mono-aromatic species in their cavitated samples. The decrease was observed to be in the range of

1.10 %wt and 3.50 %wt, with the smallest decrease experienced by Fuel 1 (BDN) and the largest decrease experienced by Fuel 4 (BD+H).

The results for the two sub-classes of mono-aromatics indicated an overall decrease in concentration for Fuels 2 to 5, while a small increase was noted for Fuel 1 (BDN). The decrease in mono-aromatic species due to cavitation has previously been reported for various commercial diesel fuels tested by Jeshani[50], however the difference in behaviours of the alkylated and naphthenic mono-aromatic hydrocarbons was not studied. It may be suggested that due to the cyclic nature of their substituted groups, naphthenic mono-aromatics are more susceptible to reactions that form poly-aromatic hydrocarbons, relative to their alkylated counterparts. However, further investigation is required to substantiate this claim; a study of chemical kinetics for the two classes of mono-aromatics, leading to the formation of PAHs, might provide further insight into the issue.

9.3 Di- and Tri (+)-Aromatics

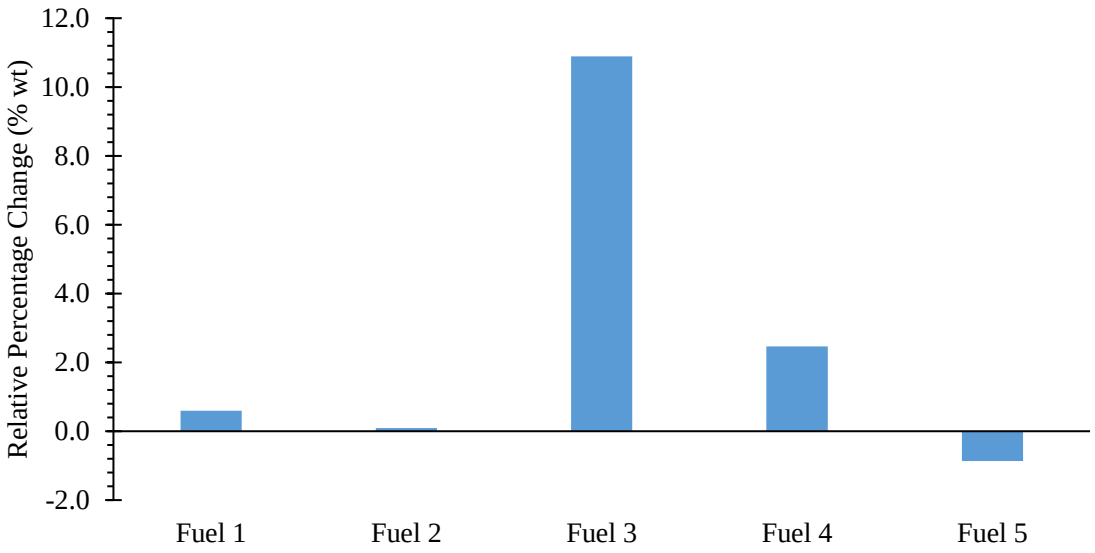

Figure 9.7 Relative change in proportions of the di- and tri(+)-aromatics in the five test fuels after forty hours of cavitation

Figure 9.7 shows the relative change in proportions of di- and tri(+)- aromatic hydrocarbon species as a percentage of their original proportions in the pre-cavitation fuels. Fuels 1 to 4 were observed to experience an increase in proportion of the di- and tri-aromatic hydrocarbons, whereas Fuel 5 (BD+MN) experienced a decrease as a result of the forty hours of cavitation. Fuel 3 (B30) had the largest increase of ~ 10.90 %wt, while Fuel 2 (B10) had the smallest increase ~ 0.10 %wt. Fuel 5 (BD+MN) had an additional 10 %wt of methyl naphthalene in its original composition as compared to the other fuels; this appeared to result in a larger destruction of the di- and tri(+)- aromatic species than their formation from the cavitating flow.

Observation of the change in proportions of just the tri(+)-aromatic species relative to their original proportions in each fuel (Figure 9.8) showed an increasing trend for all fuels. All fuels were seen to experience formation of the three or more ring aromatic structures, with Fuel 5 (BD+MN) showing the smallest increase (3.30 %wt) and Fuel 3 (B30) showing the largest increase (~ 41.05 %wt). The two biodiesel blends - Fuel 2 (B10) and Fuel 3 (B30) - had the two largest overall formation of tri(+)-aromatics of the five test fuels.

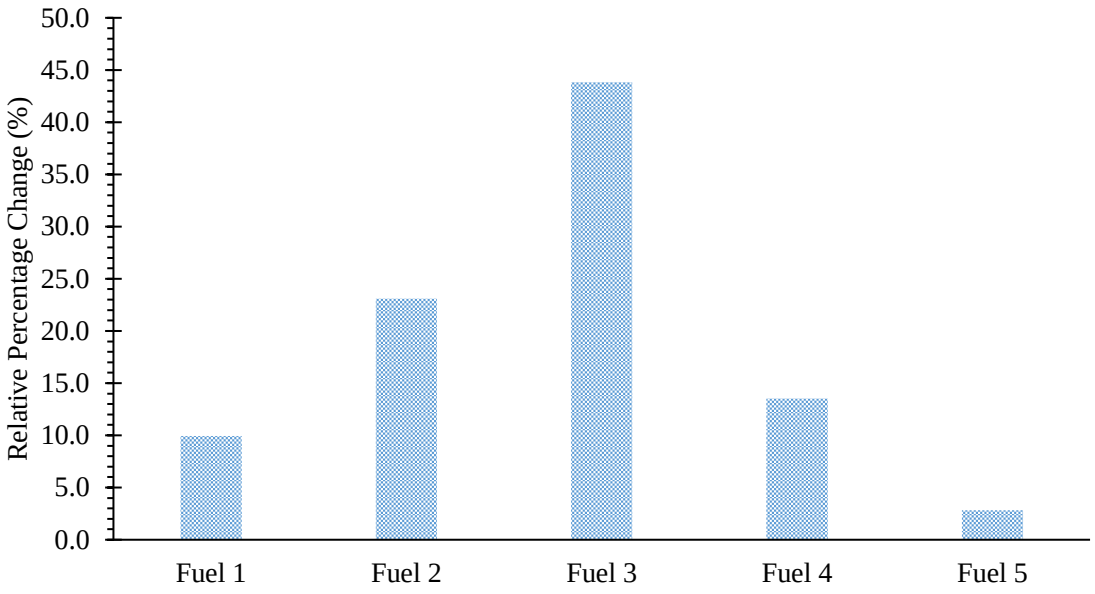

Figure 9.8 Relative change in proportions of the tri (+)-aromatic hydrocarbons in the five test fuels after forty hours of cavitation

9.4 FAME

Fuel 2 (B10) and Fuel 3 (B30) were the biodiesel blend test fuels, made from 10 %wt RME and 30 %wt RME added to Fuel 1 (BDN), respectively. RME is fatty acid methyl ester (FAME) synthesised from rapeseed oil. Figure 9.9 shows the change in proportion of FAME for the two biodiesel fuels as a result of exposure to cavitation. The changes shown are relative to the original concentration of FAME in the pre-cavitation fuel samples.

Both fuel samples experienced a reduction in proportion of FAME. Fuel 2 (B10) experienced a reduction of ~ 5.92 %wt, which was larger than the ~ 3.11 %wt of Fuel 3 (B30). The relative change in FAME from their original proportions corresponded to an absolute decrease of ~ 0.58 % and ~ 0.92 % of the total composition of Fuel 2 (B10) and Fuel 3 (B30) samples, respectively. This suggests that although FAME experienced a larger relative change in proportion in Fuel 2 (B10), the total amount of FAME consumed was larger for Fuel 3 (B30).

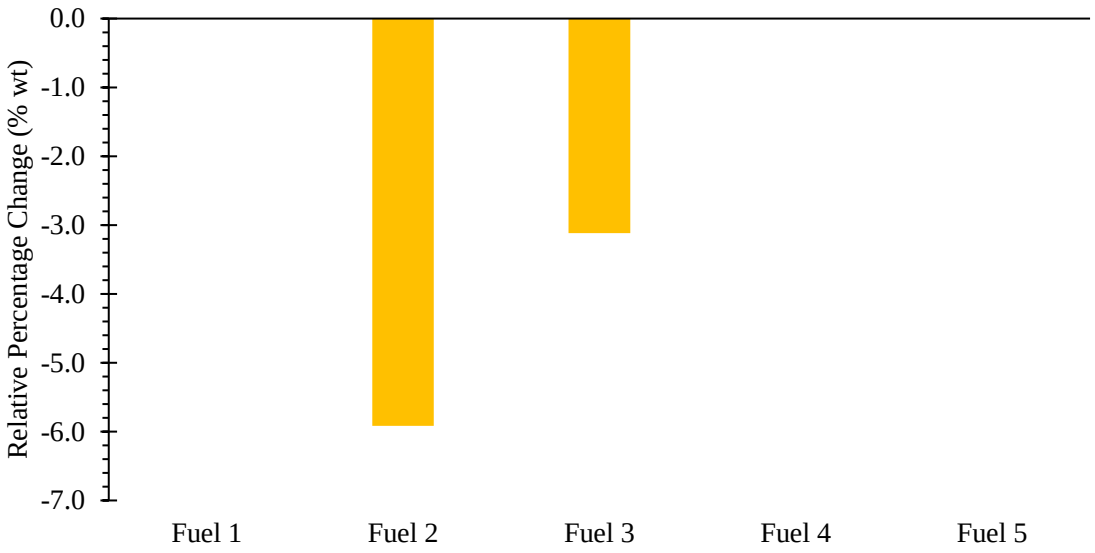

Figure 9.9 Relative change in proportion of FAMEs in the five test fuels after forty hours of cavitation

9.5 Overall Change in Chemical Composition from GC x GC Results

The overall changes in composition of the various hydrocarbon classes and subclasses, including open-chain paraffins, naphthenes, alkylated mono-aromatics, naphthenic mono-

aromatics, di-aromatics, tri-aromatics and FAME, have been presented in Figure 9.10. The changes have come-about as a result of exposure of the test fuels to forty hours of high-pressure recirculating cavitating flow. The results signify the chemical compositional changes occurring in the fuels, resulting from chemical reactions driven by the hydrodynamic cavitation of the fuels.

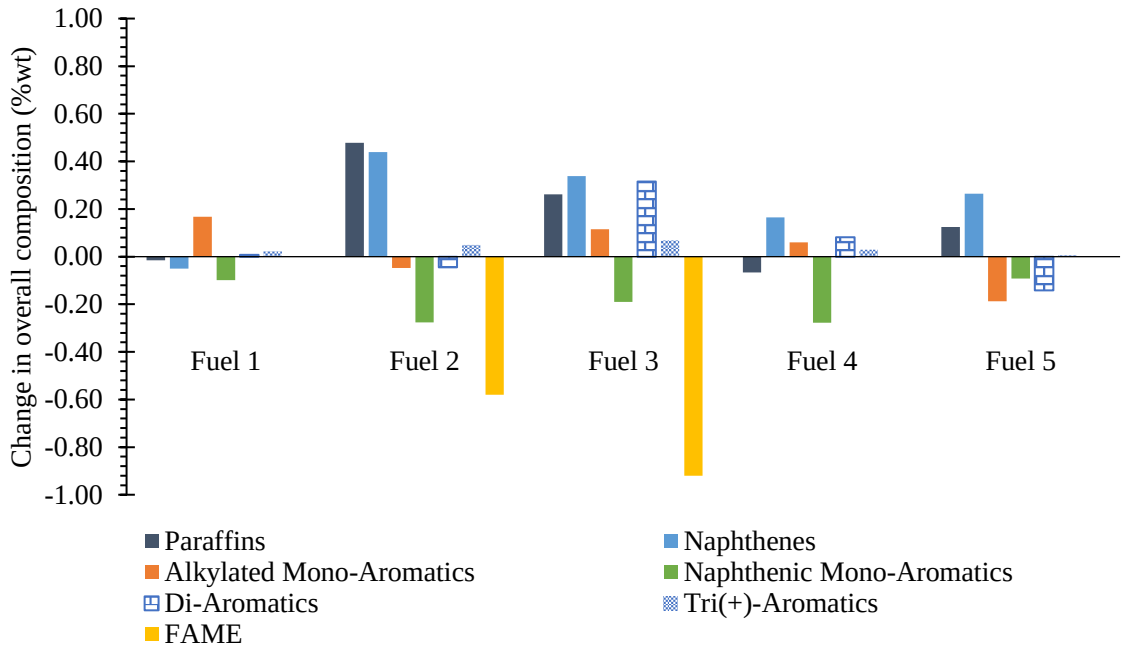

Figure 9.10 Change in fuel components (%wt) for the five test fuels obtained through GC x GC analysis as a result of forty hours of cavitation at 1,650 bar rail pressure

As observed from the overall change in fuel components (Figure 9.10), it was noticed that the component that underwent largest change was FAME. FAME was only present in Fuels 2 and 3, in both of which it was consumed as a result of cavitation. The two biodiesel fuels also showed a large formation of paraffins, of both open-chain and cyclic (naphthenes) subclasses. Open-chain paraffins were not observed to be formed in large proportions for any other fuel. Naphthenes, on the other hand, were observed to be formed in considerable proportions for all but Fuel 1 (BDN). All fuels showed an overall consumption of naphthenic mono-aromatics; these were found to be generally more active than the alkylated mono-aromatics in most fuels.

Observation of tri-aromatic hydrocarbons showed a trend of formation in all fuels when subjected to hydrodynamic cavitation for forty hours, the largest formations of tri-aromatics were observed for the biodiesel blends.

Comparison of the five fuels in terms of the changes occurring to their components suggested that the conventional diesel (Fuel 1 (BDN)) was the most stable, as it experienced the smallest overall change after forty hours of cavitation. Biodiesel blends were found to be the least stable, as they showed the largest changes in their chemical composition. Results for Fuel 3 (B30) showed the largest overall consumption of species including FAME and naphthenic mono-aromatics; while it also had the largest formation of species including the paraffins, alkylated mono-aromatics and poly-aromatic hydrocarbons (di and tri (+)).

Chapter 10
Overall Summary and Discussion of Cavitation Test Results

Diesel fuels of varying chemical composition have been subjected to hydrodynamic cavitation in a purpose-built high-pressure recirculation test-rig. In this section, the main findings from the various tests presented earlier will be summarised and discussed collectively. The overall discussion will be conducted in two parts, first part will address the fundamental observations of the hydrodynamic cavitation phenomenon, second part will focus on the chemical behaviour of the various diesel fuels that were subjected to the sustained hydrodynamic cavitation.

10.1 Fundamental Observations of Hydrodynamic Cavitation

High-pressure cavitation tests have indicated the formation of hydrodynamic cavitation in the test injector nozzles. It has also been suggested that the cavitation structures formed in the nozzle are then carried by the diesel flow into the receiver, where they eventually collapse due to flow stagnation and pressure recovery. The change in optical and chemical properties of the recirculating fuels have provided evidence for the occurrence of this phenomenon.

The intensity of hydrodynamic cavitation forming in the injector nozzle was found to be strongly dependent upon the physical characteristics of the nozzle itself. Results have indicated that higher intensity cavitating flow occurs with an injector of a smaller nozzle-hole diameter. Nozzles of two different nominal nozzle-hole sizes were tested to show that the fuel underwent faster rate of change in its optical properties when recirculated using a smaller nozzle.

Other physical properties such as honing levels and roughness of the internal flow passages were also shown to play a role. Multiple experiments indicated that an injector nozzle caused

a faster rate of change in the fuels' optical properties when it was new. After prolonged usage of the same injector nozzle, the profile of optical change in fuels' properties showed a temporal retardation. It was suggested that a new injector nozzle had manufacturing imperfections (rougher surfaces) and debris inside the flow passages that were hydro-honed after prolonged usage. The results concluded that injector nozzles with rougher internal passages were prone to forming higher intensity cavitating flow, as compared to hydro-honed or hydro-grinded nozzles of the same nozzle-hole diameter.

Investigation of the effect of injection pressure presented conflicting results for the dependence of cavitation intensity to the injection pressure. Fuel tested using a larger nozzle-hole diameter was found to show an independence from the injection pressures. The results indicated that at higher injection pressures, the fuel underwent faster changes in its optical properties; however, examination of the time-constants for the change revealed that the observed optical changes scaled with the volumetric flowrate of the recirculating fuel, rather than the intensity of cavitation.

On the other hand, fuels tested using smaller injector nozzle-holes showed a positive correlation between the injection pressure and the rate of change in fuels' optical properties. It was thus, suggested that a complicated relationship exists between injection pressures, nozzle hole sizes and cavitation intensity. While the results have suggested that smaller nozzle-hole sizes induce an injection pressure dependence in hydrodynamic systems, further investigation is required to determine the minimum nozzle-hole size required to produce this dependence.

Experimental results for downstream/ receiver pressure tests showed a positive correlation between the rate of change in recirculating fuel's optical properties and the fuel receiver pressure; thus, indicating that the intensity of cavitation bubble collapse in the receiver was higher at higher receiver pressures. However, a presence of a threshold receiver pressure was

identified, below which the effect of downstream pressure on the intensity of cavitation bubble collapse could not be realised.

10.2 Chemical Behaviour of Diesel Fuels Subjected to Cavitation

In-situ spectral attenuation coefficient measurements (at 405 nm) have shown changes occurring in the chromophoric systems of diesel fuels when they are subjected to sustained hydrodynamic cavitation. The changing chromophoric systems have indicated chemical activity in the fuels. All test fuels (including the paraffinic model fuel) have shown characteristic behaviours in their changing attenuation coefficients, which has given strong indications towards varying chemical activity of the fuels based on their initial chemical composition.

Through the fuel tests, biodiesel blends were found to be the least stable of the test fuels. The extent of instability was observed to increase with the proportion of FAME content in the blends. Stability of fuels was determined through measurements of the change in their chemical composition (2D GC analysis) and their optical properties (spectral attenuation and uv-vis spectra measurements).

2D GC analysis of the cavitated B30 biodiesel fuel showed large consumption of its FAME content and the largest formation of di-aromatic hydrocarbon species of all fuels. The large formation of di-aromatic species was reflected in the fuel's benzenoid band absorbance from the spectra measurements. The benzenoid band absorbance is known to be caused by the presence of benzene ring(s) in the primary aromatic hydrocarbon species, including mono- and di-aromatics. Fuel 3 (B30) was the only fuel that showed an increase in benzenoid band absorbance.

Fuel 3 (B30) also displayed the largest broadband absorbance increase of all fuels. This was observable in the uv-vis spectra measurements of the fuels. The broadband absorbance increase

has been linked to the formation of particulates in the fuels, which may include the formation of primary soot particles. It has been suggested that poly-aromatic hydrocarbons (PAHs) can eventually grow in mass to form soot particulates, thus an indication for particulate build-up can be obtained through observing the formation of PAHs. 2D GC analysis of the cavitated fuel samples provided an indication for the formation of poly-aromatic hydrocarbons of three or more benzene rings (tri (+)). A comparison of the broadband absorbance increase in the 361 - 365 nm range and the corresponding change in tri (+) aromatic proportions of each fuel from their GC analysis has been provided in Table 10.1 below.

Table 10.1 Comparison of the broadband absorbance decrease in wavelength range of 361-365 nm of each fuel with the change in concentration of their tri (+) aromatic content after forty hours of cavitation.

	Δ broadband absorbance (361 – 365 nm)	Δ tri(+) aromatics
Fuel 1 (BDN)	43.60 %	0.02 %
Fuel 2 (B10)	46.75 %	0.05 %
Fuel 3 (B30)	84.42 %	0.07 %
Fuel 4 (BD+H)	32.00 %	0.03 %
Fuel 5 (BD+MN)	26.49 %	0.01 %

The table shows that the broadband absorbance increase scales with the formation of tri (+) aromatic hydrocarbons. Although it might be a simplification of the phenomenon, an indication for the inter-relation of the two changes can be obtained from their comparison. The trend is not consistent in the case of Fuel 1 (BDN) and Fuel 4 (BD+H), which goes to show that the broadband absorbance increase is not solely dependent on the formation of PAHs. However, the comparison does show that Fuel 3 (B30) experienced the largest increase in both the PAH formation and the broadband absorbance increase, thus the indication of its instability.

Literature on the link between PAH formation and biodiesel fuels are often found to have contradicting views. While there are numerous studies that indicate a reduction in the total PAH engine-out emission from the usage of biodiesel[110,111], there are some that find little or no

difference between the PAH emissions of a conventional diesel and biodiesel[112]; and there are others that suggest higher PAH emissions for biodiesel blends[113,114].

A study on the pyrolysis of rapeseed oil methyl ester (RME) was conducted by Pyl et al.[115]. 2D GC analysis, using a flame ionisation detector (FID) and a time-of-flight mass spectrometer (TOF-MS), was performed on the products of RME pyrolysis. Results indicated a large consumption of methyl esters (>50 %wt) that produced short-chain C_1 - C_4 olefins (~40 %wt), mono-aromatics (~12 %wt) and poly-aromatics (~1 %wt). Karavalakis et al.[116] reported an increase in production of light PAHs (3-5 aromatic rings) from exhaust analysis of a passenger car running on RME blended diesel.

It has been suggested that although linear molecules like fatty acid methyl esters cannot easily lead to the formation of PAHs, the unsaturated and polyunsaturated fatty esters, such as methyl oleates and methyl linoleates, are susceptible to reactions involving PAH formation. RME is known to contain up to ~ 96 % unsaturated and polyunsaturated fatty esters. Thermal reactions of such unsaturated compounds has been suggested to form six-member rings (cyclic alkenes) through Diels-Alder reactions[117]. Dehydrogenation of these cyclic alkenes then leads to the production of single ring aromatic compounds, which react to form PAHs. Formation of heavy PAHs has been explained as a consequence of pyrosynthesis of the light PAHs[118].

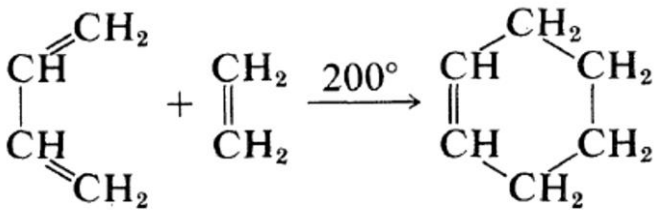

Figure 10.1 Diels-Alder reaction for addition of ethene to 1,3-butadiene to give cyclohexene. Hydrogen elimination from cyclohexene can then lead to the formation of single ring aromatics[101]

Paraffin-based model fuel was found to undergo the smallest change in its spectral attenuation coefficient at 405 nm. It was concluded that the presence of n-paraffins reduced the fuel's chemical activity. However, comparison of Fuel 4 (BD+H) (10 %wt hexadecane) to Fuel 1 (BDN) (conventional diesel) showed a different trend. Fuel 4 (BD+H) was found to undergo larger changes in both its optical properties and chemical composition. It was suggested that the various fuel components of a conventional diesel fuel interact in complicated ways, and that the absence of the different classes of hydrocarbons from the paraffinic model fuel reduced its chemical activity, leading to smaller changes.

GC analysis of the fuels revealed a trend of naphthenic mono-aromatic consumption for all test fuels. It was believed that as a consequence of this consumption, the absorbance in the benzenoid band region of all fuel spectra experienced a decrease. This was found to be true for all but Fuels 3 and 5. Fuels 1, 2 and 4 showed a systematic decrease in the benzenoid band absorbance. Fuel 5 (BD+MN) spectra in the benzenoid band was believed to have variations due to the presence of the additional methylnaphthalene; while the large formation of di-aromatics from FAMEs caused the increase in absorbance for Fuel 3 (B30).

It is suggested that, due to the cyclic nature of their substituted species, naphthenic mono-aromatics provide easier pathways to the formation of PAHs and soot-precursor species, as compared to their alkylated counterparts. In order to substantiate this statement, chemical kinetics modelling of the reactions of the fuel-borne hydrocarbon species will be investigated in the following section.

10.3 Observation of Deposit Formation

Analysis of fuel samples from the high-pressure cavitation tests have given indications of chemical changes occurring in the diesel fuels and of particulate build-up when these fuels are subjected to sustained cavitating flow conditions. Deposit formation has also been observed

through analysis of test-rig components such as the fuel receiving cylinder and high-pressure fuel flowlines.

Figure 10.2 shows photographs of the internal surface of the fuel receiving cylinder, covered in a hard-brown lacquer of polymeric appearance. The extreme conditions generated from the cavitation bubble collapse inside the receiver is suggested to provide a mechanism for deposit formation on the walls of the receiver. Interaction of cavitation bubbles with near-by surfaces have been shown to initiate their collapse[59]; thus the cavitation bubbles generated inside the injector nozzle are expected to undergo collapse as they come in contact with the receiver walls, initiating chemical changes that may result in the observed polymeric deposits.

Deposits of similar appearance have been described in literature as organic amides, and have been associated with the use of fuel detergents containing poly isobutylene succinimide (PIBSI)[5,36,40]. Chemical analysis of the deposits observed in the receiver and fuel flowlines is required to identify their origin.

Figure 10.2 Photographs of fuel receiving cylinder with its internal surface coated in a hard-brown lacquer with a polymeric appearance.

Another type of deposit was collected from the fuel-filter housing. These deposits had a powdery carbonaceous appearance and were found to be magnetic. The magnetic particles were suggested to be eroded ferrous material from the high-pressure pump and the injector nozzle. The carbonaceous appearance of the deposits suggested a coating of organic material on the ferrous particulates. However, chemical analysis of the particles is required to verify the chemical composition of the carbon-like coating and the origin of the magnetic particles.

Chapter 11
Chemical Kinetic Modelling

Chemical kinetics is the study of chemical reactions with respect to reactions rates, breaking and forming bonds, effects of variables on reactions, formulation of intermediates etc. For chemical reactions to be successful, molecules and atoms must collide with sufficient energies, with the correct orientations[119].

A rate of chemical reaction is dependent on thermodynamics and kinetics. Thermodynamics data provides information on energy changes, including the enthalpy changes. However, kinetics data provides the information required to determine the rate of reactions. The information included in the kinetics data provides the reaction specific Arrhenius factors, that are used to calculate the rate constant of a reaction (k) using the following Arrhenius temperature dependence:

$$k = A_i \, T^{\beta_i} \, e^{-E_i/RT} \qquad \textbf{11.1}$$

where, Ai is the pre-exponential factor that provides information on the frequency of successful collisions; βi is the temperature exponent; Ei is the activation energy; R is the universal gas constant and T is the absolute temperature. Together Ai, βi and Ei are referred to as the Arrhenius factors.

An overall chemical reaction consists of a series of elementary reactions or steps, these are detailed by a reaction mechanism. A reaction mechanism provides details at the molecular level of how a reaction proceeds. In this way, a reaction mechanism can be used to identify intermediate species that are formed during the proceedings of the overall reaction. The reaction rate law for the elementary reactions can be used to determine the rate of reaction for the overall reaction.

Experimental results presented in the previous section have indicated the formation of PAHs and particulates in the test diesel fuels as a result of cavitation. It was suggested that in absence of sufficient oxygen, the hydrocarbons in the fuel undergo pyrolysis like reactions to form PAHs and particulates/soot. Many researchers have experimentally studied, modelled and reviewed the reaction mechanisms of PAH formation through pyrolysis of hydrocarbons. Most of the experimental studies have been conducted using simplified systems such as one-dimensional premixed flames, diffusion flames, stirred reactors, shock tubes and constant volume bombs. The studies have led to presumption of a general mechanism of soot formation[117,120,121]. A schematic depiction of the general mechanism is provided in Figure 11.1 below.

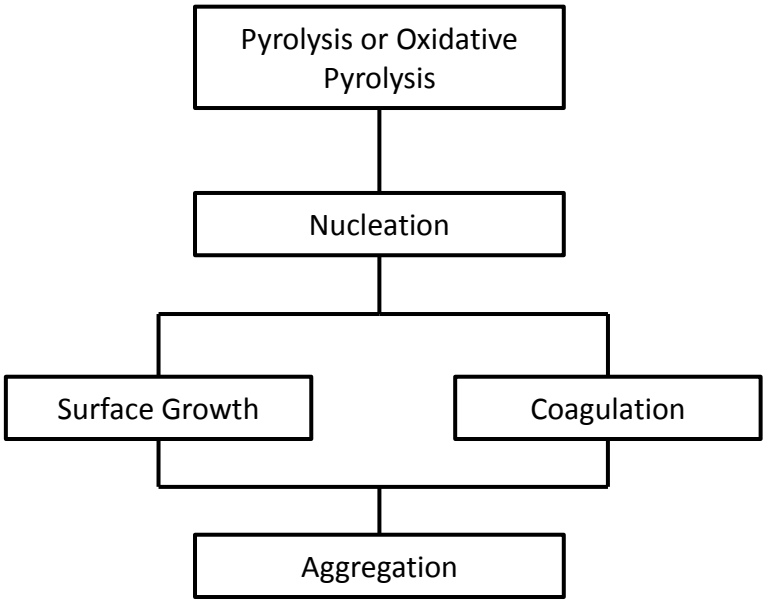

Figure 11.1 Soot formation mechanism in combustion systems (adapted from Smith[120])

The initial stage in a mechanism of fuel pyrolysis involves the formation of molecular soot precursors. Molecular precursors of soot are thought to be heavy poly-aromatic hydrocarbons (PAHs) of molecular weight 500 – 1,000 amu. The growth process of the smaller fuel molecules such as benzene to larger PAHs is found to involve the addition of C_2, C_3 or other smaller units. Among these smaller units, acetylene has received particular attention. Addition

of such species leads to the formation of PAH radicals, that can undergo PAH-PAH radical recombination and addition reactions. The types of initiation reactions are strongly dependent on the fuel composition. Aromatic fuels undergo decomposition to form smaller units like acetylene, that can later react to form larger and larger aromatics. In case of aliphatic fuels, the first aromatic ring must be formed through a series of elementary reactions. The trend for the ease of soot formation has been suggested to be paraffins < mono- and di-aromatics < benzenes < naphthalene.

Following the formation of heavy PAH molecules, the growth process continues towards the formation of nascent soot particles. Nascent soot particles are defined so when their molecular mass reaches approximately 2,000 amu and they attain an effective diameter of approximately 1.5 nm.

Nascent soot particles increase in mass through gas-phase addition of species such as acetylene, PAH and PAH radicals. These additions are chemical in nature, resulting in soot particle growth without an increase in particulate number.

Coagulation of particles also occurs through sticking collisions between soot particles. This significantly increases the particulate sizes, while reducing the particulate population. Coagulation of particles is a physical method for growth of soot particles.

High residence times under pyrolytic conditions converts the amorphous soot particles into progressively more graphitic carbon material. This process is called carbonisation. The polyaromatic material in soot particles undergoes functional group elimination, cyclisation, ring condensation and ring fusion through hydrogen abstraction, growth and alignment of polyaromatic layers.

It has been suggested that all hydrocarbon classes present in a diesel fuel can eventually lead to the formation of PAHs and soot particulates under pyrolytic conditions, albeit following different initiation mechanisms and kinetic routes.

11.1 Kinetic Model and Setup

The purpose of this study was to investigate soot formation from pyrolysis of a model diesel fuel. The composition of the surrogate diesel fuel was based on the GC x GC analysis results for the conventional diesel (Fuel 1 (BDN)). Kinetic mechanisms were obtained from multiple sources and combined to formulate a comprehensive soot-formation mechanism. The model fuel was analysed using the comprehensive soot mechanism on 'Chemkin Pro' chemical kinetics software.

The temperature and pressure profiles of the reaction were modelled as a polytropic process (n=1.21) for a collapsing cavitation bubble. The contents of the bubble were assumed to be a homogenous gas-phase mixture of the surrogate diesel fuel. The collapse time of the bubble was estimated to be around 110 µs, based on the time taken for the flow to reach stagnation after injection into the test-rig's receiver. The polytropic temperature and pressure profiles were obtained at time steps of 10 µs as shown in Table 11.1. The volume of the collapsing bubble was modelled to halve at each time step. The polytropic relationships of pressure and temperature to volume ratio are as follows:

$$p_{(t)} = \left(\frac{V_0}{V_{(t)}}\right)^n \times p_0 \qquad \textbf{11.2}$$

$$T_{(t)} = \left(\frac{V_0}{V_{(t)}}\right)^{n-1} \times T_0 \qquad \textbf{11.3}$$

Where $p(t)$ and $T(t)$ represent the pressure and temperature at time t respectively, n is the polytropic constant, the subscript 0 represents the values at time t = 0 seconds, $V_0/V_{(t)}$ is the volume ratio at time t.

The pressure and temperature at t = 0 seconds were taken to be ambient i.e. 1 atm and 300 K, respectively. The initial bubble diameter was estimated to be around 5 micrometres that gave it an initial volume V_0 of 1.25 x 10^{-16} m^3.

Table 11.1 Polytropic temperature and pressure profiles for the kinetics modelling of a collapsing bubble (n = 1.21)

Time (s)	V_0/V	Temperature T (K)	Pressure P (atm)
0	1	300.00	1.00
10	2	347.01	2.31
20	4	401.38	5.35
30	8	464.27	12.38
40	16	537.02	28.64
50	32	621.16	66.26
60	64	718.49	153.28
70	128	831.07	354.59
80	256	961.28	820.30
90	512	1111.91	1897.65
100	1024	1286.13	4389.98
110	2048	1487.65	10155.69

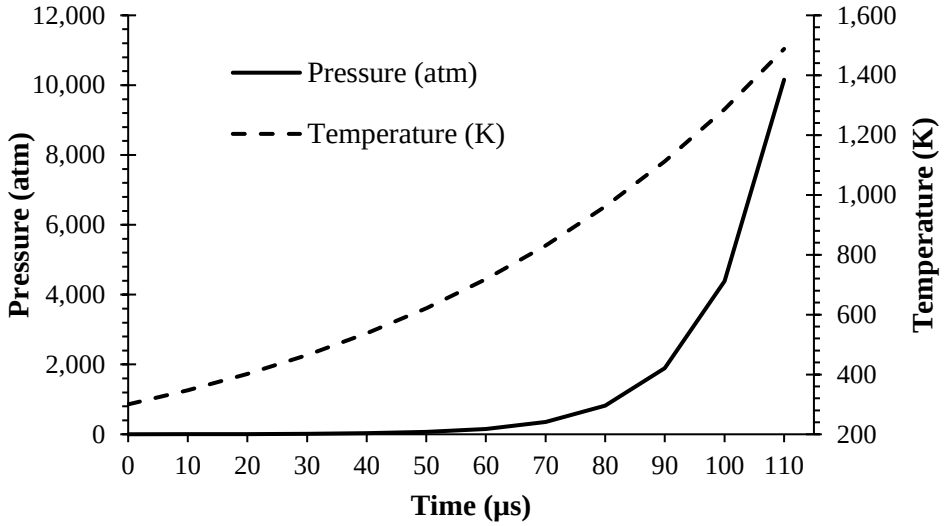

Figure 11.2 Polytropic temperature and pressure profiles for the kinetic modelling of diesel fuel pyrolysis

The time dependent polytropic profiles were entered into the kinetic modelling software that would model the pyrolysis of the model fuel in a gas reactor, given the kinetic reaction mechanism and thermodynamics input files. A closed homogenous reactor that simulated dynamic reactor conditions was used for the pyrolysis reaction. Dynamic systems allow users to specify the controlling conditions that vary as a function of time. The simulation required an input gas-phase kinetics reaction file and a corresponding thermodynamics file containing the thermodynamics data for all species present in the reaction file.

Researchers at Politecnico di Milano[122] developed a soot formation mechanism, which consisted of a gas-phase kinetic model for pyrolysis and oxidation of hydrocarbon fuels. The mechanism also proposed kinetic routes for nucleation and growth of soot particles through coagulation and surface growth. The proposed gas-phase model consisted of about 200 species and 6,300 reactions. It was developed with a modular and hierarchical approach that had been tested and refined for a wide a range of pyrolysis and oxidation conditions. The kinetic model was accompanied with the thermochemical data of each species.

The Politecnico di Milano soot model applied a discrete sectional approach to solve the aerosol dynamics and surface chemistry governing the soot nucleation and mass/size growth. Heavy PAHs were classified into 20 classes of pseudo-species called BINs. Mass of each class doubled going from one BIN to the next. PAHs of more than 20 carbon atoms (heavy PAHs) were constituted into the first four BINs (up to 160 carbon atoms), each of which were divided into three subclasses (A, B and C) based on the hydrogen to carbon (H/C) ratios. The first soot particles were defined as clusters containing 320 carbon atoms and they were classified as BIN_5. Soot particles constituted in BIN_5 to BIN_{12} were assumed to be spherical in shape with diameters up to about 10 nm. BIN_{13} to BIN_{20} were assumed to be monodisperse aggregates containing a number (N_p) of BIN_{12} particles. The different BIN classes and their subclasses have been summarised in Table 11.2. For each of the BIN species a corresponding $BIN_j^{\cdot}$ surface radical was also considered. The proposed soot mechanism considered six heterogenous reaction classes for the BINs:

1. Hydrogen-abstraction-carbon-addition (HACA) mechanism

This involved hydrogen abstraction reactions of the BIN species with $H^{\cdot}$ or $OH^{\cdot}$ to form $BIN_j^{\cdot}$ surface radicals. Acetylene addition to these aryl sites completed the HACA mechanism. HACA mechanism contributes towards soot inception and also towards surface growth of the soot particles. Examples of the hydrogen abstraction and acetylene addition reactions are given below:

- H-abstraction

  $H^{\cdot} + BIN_i \rightarrow H_2 + BIN_i^{\cdot}$

- Acetylene addition

  $C_2H_2 + BIN_i^{\cdot} \rightarrow$ products

2. Soot inception

These reactions included PAH-PAH interactions for all relevant radical-radical, radical-molecule and molecule-molecule reactions that result in the first soot nuclei i.e. BIN_5. For example (i, n< 5):

$BIN_i^{\cdot} + BIN_n^{\cdot} \rightarrow$ products

3. Surface growth

These included, addition reactions of resonantly stable radicals such as propargyl ($C_3H_3^{\cdot}$) to all BINs (radicals and non-radicals) that contributed to soot growth. The reactions are extended to include the addition of $PAH^{\cdot}$ radicals to soot particles and aggregates. Examples of both include:

$RR^{\cdot} + BIN_i \rightarrow$ products

$PAH^{\cdot} + BIN_i^{\cdot} \rightarrow$ products

4. Dehydrogenation

These included reactions where PAHs and soot particles undergo dehydrogenation to form BINs with lower H/C ratios. The removal of hydrogen can be through molecular and radical pathways. Reactions involving addition of H to molecular species with successive removal of methyl were also included in the dehydrogenation reactions.

- Dehydrogenation

$BIN_i^{\cdot} + H^{\cdot} \rightarrow BIN_i$

- Demethylation

$H^{\cdot} + BIN_i \rightarrow CH_3^{\cdot} +$ products

5. Coalescence and aggregation

Coalescence considered in these reactions was a result of particle-particle interactions. Aggregation was considered for interactions between soot aggregates, while ‘soft aggregation’ was considered as the coalescence of particles onto the soot aggregates.

Examples of coalescence, aggregation and 'soft aggregation' are given below:

- Coalescence ($5 \leq i, n < 13$)

  $BIN_i + BIN_n \rightarrow$ products

- Aggregation ($i, n \geq 13$)

  $BIN_i + BIN_n \rightarrow$ products

- Soft Aggregation ($5 \leq i < 13$ and $n \geq 13$)

  $BIN_i + BIN_n \rightarrow$ products

6. Oxidation

Soot oxidation reactions result in their mass/size reduction. Oxidation of BIN molecules and radical by $OH^{\cdot}$, $O^{\cdot}$ and O_2 were considered in the soot model.

Table 11.2 Classes of pseudo-species defined as BINs and their properties.

BIN_i	n_c	Median mass (amu)	Diameter (nm)	*H/C*		
				A	B	C
PAHs						
i=1	20	250	0.81	0.8	0.5	0.3
2	40	500	1.02	0.8	0.5	0.3
3	80	1000	1.28	0.75	0.45	0.3
4	160	2000	1.62	0.7	0.4	0.3
Particles						
i=5	320	4×10^3	2.04	0.65	0.35	0.2
6	640	8×10^3	2.57	0.6	0.35	0.15
7	1250	1.55×10^4	3.21	0.55	0.3	0.1
8	2500	3×10^4	4.04	0.5	0.25	0.1
9	5000	6×10^4	5.09	0.45	0.2	0.1
10	1×10^4	1.2×10^5	6.40	0.4	0.15	0.1
11	2×10^4	2.45×10^5	8.05	0.35	0.1	
12	4×10^4	4.9×10^5	10.14	0.35	0.1	

BIN_i	n_c	Median mass (amu)	Collision Diameter (nm)	*H/C*		
				N_p	A	B
Aggregates						
i=13	8×10^4	9.7×10^5	13.27	2	0.3	0.1
14	1.6×10^5	1.95×10^6	19.50	4	0.3	0.1
15	3.2×10^5	3.9×10^6	28.63	8	0.25	0.1
16	6.4×10^5	7.8×10^6	41.98	16	0.2	0.05
17	1.25×10^6	1.51×10^7	60.89	32	0.2	0.05
18	2.5×10^6	3.02×10^7	89.49	64	0.2	0.05
19	5×10^6	6.02×10^7	131.53	128	0.2	0.05
20	1×10^7	1.21×10^8	193.32	256	0.2	0.05

The chemical mechanism developed at Politecnico di Milano did not include paraffins. It was largely based on reactions of aromatic species leading to the formation of poly-aromatic hydrocarbons and soot. In order to include the chemistry of paraffins undergoing pyrolysis and forming aromatics, PAH formation mechanisms of C1 (methane) to C4 (butane) n-alkanes and of C8 (octane) to C16 (hexadecane) n–alkanes were integrated into the Politecnico di Milano soot mechanism. The two mechanisms of n-alkane pyrolysis to aromatics were obtained from Lawrence Livermore National Laboratory (LLNL)[123,124].

The soot formation mechanism from Politecnico di Milano and the two n-alkane mechanisms from LLNL were combined to produce a more comprehensive mechanism. The combination process involved identification of duplicate species in the three mechanisms, identification and elimination of duplicate reactions and compilation of thermodynamics data for all reacting species in the combined mechanism. The final Politecnico di Milano – LLNL mechanism consisted of 2,427 species undergoing 25,643 gas-phase reactions.

The combined soot formation mechanism was constructed by a colleague at City, University of London[125]. The mechanism was developed as part of a currently on-going project at City, University of London that is investigating the characteristics of flow inside return-valves found in modern diesel FIE.[126]

Table 11.3 General composition of the model diesel fuel based on GC analysis of Fuel 1 (BDN) sample

n-Paraffins	38 %
Naphthenes + Cycloolefins	37 %
Alkylated Mono-aromatics	11 %
Naphthenic Mono-aromatics	9 %
Di-aromatics	4 %
Tri (+) aromatics	1 %

The model diesel fuel was constituted from the results of GC x GC analysis of the conventional diesel fuel sample (Fuel 1 (BDN)). The general composition of the model fuel in terms of

hydrocarbon classes is provided in Table 11.3. Detailed composition of the model fuel with constituents of each hydrocarbon class are provided in Table 11.4

The modelling process was carried out in dynamic reactor conditions as a 'Perfectly Stirred Reactor Model'. The polytropic temperature and pressure conditions were varied at time steps of 10 microseconds (Table 11.1). Two test cases were modelled, with a difference in the fuel composition:

CASE I: Model fuel with composition as specified in Table 11.4

CASE II: Model fuel with composition specified in Table 11.4 + 0.5 %v/v oxygen gas

Table 11.4 Detailed composition of the model diesel fuel, species names are given as specified in the kinetic model along with their chemical name in parenthesis.

Hydrocarbon Class	Reactants	Molar fraction
n-Paraffins	nc10h22 (**n-decane**)	0.026
	nc11h24 (**n-undecane**)	0.048
	nc12h26 (**n-dodecane**)	0.037
	nc13h28 (**n-tridecane**)	0.041
	nc14h30 (**n-tetradecane**)	0.029
	nc15h32 (**n-pentadecane**)	0.029
	nc16h34 (**n-hexadecane**)	0.170
Naphthenes + Cycloolefins	cyc6h12 (**cyclohexane**)	0.123
	cyc6h10 (**cyclohexene**)	0.123
	mcyc6 (**methylcyclohexane**)	0.123
Mono-aromatics	c6h6 (**benzene**)	0.083
	c7h8 (**toluene**)	0.028
Naphthenic Mono-aromatics	**Indene**	0.090
Di-aromatics	c10h8 (**naphthalene**)	0.001
	c10h7ch3 (**methylnaphthalene**)	0.004
	biphenyl	0.025
	c12h8 (**acenaphthalene**)	0.010
Tri (+) aromatics	c14h10 (**phenanthrene** & **anthracene**)	0.009
	bz(a)phnthrn (**benzo(a)phenanthrene**)	0.001

In gas-liquid solutions, a proportion of the gas diffuses into the liquid until a diffusive equilibrium is reached. The diffusive equilibrium between the gas and the liquid is governed by Henry's law:

$$C_s = Hp_g \quad \textbf{11.4}$$

Where C_s and p_g are the concentration of gas dissolved in liquid (kg/m^3) and partial pressure of the gas (Pa), respectively. H is the Henry's constant for the corresponding gas in (s/m)^2.

The second case of model fuel reflects the presence of a small proportion of dissolved oxygen in the fuel. The dissolved oxygen (and other gases in air) can come out of solution inside the cavitation bubble, where they can participate in the reactions of the fuel vapour.

11.2 Modelling Results

The results presented here are based on the kinetic modelling carried out using the Aurora code of Chemkin Pro software package employing the polytropic pressure and temperature profiles described in Table 11.1, the combined Politecnico di Milano – LLNL kinetic model and the corresponding thermodynamics data file. The two test cases presented are differentiated based on the composition of the model fuel. Changes in the proportion of various species and hydrocarbon classes of interest have been monitored and presented.

Proportion of each species in the solution has been presented as their number of moles in the reaction mixture. The software package provided solutions for each species as their mole-fraction in the reaction mixture at given time-steps. The corresponding reaction mixture temperature and pressure were used to estimate the number of moles (m) of each species (x) using the following ideal-gas relation:

$$m_x(t) = mf_x(t) \times \frac{p(t) \times v(t)}{R \times T(t)} \quad \textbf{11.5}$$

Where, $m_x(t)$ and $mf_x(t)$ were the number of moles and the mole-fraction of a species *x* at a given time *t*, respectively.

$p(t)$, $T(t)$ and $v(t)$ were the pressure, temperature and volume of the reaction mixture at *t*, obtained using the polytropic relation, respectively. The initial reaction mixture volume *v(0)* was estimated to be equal to the volume of a 5 μm cavitation bubble (= 1.25 x 10^{-16} m^3).

11.2.1 CASE I: Model Surrogate Diesel Fuel without Dissolved Oxygen

Firstly, the variations in model fuel constituents over the 110 μs simulation period have been presented. Figure 11.3 - Figure 11.6 show the changes in the number of moles of the fuel's components resulting from the polytropic modelling.

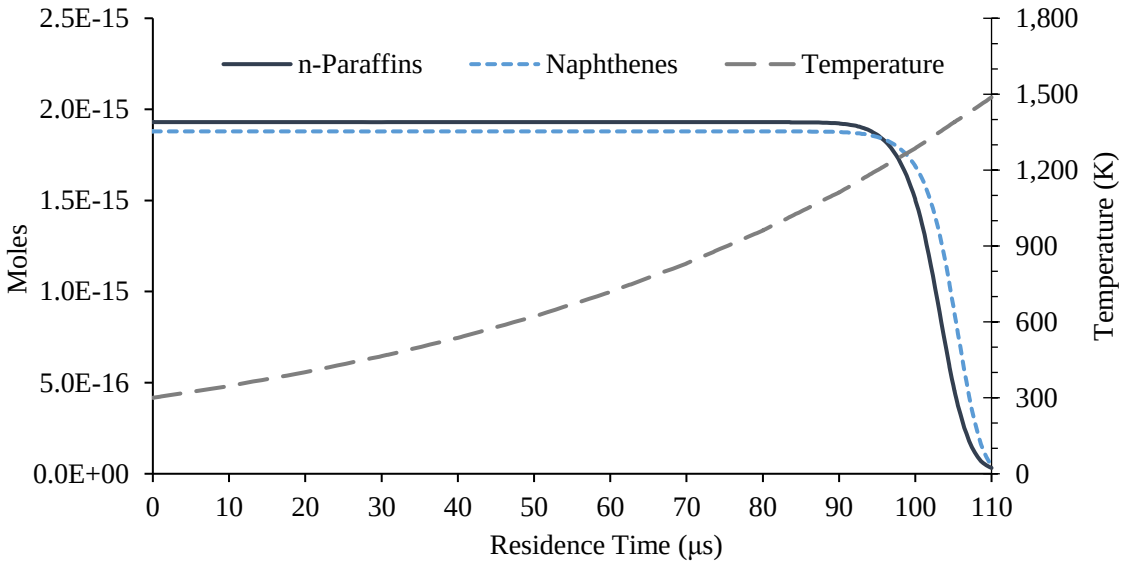

Figure 11.3 Change in the number of moles of n-paraffins and naphthenes in the model diesel fuel

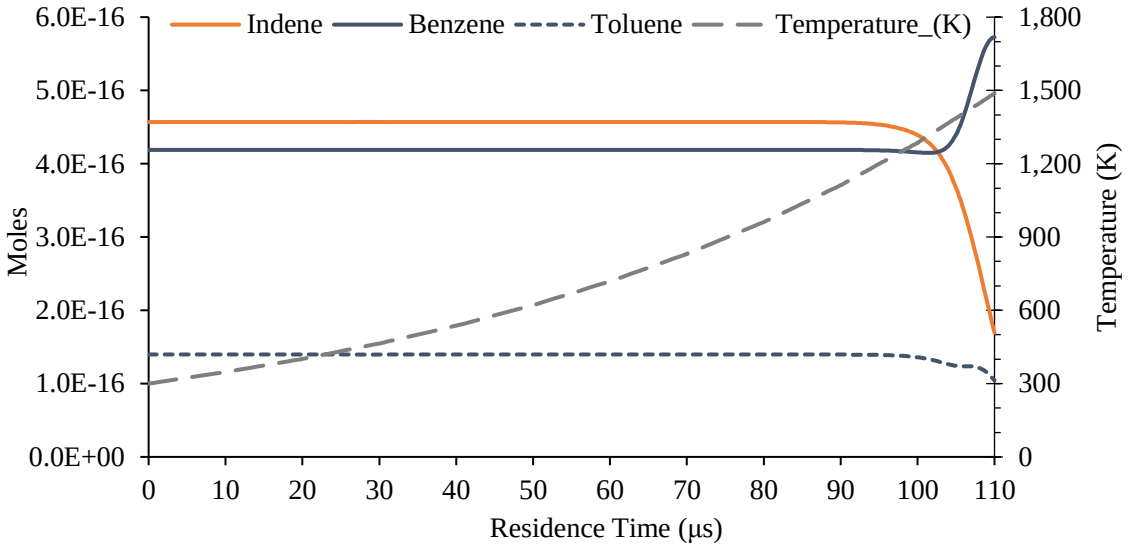

Figure 11.4 Change in the number of moles of mono-aromatic hydrocarbons in the model diesel fuel

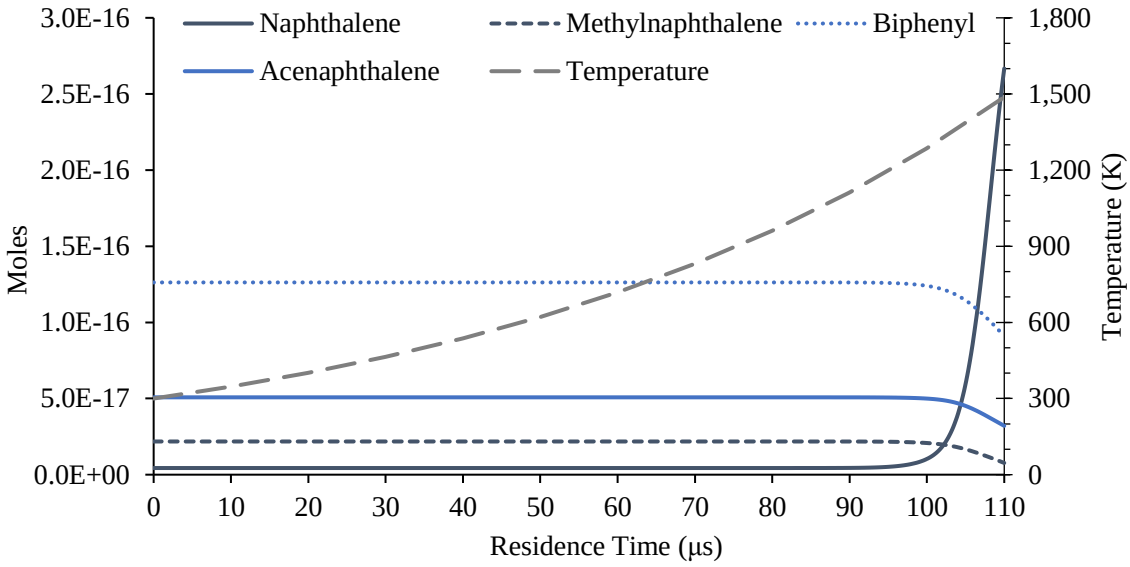

Figure 11.5 Change in the number of moles of di-aromatic hydrocarbons in the model diesel fuel

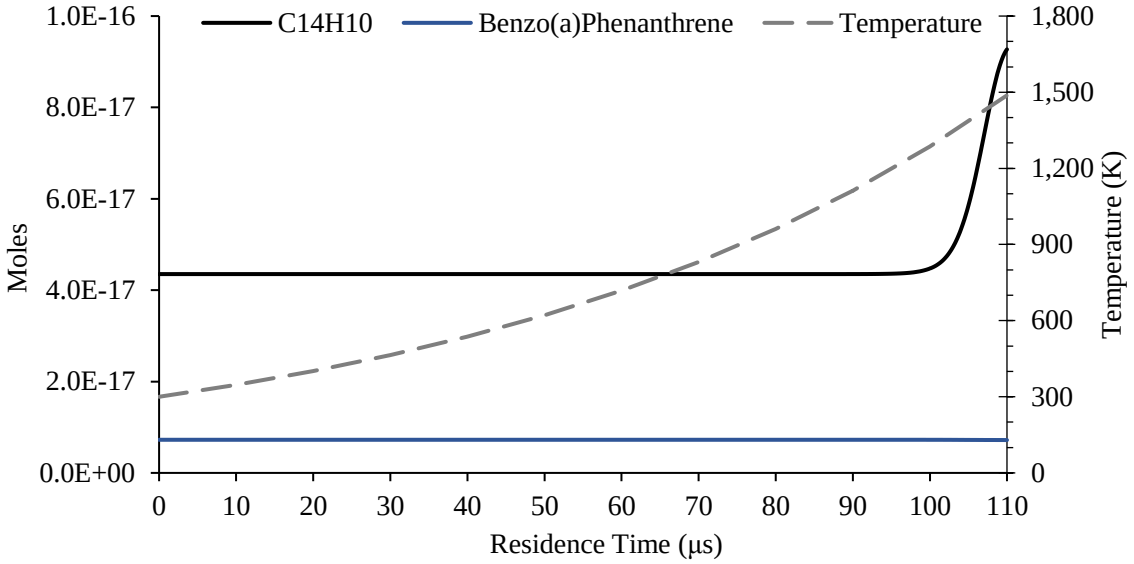

Figure 11.6 Change in the number of moles of tri (+) aromatic hydrocarbons in the model diesel fuel

As observed in the figures above, significant changes in the number of moles of the species present in the fuel start to occur around 90 μs. The temperature of the reaction mixture around this time reaches ~ 1,100 K. The first species to show significant activity are the paraffins, followed by naphthenic mono-aromatics, alkylated mono-aromatics and the poly-aromatics, in the respective order.

Both the n-paraffins and the naphthenes in the fuel experience a net consumption throughout the simulation. Change in composition of hexadecane ($nC_{16}H_{34}$) and the resulting species from its reactions were analysed. It was observed that in the early stages of the simulation, $nC_{16}H_{34}$ decomposed into various small alkyl radicals such as pentyl (C_5H_{11}) and heptyl (C_7H_{15}), while also producing hydrogen radicals and large alkyl radicals such as $C_{16}H_{33}$. The large radicals were then observed to undergo decomposition reactions to form olefins such as ethylene (C_2H_4) and smaller chain alkyl radicals, which continued to decompose into smaller and smaller radicals; eventually forming highly reactive species such as the ethyl (C_2H_5) radical. The consumption of large paraffins like hexadecane was observed to continue and accelerate through attacks from alkyl radicals throughout the modelling duration.

The alkyl radicals produced during this decomposition were also responsible for hydrogen abstraction reactions with other hydrocarbon classes such as the naphthenes and the aromatics. These reactions were found to be crucial in the production of benzene and poly-aromatic hydrocarbons.

Observing the reaction mechanism for cyclohexane (C_6H_{12}) - a naphthene - it was noticed that it underwent hydrogen abstraction reactions through attacks from the alkyl and hydrogen radicals to produce C_6H_{11} radicals. Around 60 μs (T ~ 700 K), the C_6H_{11} radicals started to decompose into olefins (ethylene and propene), small alkyl radicals (methyl and ethyl), cyclohexene (C_6H_{10}) and cyclopentene (C_5H_8). Reactions of the two cycloalkenes (cyclohexene and cyclopentene) resulted in the formation of cyclopentadiene (C_5H_6). Cyclopentadiene was found to be an important species that contributed to the formation of benzene through reactions with ethylene (C_2H_4). It was also found to react with benzene to form naphthalene, and with indene to form $C_{14}H_{10}$ (isomers of anthracene and phenanthrene). Cyclopentadiene also resulted in the production of a key radical species, the cyclopentadiene radical (C_5H_5). C_5H_5 reacted with biphenyl (present in the fuel) to produce BIN_{1a} species as early as 90 μs (T ~ 1,100 K). C_5H_5 was also found to be the largest contributor in the formation of naphthalene through reactions with benzene; this resulted in the large increase in the amount of naphthalene in the reaction mixture post 90 μs (observable in Figure 11.5).

Indene was the only naphthenic mono-aromatic present in the modelled surrogate diesel fuel. During the modelling, indene was found to be consumed in large proportions, with significant reduction in its composition occurring after ~ 92 μs. Reactions of indene were observed to commence from the beginning of the simulation at low temperatures and pressures, where two indene molecules reacted to form $C_{16}H_{10}$ (pyrene and its isomers) along with C_2H_4 (ethylene) and CH_3 (methyl) radical, as shown by the following reaction:

$$2\ Indene\ \rightarrow\ C_{16}H_{10} + 0.5C_2H_4 + CH_3 + H$$

This interaction of the indene molecules was observed to continue throughout the simulation, with the rate of reaction increasing with residence time. The rate for this reaction at t = 0 μs was found to be ~ 3.0×10^{-24}, which exponentially increased to ~ 9.4 by t = 105 μs. $C_{16}H_{10}$ formed during the combination reactions of indene were found to readily combine with other $C_{16}H_{10}$ to form BIN_1 and BIN_2 species. Due to this reason, $C_{16}H_{10}$ and indene were considered to be key soot precursor species.

Post 90 μs indene molecules underwent hydrogen abstraction reactions from alkyl radical attacks to form indenyl radicals. The indenyl radicals were then noted to react with aromatic species such as indene, biphenyl, acenaphthanlene ($C_{12}H_8$), anthracene, phenanthrene and others to form BIN 1 and 2 species.

$$Indenyl\ + Di(+)aromatic\ species \rightarrow\ BIN1\ and/or\ BIN2$$

Observation of the reactions of indene suggested that it was a more potent species in the BIN formation reactions as compared to its alkylated counterparts (toluene and benzene). A separate investigation was conducted to validate this conclusion, where a purely indene (a naphthenic mono-aromatic) based fuel and a purely toluene (an alkylated mono-aromatic) based fuel were subjected to the polytropic temperature and pressure profiles, and their BIN formation rates were compared.

Figure 11.7 and Figure 11.8 show the comparative change in number of moles of BINs 1, 2 and 3 species, post 50 μs reaction time, for indene and toluene fuels. Considering the final population of BIN_1 species at the end of the 110 μs pyrolytic modelling, it was found that indene vapour produced approximately 10^{-18} number of moles of BIN_1 species while the same volume of toluene vapour produced approximately 10^{-19} moles of BIN_1 species. The trend for other BIN classes was found to have a similar order of magnitude difference in production from

the two fuels. It was also observed that the rate of production of BIN species became noticeable at smaller residence times for indene (~ 80 µs), whereas any similar observation for toluene was only noticeable after ~ 105 µs residence time.

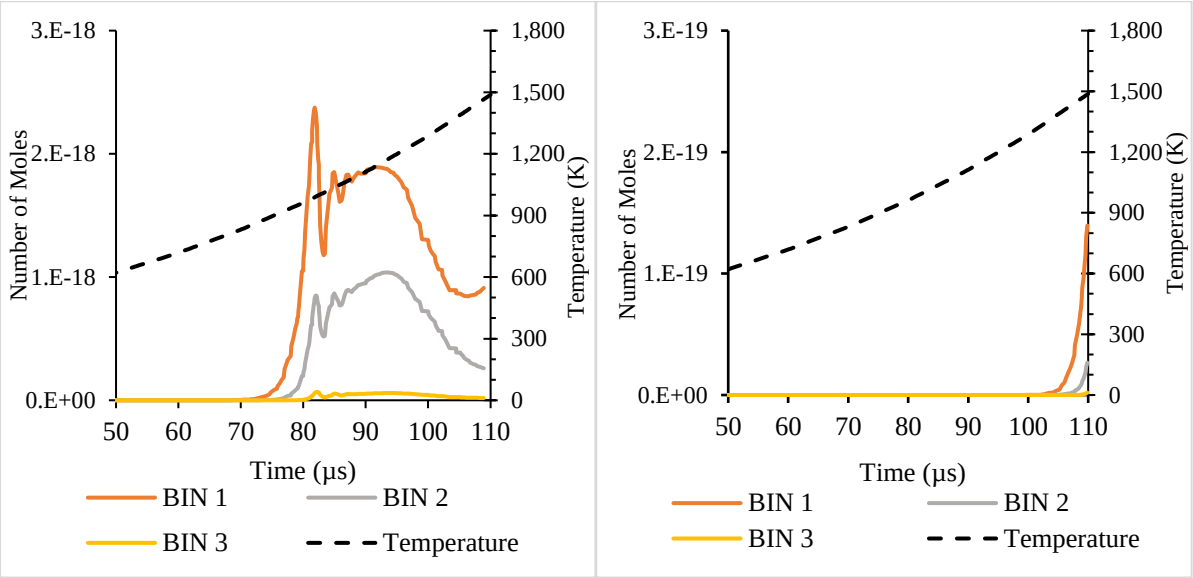

Figure 11.7 Population change of BINs 1, 2 and 3 with reaction time when pure indene (left) and pure toluene (right) are subjected to polytropic modelling (note the difference in scales for the number of moles on the two graphs).

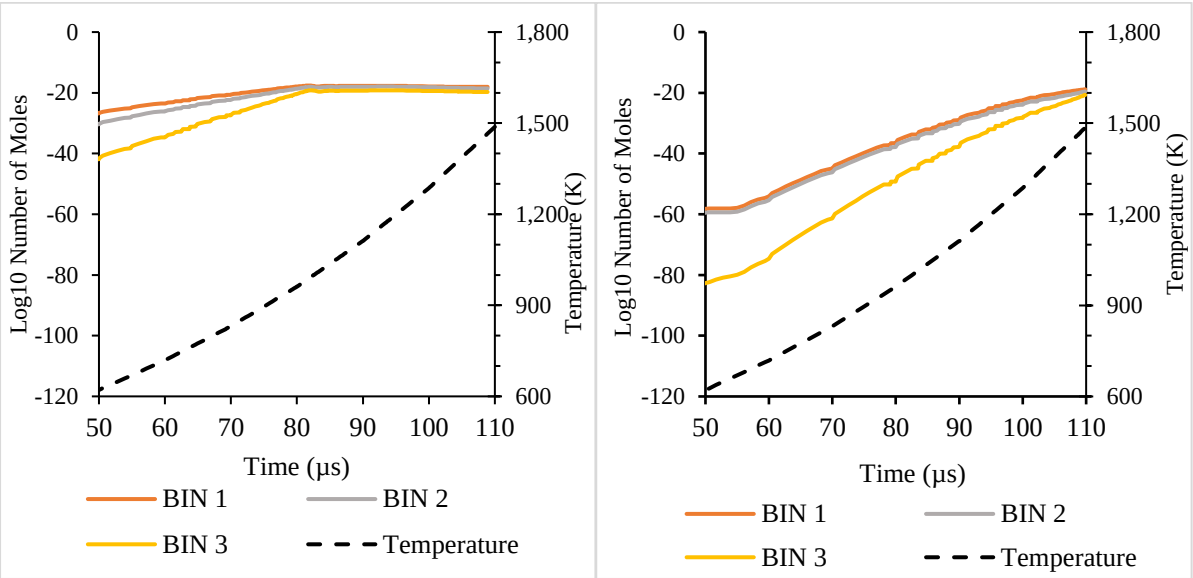

Figure 11.8 Population change of BINs 1, 2 and 3 (log10) with reaction time when pure indene (left) and pure toluene (right) are subjected to polytropic modelling.

The modelling comparison of fuel composed of the two sub-classes of mono-aromatic species indicated the higher propensity of naphthenic mono-aromatic species to form BIN species as compared to the alkylated mono-aromatic species.

BIN Formation

This sub-section will discuss the formation of BIN species in further detail, providing the routes to BIN formation from the various hydrocarbon species present and formed in the reaction mixture. Figure 11.9, Table 11.5 and Table 11.6 summarise the changes in the number of moles of BIN_1 to BIN_{10} species during the polytropic modelling. Each BIN category is a summation of their corresponding sub-categories *a*, *b* and *c*. Although BIN species for BINs larger than BIN_{10} were produced during the simulation, their concentrations were found to be minute, thus they have not been included in the summaries provided below.

Analysis of the reaction pathways from the simulation results showed that species in BINs 1 and 2 were largely produced as a result of PAH reactions, whereas BINs larger than BIN_2 were only formed through the interactions of smaller BIN species.

As observed in Figure 11.9, BIN_1 experienced the largest overall increase in quantity during the modelling, followed by the other BINs in the increasing BIN size. Although BIN forming reactions were observed to occur at lower residence times, significant increase in BIN population was only observed after ~ 86 μs (T ~ 1,050 K). Around this residence time, reactions of indenyl and biphenyl radicals with various aromatic species were found to be key in the formation of BIN_1 species. These aromatic hydrocarbons included benzene, toluene, naphthalene, indene, biphenyl, anthracene and phenanthrene, which were all present in the surrogate diesel fuel. BIN_1 and BIN_2 species were also formed from the combination reactions of pyrene isomers ($C_{16}H_{10}$), which were previously shown to be produced from indene.

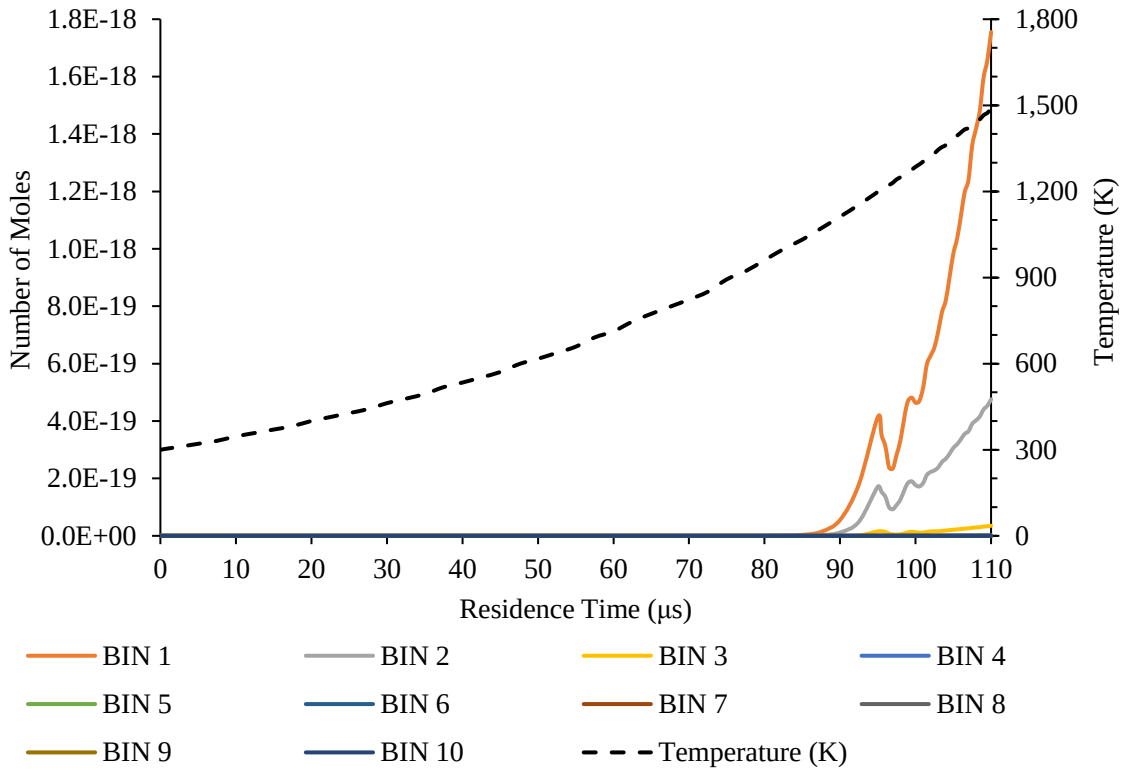

Figure 11.9 Change in the population of BINs 1 – 10 with residence time, resulting from the polytropic modelling of the surrogate diesel fuel.

After ~ 86 μs residence time, a smaller proportion of species in BINs ≥ 2 were also produced from the coalescence and aggregation of BINs ≥ 1. The general coalescence / aggregation reactions observed in the modelling are outlined below (where $1 \leq n$, $i \leq n$)

$$BIN_i + BIN_n \rightarrow BIN_{n+1} + products$$

The coalescence and aggregation reactions of BINs 1 and 2 to form larger BINs were, essentially, in competition with the BINs 1 and 2 formation reactions from the aromatics. This was also observed to be true for larger BINs, where the consumption of BIN_n to form BIN_{n+1} was found to be in competition with the formation of BIN_n from BIN_{n-1}.

Taking the example of BIN_1 - with increasing residence times (t > 86 μs), the combined rate of BIN_1 coalescence/ aggregation reactions was observed to accelerate at a faster rate than the

combined rate of BIN_1 formation reactions from the aromatic species. After ~ 95 μs (T ~ 1,200 K), the rate of coalescence/ aggregation reactions overtook the formation reactions; this resulted in a sharp decrease in the population of BIN_1 species, as observed in Figure 11.9. As a consequence of reduction in the quantity of the BIN_1 species, the rate of formation of BIN_2 species was also reduced, causing a drop in its quantity with a slight temporal delay. This decrease was observed for all BIN classes, with a consistent temporal delay in relation to the smaller BIN classes. Table 11.5 and Table 11.6 do not provide the temporal resolution required to observe this delay; Figure D.1 included in the Appendix D provides a demonstration of this phenomenon for BINs 1 to 10 in the 95 - 99 μs interval. Further oscillations of the increasing and decreasing BIN quantities were observed at larger residence times.

Time (μs)	Temperature (K)	Pressure (atm)	Number of moles for BINs				
			BIN 1	BIN 2	BIN 3	BIN 4	BIN 5
0.0	300.00	1.0	0.0E+00	0.0E+00	0.0E+00	0.0E+00	0.0E+00
10.0	346.54	2.3	7.3E-42	4.6E-43	1.1E-69	1.2E-96	4.0E-93
20.0	400.29	5.3	7.1E-38	6.6E-39	1.2E-61	1.1E-84	9.9E-85
30.0	462.38	12.2	2.5E-34	2.8E-35	1.5E-54	4.7E-74	3.8E-79
40.0	534.11	28.0	3.2E-31	4.0E-32	3.0E-48	1.2E-64	4.2E-78
50.0	616.95	64.4	1.3E-28	1.6E-29	9.5E-43	2.4E-56	1.7E-69
60.0	712.65	148.1	1.2E-26	1.3E-27	2.6E-38	2.1E-49	8.2E-61
70.0	823.19	340.5	9.1E-25	7.2E-26	3.9E-34	8.2E-43	8.4E-52
80.0	960.68	823.1	2.7E-22	2.3E-23	1.2E-28	2.5E-34	2.5E-40
90.0	1111.91	1897.6	5.5E-20	1.2E-20	5.1E-23	9.2E-26	6.4E-29
100.0	1285.79	4385.1	4.6E-19	1.8E-19	1.3E-20	6.3E-22	3.6E-24
110.0	1487.65	10155.7	1.8E-18	4.8E-19	3.5E-20	1.8E-21	1.6E-23

Table 11.5 Growth of BIN_1 to BIN_5 species as a result of the polytropic modelling of the surrogate diesel fuel.

Time (μs)	Temperature (K)	Pressure (atm)	Number of moles for BINs				
			BIN 6	BIN 7	BIN 8	BIN 9	BIN 10
0.0	300.00	1.0	0.0E+00	0.0E+00	0.0E+00	0.0E+00	0.0E+00
10.0	346.54	2.3	8.4E-114	2.2E-134	1.0E-154	8.1E-175	8.1E-195
20.0	400.29	5.3	6.1E-102	5.2E-119	6.7E-136	1.4E-152	4.5E-169
30.0	462.38	12.2	9.4E-93	1.7E-106	3.6E-120	1.2E-133	5.4E-147
40.0	534.11	28.0	6.4E-89	7.5E-100	1.0E-110	2.2E-121	6.6E-132
50.0	616.95	64.4	6.8E-78	2.3E-86	9.0E-95	5.5E-103	4.7E-111
60.0	712.65	148.1	9.9E-68	1.5E-74	3.3E-81	1.3E-87	8.0E-94
70.0	823.19	340.5	9.3E-57	1.3E-61	2.6E-66	9.7E-71	5.6E-75
80.0	960.68	823.1	4.2E-43	8.9E-46	3.0E-48	1.8E-50	1.6E-52
90.0	1111.91	1897.6	1.1E-29	2.1E-30	5.0E-31	1.7E-31	9.4E-32
100.0	1285.79	4385.1	2.3E-24	1.3E-24	6.2E-25	3.5E-25	3.1E-25
110.0	1487.65	10155.7	9.9E-24	5.3E-24	2.6E-24	1.5E-24	1.3E-24

Table 11.6 Growth of BIN_6 to BIN_{10} species as a result of the polytropic modelling of the surrogate diesel fuel.

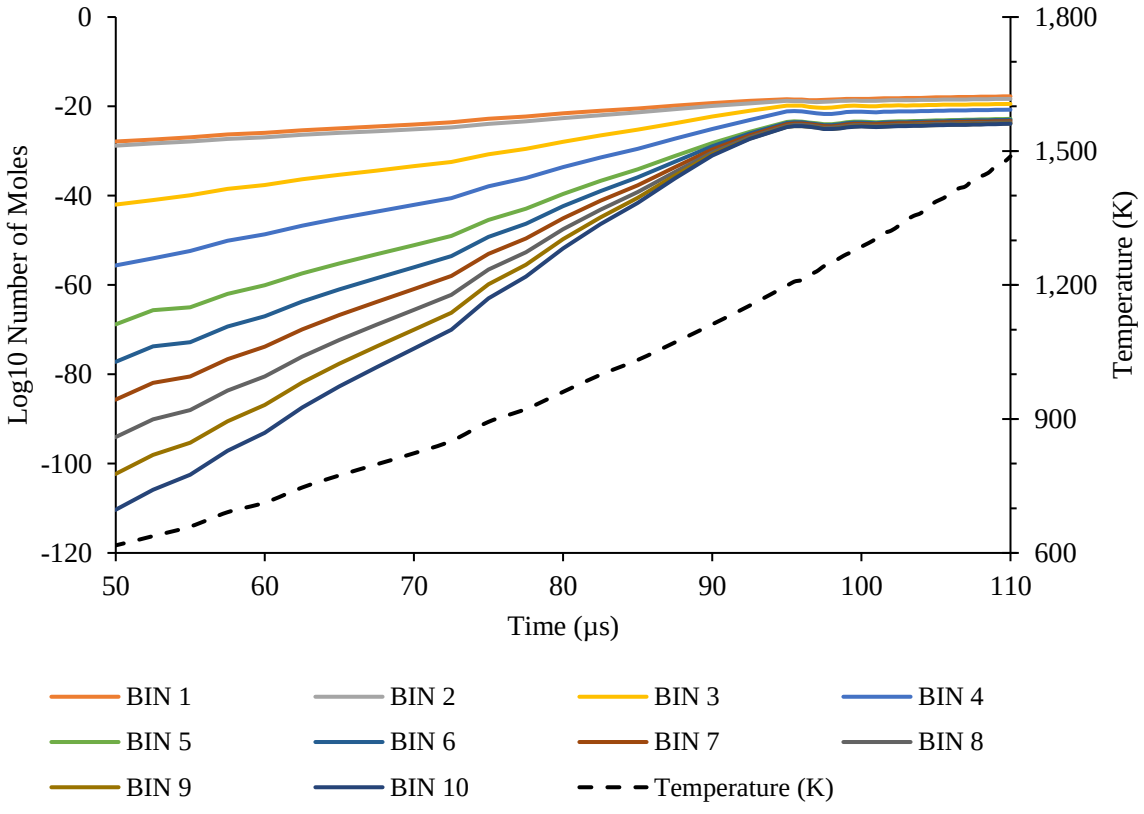

Figure 11.10 Change in the population (log10) of BINs 1 – 10 with residence time (post 50 μs), resulting from the polytropic modelling of the surrogate diesel fuel

BIN growth

This sub-section discusses the dynamics of the evolution of smaller BIN species into larger BIN classes. The applied soot mechanism included BIN growth reactions of various types including:

- Hydrogen Abstraction Carbon Addition Reactions (HACA)
- Surface growth reactions of BINs and their BINj radicals with resonantly stable radicals ($RR^{\cdot}$) and $PAH^{\cdot}$ radicals.
- Coalescence and aggregation reactions of BINs

As mentioned *a priori*, interaction of PAHs only resulted in the formation of BIN_1 and BIN_2 species. All larger BIN formations involved interactions of smaller BINs. Analysis of the modelling results was performed to determine the dominant reaction pathways towards the formation of larger BIN classes from smaller BINs. Three key types of interactions were identified in the BIN growth reactions:

$$BIN_i + BIN_n \rightarrow BIN_{n+1} + products \quad \textbf{11.6}$$

$$Monoaromatic\ radicals + BIN_n \rightarrow BIN_{n+1} + products \quad \textbf{11.7}$$

$$Monoaromatics + BIN_{nj} \rightarrow BIN_{n+1} + products \quad \textbf{11.8}$$

Reaction 11.6 shows the coagulation and aggregation reactions of BINs where $i \leq n$. The rate of coagulation reactions was found to be greater for smaller i values. Reaction 11.7 represents the addition reactions of mono-aromatic radicals to BINs, resulting in BIN growth. The most common mono-aromatic radicals found to be involved in these reactions included indenyl and biphenyl radicals. Reaction 11.8 shows the reactions of mono-aromatics with BIN radicals. The mono-aromatic species commonly found to reaction in this way included indene, benzene, biphenyl and toluene. The BIN radicals were produced as a result of hydrogen abstraction

reactions of the corresponding BIN species with radical species including alkyl radicals, hydrogen radical or mono-aromatic radicals.

$$BIN_n + radical\ species \rightarrow\ BIN_{nj} + products$$

It was observed that the relative rates of the three BIN growth reactions were constant for all BIN classes. The reactions with the highest rate were found to be the coagulation and aggregation reactions (reaction 11.6), followed by the mono-aromatic radical interactions with BIN species (reaction 11.7) and the mono-aromatic species with BIN radicals (reaction 11.8), in the respective order.

11.2.2 CASE II: Model Surrogate Diesel Fuel with Dissolved Oxygen

Figure 11.11 to Figure 11.15 show the changes in the amounts of the different fuel constituents when the model diesel fuel with dissolved 0.5 % oxygen was subjected to polytropic chemical kinetic modelling.

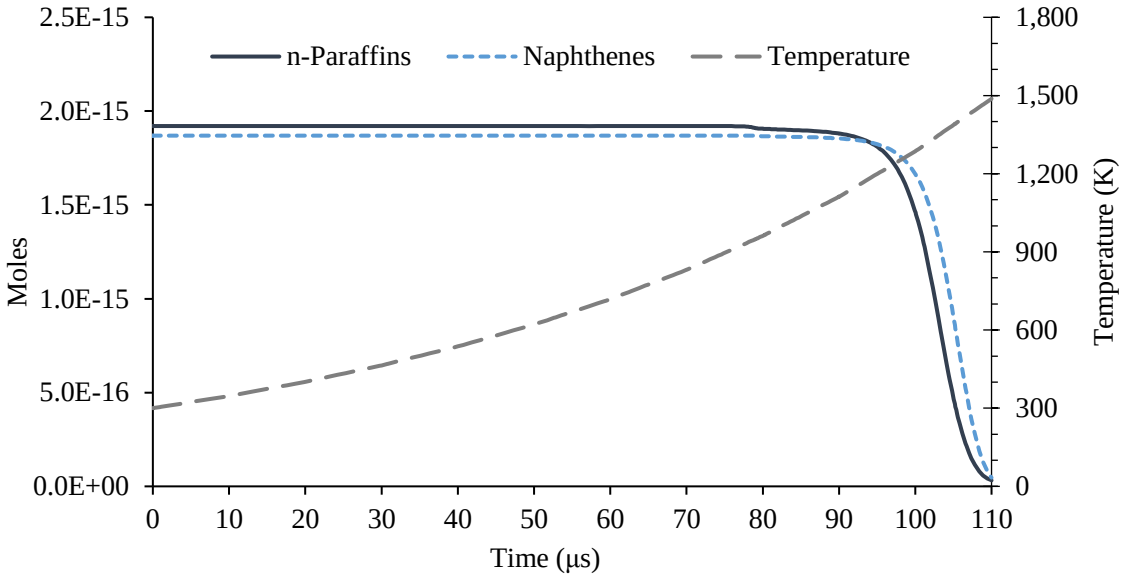

Figure 11.11 Change in the number of moles of n-paraffins and naphthenes in the model diesel fuel with dissolved oxygen

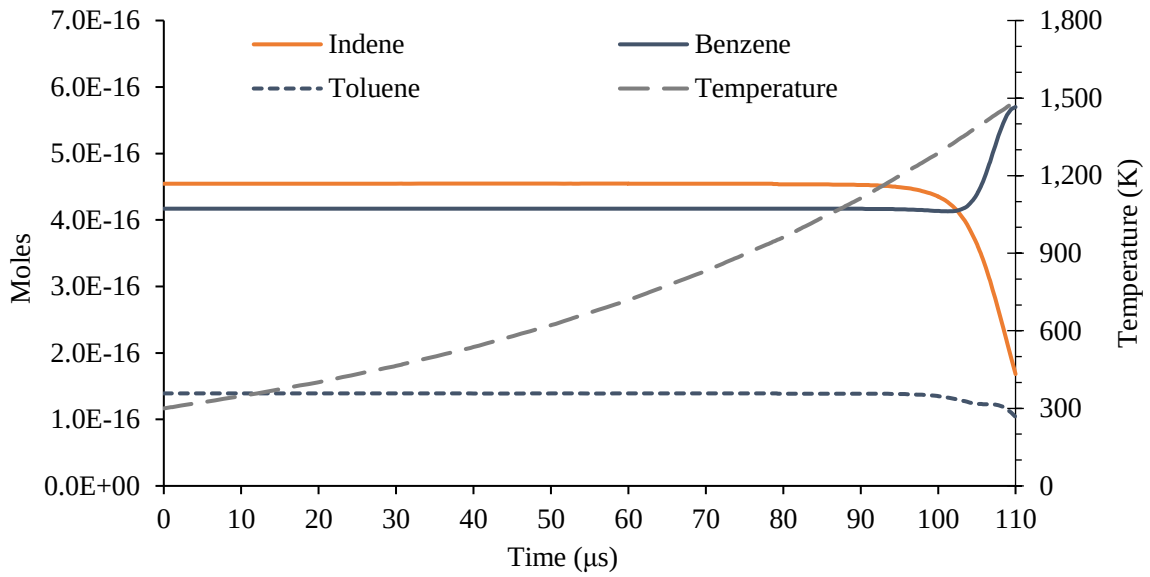

Figure 11.12 Change in the number of moles of mono-aromatic hydrocarbons in the model diesel fuel with dissolved oxygen

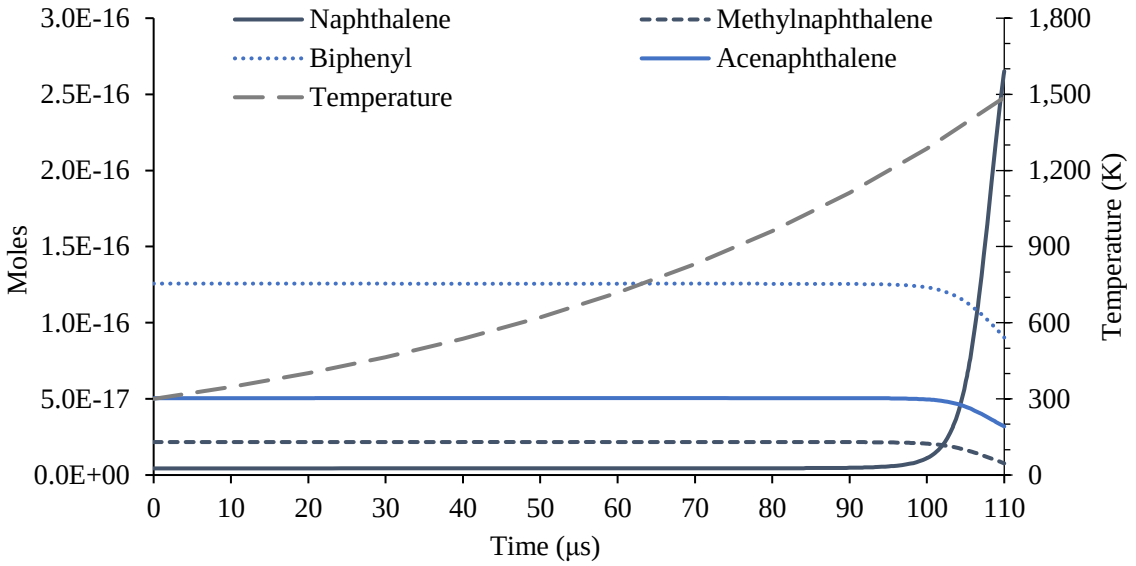

Figure 11.13 Change in the number of moles of di-aromatic hydrocarbons in the model diesel fuel with dissolved oxygen

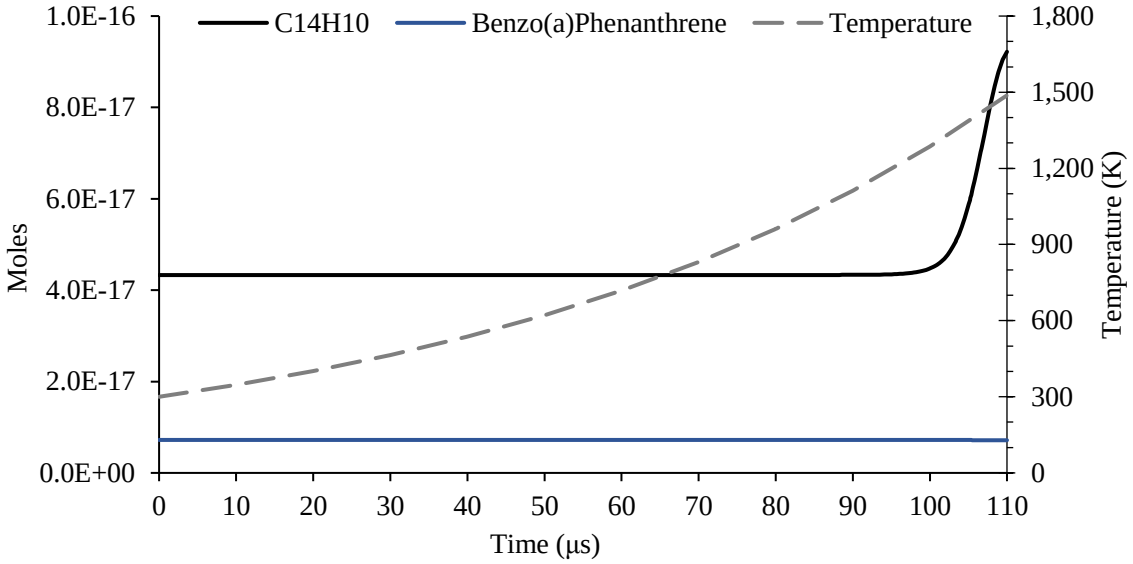

Figure 11.14 Change in the number of moles of tri (+)-aromatic hydrocarbons in the model diesel fuel with dissolved oxygen

At first sight, the changes occurring in each fuel component appear to be very similar to the first modelling case (without dissolved oxygen). However, careful observation of the plots at ~78 µs, shows small discrepancies in the population of most species. The species that noticeably show the discrepancy include the n-paraffins, naphthenes and indene. Careful comparison of the changes occurring in the reaction mixtures for case I and II reveals that the reaction mixture appears to experience noticeable changes at smaller residence times in the presence of the 0.5 %v/v oxygen.

Figure 11.15 shows the changes occurring in the population of oxygen gas with residence time during the polytropic modelling. Oxygen experiences a total consumption, with almost all the consumption occurring in the ~ 75 - 81 µs time interval (~ 900 – 985 K).

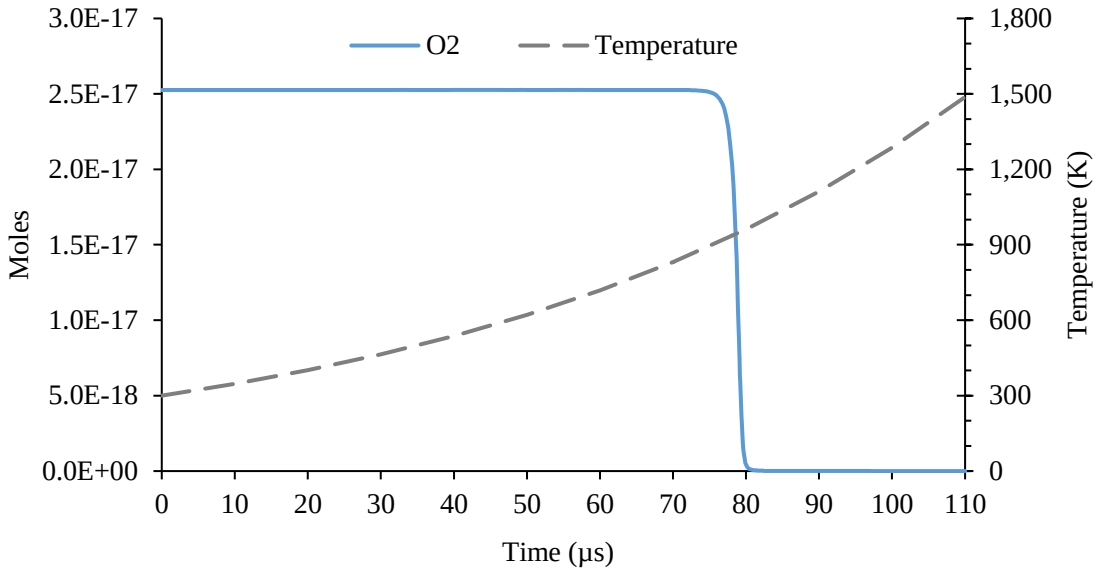

Figure 11.15 Change in the number of moles of oxygen gas in the model diesel fuel with dissolved oxygen

Observing the major oxygen consumption reactions revealed its interactions with paraffinic radicals, and further reactions with the n-paraffins, leading to the formation of alkyl peroxides (ROOH). The alkyl peroxides then readily decomposed to form the hydroxyl radicals (OH). The scheme of reactions for the production of hydroxyl radicals via alkyl peroxides is shown below:

$$O_2 + R^{\cdot} \rightarrow ROO^{\cdot}$$
$$ROO^{\cdot} + R' \rightarrow ROOH + R'^{\cdot}$$
$$ROOH \rightarrow OH + RO^{\cdot}$$

Oxygen was also found to react with alkyl and other radical species to form hydroperoxyl radicals (HO_2) through the striping of hydrogen from the radical species. Hydroperoxyl then formed hydrogen peroxides (H_2O_2) through interactions with other species, which then decomposed to form hydroxyl (OH) radicals. The scheme of hydrogen peroxide formation, leading to the formation of hydroxyl radical is shown below:

$$O_2 + R^{\cdot} \rightarrow R' + HO_2$$
$$HO_2 + R \rightarrow R^{\cdot} + H_2O_2$$
$$H_2O_2 \rightarrow 2OH$$

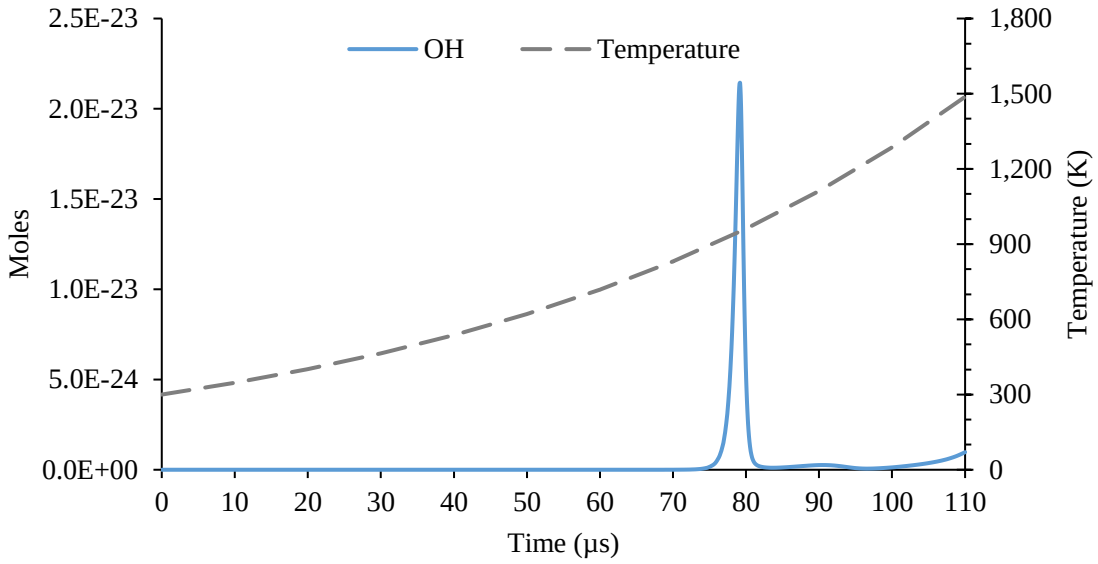

Figure 11.16 Changes in the amount of hydroxyl radicals during the modelling of surrogate diesel with dissolved oxygen

The large formation of hydroxyl radicals was observed to drive hydrogen-abstract reactions from aromatic species, creating large concentrations of aromatic radicals such as indenyl and biphenyl radicals, while also producing the highly stable water (H_2O) molecules. Figure 11.17 shows a comparison of the formation of indenyl radicals in the two modelled cases. Case II (with dissolved oxygen) showed a sharp increase in the amount of indenyl radicals after ~ 76 µs, temporally coinciding with the sharp decrease in the amount of oxygen (Figure 11.15) and the increase in the amount of hydroxyl radicals (Figure 11.16). This formation of indenyl at ~ 76 µs was not observed in modelling Case I.

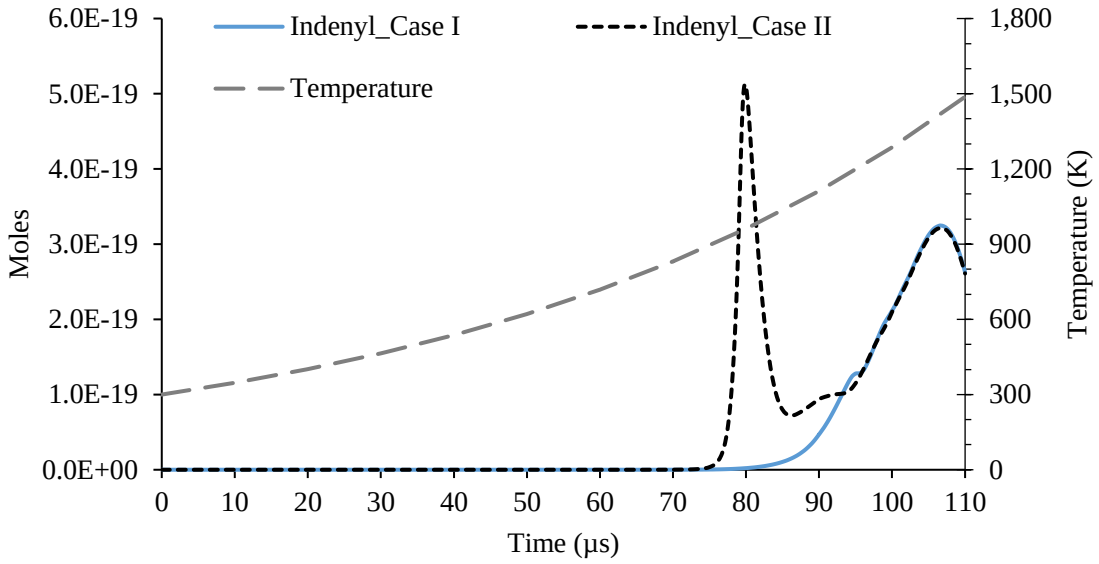

Figure 11.17 Comparison of the changes occurring in the amount of indenyl during the modelling of diesel fuel without dissolved oxygen (Case I) and with dissolved oxygen (Case II).

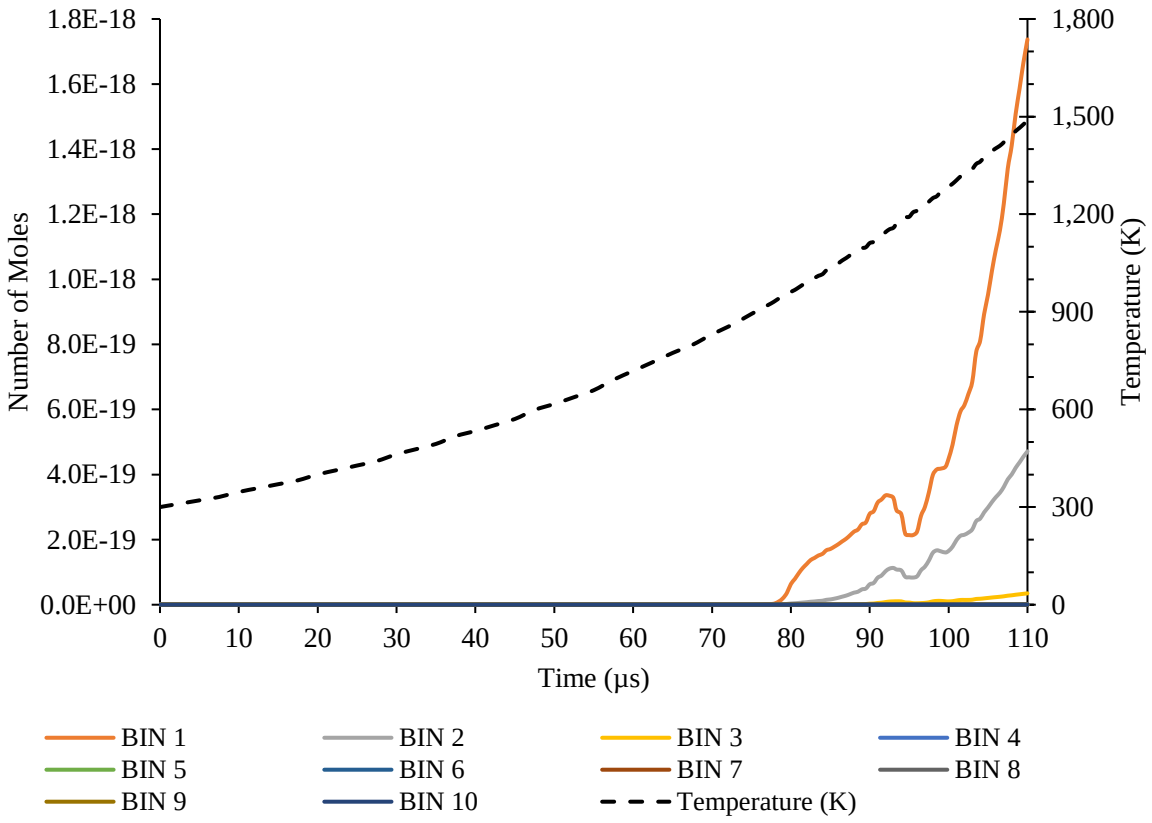

Figure 11.18 Change in the population of BINs 1 – 10 with residence time, resulting from the polytropic modelling of the surrogate diesel fuel with dissolved oxygen.

Indenyl has been shown to be a major precursor species that leads to the formation of BINs. The large production of indenyl at ~ 76 μs thus led to the formation of BINs at comparatively shorter residence times than Case I. Figure 11.18 shows the variations in the number of moles of BIN_1 to BIN_{10} species during the simulation. It is observed that the formation of BIN_1 species became prominent at ~ 78 μs, much earlier than the ~ 86 μs residence time observed for the modelling in Case I.

The total amounts of the first ten BINs formed during the polytropic modelling can be obtained from Table 11.7 and Table 11.8, below. Even with the BIN formation starting at shorter reaction times for Case II, the total number of moles of each BIN class at the end of the simulation was found to be very similar for both test cases. This suggests that once the oxygen species were consumed and eventually converted to stable water molecules (H_2O), the resulting soot-precursor radical species were consumed in reforming their non-radical counterparts. This can be observed from Figure 11.17, where the post 90 μs population of indenyl radicals recovered to match the indenyl radical population of Case I. This suggests that a temperature dependent equilibrium concentration of the precursor species is reached, which is equal to their concentrations in Case I products. Thus, by the end of the simulation, an equilibrium concentration of the BIN species is also approached.

Time (μs)	Temperature (K)	Pressure (atm)	Number of moles for BINs				
			BIN 1	BIN 2	BIN 3	BIN 4	BIN 5
0.0	300.00	1.0	0.0E+00	0.0E+00	0.0E+00	0.0E+00	0.0E+00
10.0	346.54	2.3	6.4E-42	3.7E-43	8.0E-70	7.8E-97	1.1E-91
20.0	400.29	5.3	6.5E-38	5.7E-39	1.0E-61	9.2E-85	6.7E-81
30.0	462.38	12.2	2.2E-34	2.4E-35	1.3E-54	4.9E-74	2.0E-71
40.0	534.11	28.0	2.3E-31	2.5E-32	1.7E-48	7.4E-65	3.1E-63
50.0	616.95	64.4	6.4E-29	5.8E-30	2.1E-43	3.6E-57	5.0E-56
60.0	718.49	153.3	1.5E-26	1.0E-27	2.5E-38	2.6E-49	2.3E-49
70.0	831.07	354.6	2.9E-24	1.7E-25	2.6E-33	1.6E-41	7.1E-43
80.0	961.28	825.3	6.4E-20	3.7E-21	2.9E-24	8.2E-28	2.6E-31
90.0	1111.41	1894.1	2.8E-19	6.3E-20	3.2E-21	7.2E-23	2.3E-25
100.0	1284.93	4372.8	4.5E-19	1.7E-19	1.0E-20	4.6E-22	2.6E-24
110.0	1487.65	10155.7	1.7E-18	4.7E-19	3.5E-20	1.8E-21	1.6E-23

Table 11.7 Growth of BIN_1 to BIN_5 species as a result of the polytropic modelling of the surrogate diesel fuel with dissolved oxygen.

Time (μs)	Temperature (K)	Pressure (atm)	Number of moles for BINs				
			BIN 6	BIN 7	BIN 8	BIN 9	BIN 10
0.0	300.00	1.0	0.0E+00	0.0E+00	0.0E+00	0.0E+00	0.0E+00
10.0	346.54	2.3	6.4E-42	3.7E-43	8.0E-70	7.8E-97	1.1E-91
20.0	400.29	5.3	6.5E-38	5.7E-39	1.0E-61	9.2E-85	6.7E-81
30.0	462.38	12.2	2.2E-34	2.4E-35	1.3E-54	4.9E-74	2.0E-71
40.0	534.11	28.0	2.3E-31	2.5E-32	1.7E-48	7.4E-65	3.1E-63
50.0	616.95	64.4	6.4E-29	5.8E-30	2.1E-43	3.6E-57	5.0E-56
60.0	718.49	153.3	1.5E-26	1.0E-27	2.5E-38	2.6E-49	2.3E-49
70.0	831.07	354.6	2.9E-24	1.7E-25	2.6E-33	1.6E-41	7.1E-43
80.0	961.28	825.3	6.4E-20	3.7E-21	2.9E-24	8.2E-28	2.6E-31
90.0	1111.41	1894.1	2.8E-19	6.3E-20	3.2E-21	7.2E-23	2.3E-25
100.0	1284.93	4372.8	4.5E-19	1.7E-19	1.0E-20	4.6E-22	2.6E-24
110.0	1487.65	10155.7	1.7E-18	4.7E-19	3.5E-20	1.8E-21	1.6E-23

Table 11.8 Growth of BIN_6 to BIN_{10} species as a result of the polytropic modelling of the surrogate diesel fuel with dissolved oxygen.

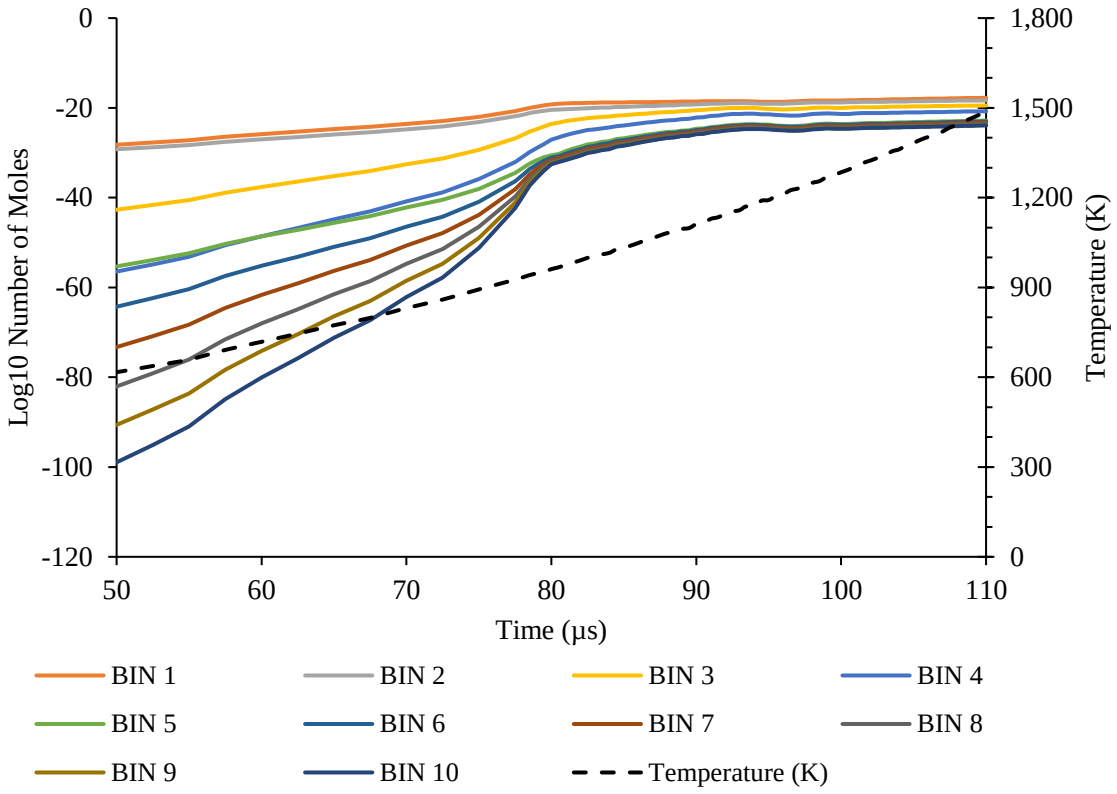

Figure 11.19 Change in the population (log10) of BINs 1 – 10 with residence time, resulting from the polytropic modelling of the surrogate diesel fuel with dissolved oxygen.

11.3 Overall Discussion of Kinetic Modelling and Comparison with Cavitation Experiments

A surrogate diesel fuel was developed and modelled under polytropic conditions that simulated the pyrolytic environment inside a collapsing cavitation bubble. The chemical mechanism used for the simulation was a comprehensive soot-mechanism that included reactions of various hydrocarbon classes towards the formation of soot particles (BINs).

Two test cases for the simulation were conducted, with the first test case (Case I) involving an initial reaction mixture of pure surrogate diesel fuel and the second test case (Case II) involving an initial reaction mixture of surrogate diesel fuel with an additional 0.5 %v/v of oxygen gas (O_2).

Chemical modelling of the two reaction mixtures indicated build-up of soot species in both test cases. All hydrocarbon classes present in the fuel, including paraffins, naphthenes and aromatics were found to have the propensity to form soot. The products resulting from the chemical reactions of all these fuel-borne species were found to interact and contribute towards the formation of soot-precursor species, that eventually led to the production and growth of soot. Various soot-precursor species and species that assisted in the production and growth of soot particles were identified; most prominent of these species included:

- Alkyl radicals – CH_3 (methyl), C_2H_5 (ethyl) and C_3H_7 (propyl)
- Radicals of naphthenes – cyclopentadiene radical (C_5H_5)
- Mono-aromatic hydrocarbons and their radicals – indene, benzene, toluene, C_6H_5 (phenyl) and indenyl
- Di-aromatic hydrocarbons and their radicals – naphthalene, biphenyl and biphenyl radicals

- Polyaromatic hydrocarbons – $C_{16}H_{10}$ (pyrene and isomers) and $C_{14}H_{10}$ (anthracene, phenanthrene and isomers)

The presence of oxygen in the initial reaction mixture (Case II) was found to activate the soot formation chemistry of the surrogate diesel fuel at an earlier reaction time (and at lower temperature). Oxygen was found to decompose and initiate reactions at ~ 900 K, producing highly reactive hydroperoxyl (HO_2) and hydroxyl (OH) species. These species were then observed to undergo hydrogen-abstraction reactions with various compounds to produce radical species, including the soot-precursor species mentioned above. Formation of the soot-precursors resulted in production of soot particles at lower residence times and at lower temperatures. However, upon complete consumption of oxygen species, the rate of soot formation was reduced, such that the total amount of soot formed by the end of the 110 μs simulations was found to be the same for both test cases. It was thus concluded that the presence of oxygen in the reaction mixture initiates soot formation chemistry at lower reaction temperatures, however, once the oxygen and resulting hydroxyl species are consumed the rate of soot formation reaches an equilibrium that is dependent on the reaction mixture temperature.

The purpose of the kinetic modelling was to gain an understanding of the chemical changes occurring to a diesel fuel when it is subjected to pyrolytic conditions. Kinetic modelling was likened to the conditions inside a collapsing cavitation bubble produced because of hydrodynamic cavitation occurring inside diesel fuel injection systems, thus the modelling results were hypothesised to give an indication of the changes occurring to diesel fuels when they are subjected to cavitation in diesel engines.

Although diesel fuels are highly complex mixtures of different chemical compounds that undergo intricate reactions to produce numerous chemical products, classifying the different compounds into classes and observing the changes occurring to them can provide an initial

indication to the types of chemical changes occurring in the diesel fuels as a whole. Following is a comparison of the changes observed in various hydrocarbon classes occurring as a result of kinetic modelling (as seen in Figure 11.3 to Figure 11.14) and the changes observed for recirculating cavitating flow tests in the high-pressure test-rig. The results obtained from 2D gas chromatography analysis on cavitated conventional diesel samples (Fuel 1 (BDN)) have been used for the comparison (Chapter 9).

N-Paraffins

The n-paraffins present in the conventional diesel (Fuel 1 (BDN)) were observed to undergo an overall consumption as a result of sustained hydrodynamic cavitation. The relative change in concentration of the n-paraffins was found to be ~ 0.12 % (reduction) after the forty hours of cavitation. Kinetic modelling results indicated an almost total consumption of n-paraffins in a cavitation bubble. However, total volume of cavitation bubbles constitutes a very small proportion of the total diesel fuel present in the rig, therefore the overall change in n-paraffins present in the diesel fuel charge is expected to be relatively small. Nonetheless, both analysis indicated an overall consumption of the n-paraffins.

Naphthenes

The cavitated test samples indicated an overall consumption of the naphthenes present in the diesel fuel. The relative consumption of the naphthenes was found to be slightly higher than that of n-paraffins. The kinetic modelling results also indicated a consumption of the naphthenes (these included cylcohexane, cyclohexene and methylhexane), in this case the naphthenes also experienced an almost total consumption inside the cavitation bubble. Therefore, the two analyses agreed on an overall consumption of the naphthenes.

Benzene and Alkylated Mono-aromatics

The cavitated Fuel 1 (BDN) samples indicated an overall increase in the concentration of the alkylated mono-aromatic hydrocarbons (including the benzene molecules). The magnitude of increase was found to be relatively larger than the magnitude of decrease in n-paraffins. Analysis of the kinetic modelling results also indicated an overall increase in the amount of the fuel-borne alkylated mono-aromatics (these included benzene and toluene). Although toluene showed a small decrease, a significantly larger increase in the amount of benzene was observed.

Naphthenic Mono-aromatics

Forty-hour cavitated Fuel 1 (BDN) sample revealed an overall decrease in the concentrations of naphthenic mono-aromatic species. The only naphthenic mono-aromatic species present in the modelled surrogate diesel was indene; indene was observed to undergo an overall consumption during the simulation.

Di and Tri (+) aromatics

GC x GC analysis of the diesel samples showed an increase in proportion of the di and tri (+) aromatic hydrocarbons after forty hours of sustained cavitation. The different di and tri (+) aromatic hydrocarbons present in the surrogate fuel were observed to undergo different relative changes during the modelling. Some di-aromatics (including methylnaphthalene, acenaphthalene and biphenyl) experienced small decreases, while naphthalene experienced a large increase in concentration. In tri (+) aromatics, benzo(a)phenanthrene was observed to experience negligible change during the simulation, whereas $C_{14}H_{10}$ (anthracene isomers) and $C_{16}H_{10}$ (pyrene isomers) were observed to be produced in large proportions. The overall change in the di and tri (+) aromatics was found to show an overall production by the end of the simulation.

The comparison of the analysis of diesel fuel under cavitation and pyrolysis conditions have shown similar trends in the changes for the different hydrocarbon classes. However, it is important to consider that the chemical kinetics simulation only considers the reactions taking place inside a homogenous cavitation bubble under collapse; whereas in the hydrodynamic cavitation tests, the products of these pyrolysis reactions can undergo further reactions in the liquid-phase.

Furthermore, the kinetic modelling considers the case where a gas bubble is composed entirely of pure surrogate diesel vapour, while in the cavitation tests the products of pyrolysis reactions undergo multiple cavitation cycles. This implies that a small proportion of the fuel vapour should include pyrolysis products produced in preceding cavitation cycles. The effect of pyrolysis on such mixtures might provide enhanced soot forming effects as compared to pure diesel vapour.

Regardless of these considerations, the chemical kinetics model provides a good indication of the chemical changes taking place inside a diesel fuel cavitation vapour. The chemical modelling performed in this study also appears to provide a good qualitative agreement with the trends obtained for the high-pressure hydrodynamic cavitation tests on diesel fuels in the high-pressure test-rig.

Chapter 12
Conclusion and Future Work

A high-pressure cavitation test-rig has been developed and employed to study the behaviour of diesel fuels of different compositions when subjected to sustained hydrodynamic cavitating flow. Spectral extinction measurements, ultraviolet-visible spectroscopy and two-dimensional gas-chromatography have been employed to determine the compositional changes occurring in the diesel fuels.

12.1 Observations for the Fundamentals of Cavitation

Variations in the high-pressure cavitation experiments allowed the investigation of some fundamental physical parameters affecting the flow characteristics of hydrodynamic cavitating systems. Key findings of these investigations are outlined below:

- Single-hole injector nozzles were employed in all cavitation tests. The geometric characteristics of these nozzles were identified to play an important role in the nature of the cavitating flow formed. Injectors with two nominal nozzle-hole sizes were utilised – 213 and 176 μm. Observing the rate of change in optical properties of diesel fuels injected through the two types of nozzles indicated a higher intensity cavitation occurring inside the smaller nozzles; the intensity of cavitation, in this context is a function of the number of cavitation bubbles formed inside the nozzles, with no reference to the intensity of bubble collapse inside the receiver.
- New injector nozzles were observed to produce larger rates of change in optical properties of fuels; the rates of change were found to decrease for repeated tests conducted with the same nozzles. It was hence suggested that the new nozzles had lower levels of honing that produced higher intensity of cavitation due to larger shear stresses

and pressure gradients occurring at the sharp nozzle inlets. Over time the nozzle passages became hydro-grinded resulting in lower intensity of cavitating flows.

- Investigation into the effect of injection/rail pressure on the behaviour of two conventional diesel fuels was conducted using the 176 µm nozzle-hole injectors. Two injection pressures were investigated – 825 bar and 1,650 bar. Both fuels showed higher rate of change in their optical properties at 1,650 bar injection pressures, suggesting that a higher intensity cavitation occurred in the system at the higher injection pressure. Higher injection pressures were suggested to produce larger pressure gradients across the nozzle hole that resulted in larger formation of cavitation structures.
- One of the conventional diesel fuels (Fuel 1 (BDN)) was also tested for injection pressure dependence using a 213 µm injector nozzle. Contradictory to the observation above, this investigation did not show a pressure dependence. The fuel sample was observed to undergo changes in its optical properties that scaled with its volumetric flowrate in the test-rig. A correlation between the injection pressure and the nozzle-hole diameter on the intensity of resulting cavitation has been suggested that requires further investigation to be quantified.
- Modifications were made to the high-pressure test-rig to allow investigation of the effects of downstream pressure on cavitation. Downstream pressure in the test-rig was varied through pressurisation of the fuel receiver. Two conventional diesel fuels were tested during this investigation at ambient, 5 bar and 10 bar receiver pressures. A positive correlation between the receiver pressure and the rate of change of fuel's optical properties was observed. The correlation was observed through calculation of the rate of decrease in spectral absorbance in the spectra of cavitated fuel samples. The findings implied that the intensity of cavitation bubble collapse inside the receiver was higher at larger downstream pressures, resulting in faster changes in the fuel properties.

However, existence of a threshold receiver pressure was identified, below which the effect of downstream pressure on the intensity of cavitation bubble collapse could not be realised.

12.2 Observations for the Chemical Behaviour of Diesel Fuels

Cavitation tests of five commercial diesel fuels of different chemical compositions provided an insight into the chemical changes occurring in the diesel fuels as a result of sustained hydrodynamic cavitation. The fuels were recirculated in the test-rig at 1,650 bar injection pressures for forty hours (10 hours per day over four successive days, and left to stand overnight). In-situ spectral attenuation coefficients of the fuels at 405 nm were determined, and cavitated samples of the fuels were drawn from the rig for uv -vis spectroscopy and 2D gas-chromatography analysis. Chemical kinetic modelling study of a collapsing bubble, comprised of surrogate diesel fuel vapour, was performed to further understand the chemical reactions of fuel components under pyrolytic conditions, similar to those estimated inside collapsing cavitation bubbles. The pyrolytic conditions were simulated through the application of a polytropic temperature and pressure profile that subjected the surrogate fuel vapour to conditions ranging from ambient to temperatures and pressures of 1,500 K and 1 GPa, respectively. Key findings from the three analyses performed on diesel samples are summarised below, supplemented with the kinetic modelling outcomes:

- All diesel fuels showed optical activity through the spectral attenuation coefficient measurements. These suggested chemical changes occurring in the fuels that were consuming and forming chromophoric moieties. All fuels displayed characteristic behaviours in their changing attenuation coefficients, which gave strong indications towards varying chemical activity of the fuels based on their chemical composition.

- Spectra of all fuels showed an increasing broadband absorbance with cavitation duration, this was indicative of particulate formation in the fuels. It was suggested that all fuels were susceptible to particulate build-up, albeit at varying rates.
- The extent of change in a fuel's chemical and optical activity was said to be indicative of its chemical stability under sustained cavitating flow. Biodiesel blend fuels displayed the largest changes in both their spectral absorbance and chemical composition (from 2D GC analysis); their instability increased with the proportion of their fatty acid methyl ester (FAME) content. Compositional analysis of fuel samples showed the largest increase in PAH formation for the B30 biodiesel blend fuel; Diels-Alder ring forming reactions of the polyunsaturated fatty esters present in the biodiesel were suspected as the leading mechanism for forming aromatic species in the fuel, that eventually grew into PAHs and soot particles.
- 2D GC analysis of all fuel samples revealed a consistent trend of decreasing naphthenic mono-aromatic compounds as a result of cavitating flow, however the same trend was not observed for the alkylated mono-aromatic compounds. It was suggested that, due to the cyclic nature of their substituted species, the naphthenic mono-aromatics provided an easier pathway towards the formation of PAHs and soot-precursors. Chemical kinetics modelling of a surrogate diesel fuel substantiated this statement, where indene (a naphthenic mono-aromatic) was found to be highly potent in production of PAHs and soot-particulates. Comparative polytropic modelling of a pure indene fuel and a pure toluene fuel reaffirmed the higher potency of naphthenic mono-aromatics toward soot formation compared to the alkylated mono-aromatics.
- Chemical kinetics modelling of the surrogate diesel revealed the importance of n-paraffins in initiating reactions that lead towards the production of soot particles. Alkyl radicals produced largely from decomposition and cleavage of n-paraffins were found

to interact with all other hydrocarbon classes present in the fuel, producing reactive radical species that contributed towards PAH and soot formation.

- Cavitation tests on a purely paraffinic model fuel showed small increase in attenuation, which suggested that paraffinic content of the diesel fuels was generally more stable when subjected to cavitation. However, comparison of the chemical activity (GC x GC results) of conventional diesel (Fuel 1 (BDN)) and diesel with additional paraffins (Fuel 4 (BD+H)) indicated larger changes in the fuel with higher paraffin content. The findings suggested that the purely paraffinic fuel displayed lower activity due to the absence of other species that could react with the alkyl radicals to form PAHs (as seen in the kinetic modelling). In contrast, Fuel 4 (BD+H) consisted of the other species (including aromatics) that the alkyl radicals could react with to form the PAHs and soot. However, the increased reactivity of Fuel 4 compared to Fuel 1 was unexplained from the experimental analyses and requires further investigation.

12.3 Recommendations for Future Work

- The particle size distributions, obtained using the laser particle counter, have indicated the entrapment of micro particles by the fuel filters. Compositional analyses of the trapped particles would provide a meaningful insight into the type of deposits formed during the cavitation tests, subsequently allowing the determination of the chemical reaction pathways leading to their formation from the various diesel fuel components.
- Experimental outcomes from the injection pressure dependence tests provided contradictory results when the tests were conducted with different sized nozzle. An interrelation between the nozzle-hole size and the intensity of resulting cavitation was suggested which needs to be further investigated.
- Fuels containing fatty acid methyl esters (FAME) have displayed larger chemical instability under cavitation conditions. Kinetic modelling for the pyrolysis of fuels

containing FAME can be undertaken to identify the chemical activity of their FAME content.

- Chemical kinetic modelling of the surrogate diesel fuel conducted for this study simulated a single polytropic compression event of a pure diesel fuel bubble (representing a cavitation bubble collapse). It is known that the chemical products resulting from this phenomenon can be subjected to multiple cavitation events as they are recirculated in a diesel vehicle, therefore, modelling investigations into the products of multiple subsequent polytropic compressions may provide a more detailed outcome for the effects of cavitation on diesel fuels in diesel vehicles.

Appendix A

Fuel Dependence Tests (40 hours)

A.1 *Spectra Measurements in the 190 nm – 405 nm range*

Following are the spectra measurements of cavitated fuel samples from the initial fuel tests.

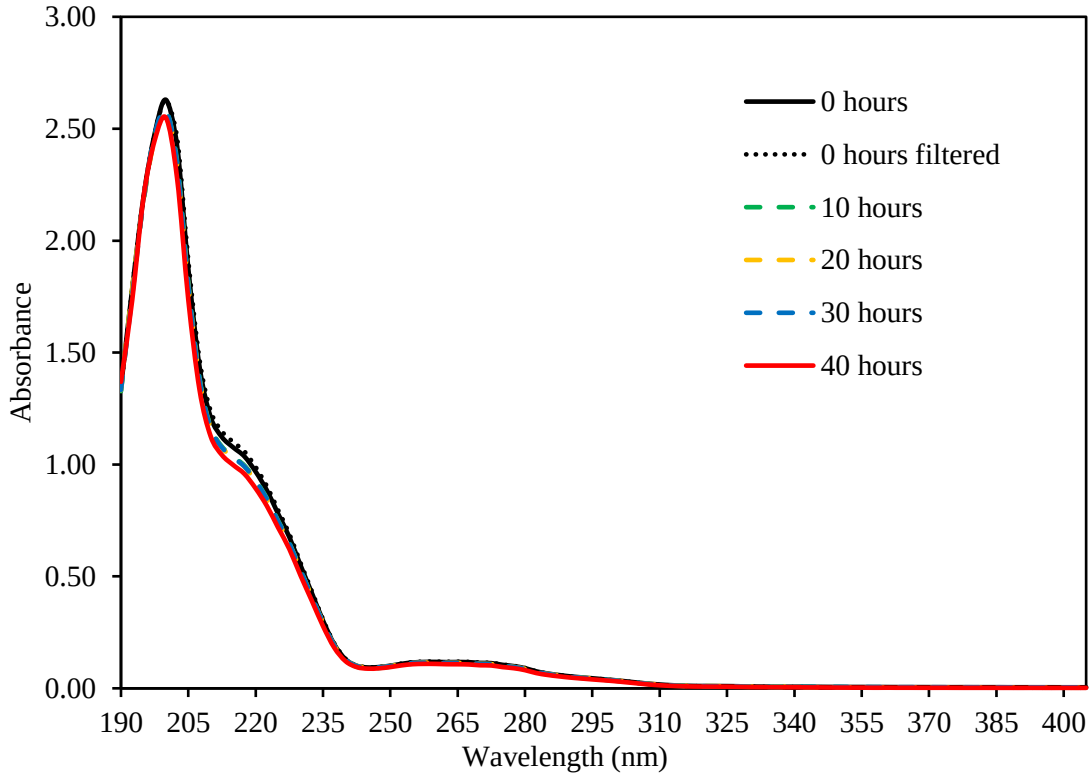

Figure A.1 Fuel 1 (BDN) discrete sample spectra for DRF 10,000 diluted samples in the 190 – 405 nm range (initial test)

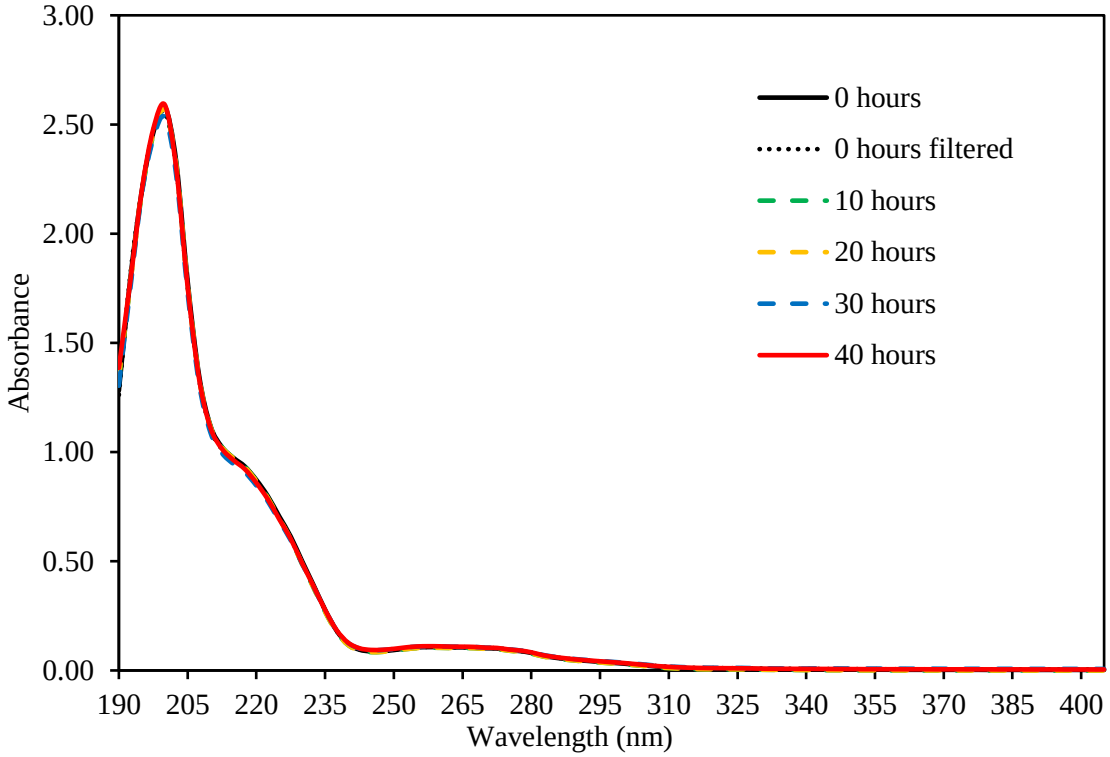

Figure A.2 Fuel 2 (B10) discrete sample spectra for DRF 10,000 diluted samples in the 190 – 405 nm range (initial test)

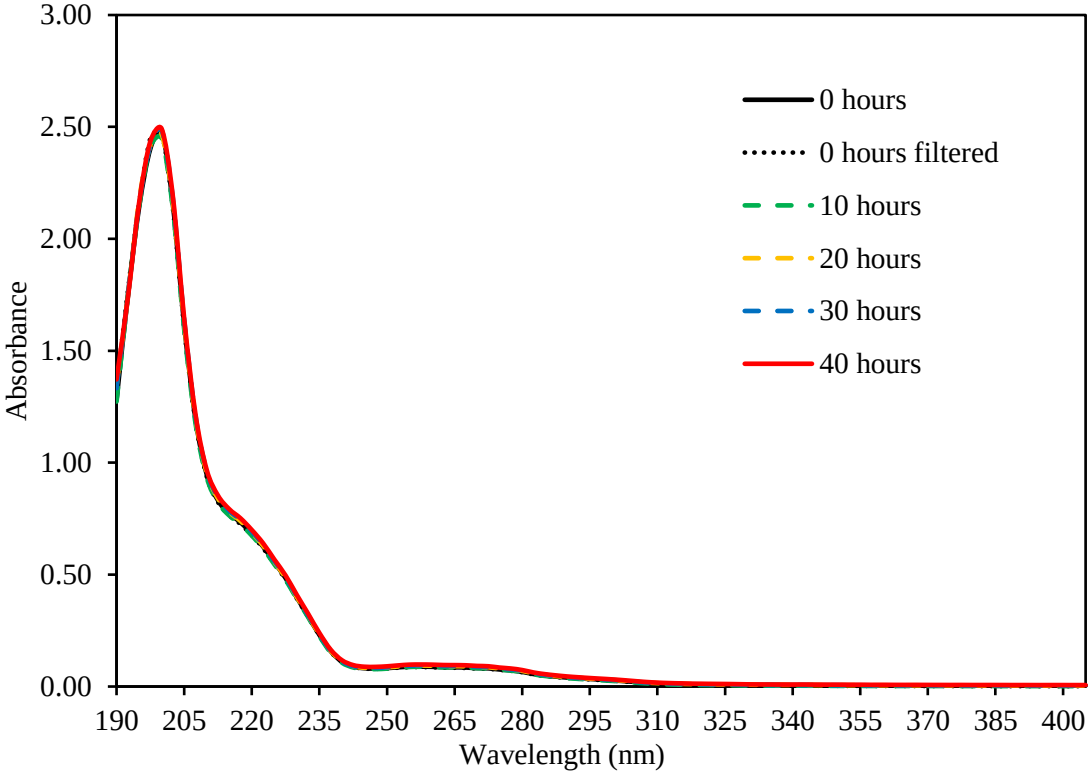

Figure A.3 Fuel 3 (B30) discrete sample spectra for DRF 10,000 diluted samples in the 190 – 405 nm range (initial test)

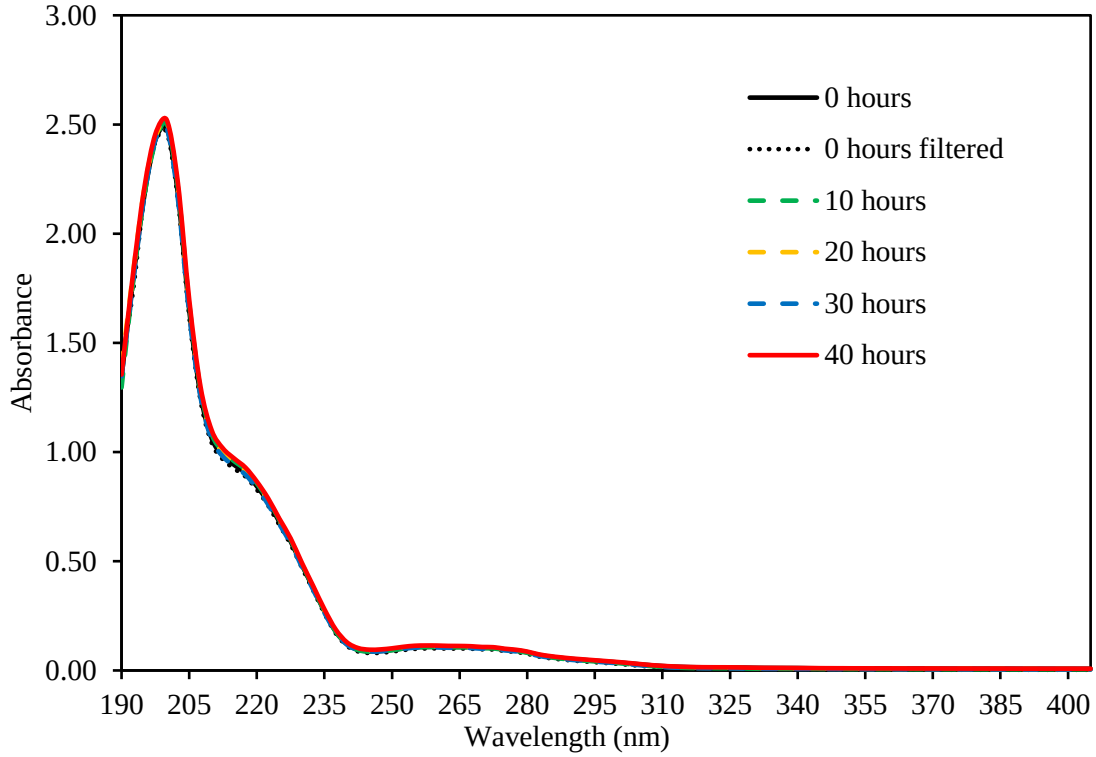

Figure A.4 Fuel 4 (BD+H) discrete sample spectra for DRF 10,000 diluted samples in the 190 – 405 nm range (initial test)

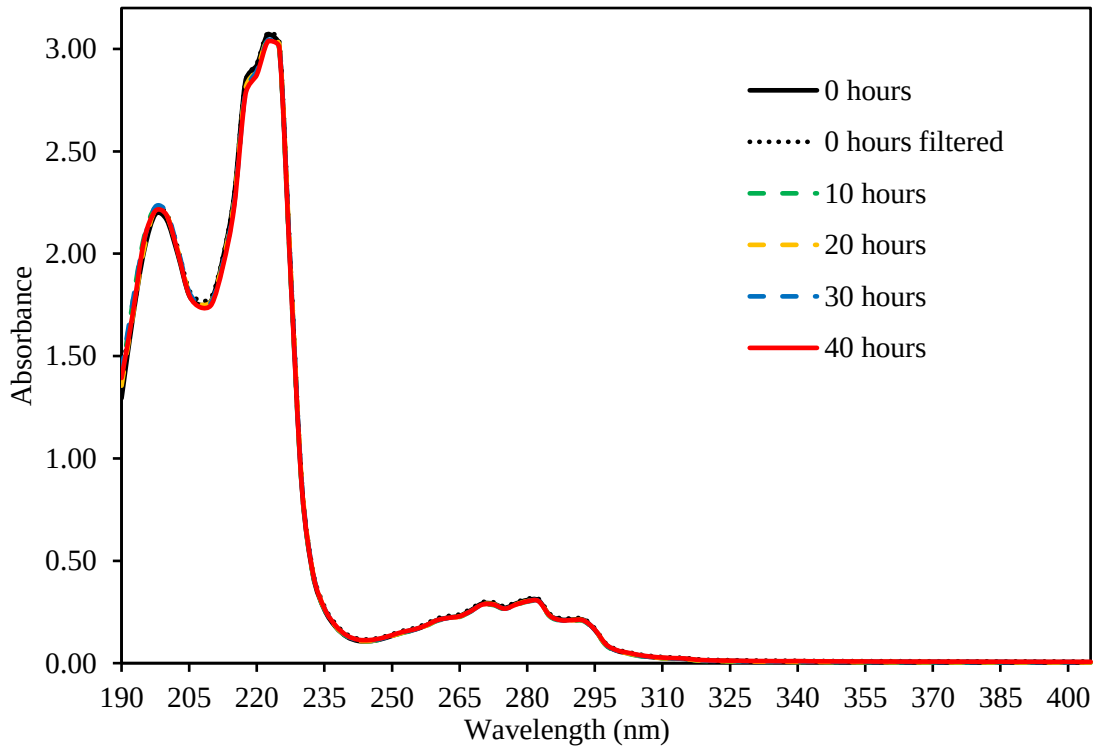

Figure A.5 Fuel 5 (BD+MN) discrete sample spectra for DRF 10,000 diluted samples in the 190 – 405 nm range (initial test)

Appendix B

Pressure Dependence Tests

B.1 *Fuel 1 (BDN) Experiments*

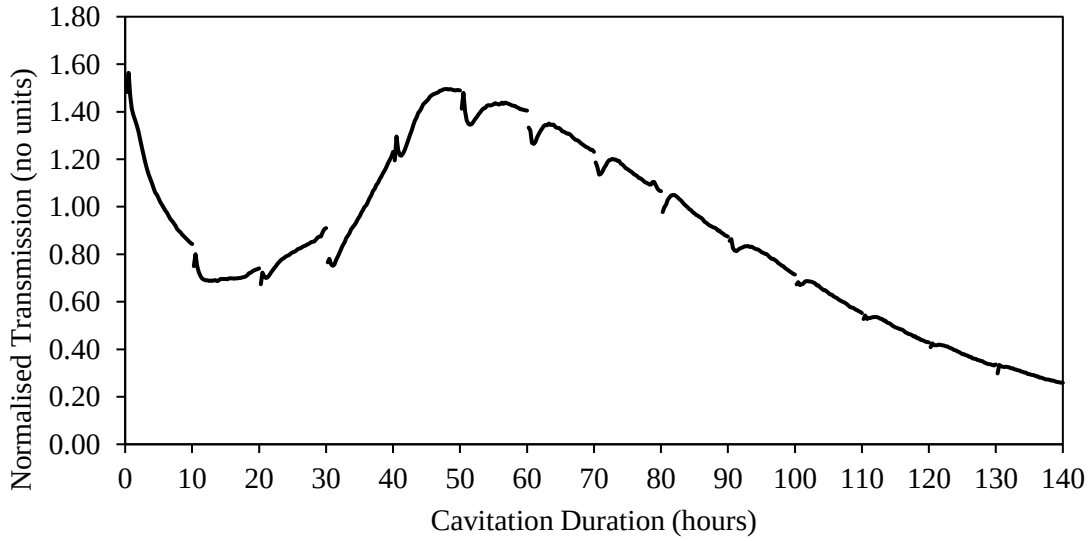

Figure B.1 Normalised spectral transmission at 405 nm against cavitation time for Fuel 1 (BDN) long-duration (140-hour) test at 1,650 bar injection pressure

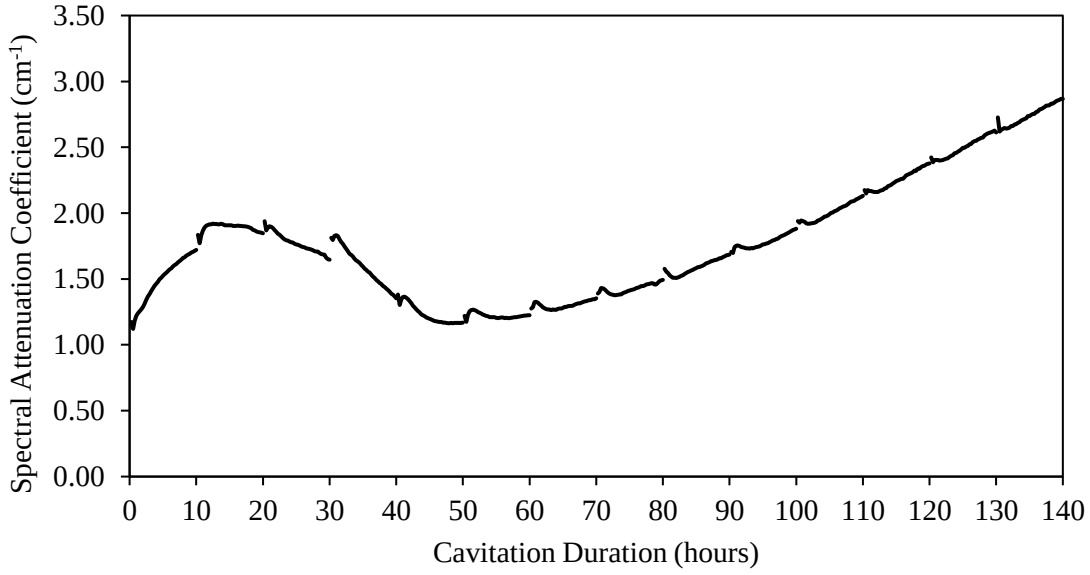

Figure B.2 Time-dependent spectral attenuation coefficient at 405 nm against cavitation time for Fuel 1 (BDN) long-duration (140-hour) test at 1,650 bar injection pressure

Appendix C

GC x GC Chromatograms for Repeated Fuel Tests

C.1 *Pre-cavitation Sample Chromatograms*

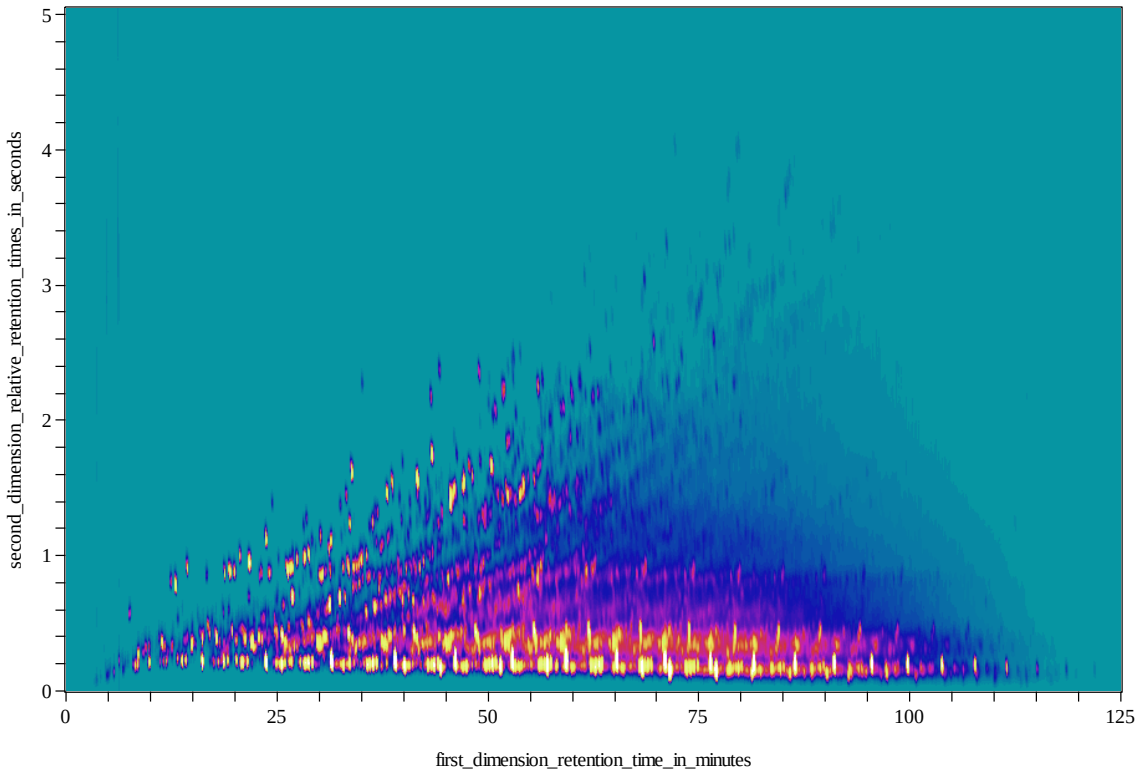

Figure C.1 GC x GC chromatogram for pre-cavitation (0 hour) sample of Fuel 1 (BDN)

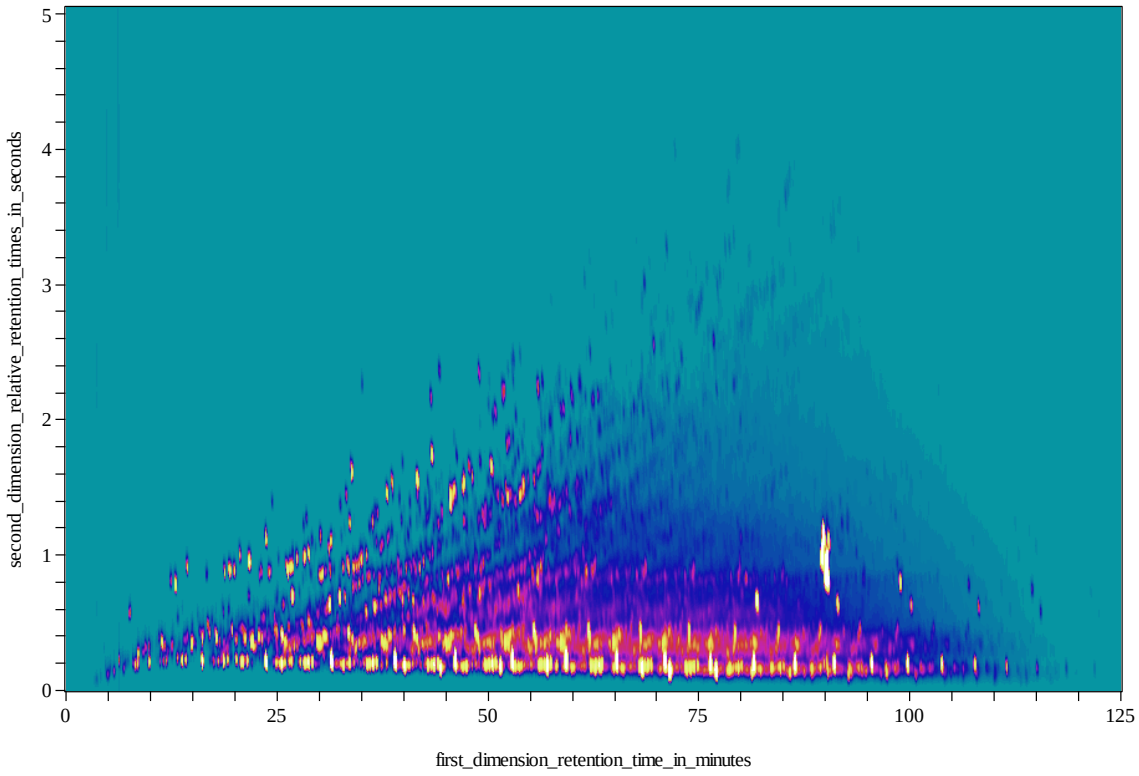

Figure C.2 GC x GC chromatogram for pre-cavitation (0 hour) sample of Fuel 2 (B10)

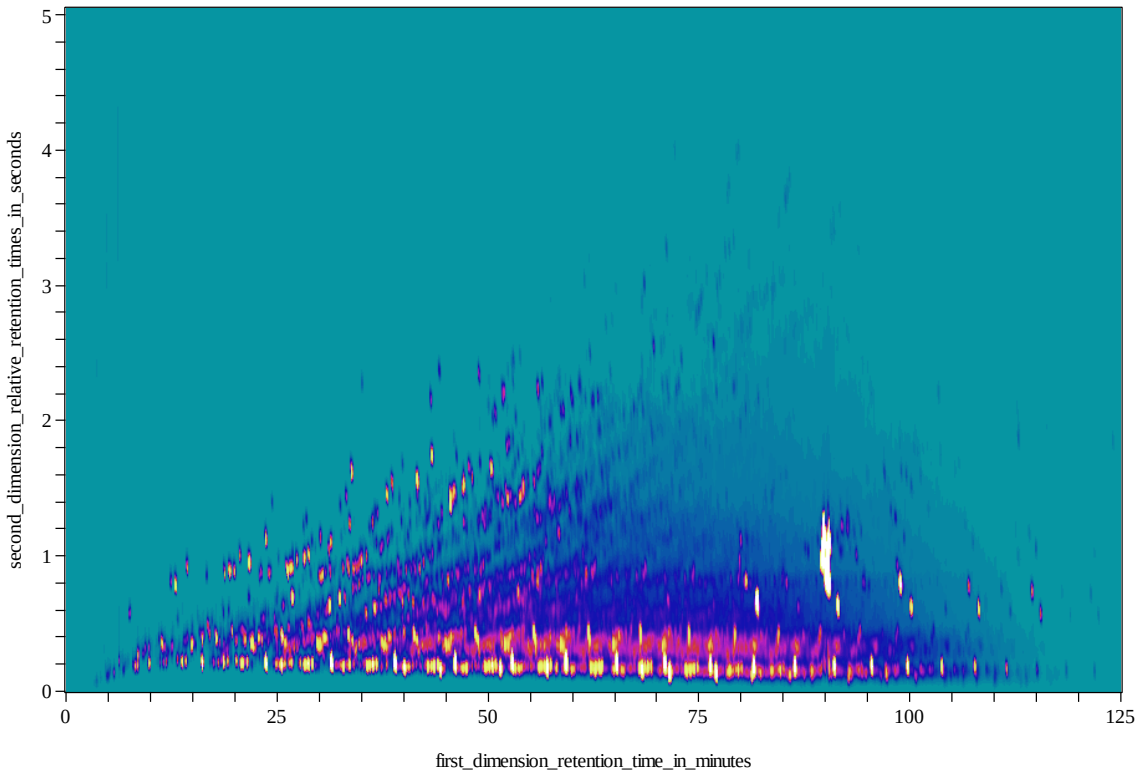

Figure C.3 GC x GC chromatogram for pre-cavitation (0 hour) sample of Fuel 3 (B30)

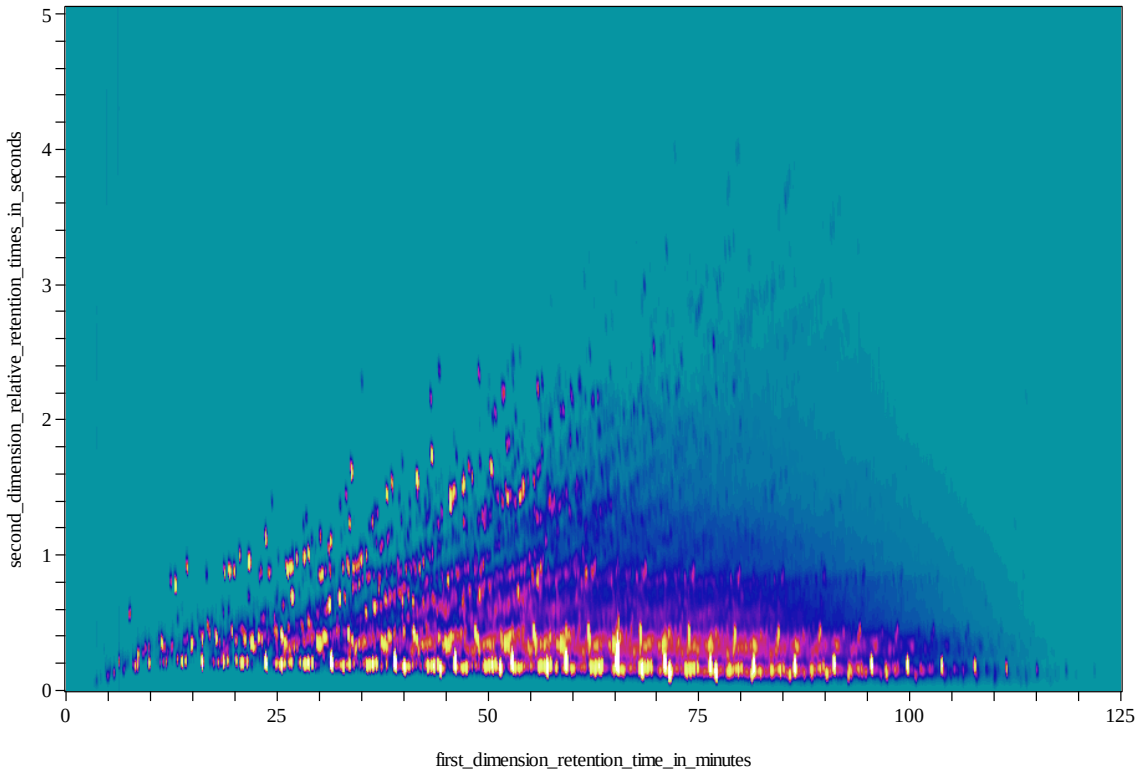

Figure C.4 GC x GC chromatogram for pre-cavitation (0 hour) sample of Fuel 4 (BD+H)

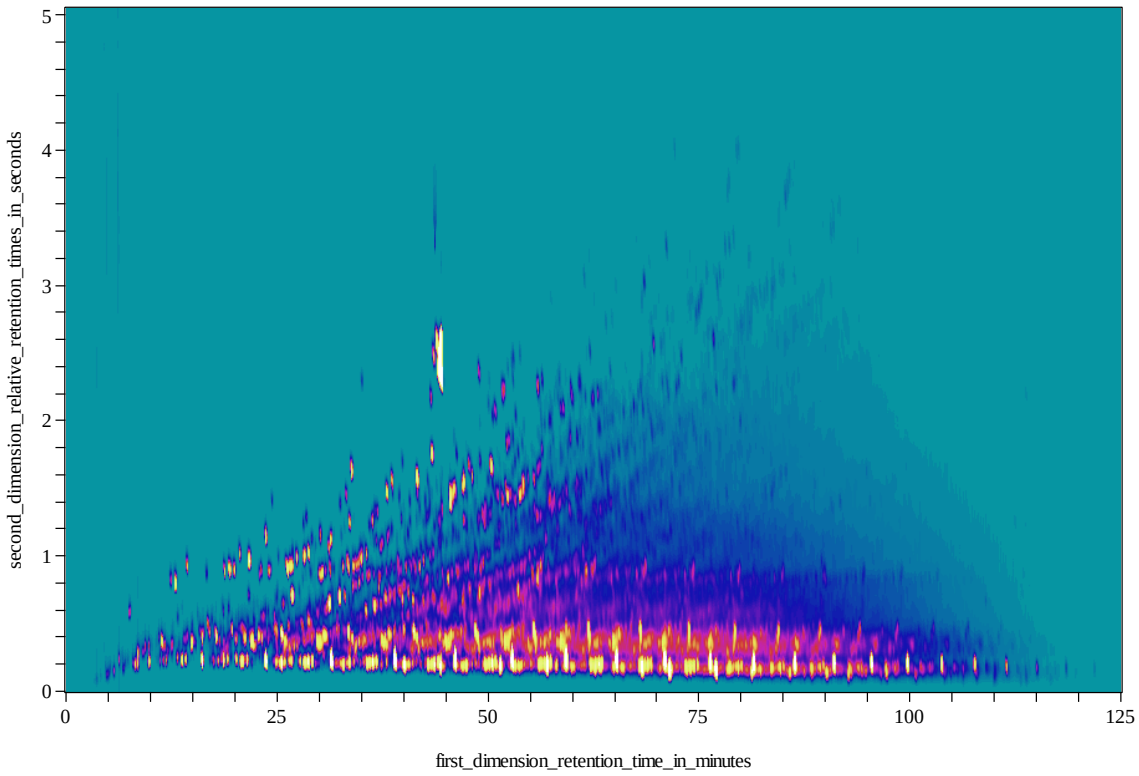

Figure C.5 GC x GC chromatogram for pre-cavitation (0 hour) sample of Fuel 5 (BD+MN)

Appendix D

Kinetic Modelling

D.1 *Model Fuel without dissolved Oxygen gas (Case I)*

Time (μs)	BIN 1	BIN 2	BIN 3	BIN 4	BIN 5	BIN 6	BIN 7	BIN 8	BIN 9	BIN 10
95.0	4.14E-19	1.71E-19	1.58E-20	6.90E-22	3.14E-24	1.91E-24	1.00E-24	4.79E-25	2.71E-25	2.36E-25
95.5	**3.51E-19**	**1.53E-19**	1.58E-20	8.53E-22	4.20E-24	2.69E-24	1.46E-24	7.08E-25	4.05E-25	3.55E-25
96.0	3.12E-19	1.36E-19	**1.40E-20**	**7.98E-22**	**4.04E-24**	**2.65E-24**	**1.45E-24**	7.10E-25	4.07E-25	3.58E-25
96.5	2.38E-19	9.90E-20	7.78E-21	4.68E-22	2.48E-24	1.73E-24	9.80E-25	**4.87E-25**	**2.82E-25**	**2.50E-25**
97.0	2.35E-19	9.29E-20	5.30E-21	2.93E-22	1.56E-24	1.09E-24	6.27E-25	3.13E-25	1.82E-25	1.62E-25
97.5	**2.84E-19**	**1.08E-19**	4.68E-21	1.92E-22	9.67E-25	6.47E-25	3.62E-25	1.79E-25	1.03E-25	9.13E-26
98.0	3.33E-19	1.26E-19	**5.68E-21**	**1.98E-22**	9.64E-25	6.12E-25	3.32E-25	1.61E-25	9.24E-26	8.11E-26
98.6	4.26E-19	1.65E-19	9.46E-21	3.34E-22	**1.64E-24**	**9.98E-25**	**5.25E-25**	**2.52E-25**	**1.43E-25**	**1.24E-25**
99.0	4.70E-19	1.85E-19	1.25E-20	5.01E-22	2.58E-24	1.58E-24	8.38E-25	4.02E-25	2.28E-25	1.99E-25
99.5	4.82E-19	1.90E-19	1.42E-20	6.49E-22	3.51E-24	2.21E-24	1.19E-24	5.73E-25	3.27E-25	2.85E-25

Figure D.1 Table showing the small temporal delay in the decrease and subsequent increase of BIN class populations for BINs 1 to 10 in the 95 - 99 μs interval, in relation to the smaller BIN classes.

Appendix E

Experimental Procedures

E.1 *High-pressure Test-rig Draining, Refilling and Flushing Procedures*

Draining Procedure for the high-pressure cavitation test-rig:

1. Make sure all equipment are turned off and mains plug for the test-rig is removed before commencing the draining procedure.
2. Use a suitable beaker/container to catch the drained fuel. It is advisable to use a 500 ml beaker for all drainage points.
3. Valve on the return line to the tank must be opened for draining. It is to be kept closed while the rig is in operation.
4. The test-rig has three drainage valves. 1. Receiver; 2. Heat Exchanger; 3. Fuel Filter. The test-rig is to be drained in this order as the vertical location of each valve is of importance.
5. Valve 1 is located at the base of the receiver (drains approximately 360 - 400 mL). The screw at the top of the receiver might need to be removed to allow the fuel to flow. Carefully place the beaker at the exit before opening the valve. Ensure that the valve is closed after the drain is completed**.
6. Valve 2 is located beneath the heat exchanger (drains approx. 460 mL). Place the beaker on the floor and put the drainage tube in the container before opening the valve. Close the valve once drained.
7. Valve 3 is located under the fuel filter (drains approx. 2050 mL). Place the beaker under the valve and open the valve. The valve will need to be opened/ closed several times

during the drain and the beaker will need to be emptied due to the large volume of fuel. Lift the hoses connected to the optical setup to allow fuel-drain from the optical setup.

8. Measure the amount of fuel extracted and compare it to the amount of fuel that was filled.
9. Clean any spills with fuel absorbent paper and absorbent sand (if required) as soon as they occur.
10. Ensure all valves, including the return valve to the tank, are closed properly and the screw in put back in place at the top of the receiver.

** Note: Depending on the receiving cylinder assembly, it is possible to have a screw instead of a valve for drainage. In case of a screw assembly, unscrew the screw from the bottom-side of the receiver. Place a beaker next to the drain hole and remove the screw from the top of the receiver to allow the fuel to flow. Once the receiver is drained, replace the two screws back to their positions.

End Matter - Appendix E

Refilling and flushing procedures for the high-pressure test-rig:

1. Before starting the refill procedure, ensure all the drain valves are closed.
2. Measure out the fuel to be refilled into a 1000 mL measuring cylinder.
3. Pour around 2500 mL of the fuel into the fuel tank, check the level marker to ensure the tank is not over-filled.
4. Following the start-up procedure, switch on the feed pump.
5. Valves on the feed and return lines of the optical system can be operated to remove trapped air from the optical setup.
6. Fill the remaining fuel quantity until the total amount of fuel in the system is around 3600 mL (2900 mL for flush).
7. Turn on the high-pressure pump and slowly turn the dial to bring the pressure to around 300 bar. Operate the rig at this pressure for 4 - 5 minutes to remove trapped air.
8. In case of flushing the test-rig, ensure there is water supply to the heat exchanger; set the HP pump pressure to around 300 bar and maintain at this level for another 45 – 60 minutes.
9. At the end of the refilling or flushing procedures turn the high HP pump dial to stop the electric motor and the pump.
10. Turn the HP pump off using the stop button.
11. Turn the feed-pump off using the stop button.
12. Press the EM stop button to stop the test-rig.
13. Turn the mains power off from the wall socket.
14. Turn the water tap off.

Safety precautions to be taken for refilling and flushing:

1. Ensure the screw on the receiver is replaced after the draining procedure.
2. The fan should be switched on for cooling the electric unit; ensure the laser is not connected to the socket.
3. Water supply must be open for cooling the fuel.
4. After the flushing duration is over, allow the fuel to cool before commencing the drainage procedure.

E.2 *Sample dilution method for UV-Visible Spectra measurements*

Preparing diluted solution of diesel samples in n-heptane.

1. Use a 4 mL cuvette that has been cleaned with n-heptane and dried completely.
2. Using a glass syringe (from Socorex Swiss) pour 2.6 mL of the diluent HPLC grade n-heptane into the cuvette.
3. Using a micro-dispenser (from Drummond) add 5 µL of the selected fuel sample to the cuvette. (dilution ratio factor DRF - 520)
4. Cap the cuvette and agitate to mix the solution well.
5. Clean the cuvette with a lint-free paper to remove any dirt or marks.
6. Place the cuvette into the spectrophotometer cell and run the spectra for the wavelength range of 240 nm to 305 nm at medium scan speed for 3 times (0.1 nm steps).
7. Repeat step 1 to step 6 further three times to get spectra of four diluted samples in the absorption range of 240 nm – 305 nm.
8. To obtain dilution for 190 nm – 405 nm range, further dilution of the first diluted sample (DRF 520) is required.
9. Add 2.6 mL of n-heptane in a 4 mL clean cuvette.

10. Using 100 μL and 20 μL micro-dispensers add 140 μL of the first diluted sample (DRF 520) into the cuvette. (approx. dilution ratio factor DRF 10,000)
11. Cap, clean and place the cuvette in the Spectrophotometer for absorption measurement in the wavelength range of 190 nm – 405 nm. Scan the sample 3 times at fast scan speed (0.5 nm steps).
12. Repeat step 9 to step 11 further three times to get spectra of four diluted samples in the absorption range of 190 nm – 405 nm.
13. The maximum absorbance at any wavelength should be below 3. In case of the absorbance being higher further dilute the solution.
14. To further dilute, remove a small (measured) volume of the solution and add n-heptane.
15. Repeat steps 5 - 9 until the maximum absorbance falls below 3.

E.3 *Sample dilution method for Laser Particle Count*

Preparing diluted solution of diesel samples in n-heptane.

1. Use the 100 mL test bottle provided by Spectrex that has been cleaned with water and ethanol and dried completely.
2. Pour 70 mL of the HPLC grade n-heptane into the bottle (measured using a measuring cylinder).
3. To start with, pour a small sample of the test diesel fuel (~1 mL) into the bottle.
4. Cap the bottle and agitate it for 15 seconds. The agitation method involves turning the bottle upside down repeatedly at a rate of ~ 2 seconds per cycle.
5. Place the bottle on the LPC stage, wait ~ 30 s to allow air bubbles to be eliminated and do a manual run, observe if the displayed count falls within the range on 600 – 1,000 counts/cc.

6. If it falls below then repeat steps 3 till 5 until the count falls within the 600 – 1,000 counts/cc range.
7. Once the desired range is reached, record the amount of fuel added to calculate dilution ratio.
8. Set the sampling time to 64 seconds on the PC.
9. Run the sample 10 - 15 times for replications.

Cleaning the test bottles and cuvettes.

1. After safely discarding the tested samples from the test bottles and cuvettes it is important to clean them out to ensure there is as little contamination as possible for the next sample.
2. Fill the bottles and cuvettes with small quantities of fresh n-heptane, agitate vigorously to clean.
3. Drain the heptane into waste bottle.
4. Leave the bottles/cuvettes to dry completely.

Bibliography

1. Horrocks, R. W. in *Advanced Direct Injection Combustion Engine Technologies and Development: Diesel Engines* (Hua Zhao) **2,** (Woodhead Publishing Limited, 2010).

2. Denbratt, I. in *Advanced Direct Injection Combustion Engine Technologies and Development: Diesel Engines* (Hua Zhao) **2,** 215 (Woodhead Publishing Limited, 2010).

3. Dohle, U., Kampmann, S., Hammer, J., Wintrich, T. & Hinrichsen, C. Advanced Diesel Common Rail Systems for Future Emission Legislation. *International Conference on Automotive Technologies-ICAT* 109–113 (2004).

4. DENSO Develops a New Diesel Common Rail System With the World's Highest Injection Pressure. at <http://www.globaldenso.com/en/newsreleases/130626-01.html>

5. Ullmann, J., Geduldig, M., Stutzenberger, H., Caprotti, R. & Balfour, G. Investigation into the formation and prevention of internal diesel injector deposits. *SAE SP* **2183,** 15 (2008).

6. Vaglieco, B. M. in *Advanced Direct Injection Combustion Engine Technologies and Development: Diesel Engines* (Hua Zhao) **2,** (Woodhead Publishing Limited, 2010).

7. Reynolds, R. *Changes in Diesel Fuel*. (2007).

8. Garrett, T. K. *Automotive Fuels and Fuel Systems: Diesel*. **2,** (Pentech Press and Society of Automotive Engineers, Inc., 1994).

9. Schwab, S. D. *et al.* Internal Injector Deposits in High-Pressure common rail diesel engines. *SAE International Journal of Fuels and Lubricants* **3,** 865–878 (2010).

10. Lacey, P., Gail, S., Kientz, J. M., Milovanovic, N. & Gris, C. Internal fuel injector deposits. *SAE International Journal of Fuels and Lubricants* **5,** 132–145 (2011).

11. Cook, S. & Richards, P. *Possible Influence of High Injection Pressure on Diesel Fuel Stability: A Review and Preliminary Study*. (2009).

12. Barker, J., Langley, G. J. & Richards, P. Insights into deposit formation in high pressure diesel fuel injection equipment. *SAE Technical Paper* (2010). doi:2010-01-2243

13. Lockett, R. D. & Jeshani, M. An experimental investigation into the effect of hydrodynamic cavitation on diesel. *International Journal of Engine Research* **14,** 606–621 (2013).

14. Altin, O. & Eser, S. Carbon deposit formation from thermal stressing of petroleum fuels. *Prepr. Pap.-Am. Chem. Soc., Div. Fuel Chem* **49,** 764 (2004).

15. Evans, D. *et al.* Thermal stressing of ultra-low sulfur diesel and low sulfur F-76 diesel fuels. in *Proceedings of the 11th International Conference on Stability, Handling and Use of Liquid Fuels* 18–22 (2009).

16. Price, R., Blazina, D., Smith, G. C. & Davies, T. J. Understanding the impact of cavitation on hydrocarbons in the middle distillate range. *Fuel* **156,** 30–39 (2015).

17. Suslick, K. S. The chemical effects of ultrasound. *Scientific American* **260,** 80–86 (1989).

18. Suslick, K. S. & Flannigan, D. J. Inside a collapsing bubble: sonoluminescence and the conditions during cavitation. *Annu. Rev. Phys. Chem.* **59,** 659–683 (2008).

19. Wellington, B. F. *Diesel engines and fuel systems*. (Barry Wellington Brisbane, 2012).

20. Lockett, R., Fatmi, Z., Kuti, O. & Price, R. An Optical Characterization of the Effect of High-Pressure Hydrodynamic Cavitation on Diesel. *SAE Technical Paper* (2016). doi:2016-01-0841

21. Suslick, K. S., Mdleleni, M. M. & Ries, J. T. Chemistry induced by hydrodynamic cavitation. *Journal of the American Chemical Society* **119,** 9303–9304 (1997).

22. Suslick, K. S., Gawienowski, J. J., Schubert, P. F. & Wang, H. H. Alkane sonochemistry. *The Journal of Physical Chemistry* **87,** 2299–2301 (1983).

23. Price, G. J. & McCollom, M. Use of high-intensity ultrasound as a potential test method for diesel fuel stability. *Fuel* **74,** 1394–1397 (1995).

24. Price, G. J. & McCollom, M. The effect of high-intensity ultrasound on diesel fuels. *Ultrasonics sonochemistry* **2,** S67–S70 (1995).

25. Misik, V. & Riesz, P. EPR study of free radicals induced by ultrasound in organic liquids II. Probing the temperatures of cavitation regions. *Ultrasonics sonochemistry* **3,** 25–37 (1996).

26. Hart, E. J., Fischer, C. H. & Henglein, A. Pyrolysis of acetylene in sonolytic cavitation bubbles in aqueous solution. *Journal of Physical Chemistry* **94,** 284–290 (1990).

27. Marketing, G. *Diesel Fuels Technical Review*. (2007).

28. Petroleum. (1998). at <hhttp://www.ems.psu.edu/~radovic/Chapter8.pdfttp://www.ems.psu.edu/~radovic/Chapter8.pdf>

29. Srivastava, S. & Hancsók, J. Fuels from Crude Oil (Petroleum). *Fuels and Fuel-Additives* 48–120 (2014).

30. Marcus, A. Diesel Fuel Basics. (1999).

31. EU: Fuels. (2015). at <https://www.dieselnet.com/standards/eu/fuel.php>

32. Srivastava, S. & Hancsók, J. Properties of Motor Fuels and Their Effects on Engines and the Environment. *Fuels and Fuel-Additives* 277–315

33. Department of Industry, S. & Resources. Operability Fuel Parameters. (2001).

34. European-Biofuels-Technology-Platform. *Fatty Acid Methyl Esters (FAME). Biofuel Fact Sheet* (2011).

35. Horrocks, R., Lawther, R. & Hatfield, L. Fuel injection systems for high-speed direct injection diesel engines. *Advanced Direct Injection Combustion Engine Technologies and Development: Diesel Engines* **2,** 61 (2009).

36. Lacey, P. *et al.* Fuel quality and diesel injector deposits. *SAE International Journal of Fuels and Lubricants* **5,** 1187–1198 (2012).

37. Barker, J., Richards, P., Snape, C. & Meredith, W. Diesel Injector Deposits-An Issue That Has Evolved with Engine Technology. *SAE Technical Paper* (2011). doi:2011-01-1923

38. Barker, J., Richards, P., Goodwin, M. & Wooler, J. Influence of High Injection Pressure on Diesel Fuel Stability: A Study of Resultant Deposits. *SAE Technical Paper* (2009). doi:2009-01-1877

39. Quigley, R. *et al.* A Study of the Internal Diesel Injector Deposit Phenomenon. in *TAE Fuels 7th Annual Colloquium* (2009).

40. Reid, J. & Barker, J. *Understanding polyisobutylene succinimides (PIBSI) and internal diesel injector deposits*. (2013).

41. Shu, G., Dong, L. & Liang, X. A review of experimental studies on deposits in the combustion chambers of internal combustion engines. *International Journal of Engine Research* **13,** 357–369 (2012).

42. Barker, J., Snape, C. & Scurr, D. A Novel Technique for Investigating the Characteristics and History of Deposits Formed Within High Pressure Fuel Injection Equipment. *SAE International Journal of Fuels and Lubricants* **5,** 1155–1164 (2012).

43. Som, S., Longman, D. E., Ramirez, A. I. & Aggarwal, S. Influence of nozzle orifice geometry and fuel properties on flow and cavitation characteristics of a diesel injector. *Fuel injection in automotive engineering. New York: InTech* 111–126 (2012).

44. Brennen, C. E. *Cavitation and bubble dynamics*. (Cambridge University Press, 2013).

45. Plesset, M. S. & Prosperetti, A. Bubble dynamics and cavitation. *Annual Review of Fluid Mechanics* **9,** 145–185 (1977).

46. Gogate, P. R., Tayal, R. K. & Pandit, A. B. Cavitation: a technology on the horizon. *Current Science* **91,** 35–46 (2006).

47. Schmidt, D. P. Cavitation in diesel fuel injector nozzles. (1997).

48. Giannadakis, E., Gavaises, M. & Arcoumanis, C. Modelling of cavitation in diesel injector nozzles. *Journal of Fluid Mechanics* **616,** 153–193 (2008).

49. Roth, H., Gavaises, M. & Arcoumanis, C. *Cavitation initiation, its development and link with flow turbulence in diesel injector nozzles*. (2002).

50. Jeshani, M. Optical characterisation of cavitating flows in diesel fuel injection equipment. (2013).

51. Rayleigh, Lord. VIII. On the pressure developed in a liquid during the collapse of a spherical cavity. *The London, Edinburgh, and Dublin Philosophical Magazine and Journal of Science* **34,** 94–98 (1917).

52. Klotz, A. R. Bubble dynamics in N dimensions. *Physics of Fluids* **25,** 082109 (2013).

53. Caupin, F. & Herbert, E. Cavitation in water: a review. *Comptes Rendus Physique* **7,** 1000–1017 (2006).

54. Franc, J.-P. & Michel, J.-M. *Fundamentals of cavitation*. **76,** (Springer, 2006).

55. Plesset, M. S. & Hsieh, D.-Y. Theory of gas bubble dynamics in oscillating pressure fields. *The Physics of Fluids* **3,** 882–892 (1960).

56. Epstein, P. S. & Plesset, M. S. On the stability of gas bubbles in liquid-gas solutions. *The Journal of Chemical Physics* **18,** 1505–1509 (1950).

57. Kuiper, G. *Cavitation in Ship Propulsion*. (2010).

58. Fujikawa, S. & Akamatsu, T. Effects of the non-equilibrium condensation of vapour on the pressure wave produced by the collapse of a bubble in a liquid. *Journal of Fluid Mechanics* **97,** 481–512 (1980).

59. Manson, T. & Lorimer, J. *Applied sonochemistry*. (Weinheim: Wiley-VCH Verlag GmbH, 2002).

60. Van Wijngaarden, L. Mechanics of collapsing cavitation bubbles. *Ultrasonics sonochemistry* **29,** 524–527 (2016).

61. Taleyarkhan, R. *et al.* Evidence for nuclear emissions during acoustic cavitation. *Science* **295,** 1868–1873 (2002).

62. Nigmatulin, R. I. *et al.* Theory of supercompression of vapor bubbles and nanoscale thermonuclear fusion. *Physics of fluids* **17,** 107106 (2005).

63. Moholkar, V., Senthil Kumar, P. & Pandit, A. Hydrodynamic cavitation for sonochemical effects. *Ultrasonics sonochemistry* **6,** 53–65 (1999).

64. Lorimer, J. P. & Mason, T. J. Sonochemistry. Part 1—the physical aspects. *Chemical Society Reviews* **16,** 239–274 (1987).

65. Bergmann, L. & Hatfield, H. S. *Ultrasonics*. *JSTOR* (1939).

66. Crum, L. A. Nucleation and stabilization of microbubbles in liquids. *Applied Scientific Research* **38,** 101–115 (1982).

67. Vazquez, G. & Putterman, S. Temperature and pressure dependence of sonoluminescence. *Physical review letters* **85,** 3037 (2000).

68. Hickling, R. Effects of thermal conduction in sonoluminescence. *The Journal of the Acoustical Society of America* **35,** 967–974 (1963).

69. Young, F. R. *Sonoluminescence*. (CRC press, 2004).

70. Barber, B. P., Hiller, R. A., Löfstedt, R., Putterman, S. J. & Weninger, K. R. Defining the unknowns of sonoluminescence. *Physics reports* **281,** 65–143 (1997).

71. Young, F. R. Sonoluminescence from water containing dissolved gases. *The Journal of the Acoustical Society of America* **60,** 100–104 (1976).

72. Flint, E. B. & Suslick, K. S. The temperature of cavitation. *Science* **253,** 1397 (1991).

73. Weninger, K., Camara, C. & Putterman, S. Energy focusing in a converging fluid flow: implications for sonoluminescence. *Physical review letters* **83,** 2081 (1999).

74. Peterson, F. B. & Anderson, T. P. Light emission from hydrodynamic cavitation. *The Physics of Fluids* **10,** 874–879 (1967).

75. Jarman, P. & Taylor, K. Light flashes and shocks from a cavitating flow. *British Journal of Applied Physics* **16,** 675 (1965).

76. Leighton, T., Farhat, M., Field, J. & Avellan, F. Cavitation luminescence from flow over a hydrofoil in a cavitation tunnel. *Journal of Fluid Mechanics* **480,** 43–60 (2003).

77. Jarman, P. & Taylor, K. Light emission from cavitating water. *British Journal of Applied Physics* **15,** 321 (1964).

78. Farhat, M., Chakravarty, A. & Field, J. E. Luminescence from hydrodynamic cavitation. in *Proceedings of the Royal Society of London A: Mathematical, Physical and Engineering Sciences* rspa20100134 (2010).

79. Arcoumanis, C., Flora, H., Gavaises, M., Kampanis, N. & Horrocks, R. *Investigation of cavitation in a vertical multi-hole injector*. (1999).

80. Gogate, P. R. & Pandit, A. B. Engineering design methods for cavitation reactors II: Hydrodynamic cavitation. *AIChE journal* **46,** 1641–1649 (2000).

81. Suh, H., Park, S. & Lee, C. Experimental investigation of nozzle cavitating flow characteristics for diesel and biodiesel fuels. *International Journal of Automotive Technology* **9,** 217–224 (2008).

82. Ghassemi, H. & Fasih, H. F. Application of small size cavitating venturi as flow controller and flow meter. *Flow Measurement and Instrumentation* **22,** 406–412 (2011).

83. Suh, H. K. & Lee, C. S. Effect of cavitation in nozzle orifice on the diesel fuel atomization characteristics. *International journal of heat and fluid flow* **29,** 1001–1009 (2008).

84. Gavaises, M. Flow in valve covered orifice nozzles with cylindrical and tapered holes and link to cavitation erosion and engine exhaust emissions. *International Journal of Engine Research* **9,** 435–447 (2008).

85. Badock, C., Wirth, R. & Tropea, C. The influence of hydro grinding on cavitation inside a diesel injection nozzle and primary break-up under unsteady pressure conditions. *Proc. 15th ILASS-Europe* **99,** 5–7 (1999).

86. Payri, R., Salvador, F., Gimeno, J. & De la Morena, J. Study of cavitation phenomena based on a technique for visualizing bubbles in a liquid pressurized chamber. *International Journal of Heat and Fluid Flow* **30,** 768–777 (2009).

87. Arcoumanis, C., Flora, H., Gavaises, M. & Badami, M. Cavitation in real-size multi-hole diesel injector nozzles. *SAE Technical Paper* (2000). doi:2000-01-1249

88. Hayashi, T., Suzuki, M. & Ikemoto, M. Effects of internal flow in a diesel nozzle on spray combustion. *International Journal of Engine Research* 1468087413494910 (2013).

89. Gavaises, M. *et al.* Comparison of cavitation formation and development in Diesel VCO nozzles with cylindrical and converging tapered holes. in *THIESEL 2008 Conference on Thermo-and fluid dynamics processes in Diesel Engines, Valencia, Spain* (2008).

90. Gavaises, M., Andriotis, A., Papoulias, D., Mitroglou, N. & Theodorakakos, A. Characterization of string cavitation in large-scale Diesel nozzles with tapered holes. *Physics of Fluids (1994-present)* **21,** 052107 (2009).

91. Andriotis, A., Gavaises, M. & Arcoumanis, C. Vortex flow and cavitation in diesel injector nozzles. *Journal of Fluid Mechanics* **610,** 195–215 (2008).

92. Misik, V. & Riesz, P. EPR characterization of free radical intermediates formed during ultrasound exposure of cell culture media. *Free radical biology and medicine* **26,** 936–943 (1999).

93. Jeffers, R. J. *et al.* Dimethylformamide as an enhancer of cavitation-induced cell lysis in vitro. *J. Acoust. Soc. Am.* **97,** 669–76 (1995).

94. Lockett, R., Fatmi, Z., Kuti, O. & Price, R. An Investigation into the Effect of Hydrodynamic Cavitation on Diesel using Optical Extinction. in *Journal of Physics: Conference Series* **656,** 012091 (2015).

95. Bouilly, J. *et al.* Biodiesel stability and its effects on diesel fuel injection equipment. *SAE Technical Paper* (2012).

96. *Instruction Manual UV-1800 Shimadzu Spectrophotometer*. (2008).

97. *Instruction Manual Spectrex Supercount Software*. (2011).

98. Bartle, K. D. & Myers, P. History of gas chromatography. *TrAC Trends in Analytical Chemistry* **21,** 547–557 (2002).

99. Górecki, T., Pani'c, O. & Oldridge, N. Recent Advances in Comprehensive Two-Dimensional Gas Chromatography (GC$\\times$ GC). *Journal of liquid chromatography \& related technologies* **29,** 1077–1104 (2006).

100. Dallüge, J., Beens, J. & Udo, A. Comprehensive two-dimensional gas chromatography: a powerful and versatile analytical tool. *Journal of Chromatography A* **1000,** 69–108 (2003).

101. Roberts, J. D. & Caserio, M. C. *Basic principles of organic chemistry*. (WA Benjamin, Inc., 1977).

102. What is a Chromophore? at <http://www.innovateus.net/science/what-chromophore#What+are+the+different+types+of+Chromophores%3F>

103. Valeur, B. & Berberan-Santos, M. N. in *Molecular fluorescence: principles and applications* 33–51 (John Wiley \& Sons, 2012).

104. Friedel, R. A. & Orchin, M. *Ultraviolet spectra of aromatic compounds*. **40,** (Wiley New York, 1951).

105. Amazon_Filters_Ltd. *Product Validation Guide - SUPASPUN II*. (2016).

106. Magalhães, K., Caires, A., Silva, M., Alcantara, G. & Oliveira, S. Endogenous fluorescence of biodiesel and products thereof: Investigation of the molecules responsible for this effect. *Fuel* **119,** 120–128 (2014).

107. Naydenova, I., Vlasov, P. & Warnatz, J. Detailed kinetic modeling of soot formation in pyrolysis of benzene/acetylene/argon mixtures. in *Proceeding of the European Combustion Meeting* (2005).

108. Ono, K. *et al.* Effect of benzene-acetylene compositions on carbon black configurations produced by benzene pyrolysis. *Chemical Engineering Journal* **215,** 128–135 (2013).

109. Ruiz, M., Callejas, A., Millera, A., Alzueta, M. & Bilbao, R. Soot formation from C< sub> 2</sub> H< sub> 2</sub> and C< sub> 2</sub> H< sub> 4</sub> pyrolysis at different temperatures. *Journal of analytical and applied pyrolysis* **79,** 244–251 (2007).

110. Ballesteros, R., Hernández, J. & Lyons, L. An experimental study of the influence of biofuel origin on particle-associated PAH emissions. *Atmospheric Environment* **44,** 930–938 (2010).

111. Cardone, M. *et al.* Brassica carinata as an alternative oil crop for the production of biodiesel in Italy: engine performance and regulated and unregulated exhaust emissions. *Environmental science \& technology* **36,** 4656–4662 (2002).

112. Durbin, T. D., Collins, J. R., Norbeck, J. M. & Smith, M. R. Effects of biodiesel, biodiesel blends, and a synthetic diesel on emissions from light heavy-duty diesel vehicles. *Environmental science \& technology* **34,** 349–355 (2000).

113. Kado, N. Y., Okamoto, R. A., Kuzmicky, P. A. & Haines, H. E. *Chemical and Bioassay Analyses of Diesel and Biodiesal Particulate Matter: Pilot Study*. (Department of Environmental Toxicology, University of California for Montana State Department of Environmental Quality and US Department of Energy, 1996).

114. Kulkarni, M. G. & Dalai, A. K. Waste cooking oil an economical source for biodiesel: a review. *Industrial \& engineering chemistry research* **45,** 2901–2913 (2006).

115. Pyl, S. P. *et al.* Rapeseed oil methyl ester pyrolysis: On-line product analysis using comprehensive two-dimensional gas chromatography. *Journal of Chromatography A* **1218,** 3217–3223 (2011).

116. Karavalakis, G., Bakeas, E., Fontaras, G. & Stournas, S. Effect of biodiesel origin on regulated and particle-bound PAH (polycyclic aromatic hydrocarbon) emissions from a Euro 4 passenger car. *Energy* **36,** 5328–5337 (2011).

117. Richter, H. & Howard, J. Formation of polycyclic aromatic hydrocarbons and their growth to soot—a review of chemical reaction pathways. *Progress in Energy and Combustion Science* **26,** 565–608 (2000).

118. Karavalakis, G. *et al.* Effects of low concentration biodiesel blends application on modern passenger cars. Part 3: Impact on PAH, nitro-PAH, and oxy-PAH emissions. *Environmental Pollution* **158,** 1584–1594 (2010).

119. Chieh, C. Chemical Kinetics. at <http://www.science.uwaterloo.ca/~cchieh/cact/c123/chmkntcs.html>

120. Smith, O. I. Fundamentals of soot formation in flames with application to diesel engine particulate emissions. *Progress in Energy and Combustion Science* **7,** 275–291 (1981).

121. Frenklach, M. & Wang, H. Detailed modeling of soot particle nucleation and growth. in *Symposium (International) on Combustion* **23,** 1559–1566 (1991).

122. Saggese, C. *et al.* Kinetic modeling of particle size distribution of soot in a premixed burner-stabilized stagnation ethylene flame. *Combustion and Flame* **162,** 3356–3369 (2015).

123. Marinov, N. M. *et al.* Aromatic and polycyclic aromatic hydrocarbon formation in a laminar premixed n-butane flame. *Combustion and flame* **114,** 192–213 (1998).

124. Westbrook, C. K., Pitz, W. J., Herbinet, O., Silke, E. & Curran, H. *A detailed chemical kinetic reaction mechanism for n-alkane hydrocarbons from n-octane to n-hexadecane*. (2007).

125. Bonifacio, A. City, University of London, Private communication. (2017).

126. Bonifacio, A. City, University of London. PhD Thesis to be published. (2018).